



Charge and spin dynamics in a hybrid circuit quantum electrodynamics architecture

Jeremie Viennot

► To cite this version:

Jeremie Viennot. Charge and spin dynamics in a hybrid circuit quantum electrodynamics architecture. Mesoscopic Systems and Quantum Hall Effect. Ecole Normale Supérieure de Paris - ENS Paris, 2014. English. <tel-01062841>

HAL Id: tel-01062841

<https://tel.archives-ouvertes.fr/tel-01062841>

Submitted on 10 Sep 2014

HAL is a multi-disciplinary open access archive for the deposit and dissemination of scientific research documents, whether they are published or not. The documents may come from teaching and research institutions in France or abroad, or from public or private research centers.

L'archive ouverte pluridisciplinaire **HAL**, est destinée au dépôt et à la diffusion de documents scientifiques de niveau recherche, publiés ou non, émanant des établissements d'enseignement et de recherche français ou étrangers, des laboratoires publics ou privés.

Département de Physique de l'École Normale Supérieure



laboratoire pierre aigrain
électronique et photonique quantiques

THÈSE de DOCTORAT de L'ÉCOLE NORMALE SUPÉRIEURE

Spécialité : Physique
Ecole doctorale de Physique en Ile-de-France (ED 564)

présentée par

Jérémie Viennot

Pour obtenir le titre de
DOCTEUR de l'ÉCOLE NORMALE SUPÉRIEURE

Sujet de la thèse :

**CHARGE AND SPIN DYNAMICS IN A HYBRID CIRCUIT
QUANTUM ELECTRODYNAMICS ARCHITECTURE**

Soutenue le 6 juin 2013 devant le jury composé de :

M.	Wolfgang WERNSDORFER	Rapporteur
M.	Gary STEELE	Rapporteur
M.	Daniel ESTEVE	Président du Jury
Mme.	Hélène BOUCHIAT	Examinateur
M.	Jean-Michel RAIMOND	Examinateur
M.	Takis KONTOS	Directeur de thèse

“Tout est facile, tout est difficile.”

Jedi master

Abstract

This thesis investigates experimentally the coupling mechanism of the charge and spin degrees of freedom in double quantum dots to high finesse superconducting microwave cavities. We use carbon nanotubes as a coherent conductor to host our quantum dots. As shown in chapter 3, we conceived an experimental setup and developed new fabrication methods in order to achieve control over these devices. With these methods, we scrutinize the resonant coupling of the dot's charge electronic transitions to a microwave cavity. We drive the system out of equilibrium to characterise its dynamics and extract its relevant intrinsic parameters, see chapter 5. We examine a possible coupling of single photons to a single electron spin, using non-collinear exchange fields induced from ferromagnetic interfaces as a key ingredient to engineer this coupling. The preliminary results in this circuit architecture, presented in chapter 6, are promising for future spin-based QED experiments with single spins.

Résumé

Cette thèse étudie expérimentalement le mécanisme de couplage entre les degrés de liberté de charge et de spin dans des doubles boîtes quantiques et des cavités supraconductrices de grande finesse. Nous utilisons des nanotubes de carbone comme conducteurs cohérents pour nos boîtes quantiques. Comme nous le montrons dans le chapitre 3, nous avons conçu une expérience et développé de nouvelles méthodes de fabrication afin de pouvoir contrôler ces dispositifs. Avec ces méthodes, nous examinons le couplage résonant entre les transitions électroniques de charge dans les boîtes quantiques et la cavité micro-onde. Nous poussons le système hors équilibre pour caractériser sa dynamique et extraire ses paramètres intrinsèques, voir chapitre 5. Nous étudions la possibilité d'un couplage de photons uniques avec un spin électronique individuel, en utilisant des champs effectifs non colinéaires induits par des interfaces ferromagnétiques comme ingrédient clef pour construire ce couplage. Les résultats préliminaires dans cette architecture en circuit, présentés dans le chapitre 6, sont prometteurs pour de futures expériences d'électrodynamique quantique en cavité avec des spins uniques.

Acknowledgements

Je tiens d'abord à exprimer ma gratitude envers les membres du jury qui ont accepté de prendre de leur temps pour porter attention à mon travail, Gary Steele, Wolfgang Wernsdorfer, Daniel Esteve, Hélène Bouchiat, et Jean-Michel Raimond.

Je me dois de remercier chaleureusement toutes les personnes qui m'ont aidé, pendant ce temps de la thèse, à toujours aller de l'avant, en direction des objectifs fixés et en dépit des innombrables difficultés rencontrées. Dans cette marche en avant, le premier acteur a bien sûr été Takis Kontos. Merci d'avoir partagé quotidiennement, culture, créativité, savoir faire, intuitions fines mais aussi motivation et optimisme, tout ceci avec une grande générosité. J'ai d'abord appris énormément, depuis les détails techniques qui font la différence jusqu'aux concepts fondamentaux importants; cette fructueuse collaboration fut un réel plaisir. Mes remerciements vont aussi à toutes les personnes qui ont fait partie de l'équipe HQC. Matthieu Delbecq d'abord, avec qui j'ai passé deux belles années au labo, mais aussi quelques soirées mémorables à Paris et ailleurs. Matthieu Dartailh qui s'est très vite adapté à la manip et qui, j'en suis sûr, saura faire parler son efficacité pour taquiner le spin de plus près. Laure, toujours souriante et entière (et aussi toujours prête à bavarder ;-). Matthieu Desjardins avec qui j'ai pu partager de bons moments à maniper et grimper, des Alpes à Bleau, malgré ses dîners intempestifs. Matthieu (encore un?!) Baillergeau, je suis sûr que les photons THz ne vont pas tarder à se montrer dans les tubes. Dora et Subha pour leur *legendary pairing*. Audrey Cottet pour son réalisme et son efficacité précieuse pour la théorie. Merci à tous nos très proches cousins de la méso, Benjamin Huard, Bernard Placais, Francois Mallet et Gwendal Fève avec qui j'ai eu la chance de pouvoir discuter et apprendre maintes et maintes fois. Merci à Emmanuel Flurin, Quentin Wilmart, Landry Bretheau, Andreas Inhofer, Phillippe Campagne, Arthur Marguerite, Mohamed Boukhicha, Danijela Markovic, Vincent Freulon pour des échanges scientifiques ou moins scientifiques, mais toujours plaisants et constructifs. Leur bonne humeur permet de travailler tous les jours dans une ambiance vraiment agréable. Merci aux plus anciens, qui m'ont intronisé dans l'équipe méso de la meilleure manière qui soit, Nicolas Roch, Erwan Bocquillon, Andi Betz, Jean-Damien Pillet, Francois Parmentier et Emiliano Pallecchi. Je tiens aussi à exprimer ma gratitude à tous les gens du département qui ont rendu ce travail possible. Merci à Michael Rosticher et José Palomo pour leur aide et leur patience, indispensables en salle blanche. Merci à Olivier Andrieu et Aurélien, infaillibles, qui nous ont permis de maniper jusque dans les moments les plus critiques. Merci à Didier Courtiade et toute son équipe, Célia , Catherine, David et Cyril. Ils ont beaucoup contribué à l'allure qu'à

la manip et le labo aujourd’hui. Merci à Jack Olejnik, Pascal Morfin, Jules Silembo et tous les membres de l’atelier mécanique qui nous ont permis de monter la manip en s’adaptant à nos besoins. Merci à David Darson, Anne Denis et Philippe Pace qui ont eu la patience de dessiner nos PCB et d’accéder à nos requêtes parfois un peu extrémistes. Merci à Jean-Marc Berroir pour une direction de laboratoire juste et diplomatique, indispensable au bon déroulement de nos recherches. Merci à Anne Matignon et Fabienne Renia pour leur efficacité même quand les commandes pleuvent. Merci à Yann Colin et Zaïr Dissi grâce à qui j’ai pu maniper en toute circonstance, depuis mon balcon ou sur l’oreiller.

Je tiens aussi à exprimer ma reconnaissance envers ceux qui ont assuré l’intendance de la soutenance, mes parents, Stina et Armand.

Merci aux Jourdanais qui m’ont suivi et supporté. Armand, Anne, Maxime, Olivia et Katten, je garderai un souvenir tout particulier de ces années. Merci à Thierry, Oriane et Hugo pour leur soutien, la porte sera toujours ouverte. Merci à Jean-René, Dmitry, Hugo et Xavier pour leur potentiel de remotivation, les bonnes séances et quelques séjours à Paris et ailleurs; les falaises du Colorado vous attendent de pied ferme. Merci à Manu, Louis, Cédric et Matou pour quelques bonnes barres de rire.

Merci à Claire, Joseph, Sarah, Gauthier, Amélie, Ben, Nico, Ida, Etienne et Augustine pour leur confiance, leur disponibilité et bien plus encore. Tack till familjen Lindén för ert stöd. Enfin merci à Stina, pour ces années avec ces rires, ces voyages, ces complicités et cette attention que j’espère partager encore longtemps. Tack så jättemycket för att du följer med mej, jag gillar dej.

Contents

	Page
Acknowledgements	iv
Acronyms and notations	1
1 Introduction	4
2 Double quantum dots for spin qubits	13
2.1 Spectrum and basic transport properties of double quantum dots	14
2.1.1 Characteristic energy scales	14
2.1.2 Stability diagram	15
2.1.3 Master equation	17
2.1.4 Out of equilibrium transport	19
2.2 Charge qubit in a double quantum dot	20
2.3 Existing spin qubit architectures	21
2.4 The ferromagnetic spin qubit proposal	22
2.4.1 Ferromagnetic interface-induced exchange fields in coherent conductors	23
2.4.2 Principle of the ferromagnetic spin qubit	24
2.4.3 Predictions and main features	26
3 Experimental methods	29
3.1 Nanofabrication	30
3.1.1 Standard nanofabrication techniques	30
3.1.2 Resonator fabrication for hybrid quantum dot - cQED devices . .	34
3.1.3 CNT growth, localisation, and contacting	35
3.1.4 Novel stamping technique for dry transfert of CNT's	36
3.1.5 Discussion	38
3.2 Measurement techniques	41
3.2.1 Low temperature setup	42
3.2.2 DC measurement	45
3.2.3 Microwave measurements	46
4 Double quantum dots for hybrid cQED: presentation and theoretical background	51
4.1 Interest of the use of cQED techniques	52
4.2 Coupling mechanism and low frequency picture	53

4.2.1	Definitions and basics	53
4.2.2	Low frequency limit: single dot picture	56
4.2.3	Coupling to leads and coupling to local gates	59
4.2.4	Low frequency capacitance of a double dot	60
4.2.5	Coupling to weakly detuned transitions	62
4.3	Equation of motion for a DQD charge qubit in a cavity	65
4.3.1	Master equation	65
4.3.2	Linear regime	68
4.3.3	Finite DC bias	69
4.3.4	Large number of photons	69
4.3.5	Microwave ("two-tone") spectroscopy	70
4.4	Input-output theory for resonator transmission phase and amplitude measurements	72
4.5	Parasitic transmission, <i>Fano</i> -shaped resonances and quadrature offsets . .	74
5	Charge qubit in a microwave cavity	77
5.1	Linear regime	78
5.1.1	Symmetric coupling	78
5.1.2	Asymmetric coupling	82
5.2	Out of equilibrium	87
5.2.1	Finite bias	88
5.2.2	Finite microwave power	88
5.3	Microwave spectroscopy	90
5.4	Decoherence and charge noise	92
6	Possible spin-photon coupling in a cQED architecture	94
6.1	Equation of motion for the Ferromagnetic spin qubit	95
6.1.1	Multilevel equation of motion	96
6.1.2	Experimentally possible regimes and associated cavity response .	97
6.2	Ferromagnetic interfaces	100
6.2.1	Magnetic Force Microscope (MFM) characterisation	100
6.2.2	Double quantum spin valve	100
6.3	Superconducting resonator measurement with external magnetic field . .	103
6.4	Magnetic field dependence of the dispersive shift	103
6.5	Microwave spectroscopy	107
6.6	Discussion and perspectives	109
7	Conclusion and perspectives	112
A	Nanofabrication processes	116
B	Dilution fridge wiring, RF setup and DC current amplification	121
B.1	Heat current - DC wires	121
B.2	Heat current - Microwave coaxial cables	122
B.2.1	General idea	122
B.2.2	Estimation of the heat power going down the fridge through the microwave wires	124

B.3	Radiation power on the microwave wires	126
B.4	Thermalisation and filtering of the DC lines	127
B.4.1	Methods	127
B.4.2	Thermalisation length	127
B.5	Attenuation, filtering and thermalisation of the microwave lines	129
B.6	Home made DC current analog amplifier	130
C	Supplementary DC current experiment	133
C.1	Observation of multiple orbital anti-crossings	133
C.2	Scattering matrix theory	135
Bibliography		138

Acronyms

AC	Alternative current
AFM	Atomic force microscope
B/AB	Bonding/Anti-bonding
CNT	Carbon nanotube
CPW	Coplanar waveguide
cQED	circuit quantum electrodynamics
CVD	Chemical vapour deposition
DC	Direct current
DQD	Double quantum dot
EOM	Equation of motion
ESR	Electron spin resonance
IPA	Isopropanol
LO	Local oscillator
MIBK	Methyl-iso-butyl ketone
NMR	Nuclear magnetic resonance
PCB	Printed circuit board
PMMA	Poly methyl methacrylate
QD	Quantum dot
QED	Quantum electrodynamics
QND	Quantum non demolition
RF	Radio frequency
RIE	Reactive ion etching
RMS	Root mean square
SEM	Scanning electron microscope
SMA	SubMiniature version A (microwave connector norm)
SNR	Signal to noise ratio
SWNT	Single wall carbon nanotube
TMR	Tunnelling magneto-resistance
UHV	Ultra high vacuum
UV	Ultra-violet
VNA	Vectorial network analyser
2DEG	Two-dimensional electron gas

Notations

$\alpha_{i/d}$	Capacitive lever-arm of electrode i on dot d
δ	Exchange field (or effective Zeeman splitting)
Δ	Frequency detuning between qubit and drive frequency (unless specified)
Δ_{cd}	Frequency detuning between cavity and drive frequency
ϵ	Energy detuning between the dots of the double quantum dot
ϵ_{in}	Driving amplitude at the input of the cavity
γ	Relaxation rate of the charge qubit
γ_{ij}	Relaxation rate of transition ij in a multilevel system
γ_d	Bare coupling rate of dot d to its nearest reservoir
Γ_2	Decoherence rate of the charge qubit (inverse of T_2^*)
$\Gamma_{2,ij}$	Decoherence rate of transition ij
Γ_ϕ	Pure dephasing rate of the charge qubit
$\Gamma_{lead,d}$	Dressed coupling rate of dot d to its nearest reservoir
Σ	Energy direction perpendicular to ϵ , (average energy of the two dots)
σ_ϵ	Noise spectral density coefficient
σ_n	Population operator of state labelled n
σ_-	Lowering operator
κ	Cavity decay rate (or bandwidth)
$\kappa_{in(out)}$	Cavity decay rate due to loss at the in(out)put port of the cavity
$\mu_{1(2)}$	Electrochemical potential of lead 1(2)
μ_B	Bohr magneton
χ	Charge susceptibility
χ_{ij}	Susceptibility of transition ij coupled to the resonator
φ	Microwave phase
$\Delta\varphi$	Microwave phase variation due to frequency shift
ψ	Electron wavefunction
ξ_0	Bare orbital level
ξ	Dressed orbital level
ρ	Density matrix operator
θ	Angle between the magnetizations of the ferromagnets (unless specified)

Ω	Larmor frequency of the charge qubit
ω_c	Cavity frequency
Ω_{ij}	Frequency of transition ij
B	External magnetic field
C_{gd}	Capacitance from dot d to its nearest local gate
C_{Ld}	Capacitance from dot d to its nearest lead
$C_{c,gd}$	Coupling capacitance between local gate d to the resonator pin
$C_{c,Ld}$	Coupling capacitance between lead d to the resonator pin
C_m	Capacitance between two coupled dots
$C_{\Sigma d}$	Sum of all capacitances on dot d
C_{res}^L	Linear capacitance of the resonator pin to ground
C_{res}	Total capacitance of the resonator to ground
L_{res}	Total inductance of the resonator
C_Q	Quantum capacitance
e	Electron charge
E_n	Eigenenergy of state labelled n
g_0	Charge-photon bare coupling strength
$g_{(ij)}$	Dressed coupling strength (to the ij transition)
f_c	Cavity fundamental mode frequency
Δf_c	Cavity frequency shift
k_B	Boltzmann constant
n_{ph}	Number of photons in the cavity
n	Charge number operator in a single dot
t	inter-dot tunnel coupling (except when it appears in time derivatives $\frac{d}{dt}$)
T	temperature
$U_{(d)}$	Coulomb charging energy on the dot (dot labelled d)
U_m	Mutual charging energy between two coupled dots
V_{gi}	Gate voltage labelled i
V_{SD}	Source-drain or bias voltage
V_i	Electrical potential on electrode i

Chapter 1

Introduction

Light-matter interaction is both a fascinating fundamental phenomenon and a powerful tool when used to control quantum machines, i.e. machines that exploit the laws of quantum mechanics to perform specific tasks. Matter is constituted of atoms holding clouds of electrons that carry a charge and therefore naturally interact with electric fields associated to light. This interaction holds at microscopic scales and single electron charges can for instance couple to single microwave photons via electric dipole (or electrostatic) interaction. This has been explored experimentally in the most essential context of single atoms interacting with single photons [1]. Electrons also carry a spin and it is the basis of magneto- or spin-electronics (*spintronics*), which studies how to control this degree of freedom in solid-state systems [2]. This thesis is taking concepts from both these fields and aims at controlling single electron spins with single photons.

Spins are generally loosely coupled to their environment, and although they can magnetically interact with photons, this effect is often weak when it comes to single photons with single electronic spins. Besides in a solid-state context, electrons interact with a complex environment that causes decoherence by randomly extracting and concealing information. One can then wonder whether it is possible to engineer a light-matter state where a spin and a photon exchange information at a rate faster than they interact with their environment. It is the purpose of this thesis to try to answer this question. This work takes place at a mesoscale, where objects are big enough to be engineered with macroscopic human-sized tools, but small enough to behave like microscopic quantum objects. The systems we consider are quantum dots and microwave cavities.

Quantum transport, quantum dots and spintronics

Since the first observation of electrical conductance quantization across a single channel [3], transport properties of many different mesoscopic systems have been explored, including various types of quantum dots. Quantum dots are electron boxes which can be formed by confining electronic charges in space using local electrostatic gate potentials [4]. The resulting quantized spectrum resembles that of an atom, and one can study the coupling of this artificial atom to metallic continua. Among possible conductors used to build quantum dots, carbon nanotubes are interesting because they provide a molecular, nearly atomistic one-dimensional host material [5]. Although growth and control of carbon nanotubes (CNT) is very challenging, they can still be handled at a macroscopic scale, nowadays with promising techniques in terms of scalability [6, 7] (see figure 1.1). It is also possible to couple CNT quantum dots to various metallic orders such as superconducting or ferromagnetic, and study proximity effects in these systems [8, 9]. CNT's are thus very versatile, and can be employed in many contexts, from molecular spintronics [10], to magnetic sensing [11] or mass sensing [12]. A CNT quantum dot connected to ferromagnetic leads constitutes a spin-valve [13], that is one of the basic building blocs of spintronics. Understanding magnetism at this scale, with a single transport channel, is of fundamental interest, but could also be used as a way to achieve local control over single spins [14].

Such a local spin control is essential for proposals in which quantum dots are taken as a platform for quantum computation using electronic spins [15]. The first coherent manipulations of a quantum dot spin qubit were demonstrated nearly a decade ago (in GaAs [16], figure 1.2). Although performance and scalability of solid state spin qubits have not improved as much as superconducting qubits (presented below), they still represent an alternative scheme for quantum computation. They also involve a complex environment, in which fundamental questions such as decoherence in many-body systems could be addressed.

Cavity and circuit quantum electrodynamics

It is possible to explore experimentally the fundamental physics related to the interaction of isolated single atoms with single photons trapped in a cavity. It has given rise to *cavity quantum electrodynamics* which is an active field of research for a couple of decades. In these experiments, prepared atoms are sent through a very high finesse Fabry-Perot cavity behaving as a quantum harmonic oscillator (figure 1.3). The interaction between these atoms and the photons in the cavity is governed by the most basic laws of quantum mechanics, that one can probe here by looking at the atomic state once it flies off the

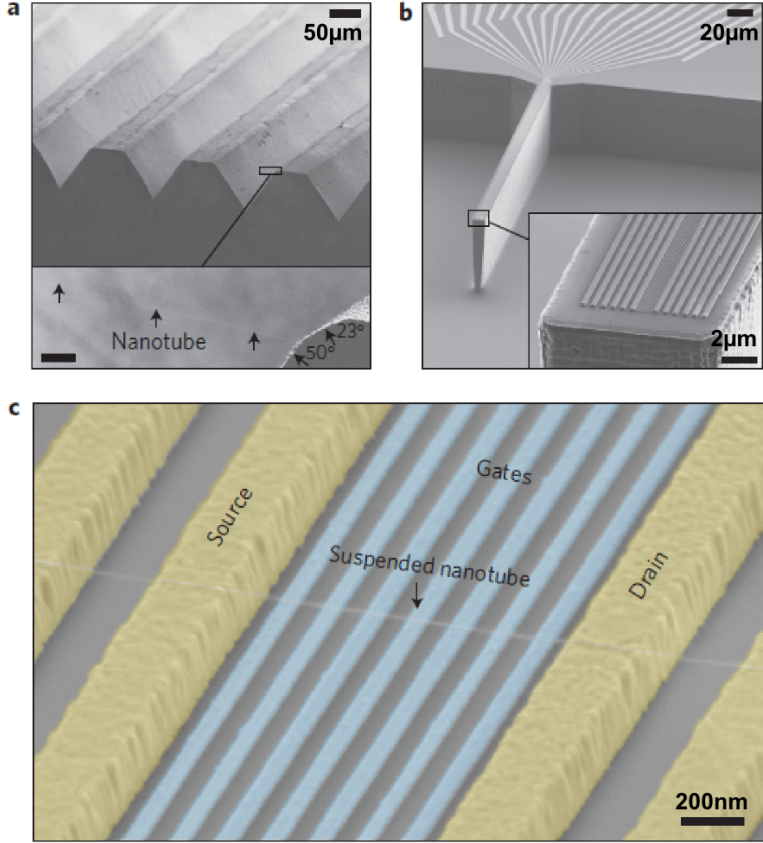


FIGURE 1.1: Scanning electron microscope (SEM) images showing an ultra-clean nanotube device fabricated deterministically. (a) Suspended nanotubes are grown between trenches. Bottom: zoom-in on a trench edge showing a single nanotube grown across the trench. (b) Circuit chip, patterned on a Si/SiO₂ wafer. Inset: zoom-in to the tip. (c) A nano-assembled device with a single nanotube connected to contacts (yellow) and suspended at a height of 130nm over seven gates. Source: [7]

cavity. Such an experiment allows for instance to prepare and characterise non-classical states of light and recently, active quantum feedback has been demonstrated to stabilize Fock States [17].

In the rather disconnected community of mesoscopic physics, pioneering experiments have shown how the rigidity and robustness of the superconducting phase can be used to engineer a macroscopic system into an effective quantum two-level system [18]. This has opened the way towards quantum information experiments with circuits instead of atoms, with a great potential in terms of scalability coming along. Since the breakthrough of a decade ago [19, 20] (figure 1.4), these macroscopic quantum devices can be routinely coupled to superconducting cavities, both in a purely two-dimensional circuit architecture, and with three-dimensional cavities. In these experiments, artificial atoms are now fixed on a chip, with a surrounding cavity, and microwave light is used to probe and control their states. This *circuit quantum electrodynamics* is still a growing area of research today, which has seen tremendous developments in last years with quantum

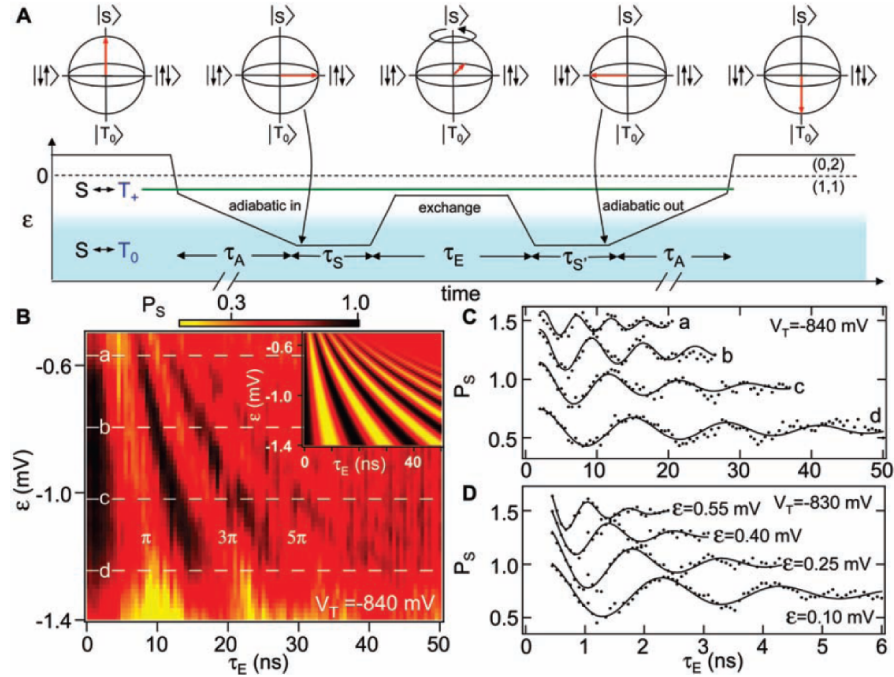


FIGURE 1.2: (A) Pulse sequence demonstrating exchange control of two coupled electron spins in a semiconducting double quantum dot. (B) Singlet state probability as a function of inter-dot detuning and time. Oscillations as a function of both detuning and time demonstrate coherent manipulation. Inset: Theoretical simulation. (C) Rabi oscillations measured at four values of inter-dot detuning indicated by the dashed lines in (B). (D) Faster Rabi oscillations are obtained by increasing tunnel coupling and by increasing detuning to positive values. Source: [16]

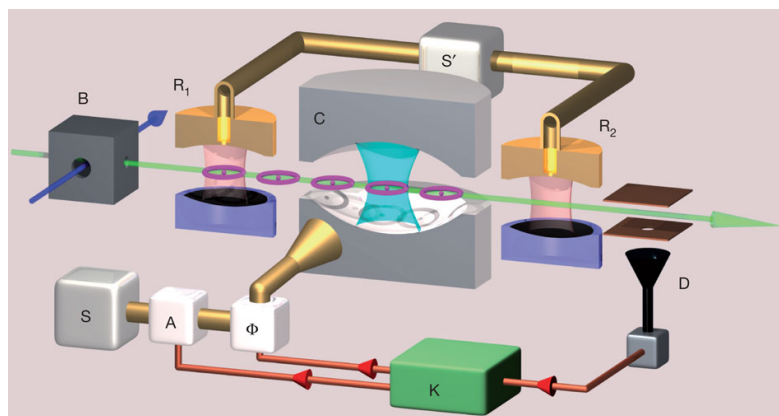


FIGURE 1.3: Scheme of a cavity QED experiment with a quantum feedback set-up. An atomic Ramsey interferometer (R1 and R2) sandwiches the superconducting Fabry-Perot cavity C. Rydberg atom qubits (purple circles) are prepared by laser excitation and measured by a field-ionization detector D. The controller K collects information from D to determine the correcting tone to be applied by S. Source: [17]

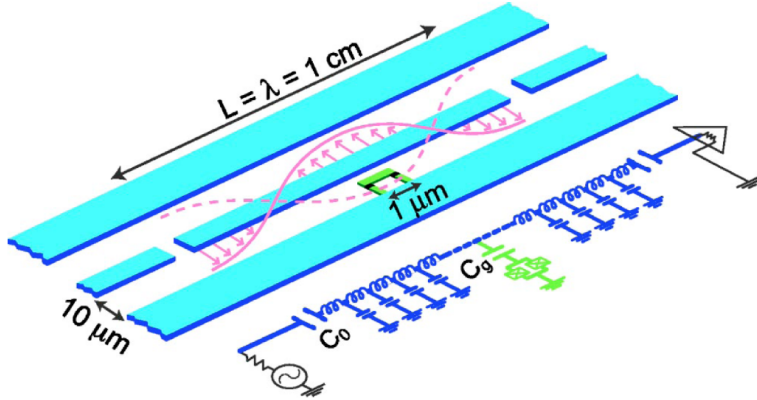


FIGURE 1.4: Schematic layout and equivalent lumped circuit representation of cavity QED using superconducting circuits. The 1D transmission line resonator consists of a superconducting coplanar wave-guide. A Cooper-pair box qubit is placed between the superconducting lines and is capacitively coupled to the center trace at a maximum of the voltage standing wave, yielding a strong electric dipole interaction between the qubit and a single photon in the cavity. Input and output signals are coupled to the resonator, via the capacitive gaps in the center line, which allow measurements of the amplitude and phase of the cavity transmission, and the introduction rf pulses to manipulate the qubit states. Source: [19]

limited amplification [21], quantum feedback [22], scalability [23, 24] and novel types of qubit schemes [25]. There is now a *quantum toolbox* available in this architecture, allowing exquisite control of mesoscopic quantum states of matter, using the light matter interaction and microwave light as a crucial source of control, entanglement, storage and readout of quantum devices. In contrast with their atomic counterpart, where nature sets relevant the parameters and constants of the device such as frequency or light-matter coupling-strength, circuit QED experiments allow one to tune these constants into a desired regime.

Hybrid circuit QED

The great advantage of circuits is their boundless potential in terms of modularity. It is for instance very appealing to use a circuit QED architecture to explore the physics of hybrid circuits that can involve all sorts of devices, from quantum dots (figure 1.6) to mechanical resonator [26, 27] (figure 1.5). Although performed in a classical regime, pioneering experiments [28] from almost two decades ago already showed how high finesse superconducting resonators can be used to probe mesoscopic systems in an alternative way. They demonstrate that such a measurement technique offers a non-invasive measurement of both dissipative and reactive response. For quantum dots, coupling to a resonator offers several perspectives. It provides a new tool to explore many body physics or screening effects with electronic interactions [29], or to simulate more general

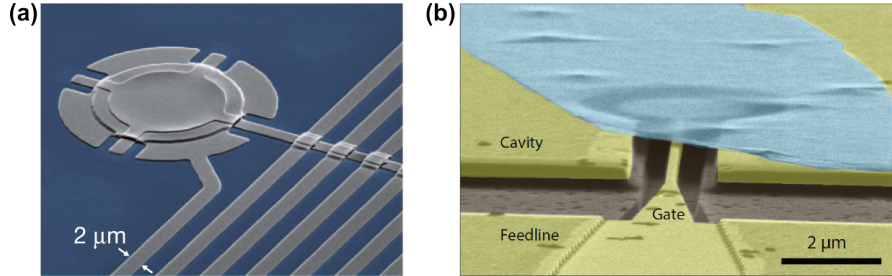


FIGURE 1.5: Hybrid circuit QED with mechanical resonators. (a) False-colour scanning electron micrograph showing an aluminium (grey) electromechanical circuit. A 15 μm -diameter membrane is suspended 50nm above a lower electrode. The membrane's motion modulates the capacitance, and hence, the resonance frequency of a coupled superconducting microwave circuit. Source: [26] (b) Tilted angle scanning electron micrograph (false color) showing a 4 μm -diameter multilayer graphene resonator (cyan) suspended 150nm above a gate. Source: [27]

condensed matter problems on a chip [30]. It also stands as a new way to manipulate and readout quantum information in these systems [31, 32]. There are now several groups investigating such hybrid devices with different host materials [33–35]. Combining high finesse microwave cavities with carbon nanotube devices is a non-trivial task as CNT growth processes lack control and generally result in very poor microwave properties [29, 30], see chapter 3. In this thesis we demonstrate the possibility to do so with a novel stamping technique [36]. With this method we achieve quality factors of few $10^3 - 10^4$ reliably, while keeping our quantum dot architecture compatible with connection to ferromagnetic or superconducting metals.

In chapter 5, we demonstrate a strong confinement in a CNT-based double quantum dot device using our stamping technique (figure 1.7). We demonstrate resonant coupling between a charge qubit and the fundamental mode of a superconducting coplanar wave-guide resonator [37]. By driving the system out of equilibrium, we investigate the charge dynamics in the system and characterise how non-linear transport can affect the microwave response of the device. Together with a microwave spectroscopy, this allows us to determine the relaxation and dephasing rates of the charge qubit. We use the decoherence properties of this carbon nanotube device to estimate the charge noise spectral density. It turns out to be as low as in the quietest solid states systems such as two-dimensional electron gases, lower than in other nanowires by almost an order of magnitude. This feature is essential and it is promising for further experiments exploiting spin or valley, as it will ultimately limit their dephasing time.

The emerging field of hybrid cavity-quantum dot has also created a rather large theoretical activity, with proposals for non-local electronic and heat transport [38–41] or photon emission and lasing with quantum dots [42, 43]. A more coherent degree of freedom that one can try to couple to a cavity is the electronic spin, and this is the aim of this thesis.

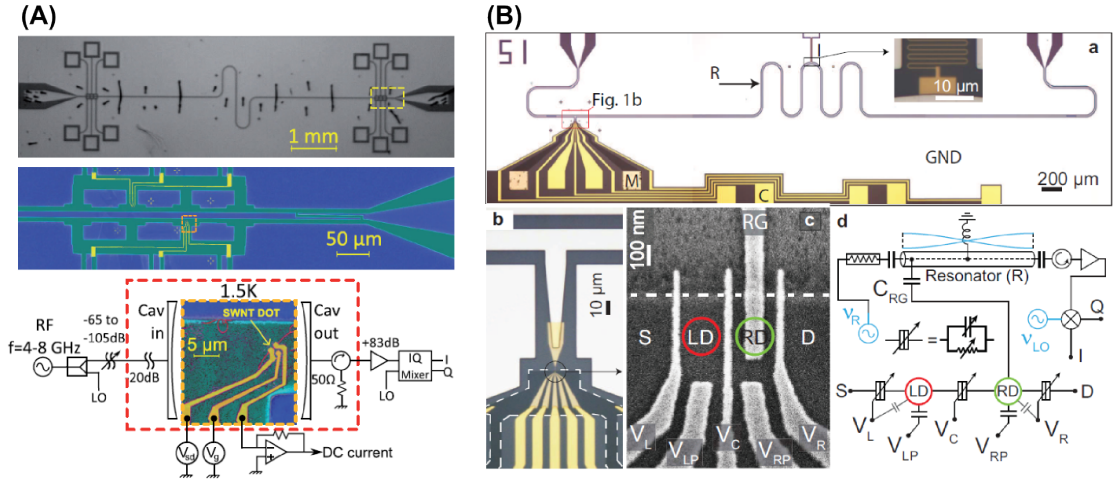


FIGURE 1.6: (A) Optical and scanning electron micrograph of a CNT-based single dot device embedded in a cavity architecture. Source [29]. (B) Optical and scanning electron micrograph of a double dot made out of a two-dimensional electron gas (GaAs). The device is asymmetrically coupled to a cavity via one gate electrode (RG). Source: [31]

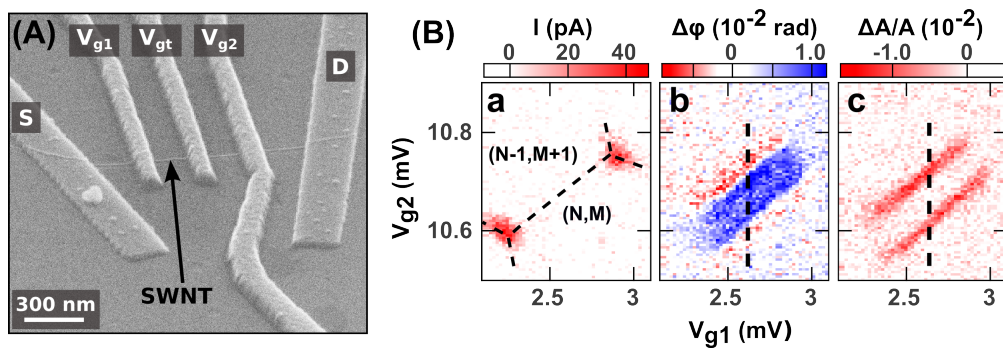


FIGURE 1.7: (a) Scanning electron micrograph of a CNT-based double quantum dot device. A single wall carbon nanotube is connected to source and drain electrodes (S and D), as well as three top gates (V_g 's) for electrostatic control and coupling to a cavity. (b) DC current and cavity microwave response of the device demonstrating resonant coupling and low charge noise spectral density.

Spins can be coupled to photons trapped in a cavity via the magnetic field component of the corresponding standing wave. The associated coupling strength is very weak (typically 10Hz), and one can increase the spin-photon cooperativity by coupling to a large spin ensemble. Strong coupling of such large ensembles has been demonstrated at the single photon level [44, 45] (figure 1.8(a)). Although a large spin ensemble cannot be employed as a qubit as it behaves like a linear harmonic oscillator, it could be used as quantum memory thanks to its long coherence time. It has already been implemented in hybrid devices coupling to superconducting qubits [46] (see figure 1.8(b)). It is also possible to couple strongly to macrospins constituted by collective spin modes (zero-frequency magnons) [47], see figure 1.8(c).

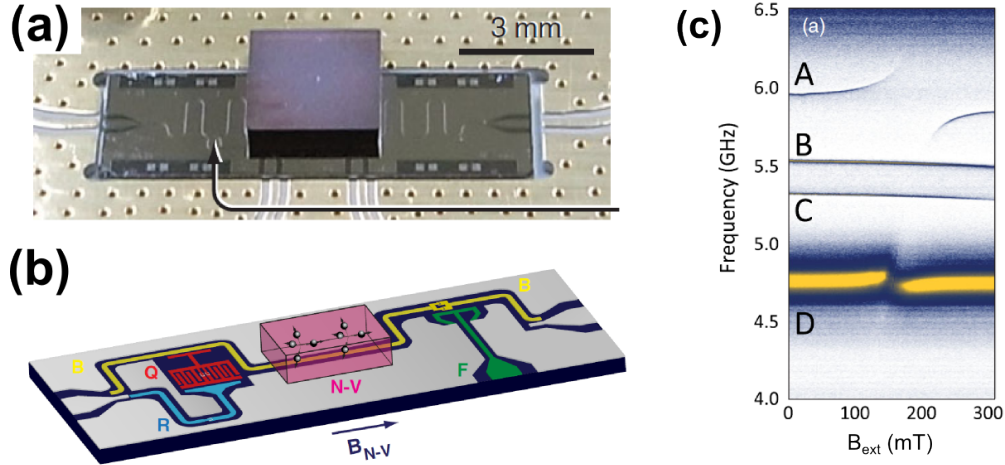


FIGURE 1.8: Hybrid circuit QED with spin ensembles. (a) Photograph a diamond crystal hosting a large ensemble of nitrogen-vacancy centers, glued on top and in the middle of a superconducting coplanar resonator. (b) Hybrid device with a transmon qubit (red) capacitively coupled to a resonator R used to readout its state. A bus (yellow) is electrostatically coupled to the qubit and magnetically coupled to the N-V centers. Source: [44, 46]. (c) Transmission spectrum of a resonator A strongly coupled to a macrospin of which frequency linearly depends on B_{ext} Source: [47]

Spin-photon coupling for spin-based circuit QED

A single electronic spin is the paradigm of a two level system that can carry quantum information. Strong coupling between a single spin and a resonator at the single photon level would allow one to tackle fundamental problems such as the coupling of distant spins, and would open a path towards spin-based quantum information processing using the successful QED techniques. Achieving such a strong coupling is however very challenging and any coupling of a single spin to a cavity mode remains to be demonstrated. To enable such a coupling, one strategy is to coherently (but weakly) hybridise the spin quantum state with a charge component that will provide natural electrostatic coupling to a photon in a cavity. This has to be done carefully as charge is subject to strong decoherence in solid state devices [48]. This is the aim of this thesis, and chapter 6 presents preliminary results pointing towards it.

In contrast with other spin qubits proposals, we are trying to obtain a local spin control with an extrinsic engineering, using effective magnetic fields induced by interfaces with ferromagnetic contacts (figure 1.9(a)). This technique should enable strong spin-photon coupling in a nuclear spin free environment such as a carbon nanotube [14]. We demonstrate here the possibility to technically implement this device, with controlled and active ferromagnetic interfaces (figure 1.9). Preliminary measurements indicate the presence of extra energy levels in the spectrum (see figure 1.10). Microwave spectroscopy indicates that some transitions are magnetic field dependent, and coupled to the microwave cavity.

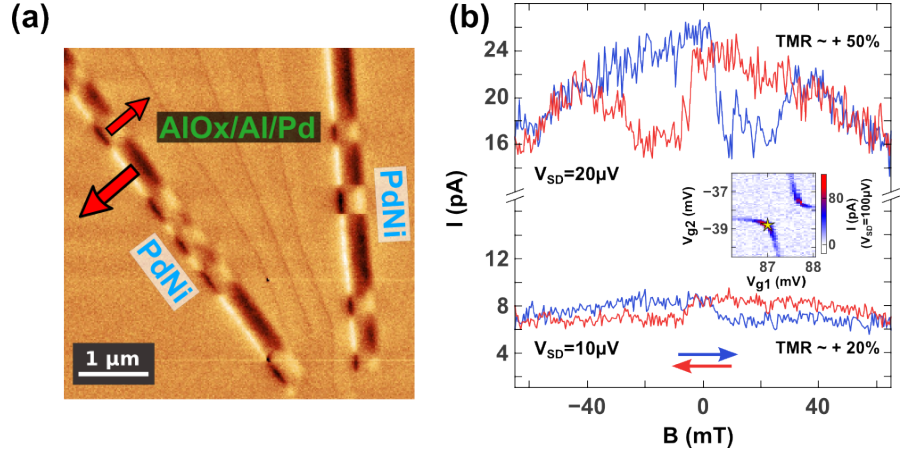


FIGURE 1.9: (a) Magnetic Force Microscope image of a CNT-based double quantum dot device connected to three top gates and two non collinear ferromagnetic PdNi electrodes. (b) DC current characterisation of the ferromagnetic electrodes by performing a tunnelling magneto-resistance measurement.

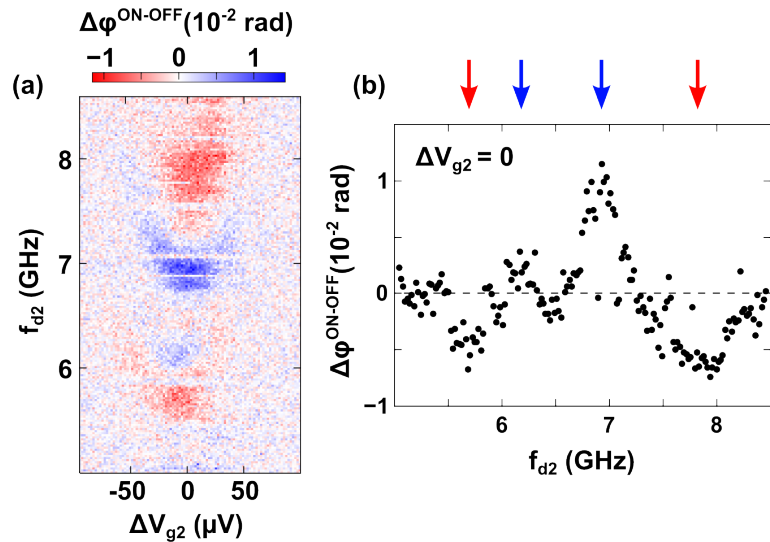


FIGURE 1.10: Microwave spectroscopy of a double quantum dot device connected to ferromagnetic leads as a function gate interdot-detuning ΔV_{g2} . This measurement indicates the presence of several transitions with different phase responses (red and blue arrows).

Chapter 2

Double quantum dots for spin qubits

2.1	Spectrum and basic transport properties of double quantum dots	14
2.1.1	Characteristic energy scales	14
2.1.2	Stability diagram	15
2.1.3	Master equation	17
2.1.4	Out of equilibrium transport	19
2.2	Charge qubit in a double quantum dot	20
2.3	Existing spin qubit architectures	21
2.4	The ferromagnetic spin qubit proposal	22
2.4.1	Ferromagnetic interface-induced exchange fields in coherent conductors .	23
2.4.2	Principle of the ferromagnetic spin qubit	24
2.4.3	Predictions and main features	26

Quantum dots are potential wells allowing to confine electrons in space, behaving like artificial atoms. Different host materials are available, from two-dimensional electron gases fabricated with semiconducting hetero-structures (typically GaAs/GaAlAs, [49, 50]) to wires such as semi-conducting nanowires (e.g. made out of InP, InAs or SiGe, [51, 52]) or carbon nanotubes [8, 53–55], that were used for this thesis. The use of electrostatic gate electrodes in nano-structures allows to go from the two- or one-dimensional confinement of these materials, to zero-dimensional confinement. Several materials are now well controlled, and it has become routine to achieve confinement on a length scale smaller than the mean free path, thus achieving a clean confinement in the 3-D space¹. Such quantum dots, and especially double quantum dots, have proven to be a possible platform to control quantum information encoded in two-level systems. These two-level systems, or quantum bits (qubits) can be charge orbitals [48, 56], but also spin states [57, 58], which are promising for applications as they can potentially be long-lived states, with slow dephasing rates. This chapter recalls first some of the basic transport properties of double quantum dots as well as possible ways to encode qubits in charges states. Section 2.3 then reviews existing spin qubit architectures in double quantum dots, and section 2.4 finally presents the theoretical proposal of the ferromagnetic spin qubit.

2.1 Spectrum and basic transport properties of double quantum dots

The most conventional way to characterise a quantum dot coupled to fermionic reservoirs is to perform quantum transport measurements. Applying a potential difference between the reservoirs can result in a direct current flowing through the device, that can be measured experimentally using analog electronics. The conductance of such a device gives information about its spectrum, which can be explored by tuning voltages applied on local gate electrodes. The same principle applies for a double quantum dot, of which main features are reviewed below. In sections 2.1.3 and 2.1.4, we show how to calculate the conductance of a double quantum dot in both the linear and non-linear regime (i.e. large bias) using a master equation approach.

2.1.1 Characteristic energy scales

Several energy scales can be identified in double quantum dots. The confinement within a quantum dot yields an energy spacing between discrete orbitals. Depending on the

¹The order of magnitude for the mean free path is typically $1\mu\text{m}$ in carbon nanotubes.

material and the experimental conditions, one or several electrons can enter an orbital with different quantum numbers, for instance different spins or different valley for carbon nanotubes or graphene. Moreover, carbon nanotube quantum dots exhibit a large charging energy. This represents the energy that is needed to add an extra electron charge on the dot and overcome the electrostatic repulsion energy given by coulomb interactions. We label this energy by $U_{1(2)}$ for the on-site charging energy on dot 1 (dot 2), and U_m for mutual repulsion between two dots (see below). In general, in the devices we consider, we find $U_{1(2)} \approx 10\text{meV}$ (few THz). Two types of tunnelling rates rule the dynamics of double quantum dots. Each of the dot is couple to a fermionic reservoir with a rate $\Gamma_{\text{Lead},1(2)}$, which sets the maximum number electrons that can tunnel from a lead to an orbital on average per second. Two neighbouring dots can also be tunnel coupled through a thin barrier, and we label the associated tunnel rate t . All these tunnel rates are often in the range of $1 - 100\mu\text{eV}$ (few $1 - 10\text{GHz}$) here. These energies have to be compared with temperature, that is around $20mK$ ($\approx 2\mu\text{eV}$) for these experiments. As discussed later, it is also to be compared to the frequencies at which we probe or excite the system, as well as the time scale over which the system relaxes, or loses its phase coherence.

2.1.2 Stability diagram

A standard quantum dot transport spectroscopy consists in measuring the current (or conductance) flowing through the device, as a function of a local gate(s) controlling the potential of the dot(s). Current can only flow if there is at least one electronic state, or a density of state in the device, that is lying close to the Fermi level of the reservoirs. If the device is in a coulomb blockade regime², the electronic states are well separated in energy. When the electrochemical potential of these electronic states is away from the Fermi level of the reservoirs, the charge on the dot is blocked and no current can flow. This allows to *count* the average number of electrons on the device as energy levels pass the Fermi level of the reservoirs. In the linear regime ($V_{SD} < k_B T$), the stability diagram of a device reveals what is the stable charge state, or occupation number of the dot(s), as a function of the local gate voltage(s). It can be obtain experimentally, either by measuring the current or by doing charge sensing, that is measuring the electric charge on a dot with a capacitive sensor such as an auxiliary quantum dot. Figure 2.1 depicts the principle of the DC current measurement a double quantum dot stability diagram [4].

We can identify several key features on the stability diagram of a double quantum dot. The semantic can change depending on the inter-dot tunnel coupling strength t and

²A regime where coulomb interactions are strong and dominate the other energy scales

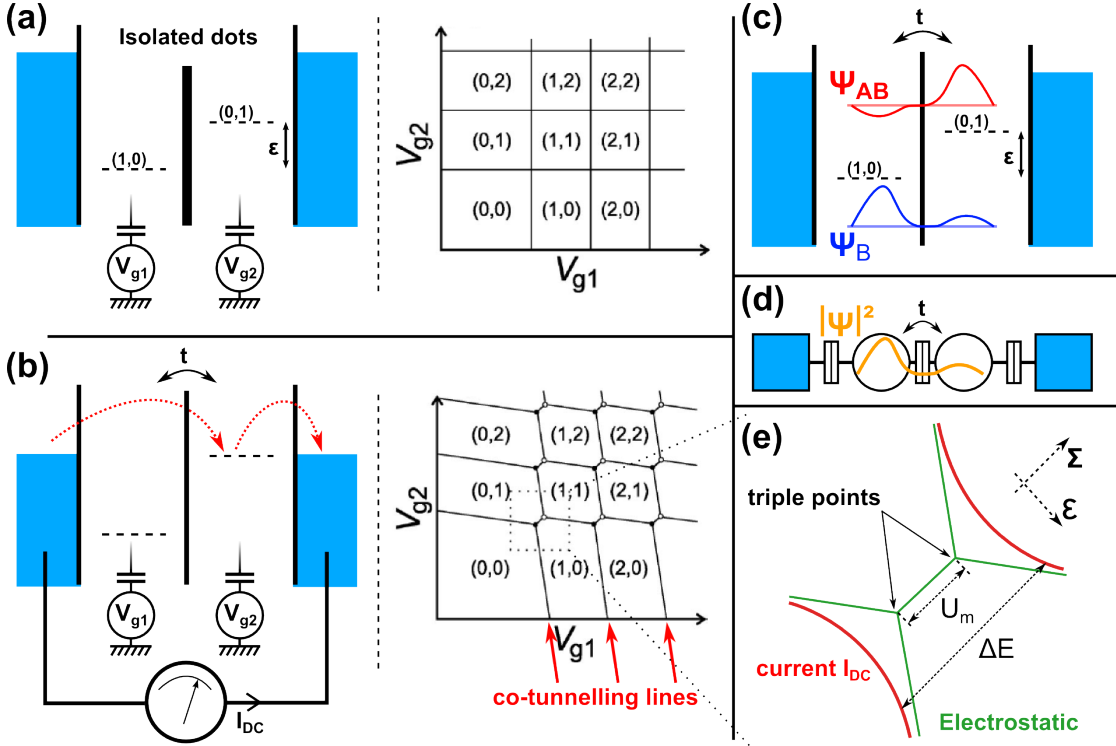


FIGURE 2.1: Basic transport properties of double quantum dots in the linear regime ($V_{SD} \approx 0$). (a) Schematic of a singly occupied double quantum dot (DQD) with one orbital depicted in each dot, tunnel coupled to fermionic leads (light blue). Energy detuning ϵ between the two orbitals is controlled by means of local gate voltages V_{g1} and V_{g2} . In the case of isolated dots, the charge stability diagram shows vertical and horizontal lines corresponding to gate regions where energy level of dot 1 and 2 pass the Fermi level of the electrodes. (b) Principle of the DC transport spectroscopy. The two dots are electrostatically- and tunnel-coupled, yielding avoiding crossings (as detailed in (e)). When the orbital of dot 1(2) is aligned with the Fermi level, current can flow (though this might be through co-tunnelling, i.e. 2nd order tunnel event) and this corresponds to the tilted vertical (horizontal) lines on the stability diagram. (c) Close to zero detuning, left and right dot's orbitals hybridise and form molecular bonding and anti-bonding states. (d) Simplistic circuit representation of the DQD with the electronic corresponding wave-function. (e) Zoom on the stability diagram close to an avoided level crossing. The two triple points are separated by the electrostatic mutual charging energy U_m . Finite tunnel coupling yields a curvature (hyperbola) of the molecular states, thus moving away from the purely electrostatic position of the triple points.

lead coupling Γ_{lead} compared to temperature, but the physics is globally similar. In the coherent regime ($t > k_B T$), there can be both an electrostatic repulsion and a tunnel coupling between the left and right orbitals. This yields anti-crossings between the dot's energy levels such as shown in figure 2.1(b and e). The distance between the two current lines at the anti-crossing simply reads:

$$\Delta E = U_m + \sqrt{\epsilon^2 + 4t^2} \quad (2.1)$$

where U_m is the mutual charge energy arising from Coulomb repulsion between the two dots and ϵ is the energy detuning between the two dots. When the inter-dot tunnel coupling is much larger than $\Gamma_{lead,1(2)}$ and $k_B T$, this can be used to estimate t (and U_m), see figure 2.2. For small energy detuning ϵ between left and right orbitals (smaller than the inter-dot coupling t), they hybridise to form the so-called molecular bonding and anti-bonding states. The device therefore behaves like an artificial molecule made out of two atoms coupled to fermionic continua. In the incoherent regime ($t < k_B T$), bonding and anti-bonding orbitals reach the triple points (see figure 2.1(e)) which are then the only points of the gate voltage map where current can flow through the device via 1st order tunnel events. The segment spanning between these two points will be very often referred to as the *zero-detuning line*, as left and right orbitals are brought to degeneracy along that segment.

Away from the triple points, the current lineshape depends on the coupling to the leads $\Gamma_{lead,1(2)}$. Even in the coherent regime, these are often called co-tunnelling lines, as they involve a tunnelling event from lead 1(2) to a state (mainly localised) in dot 2(1), see figure 2.1. By analogy to the single dot case, we can deduce that the amplitude of the co-tunnelling lines mainly depend on the coupling rate involved in the first order tunnel event³. This allows a quick estimation of the asymmetry between the lead couplings on both sides from a direct current measurement of the stability diagram, see figure 2.2.

2.1.3 Master equation

One can formally calculate the current flowing through the device as a function of the different coupling rates using a master equation approach. In the Markovian approximation and assuming that the reservoirs are much larger than the system⁴, we can write the traditional master equations⁵ on the populations (i.e. the diagonal terms) [59]:

$$\frac{d}{dt} \langle \sigma_n \rangle = \sum_m (\Gamma_{n \leftarrow m} \langle \sigma_m \rangle - \Gamma_{m \leftarrow n} \langle \sigma_n \rangle) \quad (2.2)$$

where $\langle \sigma_n \rangle$ is the (average) population of the state $|n\rangle$ in the double quantum dot, and the Γ 's are given by:

³that is to say the tunnelling event from a dot to the nearest reservoir

⁴So that they stay at thermal equilibrium

⁵Equation of motion of the density matrix, $i\hbar\rho = [\mathcal{H}, \rho]$

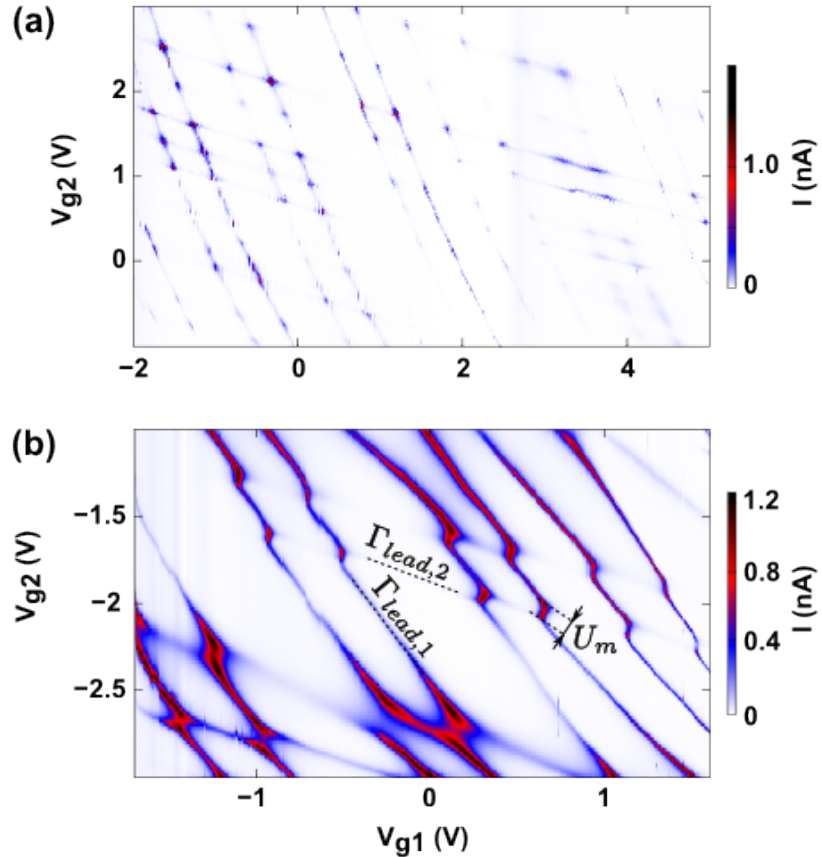


FIGURE 2.2: Experimental colour-scale plot the DC current as a function of side gate voltages V_{g1} and V_{g2} . One can get quick order of magnitudes for the tunnel rates involved in this double quantum dot device. **(a)** Stability diagram revealing two *weakly* coupled dots, with a small tunnel coupling $t \lesssim \Gamma_{lead}$ and a small mutual charging energy $U_m < \Gamma_{lead}$; Γ_{lead} being roughly given by the width of the current lines. It resembles that of figure 2.1(a), except lines are tilted due to capacitive cross talks between the two side gates and the two dots. **(b)** Stability diagram a double quantum dot device asymmetrically coupled to leads ($\Gamma_{lead,1} \gg \Gamma_{lead,2}$). Indeed tilted horizontal are almost invisible compared to tilted vertical ones. In this region there is a fairly large electrostatic repulsion U_m between the two dots, which can be estimated after extracting the conversion factor between gate voltages and energy. There is also an observable curvature of the current lines, especially at the bottom left of the diagram, which signal a tunnel coupling comparable to the lead coupling $\Gamma_{lead,1}$. **(a)** and **(b)** were taken on the same device, in two different center gate voltages V_{gt} ($-100\mu V$ and $+200\mu V$ respectively). In both plots, DC bias is $V_{SD} \approx 150\mu V$.

$$\begin{aligned}\Gamma_{\alpha \leftarrow \beta} &= \Gamma_{\alpha \leftarrow \beta}^L + \Gamma_{\alpha \leftarrow \beta}^R + \gamma_{\alpha \leftarrow \beta} \\ \Gamma_{\alpha \leftarrow \beta}^{r=1(2)} &= \frac{2\pi}{\hbar} |\gamma_r|^2 \nu_r f_r (E_\alpha - E_\beta)\end{aligned}\tag{2.3}$$

where $\nu_{r=1(2)}$ is the density of state in reservoir 1(2) and $f_{r=1(2)} (E_\alpha - E_\beta)$ its Fermi function taken at the energy difference between states $|\alpha\rangle$ and $|\beta\rangle$. $\gamma_{\alpha \leftarrow \beta}$ is an internal relaxation rate depending on microscopic details. Depending on how many occupation numbers and/or excited states are considered, the system of equations 2.2 will be valid around different regions of the stability diagram. One relevant case is to consider empty, singly and doubly occupied states with no excited states in either of the dots. The current flowing through the DQD can be computed for instance at the left lead:

$$\begin{aligned}I_L = e \Big[&\langle \sigma_2 \rangle (\Gamma_{AB \leftarrow 2}^L + \Gamma_{B \leftarrow 2}^L) + \langle \sigma_{AB} \rangle (\Gamma_{0 \leftarrow AB}^L - \Gamma_{2 \leftarrow AB}^L) \\ &+ \langle \sigma_B \rangle (\Gamma_{0 \leftarrow B}^L - \Gamma_{2 \leftarrow B}^L) - \langle \sigma_0 \rangle (\Gamma_{AB \leftarrow 0}^L + \Gamma_{B \leftarrow 0}^L) \Big]\end{aligned}\tag{2.4}$$

where e is the electron charge and $\langle \sigma_0 \rangle$, $\langle \sigma_B \rangle$, $\langle \sigma_{AB} \rangle$ and $\langle \sigma_2 \rangle$ are the populations of the empty, singly occupied bonding/anti-bonding and doubly occupied states respectively. In our case, $\gamma_{\alpha \leftarrow \beta}$ is only non zero for $\alpha = B$ and $\beta = AB$ and we note $\gamma_{B \leftarrow AB} = \gamma$. Although γ does not appear explicitly in equation 2.4, it enters in the populations which are determined by solving equation 2.2. This is valid in the whole area around the triple points associated to these occupations, and is qualitatively correct for the whole stability diagram if the spin degree of freedom is neglected.

2.1.4 Out of equilibrium transport

One can measure the stability diagram at finite bias, when a large potential difference is applied between source and drain electrodes. The master equation formalism presented above allows to compute the current in this non-linear regime, by adding the electrical potential eV_{SD} to the energy of the corresponding states in the Fermi functions of equation 2.3. Figure 2.3 shows the current calculated from equation 2.4 for realistic parameters at two different biases. Two characteristic *bias triangles* develop next to the triple points. In these regions DC transport occurs and the $I - V_{SD}$ characteristic

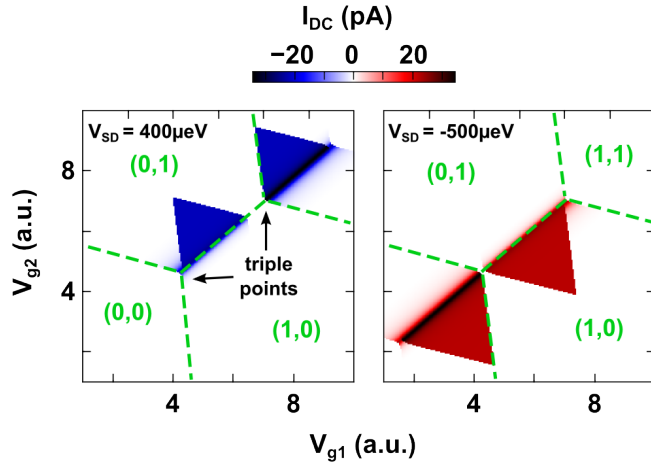


FIGURE 2.3: Theoretical colour-scale plots of the DC current flowing through a double quantum dot in the non-linear regime. In both panels, mutual charging energy is $U_m = 500\mu eV$, bare coupling to the leads are $\gamma_{1(2)} = 0.3(1.6)GHz$, relaxation rate is $\gamma = 300MHz$, inter-dot tunnel coupling is $t = 2.5GHz$ and temperature is $20mK$.

of the device becomes *non-linear*. Measurements in the non-linear regime are useful to estimate all the lever-arms⁶, and eventually the capacitances involved between gate electrodes and the two dots [4]. Moreover they can provide a transport spectroscopy of the excited states in the device [60–65] or be used to perform the readout of spin blockaded states for spin qubits (see section 2.3). The theoretical plots of figure 2.3 can be compared to the experimental measurements obtained in the non-linear regime, see figure 4.9(left pannel).

2.2 Charge qubit in a double quantum dot

As a double quantum dot appears as two coupled and tunable electron boxes, it can be used as a two level system in which it is possible to encode quantum information. The eigenstates carrying this information can be either left/right dot's orbitals or their hybridised bonding/anti-bonding version, relevant when the coupled left and right orbitals are close to degeneracy ($\epsilon \sim 0$), see figure 2.5 and 2.4. The control over such a qubit is naturally provided by the surrounding gate electrodes, which can be engineered to have wide bandwidth and therefore carry GHz driving tones to the device. The readout can be done via DC current or charge sensing, in the latter case using the $(0,1)$ and $(1,0)$ basis. Chapter 4 presents the more recent technique using high frequency superconducting resonators which provide a natural AC architecture for these devices, and promising for experiments going beyond charge qubits. Coherent manipulations of such charge qubits were demonstrated a decade ago [48], but they are still investigated today

⁶coefficients that convert gate voltages into energies on the dots, see section 4.2.1

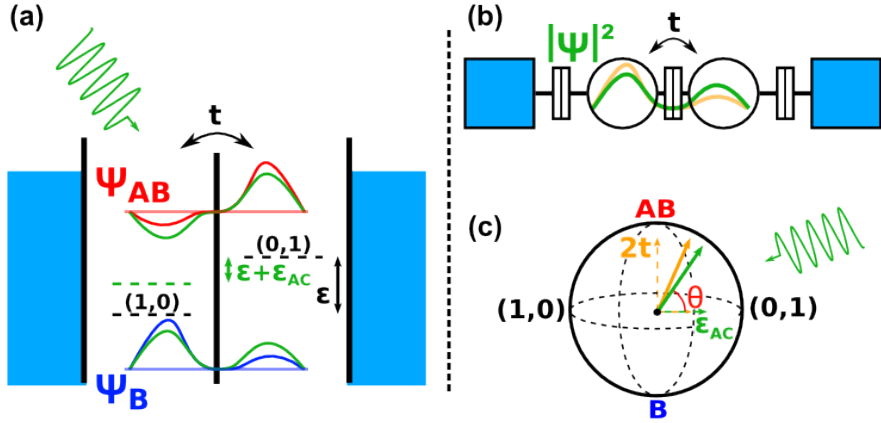


FIGURE 2.4: Principle of the double quantum dot-based charge qubit and its coupling to the electric field associated to the photons in the cavity. (a) Simplistic schematics of the DQD with Fermi seas (light blue), left and right orbitals coupled through the tunnel barrier t and thus forming bonding and anti-bonding states. If the AC electric field of the cavity is coupled to the detuning ϵ , it acts on the hybridisation of the two orbitals, or equivalently on the delocalisation of the charge probability density $|\psi|^2$ as depicted in (b). (c) Bloch sphere of the charge qubit. If tuned with the qubit, an AC drive ϵ_{AC} yields transverse torque.

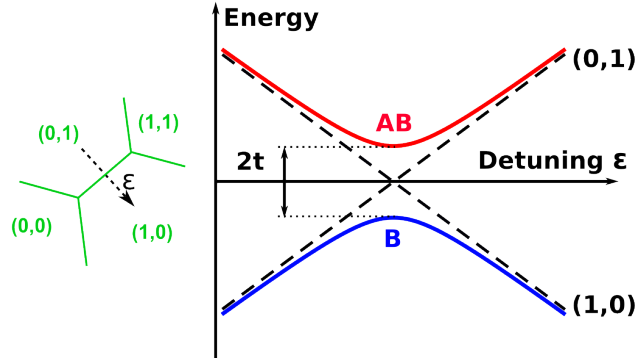


FIGURE 2.5: Dispersion relation of the bonding and anti-bonding states of a double quantum dot close to zero inter-dot detuning. These two molecular states can be used as a charge qubit with Larmor frequency given by $\hbar\Omega = \sqrt{\epsilon^2 + 4t^2}$.

in several context [66, 67]. Although these qubits have poor coherence properties, they are at the basis of many proposals for more complex and efficient qubits such as spin qubits (see section 2.4 and chapters 5 and 6).

2.3 Existing spin qubit architectures

Quantum dots have proven to be a possible platform for controlling the electronic spin in the last decade [62]. One possible target is spin-based quantum information processing [15], and the first step to achieve this goal is the realisation of single qubit gates. This requires coherent control and readout of a single electronic spin. Although the first

single-spin readout demonstration [68] was done in a single dot, most schemes rely on double dot devices. In all case, a spin-to-charge conversion mechanism such as Pauli spin blockade [16, 69–71] is required to read out the spin state, either via direct current or charge detection (using a quantum point contact or an auxiliary dot). The electron carrying the spin is then lost into a reservoir, yielding a destructive measurement.

As in NMR experiments, the coherent manipulation of spins (or ESR⁷) requires non collinear magnetic fields. *Brute force* coherent manipulation has been achieved with real magnetic fields in double quantum dots [72]. However it is tricky to implement large amplitude and high frequency (GHz) magnetic fields at low temperature. Large magnetic fields are moreover not very much compatible with the high finesse superconducting cavities that we would like to implement in our setup (see chapter 5). Finally they do not provide a local control as they spread in space on a scale larger than typical quantum dot sizes. Intrinsic local properties of the host materials have therefore turned out to be much more efficient for local spin control. They allow the conversion of local AC electric fields, that can be easily carried down to low temperature, into local (effective) AC magnetic fields. These local properties can be Overhausser fields [16], spin orbit [57, 73, 74], hybridisation with valley degree of freedom [6, 75] or exchange fields with neighbouring spins [76]. These have yielded different spin qubit architectures, namely singlet-triplet qubits, spin-orbit qubits, valley-spin qubits or exchange-only spin qubits. Interestingly, there also has been experiments using magnetic stray fields gradients of a nearby micromagnet for local spin control [77, 78]. Although recent works investigate novel material such as SiGe [58], the large majority of the above spin qubit architectures are hosted by materials with nuclear spins. The hyperfine interaction between electronic spins and this nuclear spin bath results in large dephasing rates of these qubits, in general down to few $1 - 10ns$. Among the alternatives for nuclear spin-free host materials, carbon nanotubes (CNT) are possible candidates. There has been experiments on spin-blockade measurements in CNT's [65, 79] and valley-spin blockade [6], but the pure spin dephasing time has not been measured yet. The next section presents our strategy to implement a spin qubit in a carbon nanotube with arbitrarily pure spin states and electric field control using ferromagnetic contacts.

2.4 The ferromagnetic spin qubit proposal

The goal of this work is to go towards the realisation of a long-lived spin qubit in a carbon nanotube, compatible with a circuit QED implementation which would provide spin-photon coupling in a scalable architecture [14]. In the absence of nuclear spins, the

⁷Electron Spin Resonance

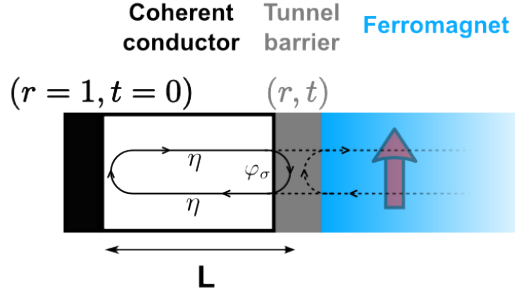


FIGURE 2.6: Principle of the confinement-induced exchange field arising from tunnel coupling to a ferromagnetic lead. φ_σ is a spin-dependent interfacial phase shift and η is the electronic path acquired by the electronic phase when propagating through the coherent conductor over a length L .

electronic spin dephasing time can be very large [80, 81]. The idea here is to weakly hybridise the spin states with gate-dependent charge states in order to enable coupling to the electric field and thus strongly increase spin-photon coupling in a cQED context (see chapter 4 and 6). In solid state quantum dots, low frequency charge noise is generally large (see section 5.4) and yields dephasing as soon as there is a charge component in a wavefunction. Such a charge component is nevertheless a priori needed for pure electric manipulation; one therefore has to engineer the spectrum in order to obtain a sufficient charge component to achieve a large coupling to the electric field, while being as insensitive as possible to charge noise.

2.4.1 Ferromagnetic interface-induced exchange fields in coherent conductors

The key ingredient of our setup is the effective magnetic field induced by the interface with a ferromagnetic lead, analogue to proximity effect in superconductors. In a non interacting picture, one can use the scattering matrix formalism to compute the spectrum of a confined portion of coherent conductor connected to a ferromagnet via a barrier with transmission and reflection probabilities (see figure 2.6). The spin dependence of the quantized spectrum in the dot can arise from both the transmission probability and the phase of the reflection coefficient. If the transmission probability is spin dependent and non-zero, there must be an evanescent part of the electronic wavefunction in the ferromagnet. This can be interpreted as a hybridisation with the first atomic layers of the ferromagnetic lead which naturally provide spin polarisation of the total quantum state and that can be referred to as *tunnelling exchange field*. This contribution strongly depends on the amplitude of the transmission probability⁸ and vanishes for a totally reflecting barrier ($\Gamma_{lead} = 0$). It has been observed in quantum dot spin valves [13, 82]

⁸which directly relate to coupling rates Γ_{lead} 's

and studied as a function of lead coupling Γ_{lead} on a Kondo resonance [9]. However the spectrum of the dot can also be spin polarized from spin dependent phase φ_σ at the reflection. One can thus think of a very opaque barrier with a different shape for spin pointing up and down, as it could happen for a connection to a ferromagnetic insulator for example. In the non-interacting picture considered here, this *confinement-induced exchange field* yields an effective Zeeman splitting [83]:

$$2\delta \equiv E_{ex} = \frac{\hbar v_F}{2L} (\varphi_\uparrow - \varphi_\downarrow) \quad (2.5)$$

where v_F is the Fermi velocity, L is the length of the dot and $\varphi_{\uparrow(\downarrow)}$ is a spin-dependent interfacial phase shift. Because the dot spectrum is gate controlled (via η in this model, see 2.6), it is in principle possible to tune the exchange field and in particular the tunnelling contribution since it is Γ_{lead} dependent.

2.4.2 Principle of the ferromagnetic spin qubit

The idea is now to use this interface effect to engineer a local spin control with electrical potentials applied on local gates. Figure 2.7 depicts the principle of our scheme. Two dots are connected to two ferromagnetic reservoirs with non-collinear magnetization, tilted by θ from each other. For zero inter-dot coupling, we recover a situation such as in figure 2.6, with a spin degeneracy lifted in both the dots, but with non-collinear quantization axis. When the coupling between the dots is turned on, both charge and spin components hybridise thanks to this non collinearity and show multiple anti-crossings (see figure 2.8). For homogeneous exchange fields δ in both the dots, tilted by θ , and an inter-dot tunnel coupling strength t , away from the triple points the Hamiltonian of the singly occupied double quantum dot writes in $\{(\uparrow, 0), (\downarrow, 0), (0, \nearrow), (0, \searrow)\}$:

$$\mathcal{H}_{SQB} = \begin{pmatrix} -\epsilon/2 - \delta & 0 & t \cos\left(\frac{\theta}{2}\right) & -t \sin\left(\frac{\theta}{2}\right) \\ 0 & -\epsilon/2 + \delta & t \sin\left(\frac{\theta}{2}\right) & t \cos\left(\frac{\theta}{2}\right) \\ t \cos\left(\frac{\theta}{2}\right) & t \sin\left(\frac{\theta}{2}\right) & \epsilon/2 - \delta & 0 \\ -t \sin\left(\frac{\theta}{2}\right) & t \cos\left(\frac{\theta}{2}\right) & 0 & \epsilon/2 + \delta \end{pmatrix} \quad (2.6)$$

All transitions now involve charge and spin, with a weight controlled by the inter-dot detuning ϵ and depending on all the parameters (t , θ and δ). This naturally provides an artificial spin-orbit coupling⁹ between the two dots since all transitions involving a

⁹Spin-orbit in a sense that a change of dot's orbital now results in a change of spin and vice versa. However this extrinsic kind of *spin-orbit* breaks time reversal symmetry and is not subject to Kramers degeneracy.

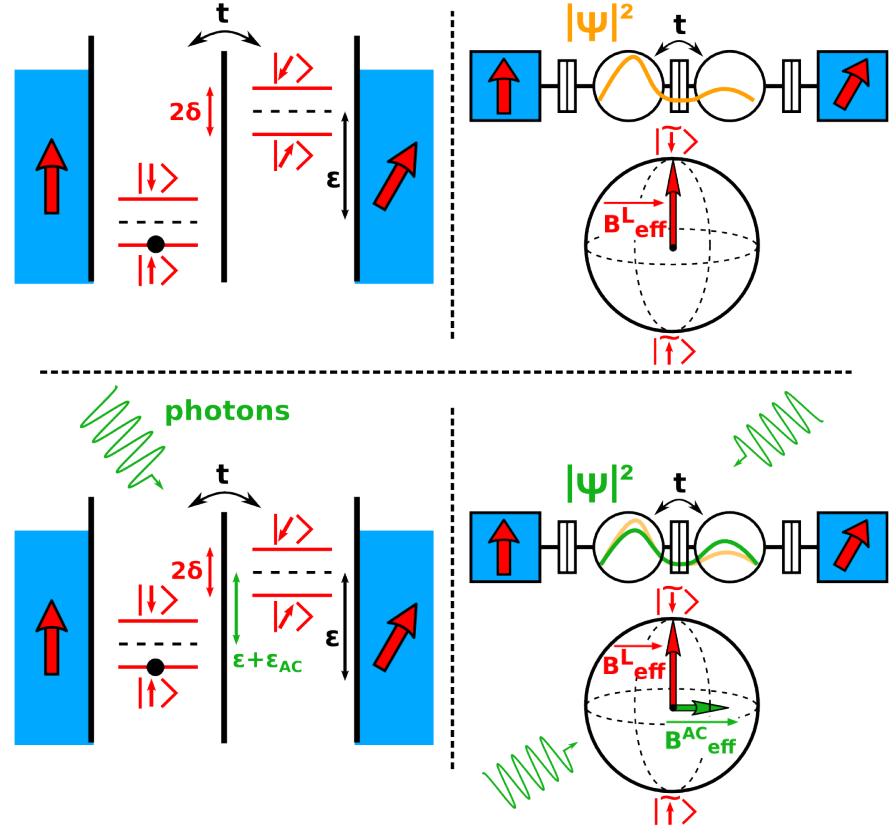


FIGURE 2.7: Upper panel: simplistic scheme of a double quantum dot connected to non-collinear ferromagnets. Interface exchange fields induce effective Zeeman splittings in both the dots with tilted quantization axis. The coherent delocalisation of the charge probability density $|\psi|^2$ is controlled via the inter-dot detuning ϵ . The total contribution of the exchange fields δ 's and tunnel coupling t corresponds to a longitudinal effective field B_{eff}^L on the Bloch sphere of $|0\rangle = |\uparrow\rangle$ and $|1\rangle = |\downarrow\rangle$ in this situation. Lower panel: when properly coupled to a photonic cavity (see chapter 4), the electric field can induce a change in the charge wavefunction giving rise to an AC transverse component of the effective magnetic field.

change in the orbital part of the wavefunction must also involve a change in the spin part of it. In the appropriate regime of parameters of figure 2.8, one interesting working point appears at finite detuning ($\epsilon \sim 3\delta$, highlighted light blue region). The spectrum is strongly anharmonic and $|0\rangle$ and $|1\rangle$ states can be used as a qubit. This 01 transition is almost a pure spin transition here, as it involves arbitrarily pure spin states (pure spin states in the limit of large detuning $\epsilon \gg \delta$). Furthermore, this transition is weakly dependent on the detuning in this region, as $|0\rangle$ and $|1\rangle$ show almost parallel dispersion. This allows protection against charge noise (again, in the limit $\epsilon \gg \delta$, dephasing is not charge noise-limited but spin noise-limited). This transition still has a transverse coupling to the electric field, and can therefore be gate coupled to a cavity (see chapter 4).

Qualitatively, one can understand the origin of the transverse coupling in the following

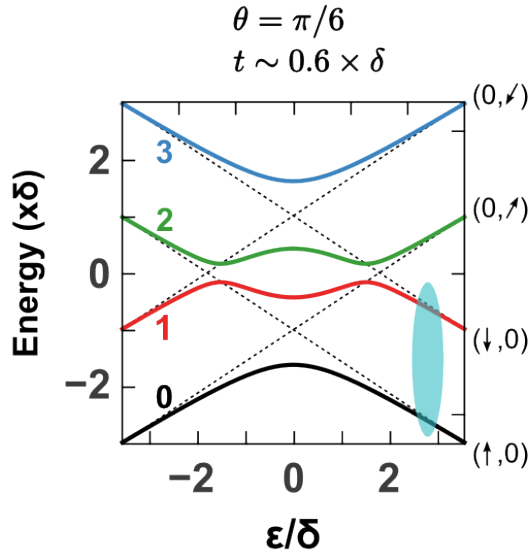


FIGURE 2.8: Ideal spectrum of the ferromagnetic spin qubit for homogeneous exchange fields in both the dots (obtained from diagonalisation of equation 2.6). The light blue region is where the system behaves almost as a pure spin qubit, while keeping a coupling to the electric field.

picture. The upper right panel of figure 2.7 shows a hypothetical charge probability density $|\psi|^2$ at a given detuning ϵ . This configuration yields a longitudinal coupling to the electric field on the Bloch sphere of $|0\rangle = |\tilde{\uparrow}\rangle$ and $|1\rangle = |\tilde{\downarrow}\rangle$ which is almost a pure spin qubit. This longitudinal component thus plays the role of an effective magnetic field, here mainly determined by the axis of the left ferromagnet, in which the spin precesses. Let us now consider a slightly reduced detuning ϵ as in the lower panel of figure 2.7; $|\psi|^2$ is now more coherently delocalised over the two dots. This results in a stronger contribution of the right dot's exchange field. The total effective magnetic is therefore tilted and show a transverse component on the Bloch sphere. If one now changes ϵ with a small AC contribution at the Larmor frequency of the 01 transition, it provides the transverse torque in the rotating frame of the precessing spin necessary to perform any coherent manipulations of this spin qubit.

2.4.3 Predictions and main features

Although it is in principle possible to perform DC current readout of the ferromagnetic spin qubit, this system has the very strong point of being compatible with microwave resonator dispersive readout. Properly coupled to such a resonator (see chapter 4 and 6), the spectrum showed in figure 2.8 has a spin susceptibility. It is therefore possible to perform the readout of this spin qubit without any transport or spin blockade techniques, in contrast with ref. [32] for instance. This spin-photon coupling would enable the

possibility to perform QND¹⁰ measurements of spin states. The manipulation of such a spin qubit could also be done via the cavity photons using the standard QED techniques.

One can compute the matrix elements \mathcal{C}_{ij} , giving the coupling of all transitions ij to an AC electric field $\epsilon_{AC} \cos(\omega t)$ asymmetrically coupled¹¹ to the double quantum dot. Taking the eigenenergies E_i and the corresponding eigenstates $|i\rangle$ of the Hamiltonian \mathcal{H}_{SQB} (equation 2.6):

$$|i\rangle = a_{L\uparrow}^i |\uparrow, 0\rangle + a_{L\downarrow}^i |\downarrow, 0\rangle + a_{R\nearrow}^i |0, \nearrow\rangle + a_{R\swarrow}^i |0, \swarrow\rangle \quad (2.7)$$

then the \mathcal{C}_{ij} formally appear as:

$$\langle i | \mathcal{H}_{SQB} | j \rangle = E_i \delta_{ij} + \underbrace{(-a_{L\uparrow}^j a_{L\uparrow}^{i*} - a_{L\downarrow}^j a_{L\downarrow}^{i*} + a_{R\nearrow}^j a_{R\nearrow}^{i*} + a_{R\swarrow}^j a_{R\swarrow}^{i*})}_{\mathcal{C}_{ij}} \epsilon_{AC} \cos(\omega t). \quad (2.8)$$

The coupling of a transition to the electric field is then simply given by $g_{ij} = g_0 \mathcal{C}_{ij}$ with g_0 the bare coupling to the charge. The charge noise sensitivity of the dephasing rate for a transition ij is here given by the derivative of its frequency with respect to detuning $\frac{\partial f_{ij}}{\partial \epsilon}$ (see section 5.4 for the semi-classical dephasing model). Figure 2.9 compares the coupling matrix element of the 01 transition and the charge noise sensitivity coefficient as a function of ϵ and θ . For realistic charge noise and sufficiently large charge coupling, there should exist a possible compromise for which the coupling rate g_{01} between this spin qubit and a single photon in the cavity exceeds the decoherence rate Γ_2 of the qubit given by charge noise. Together with a high finesse cavity (decay rate κ), this would be the *strong coupling* limit, where $g > \Gamma_2, \kappa$. In this situation a single spin and a single photon can exchange coherent information before loosing their phase coherence. This allows to entangle and prepare coherent superpositions of spin states and Fock states in the resonator. Eventually, a strong spin-photon coupling would enable the possibility to couple distant spins and entangle them to perform two/multiple spin-gates.

It is also worth noticing that since both coupling rate and dephasing decrease with increasing detuning ϵ (see figure 2.9), this qubit can potentially reach even longer coherence times and thus behave as an isolated quantum memory at large detuning ϵ , that could be retrieved later on, simply by pulsing the system back to small detuning and without changing the qubit frequency significantly¹². One can easily understand this

¹⁰Quantum non demolition, i.e. a measurement that can be projective, but still preserving the state: one then knows exactly the state of the system right after the measurement.

¹¹see chapter 4

¹²since the 01 transition frequency is almost independent on detuning in this region

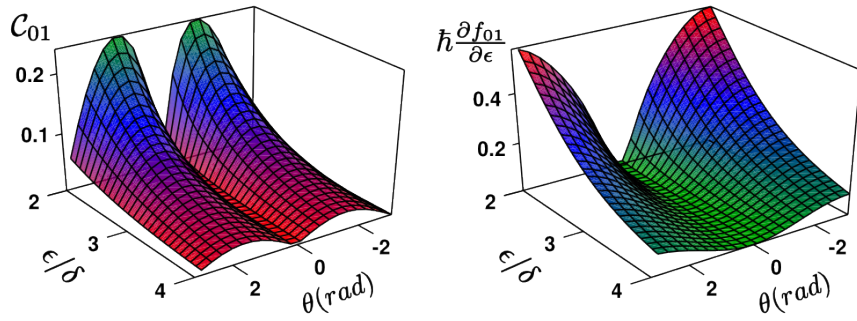


FIGURE 2.9: Coupling matrix element C_{01} and first order sensitivity to charge noise for the 01 transition ($\partial f_{01}/\partial \epsilon$) as a function of inter-dot detuning and tilt angle between the magnetisations of the electrodes. In this plot $t \sim 0.6 \times \delta$.

qualitatively: at large detuning ϵ , the electron wavefunction is fully localised in one dot and the small AC contribution of the cavity on ϵ cannot induce a transverse coupling any more. This strategy could for instance solve the problem of *spectral crowding* in current transmon-based cQED architectures (see e.g. [84]).

Chapter 3

Experimental methods

3.1 Nanofabrication	30
3.1.1 Standard nanofabrication techniques	30
3.1.2 Resonator fabrication for hybrid quantum dot - cQED devices	34
3.1.3 CNT growth, localisation, and contacting	35
3.1.4 Novel stamping technique for dry transfert of CNT's	36
3.1.5 Discussion	38
3.2 Measurement techniques	41
3.2.1 Low temperature setup	42
3.2.2 DC measurement	45
3.2.3 Microwave measurements	46

Progress towards a better understanding and control over nanoscale hybrid devices goes hand to hand with improvements in both the nanofabrication and the measurement techniques. These two aspects represent a major part of the work done for this thesis and are detailed in this chapter.

It is of great interest to understand the influence of specific fabrication steps over the physical properties of our devices, and feed this back in the nanofabrication developments in order to gain control and reliability. Developing new nanofabrication processes, optimizing existing ones, and using these recipes extensively is required to fabricate competitive samples. This aspect is developed in section 3.1. Besides, one also has to be able to control and read out physical quantities characterising a device and is therefore required to develop a suitable measurement setup, as discussed in the second part of this chapter.

3.1 Nanofabrication

Fabricating CNT-based hybrid cQED devices is a challenge due to the lack of control in the *state of the art* SWNT growth technology [85, 86]. This arises from the non-compatibility between conventional superconducting metals and the standard (high temperature) CVD growth of CNT's. In order to overcome this issue, we developed a dry transfer (stamping) technique which allows us to solve these problems. Specifically, we are able to combine high finesse microwave cavities with high quality carbon nanotube-based devices.

Several machines were used and many recipes were tried to achieve different fabrication processes, but all use similar basic principles given in section 3.1.1. All the fabrication was performed in the clean room of the ENS except most of the thin film evaporation, which were done at the ESPCI.

3.1.1 Standard nanofabrication techniques

e-beam Lithography

Lithography consists in etching patterns on a physical mask that will be later on used to *draw* this pattern on a surface with *e.g.* metallic thin films. The principle of (nano)lithography is shown in figure 3.1. An electro or UV-sensitive polymeric resist is spin coated onto a clean substrate. It is then exposed with either electrons or UV's in order to degrade the polymeric chains over a desired area. For a positive resist, these regions can then be removed using a *developer*, while only these regions stay on the

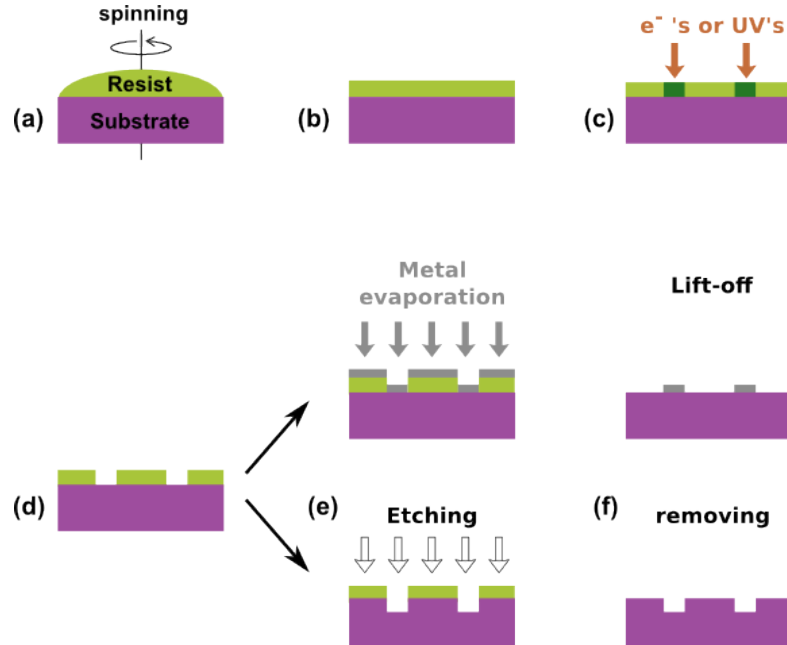


FIGURE 3.1: Basics of standard lithography techniques. (a) Deposition and spin coating provides a flat and homogeneous layer of resist (b). (c) Writing the resist using electrons in the SEM or UV's for photo-lithography, one can obtain a mask with a given pattern, once processed with a suitable developer (d). (e) and (f) depict lift-off technique for thin film deposition and an example of etching process simply using the resist as a protection.

substrate for a negative resist. This yields a resist mask that can be used for etching or lift off processes. In the case of etching, the resist protects the surface underneath it, other regions being etched away. In the case of a lift-off, a thin film is evaporated over the resist mask, which can then be removed using a solvent. The thin film therefore only sticks in regions where the resist was developed away.

A powerful instrument to fabricate this mask is the scanning electron microscope (SEM). It allows writing structures with a resolution down to a few nanometres, enabling us to partly bridge between our macroscopic world and the mesoscopic scale where quantum phenomena emerge. We use this instrument for patterning all the electrodes next to the CNT's, achieving 100nm resolution and 10nm alignment precision. Since our SEM is equipped with an interferometric stage, it also used to fabricate the optical masks used for patterning CPW resonators.

Details about the parameters used for the e-beam lithography are given in Appendix A. Although alternative resists like *AZ5214* can be used for e-beam writing, we mostly used the popular *PMMA* (A1), either plain or diluted with anisole in order to achieve thinner layers. It is indeed preferable to use a layer thickness comparable to the smallest characteristic size of the pattern in order to avoid collapsing of the resist (too deep and narrow trench). Development is performed with Methyl isobutyl ketone (MIBK)

and removing with acetone. It is convenient to use non-insulating substrates like silicon (Si/SiO_2) to avoid charging effects which alter scanning and writing with the SEM. However, sometimes one has to use substrates like quartz or sapphire which are insulators. It is then necessary to deposit a very thin layer of metal (*e.g.* aluminium) on top of the resist layer. Provided an exposure dose adjustment, lithography works the same way, with electrons going through the metallic layer. This layer is then removed before development of the resist; for aluminium, it is etched away with a KOH solution.

UV Lithography

UV (or photo)-lithography uses ultraviolet light instead of an electron beam. Large masks can be used to expose several cm^2 in a few seconds, and possibly do it again on the same substrate a few minutes later if the first try came out wrong. It is a very efficient process for fabricating bigger structures with a resolution of about $2 - 3\mu m$ and is therefore naturally suited for fabricating CPW resonators in the microwave range. The widely used *AZ5214* is easily reversed from positive to negative lithography with a simple re-bake and an extra exposure. The *AZ5214* is moreover thicker than PMMA and allows for thicker metal deposition, which turns out to be useful in section 3.1.4 for instance. Details about the parameters used for the UV lithography steps are given in Appendix A.

Thin film deposition

Although our hybrid circuits include semiconducting or molecular quantum wires, the main ingredient for fabricating them is still metal. It is thus essential to be able to perform evaporation of pure and clean metallic, superconducting and ferromagnetic thin films (figure 3.1). This is achieved using an ultra high vacuum (UHV) electron gun (or joule) evaporator or a sputtering machine.

Electron gun evaporation is performed by focusing a beam of accelerated electrons on a crucible containing metal ingots. This is carried on until exceeding the melting point, thus creating a jet of metallic atoms in which we place the substrate. The evaporation rate and total thickness are monitored reading out the resonant frequency of a mechanical quartz oscillator placed in the stream of atoms. Depending on the metal, it can be fundamental (but also difficult in practice, *e.g.* for superconducting Nb) to do this operation in high vacuum to ensure the purity of the film deposited on the substrate. Many of the evaporation for this work were done at the ESPCI where a UHV system used to have a base pressure of few $10^{-9} mbar$ (and for example easily reaches an evaporation rate of $15\text{\AA}/\text{s}$ for aluminium). Most of the devices presented in this thesis were however

done with a working pressure of few 10^{-7}mbar for Pd, PdNi, Al, and Pt. We also used a careful oxidation process to fabricate top gates over our CNT devices. This consists in 3 steps of evaporation of 3nm of Al at few 10^{-7}mbar and 10min oxidation at 1mbar of O_2 . The top gates are usually subsequently covered by 30nm of Al and 10nm of Pd for protection.

Another way to deposit thin films is sputtering. It is a very efficient technique for metals which are trickier to evaporate such as niobium, and get a higher deposition rate. The principle is the following. Starting from high vacuum, an argon plasma is activated at 10^{-2}mbar and bombards a few mm thick target of metal placed next to the substrate. Metallic atoms are extracted off the target and the deposition takes place with a rather high rate of about 2nm/s , thus avoiding too much impurities. The drawback of this method is that it is not very well compatible with lift-off techniques due to a more isotropic deposition (which creates flags of metal), and the heating of the resist¹. We however did lift-off of Nb for resonators, keeping deposition time short, and thickness small compared to resist thickness (e.g. 100nm of Nb for $1.4\mu\text{m}$ of *AZ5214*). Note that this is not as reliable as etching techniques or standard lift-off and sometimes requires ultrasonics for example, which one prefers to avoid for CNT's.

Etching

Etchings processes are crucial for creating mesas or holes on substrates, cleaning substrates, removing intermediate auxiliary metal layers, or defining clean patterns on chips entirely covered with metals such as niobium. One can use chemical wet etching solution such as *KOH* to remove aluminium, or reactive ion etching (RIE), that consists in a dry chemical and/or physical etching using plasmas such as *SF₆* to etch niobium. The latter technique often has the advantage of being more reproducible and producing less side effects such as lateral etching for instance.

In addition to the common etching processes detailed in Appendix A, we used processes to create mesas on quartz substrates as well as holes in *Si/SiO₂* substrates. These enabled us to perform dry transfer (stamping) of CNT's, see section 3.1.4 and go towards the dry transfer of pristine CNT's, see section 3.1.5. For creating mesas on a quartz substrate, we first cover it with two layers of $\simeq 500\text{nm}$ of PMMA and a thin layer of 10nm of Al (to avoid charging effects). The chips are then exposed using e-beam lithography in order to pattern the mesa shape and some alignment markers. After development, a layer of 500nm of Al is evaporated at $\approx 10^{-6}\text{mbar}$. After lift-off, the quartz substrate with resulting aluminium mask is etched with reactive ion etching (*SF₆*)

¹The resist gets reticulated (like *burnt*) and badly dissolves in acetone

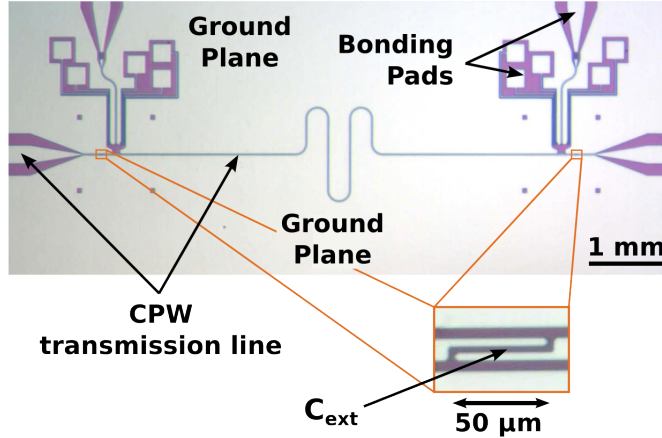


FIGURE 3.2: Optical micrograph of a typical resonator made out of aluminium, showing the transmission line and ground plane of the CoPlanar Waveguide geometry. The transmission line is interrupted at both ends with an *access* capacitance C_{ext} determining the coupling of the resonator to the rest of the transmission line. These capacitances play the role of mirror for this Fabry-Perot cavity. Bonding pads are added, isolated from the ground plane in order to carry DC voltage, DC current or additional microwave signal to the CNT device.

for overall 60min . The remaining Al is then dissolved in a solution of KOH , yielding mesa structures of $3\mu\text{m}$ height.

3.1.2 Resonator fabrication for hybrid quantum dot - cQED devices

The fabrication of our CPW microwave resonators is a crucial point and should be as reliable as possible, to allow us to do a post selection on finished devices, for which CNT's properties cannot be fully controlled. The goal is to maximize the coupling to the quantum dot devices while keeping dissipation, microwave leakage and cross-talks as low as possible (see for example figure 5.1 and 5.4). In order to do so, various kinds of geometries were investigated, such as the one displayed in figure 3.2. The resonator quality factor is then determined by lithographically defined coupling capacitances and internal details ².

High finesse microwave resonators require a low loss substrate, while quantum dot devices need to be placed on an insulator for DC gating. However, corresponding materials such as sapphire are strenuous since they need an extra aluminium evaporation for every e-beam lithography to avoid charging effects. Our choice thus resulted in undopped high resistivity ($10k\Omega\cdot\text{cm}$) Si/SiO_2 substrates, with 500nm oxide. Such substrates combined with standard fabrication techniques for 100nm thick aluminium resonators yield to

²The total quality factor Q_{Loaded} of a resonator is given by $\frac{1}{Q_{Loaded}} = \frac{1}{Q_{ext}} + \frac{1}{Q_{int}}$. Q_{int} is determined by internal resonator losses or leakage/dissipation through the dot device. Q_{ext} is best optimized when $Q_{ext} \approx Q_{int}$ in order to preserve Q_{Loaded} while keeping a high signal/noise ratio, maximising the transmission $S_{21} = -\frac{Q_{Loaded}/Q_{ext}}{1+2iQ_{Loaded}(\omega-\omega_c)/\omega_c}$

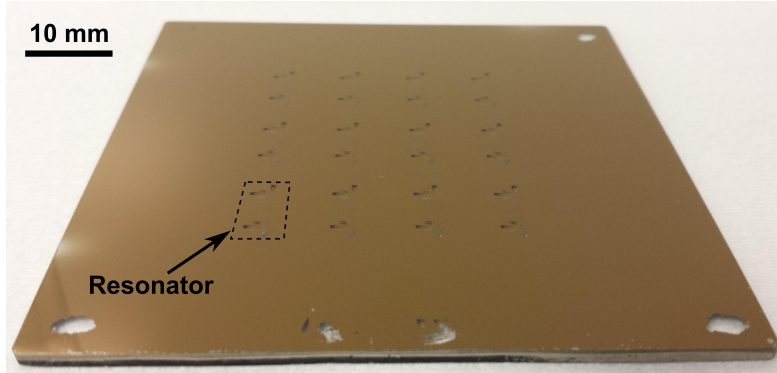


FIGURE 3.3: Photography of a UV mask (Cr on transparent glass) fabricated to allow quick photo-lithography of microwave resonators. (*Stylish photo: courtesy of M.C. Dartailh*)

internal quality factors greater than 10^5 at large microwave powers (see figure 3.13), far more than needed for our application.

Once a geometry is chosen, we decide to fabricate our resonators using UV lithography techniques for the sake of speed and reliability, and either lift-off or RIE etching techniques (see figure 3.2 for an example of resonator). The first step is therefore the fabrication of an optical mask such as shown in figure 3.3. Masks are commercially available, and can also be made rather quickly using laser lithography (which is available at the ENS). Unfortunately, it turns out that very little homothetic difference or distortion between the machine used to fabricate the mask and the SEM used for all the other lithographic steps are an issue when one wants to align structures distant from a cm with a precision of $2 - 3\mu m$. As a result, we fabricate our masks using the same SEM as the one used for the other e-beam steps. We start with a commercial UV-transparent glass substrate covered with an opaque layer of chromium . It is then spin coated with PMMA and e-beam exposed to pattern few resonators. After development we perform chemical etching with a $HClO_4 + Ce(NH_4)_2(NO_3)_6$ solution and remove the unwanted resist residues with acetone. This process has a reasonable yield of $\simeq 30\%$ of *defectless* resonator masks. These masks include bonding pads and all the big structures in order to minimize the time spent on e-beam lithography to connect the dot devices. They also include alignment marks that match other marks on the device chip.

3.1.3 CNT growth, localisation, and contacting

We grow all our carbon nanotubes using a chemical vapour deposition (CVD) growth, performed in a furnace at $900^\circ C$. We use a standard methane process of which parameters are given in Appendix A. In order to start the reaction, we use catalyst nanoparticles from which CNT's start growing. This catalyst is a solution that can be either

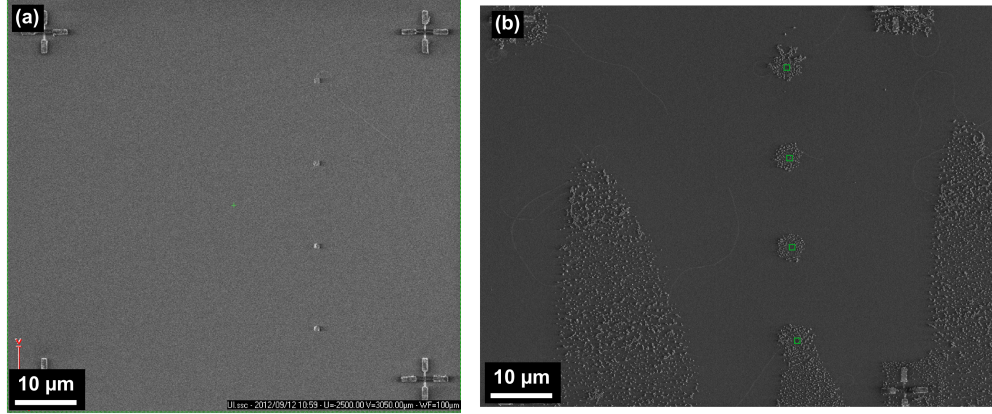


FIGURE 3.4: SEM pictures of catalyst depositions using lithographically defined resists masks. The technique is similar to what is explained for thin films in figure 3.1. (a) Successful deposition (after CVD growth) (b) Unsuccessful deposition (after CVD growth). Particles are not localised at the wanted region (green squares) and are spread over a large region of the chip

deposited on a full chip, or a previously lithographically patterned chip in order to get catalyst only in specific regions. This last technique was widely used during this work, but turns out to be random in terms of reliability (see figure 3.4). This fact was also part of the motivation for developing the technique explained in section 3.1.4.

The catalyst is made using 39mg of $Fe(NO_3)_3 - H_2O$, 7.9mg of MoO_2 and 32mg of Al_2O_3 nanoparticles diluted in 30mL of IPA. It is sonicated for 1h and sedimented for 45 min before spreading it on a substrate. After CVD growth we use the SEM to take pictures of the CNT's with a precise alignment ($\simeq 10nm$) in order to draw masks on the SEM software later on. These masks are then used to perform fine lithography steps to contact the CNT's. Contacting CNT's requires over-exposure and over-development of the resist in order to optimize the contact between the metallic film and the CNT's. It is possible to make a galvanic contact for source and drain electrodes carrying current (e.g. with Pd, PdNi, Al, Au,...) or a capacitive contact (e.g. with Al_2O_3 as a dielectric) for electrodes playing the role of gates.

3.1.4 Novel stamping technique for dry transfert of CNT's

Combining the advantages of CVD-grown CNT's with superconducting cavities made of metals such as Al or Nb is a priori an experimental challenge since these metals are not compatible with the growth conditions (for example $900^\circ C$, flow of CH_4 and H_2 ,...). In addition, the residues of growth of carbon nanotubes (for example catalyst or amorphous carbon) provide in general very strong dissipative media for microwave signals, resulting in poor microwave properties of the devices, see [29, 30].

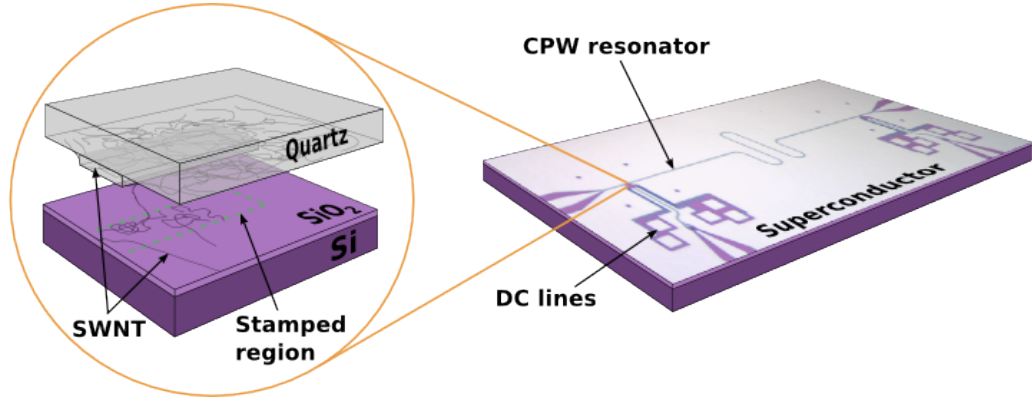


FIGURE 3.5: Principle of the stamping technique for combining high finesse microwave cavity with CVD-grown single wall carbon nanotubes (SWNT). The standard CVD growth is performed on a quartz substrate containing mesas which we use as stamps in order to transfer SWNT's on a clean silicon RF substrate. This can be done at chosen locations, in this case in the ground plane openings of a superconducting co-planar microwave resonator.

The principle of our stamping technique is depicted on figure 3.5. The single wall nanotubes are grown on a quartz substrate containing RIE-etched quartz islands, following the process explained in section 3.1.3. These islands are aligned with respect to metallic alignment markers made on the device substrate and stamped onto it in locations matching the ground plane openings which one can see in figure 3.5 right panel and 3.6c.

We first make the quartz stamps which have typical size of $100\mu\text{m} \times 10\mu\text{m}$ with $3\mu\text{m}$ height. They are the simplest stamps that one can make and optimization of the process has led us to use variants of this geometry e.g. 8 stamps of $10\mu\text{m} \times 10\mu\text{m} \times 3\mu\text{m}$ forming a square array with a $10\mu\text{m}$ pitch. Note that, at the same time as the stamp is etched using RIE, alignment markers are also formed. They are used at a later stage to align the stamp to the desired location of RF Si substrate. The latter is prepared separately with sputtered Nb alignment markers matching exactly those of the quartz structure.

We deposit catalyst over the whole quartz chip, yielding a high density of nanoparticles on the stamp and around it, as it can be seen on figure 3.6a. This means that the density of single wall carbon nanotubes grown on the quartz stamp is rather high. After stamping the quartz on the Si/SiO_2 substrate (which can be any substrate in principle), several single wall nanotubes are transferred, see figure 3.6b. Depending on the stamping process, the stamped region highlighted by the green dashed lines can contain a more or less dense arrangement of nanotubes. In the situation shown in figure 3.6b, rather long SWNTs ($\approx 10\mu\text{m}$) can be isolated within that region. Usually, SWNTs can also be found apart from the stamp region as shown in figure 3.6b. They probably arise from the breaking of SWNTs grown between the bottom and the top of the quartz mesa.

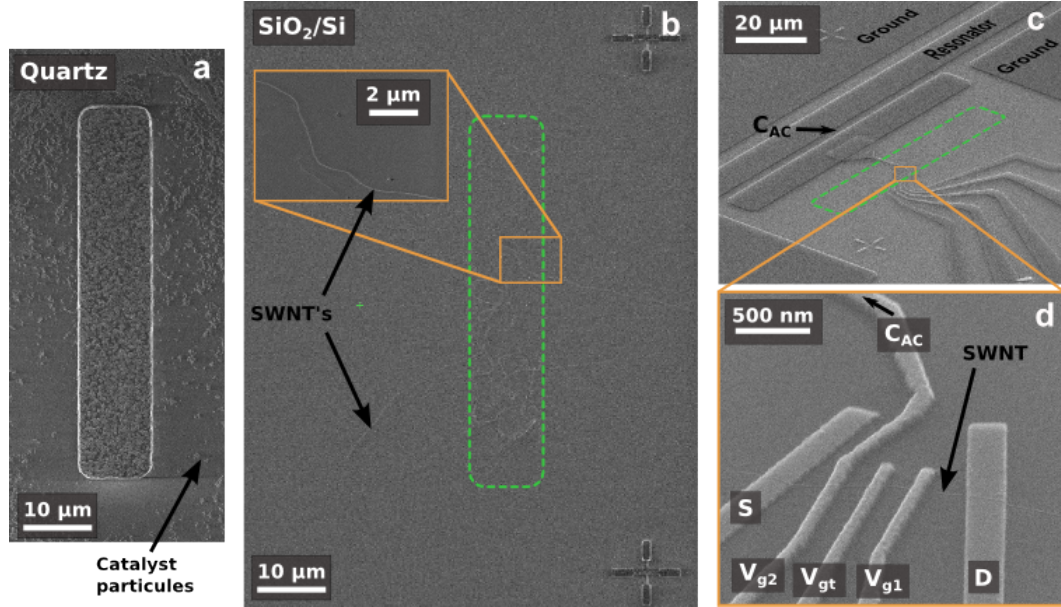


FIGURE 3.6: SEM images of the key fabrication steps: (a) mesa on the quartz substrate after catalyst deposition; (b) Region of the silicon substrate where stamping has been performed. Green dashed rectangle is the print of the stamp. Inset: zoom on a SWNT used for fabricating the DQD device. (c) Tilted view of the device after e-beam lithographies and metal deposition corresponding the electrodes of the DQD as well as photolithography and metal deposition for the resonator. (d) Same tilt as (c), zoomed on the DQD.

From this point, the device is fabricated using the conventional nanofabrication techniques (figure 3.6b, section 3.1.3 and section 3.1.2). An example of device is shown in figure 3.6c and d. A double quantum dot structure with Al/Al_2O_3 top gates and two non-collinear $Pd_{75}Ni_{25}$ ferromagnetic leads has been embedded in an Al microwave cavity.

We demonstrate the interest of our technique in chapter 5, with a very closed double quantum dot (*Sample SQBRES35R*). Our technique has the advantage of simplicity over previous stamping techniques [6, 7, 87]. It also provides a high yield of single wall carbon nanotube transfer. It could easily be extended to other microwave setups with nanotubes [88–91].

3.1.5 Discussion

Issues

Once recipes are set, successfully doing a whole process from beginning to end can still be a tedious work given the non perfect yields of nanofabrication processes and the lack of control over CNT growth. But even a finished device does not always behaves like

wanted and the tunability of CNT-based devices is very often limited. It is fundamental to understand that this is intrinsically related to the fabrication processes:

- The growth can obviously have an impact on the quality of the CNT crystal structure, and for instance does not provide control over the gap of the CNT's (or even their semiconducting character).
- Techniques such as the ones presented in the previous sections make the CNT's go through processes during which they are coated with polymeric resist, dipped in many organic solvents, exposed to highly accelerated electrons (e.g. 20keV in the SEM), etc..
- The CNT supporting the final device is lying directly on SiO_2 substrate.

Among all the fabricated samples, we have connected about 70 devices and cooled down approximately half of them. Over this statistical sample, our experience is that very often, the combination of these factors yields transport properties that are very likely to be dominated by defects. In practice, we observe a dramatically limited tunability of the electrostatic confinement and we associate this fact with the points listed above (see also [92], or older works [93]). This is an important issue when one wants to use such devices as hosts for qubits, which require a very close system and a strong confinement in general. Direct contact on the substrate is also suspected to increase charge noise.

Remarkably, defects can also be used to obtain a strong confinement as it was our strategy to obtain devices such as the one (*SQBRES35R*) presented in section 5.1.2.

Perspectives: stamping single pristine CNT's

There exists techniques to solve the issues raised above, at least partially, or on statistical average.

It is possible to obtain “as grown”, or “ultra-clean” CNT's by performing the CVD step at the very end of the fabrication process, thus avoiding any alteration to the device. Despite it is not easy, this can be done using platinum electrodes, which can survive well controlled CVD conditions. It is even possible to grow ultra clean CNT's over tranches to obtain suspended devices [85, 94, 95]. This technique is however not compatible with the use of other essential metals (such as Pd, PdNi or Al for going hybrid and study other orders) and cannot be used for cQED devices using conventional cavities.

However another stamping technique, first demonstrated by reference [87] and recently further developed [6, 7, 75], seems to provide SWNT's with outstanding properties and be

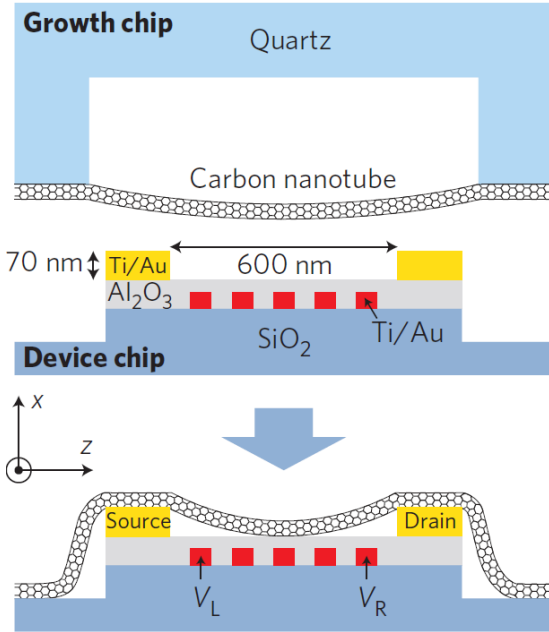


FIGURE 3.7: Principle of the pristine CNT stamping technique. Source: [6]

able to solve the problems discussed in the previous section. It would be therefore highly desirable, though very challenging, to adapt this in a microwave cavity architecture.

The principle of such a technique is depicted in figure 3.7. First, one must be able to grow SWNT's across a wide and deep trench on an auxiliary transparent substrate such as quartz. Second, gate and source-drain electrodes are prepared on a separate substrate, ensuring they are placed on a mesa structure. The growth substrate is then flipped, aligned over the device chip, and brought down in contact with it. Eventually, the growth substrate is lifted up and the CNT should stick on the electrodes, suspended or not depending on the geometry and success of the stamping.

For a potential use in a cavity, one must be able to control the position of the CNT very precisely in order keep a sufficient coupling to the electric field. For that reason we started growing CNT's between pillars and not over tranches, thus unfortunately reducing growth yield drastically. But pillars also have the advantage to only require small holes on the device chip; this avoids the mesa structure used in [6, 7, 75], which is hard to implement and not very compatible with a cavity setup (resist coating, oxyde layer,...). Besides, the geometry of our ferromagnetic electrodes also required fine alignment and therefore pillars instead of trenches. We have started to work towards that goal and further investigation is ongoing to improve CVD growth control and directionality, necessary for achieving a reasonable yield, see Appendix A. So far, we are able to perform all the lithographic, etching and alignment steps including the alignment of the growth and device chips with our photolithography aligner (*Suss Microtech, MJB4*). Figure

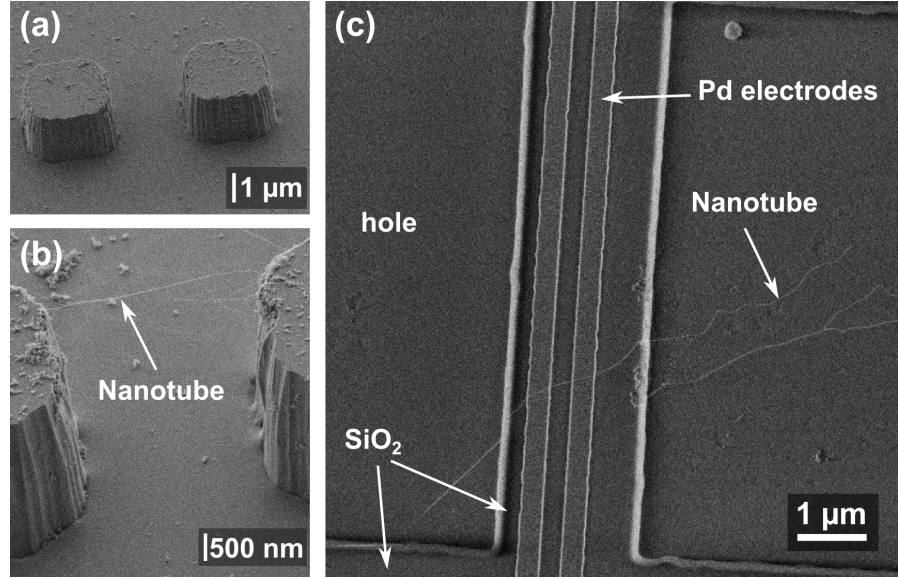


FIGURE 3.8: Preliminary tests for CNT stamping in a geometry compatible with a future implementation in a cavity (SEM images) **(a)** Pair of pillars obtained by etching a quartz substrate. **(b)** Zoom on a pair of pillars after CVD growth, showing multiple CNT's and one CNT spanning between the two quartz pillars. **(c)** Image of a device after stamping. A nanotube is deposited over two Pd electrodes. Holes are etched on both sides of the quantum dot geometry to allow the quartz pillars to go below the sample' surface. The chip was backgated.

3.8 shows example of key development steps realised for cavity-compatible stamping of pristine CNT's.

Finally, even if one can provide a reliable CVD growth and pristine stamping technique, it is not certain that confinement would be sufficiently strong (tunnel rates in the *GHz* range, similarly to section 5.1.2). Indeed one can manage to go in the single electron regime and still observe coupling to the leads of the order of few 100*GHz* ($\simeq meV$) next to the semiconducting gap.

3.2 Measurement techniques

Though low temperature, high frequency and low frequency measurements are routinely performed in many labs, it remains a challenge to set up an experiment with competitive characteristics for hybrid cQED experiments.

3.2.1 Low temperature setup

Wiring, filtering, amplification

The work for this thesis started with wiring up a wet dilution fridge freshly received from *Oxford* (Kelvinox MX 250). It is a substantial task to fit all the necessary measurement apparatus in such confined space. The goal is to achieve low heat power on the cryostat while bringing down all the required DC and microwave components and cables. Details of the calculations and resulting choices are given in Appendix B.

Figure 3.9 shows photographs of the fridge. Both flexible DC lines and semi-rigid RF cables run from 300K to the mixing chamber plate of the insert, thermalised at every intermediate plate. DC thermalisation is done by including portions of copper strip lines running over a kapton sheet that is glued with *Stycast* on the fridge frame (see figure 3.9c,d). Thermalisation of the inner and outer conductor of the RF cables is ensured by two means. Some gold plated adapted copper parts are strongly crimped on the outer shield, and others on attenuators and 50Ω terminations (figure 3.9c). These clamps are well thermally anchored to the fridge using thick gold plated copper wires.

RF cables going downwards are strongly attenuated to preserve input signal/noise ratio, to prevent from letting hot photons degrading the electronic temperature (and the fridge temperature) and to ensure a small thermal photon number in the cavity. The latter fact is wanted to reach the quantum regime³. In order to maximise the output signal/noise, we use superconducting (NbTi) cables to minimise the attenuation of the signal going upwards to the measurement chain. Superconducting cables also allow avoiding the use of thermalisation as they carry negligible heat. The output RF port of the sample holder is connected to two circulator in series shown in figure 3.9d. These chiral components strongly reduce ($\simeq 18dB$ each) the back-action of the cryogenic amplifier on the cavity and thus keep the thermal occupation low. Then comes a cryogenic amplifier, thermalised on the liquid He bath (see figure 3.9c) and connected to the rest of the measurement chain at room temperature. An example of wiring scheme is given in figure 3.10, summarizing filtering, attenuation, thermalisation and amplification.

We also specifically designed the sample holder and the PCB showed in figure 3.9 in order to embed together DC lines, cavity line and extra RF excitation lines, 50Ω until micro-bondings, finally bridging to the sample.

³cavity in the ground state with photon number small than 1 at equilibrium ($20mK = k_B T \approx 500MHz \ll f_{cavity} \approx 7GHz$)

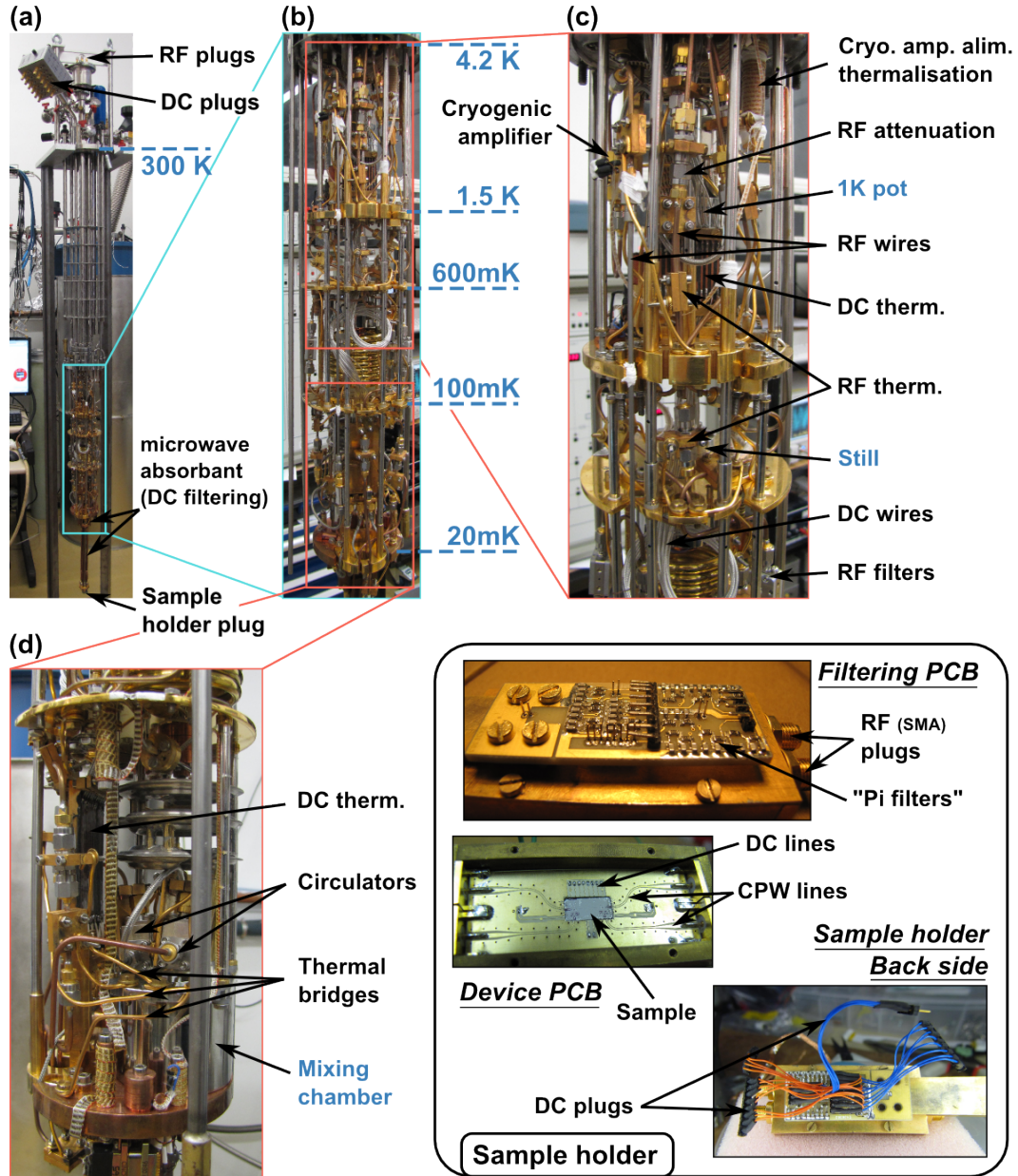


FIGURE 3.9: Photographies of the dilution fridge insert and sample holder. (a) Whole view of the insert with the room temperature connections on top, then shields for the helium bath underneath and space corresponding to the inner vacuum chamber (IVC), see light blue rectangle zoomed in in (b). The different temperature stages are given by fridge plates on which cryogenic equipment sets the temperature (blue dashed lines). (c), (d) Zoom on the higher and lower part of the IVC showing all the fitted measurement apparatus.

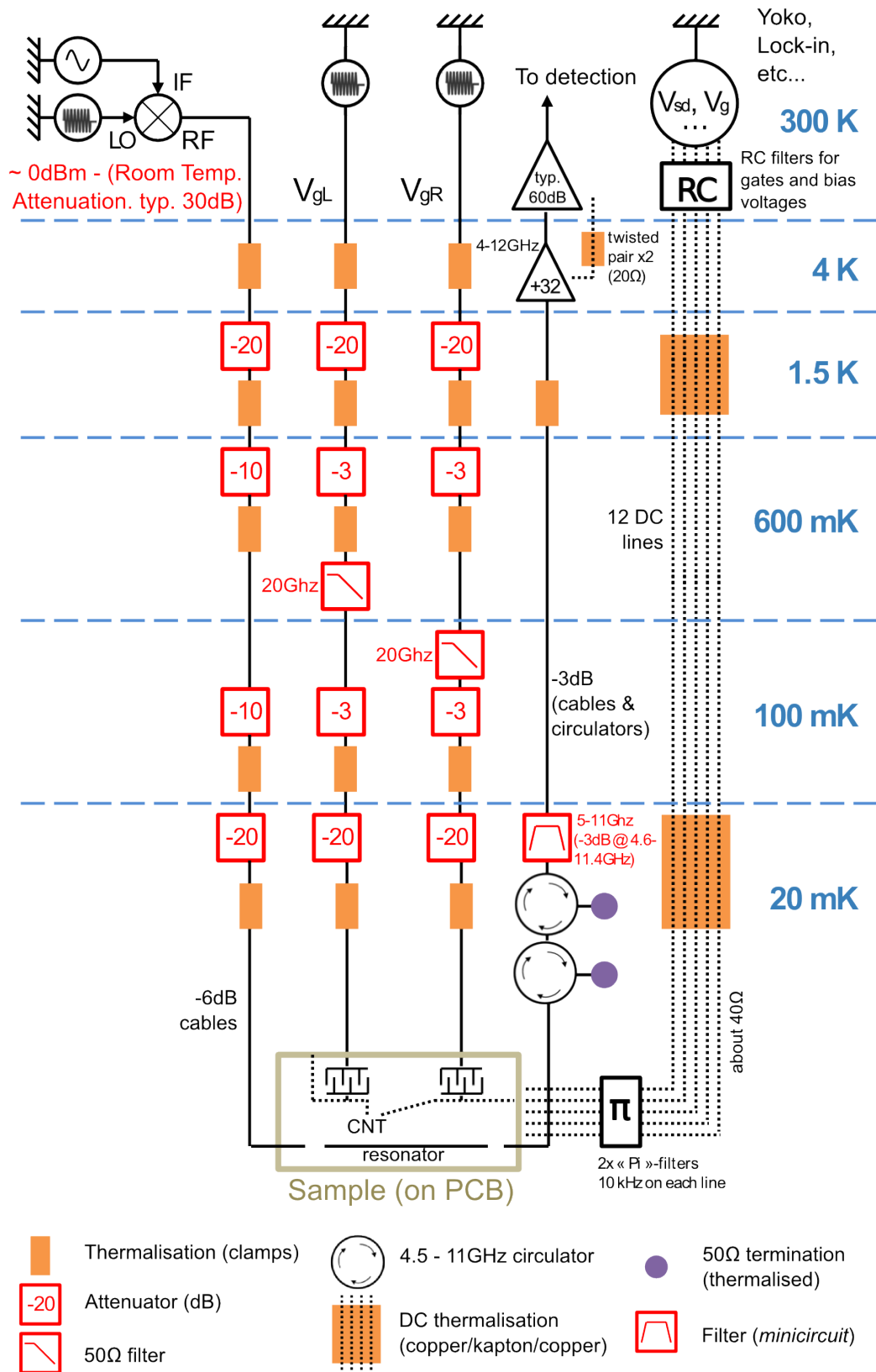


FIGURE 3.10: Typical example of wiring scheme we used (room temperature setup not detailed, see next section).

3.2.2 DC measurement

Although DC measurement techniques might seem simpler than those of high ($10Ghz$) frequencies, they are not provided with commercially available components and thus require more *do-it-yourself* hand work. This starts with wiring (section 3.2.1 and figure 3.9a,b,c) and continues with filtering and low noise current measurements.

Three discrete filtering sections are added to the continuous RC filtering of the resistive coaxial wires (flexible, stainless steel, *LakeShore*, $24\Omega/m$ and $174pF/m$ over $\simeq 1.70m$). For electrostatic gate voltages and voltage bias, room temperature filtering consists in shielded boxes with 2 stages of RC filters in series, cutting off at kHz frequencies depending on gates (but likely going back up after $100MHz$). Voltage bias is also diminished by a factor of 1000 with a voltage divider. The second filtering stage is strongly dissipating microwaves, $3dB/cm@1Ghz$ and up to $120dB/cm@18Ghz$. This is done by crumpling up manganese wires and embedding them into copper boxes and cylinders filled up with *Eccosorb MF 117*. The last filtering stage is directly connected to the sample holder, see bottom right panel in figure 3.9. Two pi-filters (symmetrised RC circuits, $1k\Omega$, $1nF$) in series are made up with surface mount components which supposedly hold on up to frequencies $> 100MHz$. We mostly used *Yokogawa GS200* as DC voltage sources.

While DC voltage biasing, we measure DC current flowing through the device using an analogical current amplifier. The basic idea of such an amplifier, given in figure 3.11, is first year textbook. It becomes however totally non trivial to realise such a circuit able to measure currents of the order of $100fA$ in a reasonable integration time, through the whole setup. Because issues on that matter can arise from several causes (ground loops, ground definition, amplifier instability and non linearities, amplifier power supply stability, etc...), building an efficient amplifier can be a tedious work. Along with electronics staff, a home made amplifier has been realised and its circuit is given in Appendix B.

We performed both lock-in (*SR7265LI* @ $77Hz$) and pure DC (*Keithley 2000*) measurements as shown for instance in figure 3.12 and 5.3. However we often found ourselves better suited with pure DC measurement, especially for very closed (high impedance) double quantum dots. For a purely DC measurement, the current resolution intrinsically related to the experimental setup is about few $100fA$ for $20ms$ integration time ($60ms$ per point). However samples are also sometimes unstable; besides we often measure with a resolution rather in the range of few pA for $20ms$ integration time.

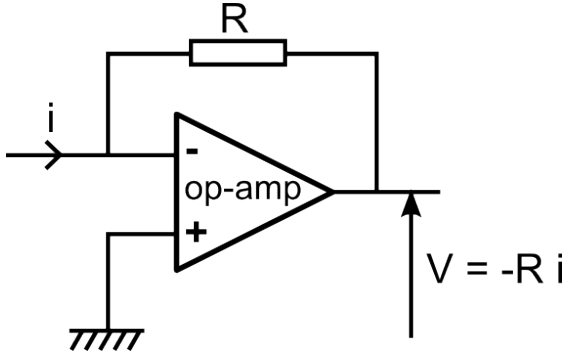


FIGURE 3.11: Simplest circuit of an analog current amplifier using an operational amplifier (op-amp). Output voltage is amplified with a gain given by the backaction resistance.

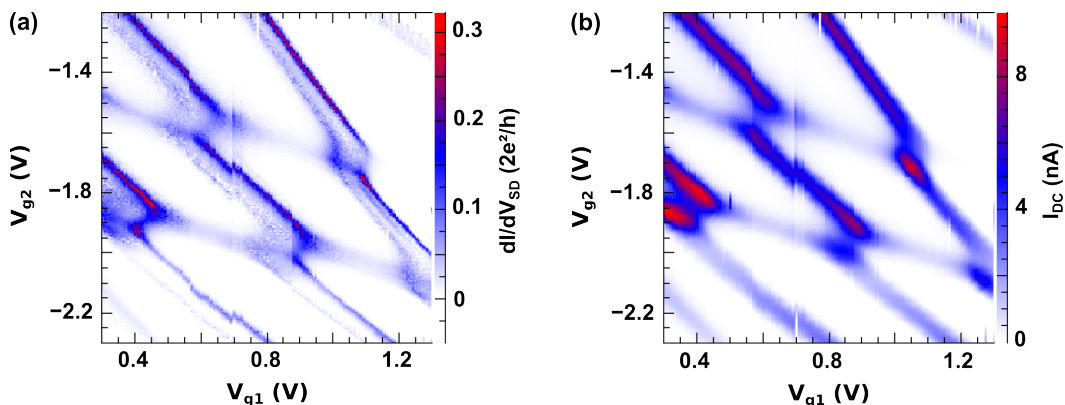


FIGURE 3.12: Double quantum dot stability diagram measured with a transport spectroscopy. (a) is a differential conductance measurement performed with a standard low frequency lock-in (77Hz), whereas (b) is a pure DC measurement. The applied DC bias is $V_{sd} = 1mV$.

3.2.3 Microwave measurements

To some extent, microwave measurements have the advantage of being preserved from ground definition issues and $1/f$ noise. Combined with cQED techniques, they provide a very powerful platform in terms of sensitivity and access to physical quantities different from the ones of DC measurements. However it is tricky to engineer large coupling strength between a CPW resonator and a system as small as a DQD. As a results the signals measured here are rather small compared what found in the superconducting qubit community for example (see for instance [20, 96]). The next sections describe respectively our measurement setup and the principle of dispersive shift measurements.

Measurement setup

Though we fabricated a few RF components (e.g. see Appendix B, B.5 for a dissipative filter), most of the RF components we used are commercially available (and often cost

an arm and a leg).

The input line of the cavity is rather heavily attenuated ($66dB$ along the fridge and $30 - 60dB$ at room temperature), and can allow us to go down to the single photon regime , typically $-130dBm$, i.e. $10^{-16}W$ with our cavity Q factors and transmissions⁴. This also preserves the signal to noise ratio (input power at room temperature $\approx 0dBm, 1mW$). On the contrary the measurement line is attenuated as little as possible until the first stage of amplification at $4K$: *LNA Caltech SNL012* with a noise temperature of $T_N \approx 4K$ ($+40dB$ gain, $4.5 - 12GHz$ bandwith). If the measurement chain is well designed, this amplifier determines the whole signal to noise ratio of the detection:

$$\sigma_A = \sqrt{4Rk_B T_N \Delta f} = 5 \times 10^{-11}V @ \Delta f = 1Hz. \quad (3.1)$$

Where σ_A is the amplitude standard deviation, $R = 50\Omega$ and Δf is the detection bandwith (e.g. defined by lock-in time constant). In pratice we measured S/N of the order of

$$\sigma_\phi(rad) = \frac{\sigma_A}{A} = 6 \times 10^{-3}(rad) @ n \approx 10 \text{ photons (uncalibrated)} \text{ and } \Delta f = 1Hz. \quad (3.2)$$

where σ_ϕ is the phase standard deviations. It is a factor of ≈ 4 worse than theoretical SNR ratio of the amplifier, but seemed optimized (powers remain uncalibrated and errors of $6dB$ over the whole setup would not be extremely surprising). Figure 3.13a and b shows examples of resonances we measured for an empty (no CNT device) resonator at high power and for the complete device presented in section 5.1.2, here in the single photon limit.

We mainly measured the RF signal in two ways, with a home made kHz homodyne-like detection and with an *Agilent PNA* vectorial network analyser (VNA). The latter is the most reliable in terms of calibration and optimal settings whereas the home made detection is better adapted to continuous measurements where external parameters such as gate voltage or magnetic field are swept. Figure 3.14 shows our homodyne-like detection scheme. This method suffers from calibration issues in the very low power limit concerning the field quadratures. Indeed at such low frequencies, there can be cross talks between the different components involved in figure 3.14. These cross talks will result in device-independent offsets on the quadrature and therefore yield distortions on

⁴see equation 4.45

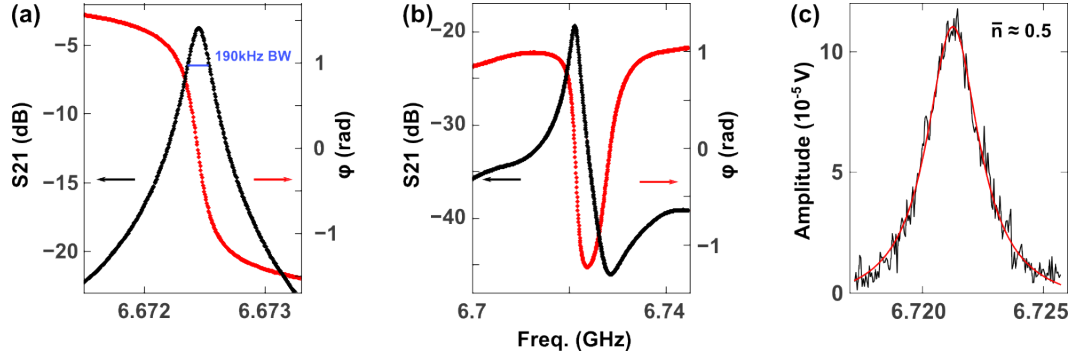


FIGURE 3.13: (a) Amplitude and phase response of a clean (empty, no CNT device) CPW cavity at fundamental mode in the high power limit, $Q_{tot} \approx 35000 \Rightarrow Q_{int} > 10^5$ (b) Resonance of a device including a DQD measured in the high power limit, $Q_{tot} \approx 3500 \approx Q_{int}$. The amplitude exhibits a “fano-shape” resonance, likely to be related to a parasitic crosstalk between SMA connectors inside the sample holder. (b) Same device as in (b), but in the single photon limit, $n \approx 0.5$. Lorentzian fit extracts $Q \gtrsim 2500$.
Sample in (b) and (c): SQBRES35R

the signal, see section 4.5. It also has the drawback of sending two (very close) frequencies to the device. This latter fact can be often ignored but can in principle produce aberrations for example if the device has some non-linearities. As a result we started experimenting higher frequency (few $10MHz$), heterodyne detection schemes such as the ones presented in figure 3.15, which approach more the reliability of VNA’s.

Cavity frequency shift

This section describes the principle and basics of cavity frequency shifts. We read out the modulated microwave field transmitted through the cavity at its resonant frequency and thus obtain both amplitude and phase of the signal, see figure 3.13. Electronic transitions, or charge fluctuations across tunnel barriers in the quantum dot systems coupled to the cavity yield a change in the cavity frequency, defined as a *cavity pull*. In practice, we mainly monitor the phase signal since it has a very steep change at the resonant frequency and is thus a good sensor⁵. One can think of the following heuristic argument: the fundamental frequency is given by

$$f_c = \frac{c}{n_{eff}} \frac{1}{2L} \quad (3.3)$$

where $n_{eff} = \sqrt{\epsilon_{eff}}$ is the optical index, L is the length of the cavity and c the speed of light. The effective dielectric constant ϵ_{eff} of the propagating media also includes the DQD device placed in proximity. A change of the DQD properties (more precisely a

⁵Besides, the non perfectly lorentzian character of our resonances can have a major impact on the amplitude variation, see figure 3.13b and more particularly section 4.4. It is also trickier to analyse from the physical and theoretical point of view (though could be then rich and meaningful).

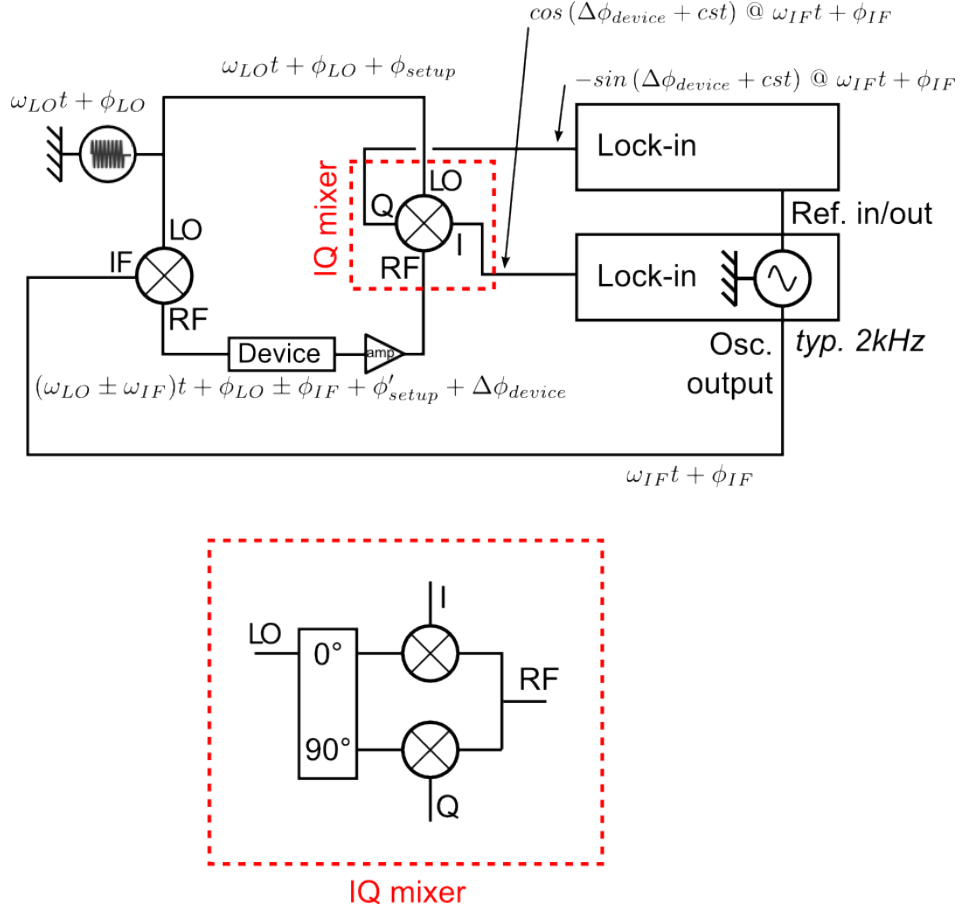


FIGURE 3.14: Homodyne-like detection for microwave measurements such as the one widely used for the work of this thesis. The operation of the IQ mixer is given by $I = \widetilde{A}_{IF} \cos(\omega_{LOT} + \phi_{LO} + \phi_{setup}) \cos((\omega_{LO} \pm \omega_{IF})t \pm \phi_{IF} + \phi_{LO} + \phi'_{setup} + \Delta\phi_{device})$, where $\widetilde{A}_{IF} = A_{IF} \cos(\omega_{IF}t + \phi_{IF})$ and A_{IF} is the lock-in output amplitude (diminished by conversion losses). Keeping the band oscillating at ω_{LI} , one gets $I = A_{IF}/2 \cos(\omega_{IF}t + \phi_{IF}) \cos(\omega_{IF} + \phi_{IF} + \phi'_{setup} - \phi_{setup} + \Delta\phi_{device})$. The Q quadrature reads the same formula with 90 degrees dephasing on the LO, $\cos(\omega_{IF} + \phi_{IF} + \phi'_{setup} - \phi_{setup} + \Delta\phi_{device}) \rightarrow \sin(\omega_{IF} + \phi_{IF} + \phi'_{setup} - \phi_{setup} + \Delta\phi_{device})$. The phase can then be extracted doing $\Delta\phi_{device} = -\arctan\left(\frac{Q}{I}\right)$.

change of its total capacitance) slightly changes ϵ_{eff} and thus f_c . Although this change Δf_c is small, it is compensated by the high finesse Q of the cavity which increases the sensitivity of the phase signal $\Delta\phi$:

$$\varphi = -\arctan\left(\frac{2Q(f - f_c)}{f_c}\right)$$

$$f_c \rightarrow f_c + \Delta f_c \Rightarrow \Delta\varphi \approx \frac{+2Q}{f_c} \Delta f_c$$
(3.4)

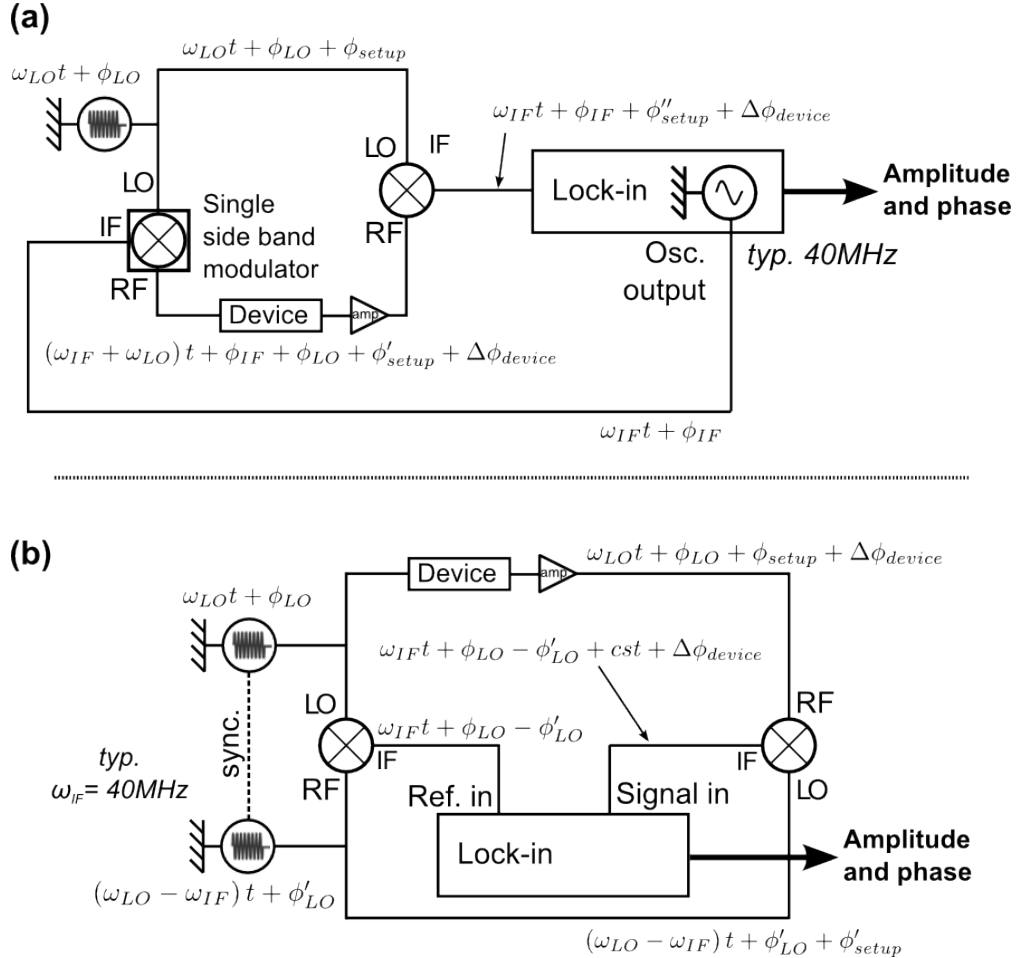


FIGURE 3.15: Possible heterodyne detection schemes for microwave measurements. In both these methods, high ($\approx 40\text{MHz}$) frequency lock-in's can be replaced by digital acquisition cards. **(a)** can easily get rid of the cross-talk problems of the above homodyne detection and is only sending one tone in the device thanks to the single side band modulator which is (commercially) designed to reject the other. However it still suffers from calibration issues concerning this component. **(b)** is probably the best detection scheme but requires a second high frequency source to generate the second local oscillator at $\omega_{LO} - \omega_{IF}$. However this second source should not have to be very expensive: it is synchronised on the first one and its phase drifts are naturally accounted for by the lock in reference. Source: *V.E. Manucharyan, private communication*

As explained in chapter 4, Δf_c is directly proportional to the susceptibility of the DQD (see section 4.4 in particular). This is the physical quantity we extract, and it is indeed related to change a capacitance, or charge fluctuations.

Chapter 4

Double quantum dots for hybrid cQED: presentation and theoretical background

4.1	Interest of the use of cQED techniques	52
4.2	Coupling mechanism and low frequency picture	53
4.2.1	Definitions and basics	53
4.2.2	Low frequency limit: single dot picture	56
4.2.3	Coupling to leads and coupling to local gates	59
4.2.4	Low frequency capacitance of a double dot	60
4.2.5	Coupling to weakly detuned transitions	62
4.3	Equation of motion for a DQD charge qubit in a cavity	65
4.3.1	Master equation	65
4.3.2	Linear regime	68
4.3.3	Finite DC bias	69
4.3.4	Large number of photons	69
4.3.5	Microwave ("two-tone") spectroscopy	70
4.4	Input-output theory for resonator transmission phase and amplitude measurements	72
4.5	Parasitic transmission, <i>Fano</i>-shaped resonances and quadrature offsets	74

Circuit quantum electrodynamics architectures have been developed and extensively used in the superconducting qubit community (see for instance [19, 20, 24, 96–100]). As discussed in section 4.1, this type of setup offers powerful tools for readout, protection and scalability of mesoscopic devices, using properties of resonant circuits with a high finesse such as superconducting CPW cavities. The work presented in this thesis is about the integration of hybrid systems and more specifically double quantum dots in these resonators. Quantitative understanding of the coupling mechanisms between a resonator and a DQD is thus of fundamental interest here, especially for going towards quantum information devices which require fine control. Section 4.2 introduces a frame for discussing the dot-cavity coupling, starting with a low frequency picture for a single and then a double quantum dot. Section 4.3 investigates quantitatively the resonant coupling of a DQD charge qubit to a cavity in a semi-classical regime. Section 4.4 gives details of the input-output theory used to confront directly with experimental results discussed in chapter 5. The last section of this chapter gives a possible explanation for discrepancies observed in dissipative responses, accounting for some imperfections of our experimental setup.

4.1 Interest of the use of cQED techniques

Using an oscillator as a detector to readout the state of a system coupled to it is a widely utilized method in classical and quantum physics (Atomic Force Microscopy [101], Nuclear Magnetic Resonance spectroscopy [102], mass sensing, etc). This idea is now applied on chip, using lumped element or CPW resonators. In *circuit QED*, these resonators can be in a quantum regime with discrete photon states interacting with mesoscopic devices. For devices such as quantum dots, the high frequency capacitive measurement offered by superconducting resonators is to be compared to the usual electronic transport techniques. In contrast with low frequency conductance measurement or charge sensing, high finesse GHz resonators potentially provide a high speed, and high sensitivity measurement. It can also give access to distinctive quantities such as quantum capacitance [103] thanks to finite frequency [104], or more generally susceptibilities associated with different transitions (see following sections). By avoiding transport, cQED readout techniques could also eventually yield to QND [19, 20] (quantum non-demolition) measurements of charge or spin states in quantum dot devices.

Another significant potential of cQED architectures is the scalability. With their recent developments, superconducting qubits might seem far ahead in terms of quantum information integration [24, 105]. However cQED scalability combined with spin-coupling would allow us to tackle fundamental problems such as the coupling and entanglement

of distant spins [14, 32, 106–109], which is of wide interest, besides investigated following different proposals [110–112].

Microwave cavities also act as very narrow bandpass filters and thus protect devices from the external world. They can potentially enhance qubits lifetimes thanks to inverse Purcell effect [19, 97, 113], and by providing a non invasive detection technique, they allow in principle isolation of the system from an electromagnetic environment otherwise resulting in decoherence.

Because circuits, in general, allow one to build devices with arbitrary complexity, cQED provides a conciliating platform for going towards hybrid systems which can couple to other quantum degrees of freedom. Superconducting circuits have already been used to couple microwave photons to other systems such as mechanical resonators [26, 114], large spin ensembles [44–46], or optical photons [115]. It is therefore desirable to work in such promising architecture for further implementation of hybrid circuits.

4.2 Coupling mechanism and low frequency picture

The following sections introduce notations and give a general picture of possible charge coupling mechanisms. This is presented in a low frequency limit, where the frequency of the resonator is much smaller than the characteristic frequencies of the dot system ¹. This description cannot be used to predict the resonator behaviour in the limit where the dot characteristic frequencies and the resonator frequency are comparable but it provides a framework to understand how the electronic charge couples to the resonator electric field.

4.2.1 Definitions and basics

A double quantum dot tunnel-coupled to metallic electrodes is generally an open quantum system and it can couple to the electric field of a CPW resonator mode in different ways. More precisely, the electric field can be coupled to the electrochemical potential of the dots by local gates, but also to the Fermi levels hosted by source and drain electrodes. Depending on the dominating mechanism, different effective dipoles can be identified, with significantly different physics. The overall behaviour is set by the ratios of the different capacitances involved, see figure 4.1. One can start by investigating the change of the potential on the dots due to the AC contribution of the resonator. We

¹the dot undergoes an adiabatic AC modulation

can write the total electrostatic² charge $Q_{1(2)}$ on dot 1(2) as the sum of the charges on all the capacitors connected to the dot [4] (see figure 4.1):

$$Q_{1(2)} = \sum_i C_i (V_{1(2)} - V_i) \quad (4.1)$$

where V_i is the electrical potential on dot or electrode i . We can then define the capacitances ratios as lever-arms, for electrode i with respect to dot 1(2):

$$\alpha_{i/1(2)} = \frac{C_i}{C_{\Sigma 1(2)}} \quad (4.2)$$

with

$$C_{\Sigma 1(2)} = C_{L1(2)} + C_{g1(2)} + C_m + C_{parasitic} \quad (4.3)$$

Hence the dots' potentials:

$$V_{1(2)} = \frac{Q_{1(2)}}{C_{\Sigma 1(2)}} + \sum_i \alpha_{i/1(2)} V_i \quad (4.4)$$

In general, the capacitances C_i 's of leads or top gates to our nanotube-based dots are of the order of few aF (even less for side gates). On the contrary, lithographically defined capacitances $C_{c,i}$ between the electrodes and the transmission line can go up to few $10fF$. The AC component of an electrode potential is therefore defined by its coupling to the transmission line if parasitic capacitances are negligible. One can therefore engineer the coupling by changing the capacitances $C_{c,i}$. In the case where all the parasitic capacitances can be neglected, one can also compute the electrochemical potential, which accounts for coulomb interactions on the dots³.

Equation 4.4 rules the effect of the surrounding electrical fields on the dot electrical potential. However, cQED architectures offer experimental access to a frequency shift, as explained in section 4.4 and 3.2.3. We can estimate an order of magnitude of this shift by computing the total DQD's capacitance participation to the resonator capacitance. Start by simply modelling the resonator as an LC circuit with resonant frequency f_c :

²The characteristic scale of the device (few μm) is much smaller than the wavelength of the AC field in the cavity ($1cm$), so the AC contribution can still be accounted for with an electrostatic model.

³In the linear regime, for a charge occupation number $n_{1(2)}$ [4], $\mu_{1(2)}(n_1, n_2) = (n_{1(2)} - 1)U_1 + n_{2(1)}U_m - \frac{2U_{1(2)}}{e}C_{g1(2)}V_{g1(2)} - \frac{2U_m}{e}C_{g2(1)}V_{g2(1)}$ where e is the electron charge and U 's are the charging energies $U_{1(2)} = \frac{e^2}{2} \left(\frac{C_{\Sigma 2(1)}}{C_{\Sigma 1}C_{\Sigma 2} - C_m^2} \right)$ and $U_m = \frac{e^2}{2} \left(\frac{C_m}{C_{\Sigma 1}C_{\Sigma 2} - C_m^2} \right)$

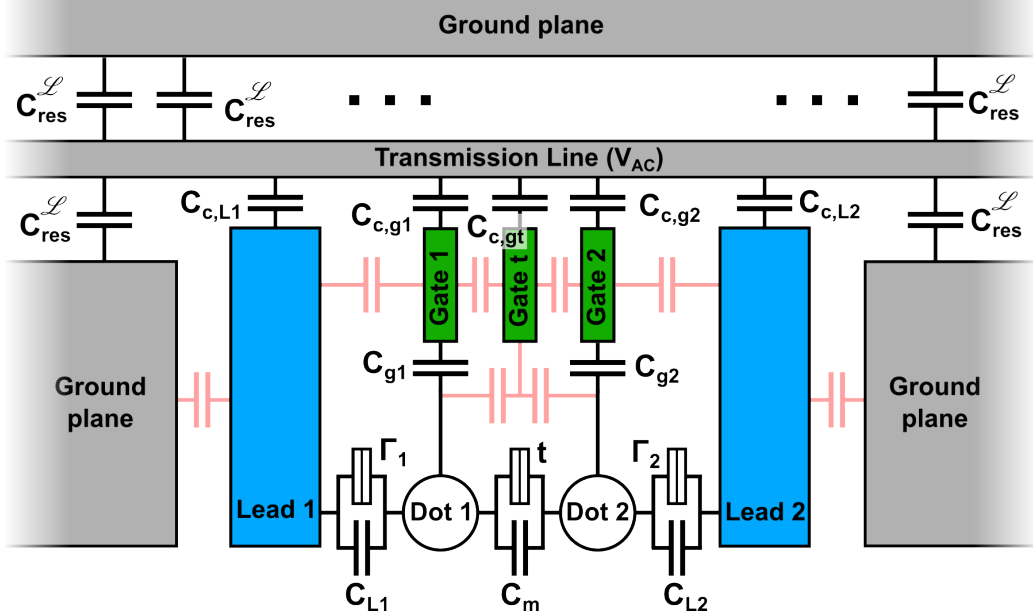


FIGURE 4.1: Scheme of a DQD coupled to the transmission line of a CPW resonator summarizing the capacitances possibly involved, plus some potential parasitic capacitances (light pink). C_{res}^L is the linear capacitance of the resonator to ground ($\int C_{res}^L = C_{res}$). The capacitances of the electrodes to the transmission line, $C_{c,i}$ can be replaced by a galvanic connections to increase coupling strength and/or selectivity. Connections to DC voltage sources and associated capacitances are not represented.

$$f_c = \frac{1}{2\pi\sqrt{L_{res}C_{res}}} \quad (4.5)$$

L_{res} is the total inductance of the transmission line and C_{res} its total capacitance to the ground, $L_{res} \approx 0.5nH$ and $C_{res} \approx 1pF$ (see e.g. [116]). A small change in C_{res} due to DQD total capacitance ⁴ leads to a change in f_c

$$f_c + \Delta f_c = \frac{1}{2\pi\sqrt{L_{res}(C_{res} + \Delta C_{dot})}} \approx f_c \left(1 - \frac{\Delta C_{dot}}{2C_{res}} \right) \quad (4.6)$$

$$\Delta f_c \approx -\frac{f_c}{2C_{res}} \Delta C_{dot} \quad (4.7)$$

Equation 4.7 is not true in general (in the strong coupling regime for instance), but gives an idea of the physics underlying such measurements. Moreover, this picture holds for most of the results presented in this thesis. The goal is therefore to calculate ΔC_{dot} , also associated to a charge susceptibility, which can take very different forms depending on the regime of parameters considered.

⁴We assume here a purely capacitive coupling. One could also implement inductive coupling and calculate a participation factor the same way

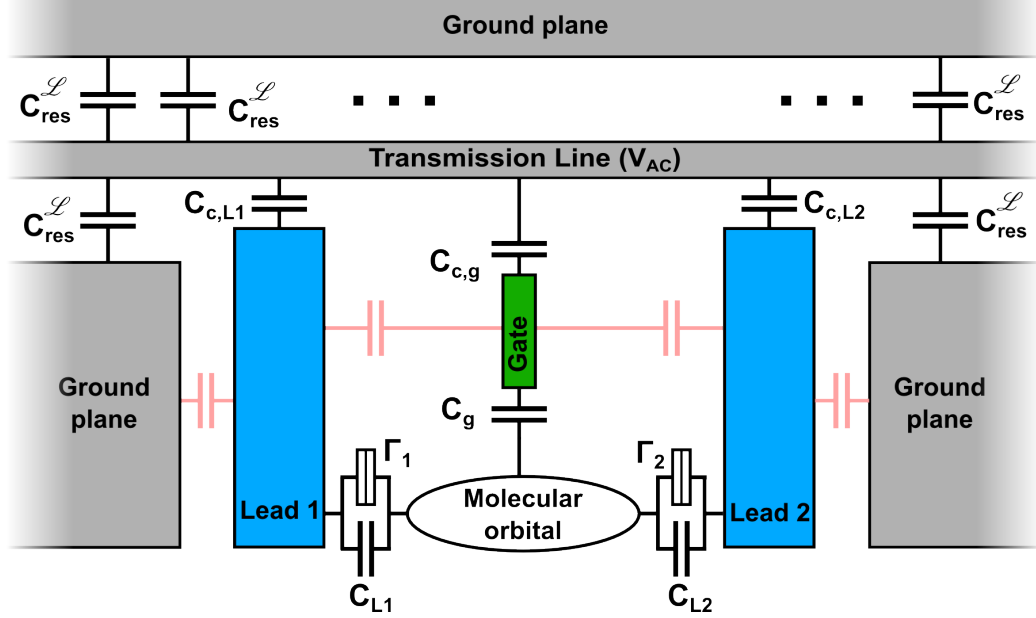


FIGURE 4.2: Scheme of a single dot coupled to the transmission line of a CPW resonator, analogous to figure 4.1. Connections to DC voltage sources and associated capacitances are not represented.

The following sections (from 4.2.2 to 4.2.4) give theoretical elements to calculate the Δf_c (through ΔC_{dot}) in the low frequency limit, $\Gamma_{\text{lead},1(2)}, t \ll f_c$. It constitutes a good starting point to understand several aspects of the charge coupling mechanism.

4.2.2 Low frequency limit: single dot picture

It is instructive to start by considering the simpler case of a single dot, coupled to a gate through capacitance C_g and to source and drain electrodes, see figure 4.2. It is also very much related to the situation where the states of the dots 1 and 2 are coherently hybridised (i.e. $t \gg k_B T$) and symmetrically coupled to the resonator, so that we can consider the double dot state as one single molecular state. Most of this section's material arises from [117].

One can compute the average charge on the capacitor plate i using Kirchhoff's voltage law:

$$\langle Q_i \rangle = -e\alpha_i \langle n \rangle + C_i V_i + \alpha_i \sum_j C_j V_j \quad (4.8)$$

Where α_i is now C_i/C_{Σ} . The total capacitance of the device viewed from the corresponding electrodes is then:

$$\begin{aligned}
\tilde{C}_i &= \frac{\partial \langle Q_i \rangle}{\partial V_i} \\
&= \underbrace{-\alpha_i e \frac{\partial \langle n \rangle}{\partial \xi} \frac{\partial \xi}{\partial V_i}}_{\text{Quantum capa. } C_Q} + \underbrace{C_i(1 + \alpha_i)}_{\text{Geometric capa.}}
\end{aligned} \tag{4.9}$$

where $\partial \langle n \rangle$ is the average occupation of the dot and ξ the dot energy level. The geometric capacitance only depends on lever arms and would correspond to the capacitance if the dot could be turned off ($\Gamma_{lead,1} = \Gamma_{lead,2} = 0$). The quantum capacitance is therefore directly $\Delta C_{dot} = C_Q$ entering the frequency shift in equation 4.7.

Defining $V_{RMS} = \sqrt{\frac{f_c}{2C_{res}}}$ the root mean square voltage associated to one photon at f_c trapped in the resonator, we can identify the coupling strength g as being a lever arm (i):

$$\Delta f_c = g^2 \frac{\partial \langle n \rangle}{\partial \xi} \tag{4.10}$$

with

$$g = \sqrt{e\alpha_i \frac{\partial \xi}{\partial V_i}} V_{RMS} \tag{4.11}$$

Several difficulties can appear when it comes to fully determine the above two partial derivatives in the general case of finite charging energy (coulomb interactions) U and Γ_{lead} :

Open system and finite density of states

The first one, $\frac{\partial \xi}{\partial V_i}$, potentially acts as a lever arm on the capacitive response. In the mean field approximation, the electrostatic of the dot reads:

$$\xi = \xi^0 - e \sum_i \alpha_i V_i + U \langle n \rangle \tag{4.12}$$

where ξ^0 is the bare dot energy level, ξ the dressed one, and $U = e^2/2C_\Sigma$. If the occupation number $\langle n \rangle$ is a function of the AC voltage V_i carried by the coupling electrodes, one has to compute a self-consistent equation on $\langle n \rangle$. This becomes important when

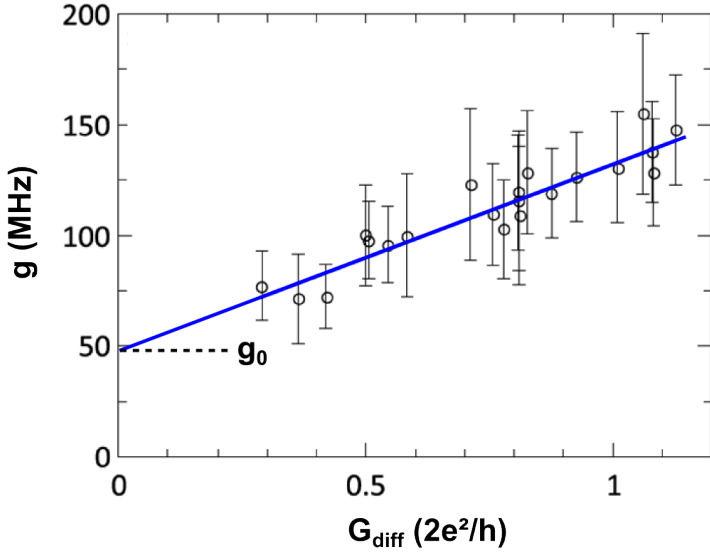


FIGURE 4.3: Coupling strength of a lead-coupled single quantum dot as a function of the dot's differential conductance. Coupling strength increases with conductance, therefore with Γ_{Lead} . The intercept at zero conductance (closed dot) gives an estimate of the geometric bare coupling strength.

the system is sufficiently interacting and open $\Gamma_{lead} \sim U$, with a large density of states slowly modulating with gate voltage. These complex effects are related to the general problem of electron screening in many body systems and are not the purpose of this thesis; (see [30] for further details). Generally $\frac{\partial\xi}{\partial V_i}$ happens to be a function of U , Γ_{lead} , α_i 's and V_g , and it's behaviour depends on whether the system is gate coupled or lead coupled (see also section 4.2.3). Thus $g = e\alpha_i V_{RMS} + f(U/\Gamma_{lead})$, and in the case of lead coupling, the effective coupling strength is linearly increased with Γ_{lead} , see figure 4.3.

Isolated system

For the purpose of building qubits, one wants to have a very isolated (closed) system, and therefore only the geometrical part of the coupling matters:

$$\begin{aligned}
 \frac{\partial\xi}{\partial V_i} &\xrightarrow{\Gamma_{lead} \rightarrow 0} e\alpha_i \\
 \Rightarrow g &\xrightarrow{\Gamma_{lead} \rightarrow 0} g_0 = e\alpha_i V_{RMS}
 \end{aligned}
 \tag{4.13}$$

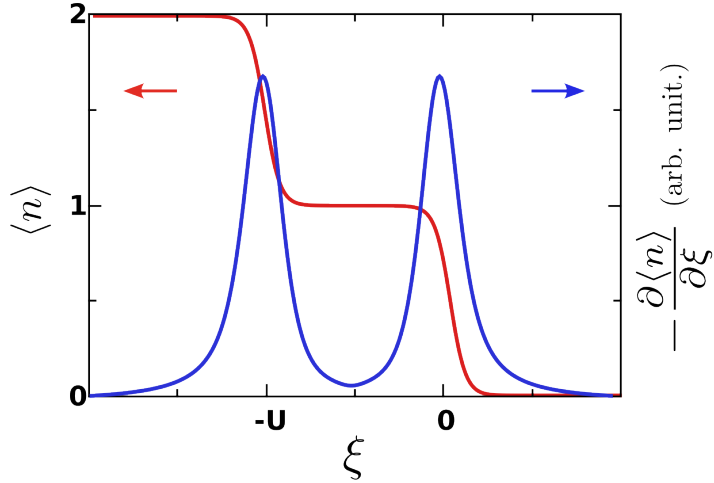


FIGURE 4.4: Qualitative behaviour of the average charge occupation number $\langle n \rangle$ (coulomb staircase) and corresponding charge capacitance. Source: [117]

g_0 is now simply associated to a lever arm. In this case, the low frequency response is determined only by the quantum capacitance $\frac{\partial \langle n \rangle}{\partial \xi}$. It can be exactly calculated in the non interacting case (see [103, 117]):

$$\left. \frac{\partial \langle n \rangle}{\partial \xi} \right|_{U=0} = C_Q|_{U=0} = \frac{2e^2}{\pi \Gamma_{lead}} \frac{1}{1 + \left(\frac{2\xi^0}{\Gamma_{lead}} \right)^2} \quad (4.14)$$

There are corrections in the interacting case, but the general behaviour is qualitatively similar. One can understand the qualitative behaviour of this capacitance by directly taking the derivative of a coulomb staircase, see figure 4.4. In particular, $\Delta f_c \propto -\frac{g^2}{\Gamma_{lead}}$ in the non interacting, coherent regime (or resonant tunnelling), and $\Delta f_c \propto -\frac{g^2}{k_B T}$ in the sequential regime.

4.2.3 Coupling to leads and coupling to local gates

The sign of the cavity frequency shift depends on whether the dot system is coupled via leads or local gate. For local gate coupling, in the low frequency picture, ξ oscillates at cavity frequency with respect to the grounded Fermi level of the electrodes $\mu_{1(2)}$. For lead coupling on the contrary, it is $\mu_{1(2)}$ that oscillates with respect to a grounded ξ . Energy conservation yields $\xi + (\mu_1 + \mu_2)/2 = cst$, and therefore $\frac{\partial \langle n \rangle}{\partial \xi} = -\frac{\partial \langle n \rangle}{\partial \mu_{1(2)}}$. One can see that $\frac{\partial \langle n \rangle}{\partial \xi} < 0$ (e.g. figure 4.4) and therefore $\Delta f_c < 0$ for direct local gate coupling and $\Delta f_c > 0$ for indirect lead coupling. This is observed experimentally in chapter 5, figure 5.2 and 5.3, keeping in mind that $\Delta f_c \propto +\Delta\varphi$ since $\varphi(f) = -\arctan\left(2Q \frac{f-f_c}{f_c}\right)$ (Q being the resonator quality factor). This argument survives out of the low frequency

approximation. However, note that the sign of the Δf_c can also change with resonant phenomena for example, see section 4.3.2; the capacitive response of the system is then dominated by another parameter such as the detuning between the cavity and characteristic frequency of the dot's transitions $\Delta = f_{dot} - f_c$. Moreover, this is only valid if the dipole considered involves tunnelling to the leads (it does not hold for inter-dot transitions for instance). See also section 4.4, (e.g. equation 4.44) for quantitative description.

4.2.4 Low frequency capacitance of a double dot

The situation presented here corresponds to the experimental observations of section 5.1.1. In this case the dot-lead capacitances C_L 's are dominating, so that even if the coupling capacitances $C_{c,x}$'s are all similar, the coupling to the lead dominates. We can refer to this as an *indirect* coupling. Experimentally, this yields coupling rates Γ_{lead} 's much larger than cavity frequency, $\Gamma_{lead,1(2)} \gg f_c$, and this is assumed throughout this section. Most of the following material is adapted from [118].

Looking at figure 4.1, three dipoles can be identified and coupled to the cavity. They correspond to two dot-lead transitions through tunnel barriers $\Gamma_{lead,1(2)}$ and one inter-dot transition between states coupled through t . They are coupled with lever arms

$$\begin{aligned} g_{dot-lead,1(2)} &= e\alpha_{d1(2)}V_{RMS} \\ g_{inter-dot} &= e|\alpha_{d1} - \alpha_{d2}|V_{RMS} \end{aligned} \tag{4.15}$$

where $\alpha_{d1(2)} = \sum_i \alpha_{i/1(2)}$. It turns out that whether the cavity coupling to the two dots is symmetric or asymmetric changes what transitions are addressed. The symmetric case recalls results given in section 4.2.2 with a molecular orbital instead of a single dot orbital. In contrast, asymmetric coupling allows to explore:

- Inter-dot transitions, by engineering for example $\alpha_{d1} \approx 0$. See for instance [119].
- Single dot - single contact transitions, for example by engineering $\alpha_{d1} \approx 0$ and turning off dot 1 ($\Gamma_{lead,1}, t \ll k_B t \ll f_c$). See for instance [120] which also goes beyond the low frequency limit.

These transitions can be compared to those involved in the transport mechanisms yielding DC transport. The goal is now to determine what does the stability diagram of a

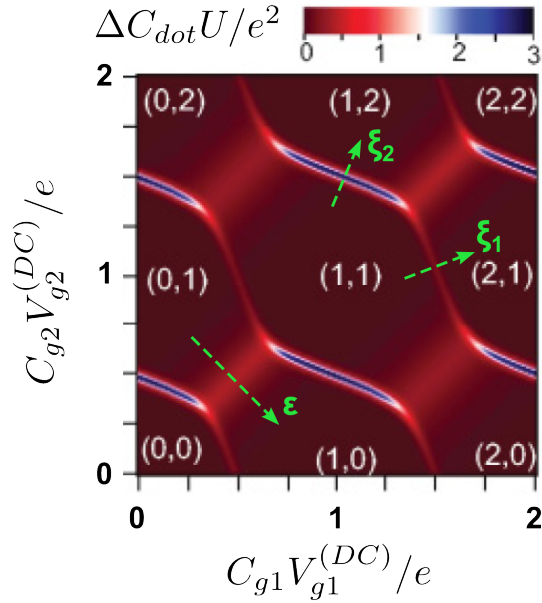


FIGURE 4.5: Calculated low frequency capacitance of a double quantum dot coupled to a resonator, as a function of the DC gate voltages of the two dots. Source: [118]

DQD look like when readout via the cavity frequency shift. To obtain this frequency shift, one must calculate the capacitance variations ΔC_{dot} 's associated to the different transitions and entering equation 4.7. Adapting [118], in the sequential tunnelling approximation $0 < \Gamma_{lead,1(2)} \ll k_B T \ll t \ll U, U_m$, and away from the triple points (see figure 4.5), these capacitances read:

$$\begin{aligned} \Delta C_{dot-lead,1(2)} &\approx \frac{1}{4} \beta e^2 \alpha_{d1(2)}^2 \frac{1}{\cosh^2(\beta \xi_{1(2)}/2)} \\ \Delta C_{inter-dot} &\approx e^2 (\alpha_{d1} - \alpha_{d2})^2 \frac{t^2}{(\epsilon^2 + 4t^2)^{3/2}} \end{aligned} \tag{4.16}$$

where $\beta = 1/k_B T$ and $\epsilon = \xi_1 - \xi_2$ is the inter-dot detuning energy, see figure 4.5. $\Delta C_{inter-dot}$ can behave differently for transitions with doubly occupied dots, but parity effects arising from spin are not considered here. By analogy to the single-dot case, we can expect $\Delta C_{dot-lead,1(2)}$ to be qualitatively similar in the coherent tunnelling regime $k_B T \ll \Gamma_{lead,1(2)} \ll U, U_m$, but with a Lorentzian peak shape $\sim \frac{\Gamma_{lead,1(2)}}{(\xi_{1(2)})^2 + (\Gamma_{lead,1(2)}/2)^2}$ (not shown).

Effective coupling strength and parasitic capacitances

Importantly, the total coupling strength involved in either of the transitions discussed above can be strongly diminished mainly for two reasons. First, the cavity frequency shift can be reduced or even cancelled by summing up the contributions from gate and lead coupling (see section 4.2.3). Second, another factor, harder to avoid for direct gate coupling, is the capacitive cross-talks between the gates at microwave frequencies as depicted in figure 4.1(pink). This is particularly troublesome for achieving a large and strongly asymmetric coupling.

4.2.5 Coupling to weakly detuned transitions

Bringing CNT based devices into a regime where tunnel barriers rates are resonant with a cavity at $\approx 7\text{GHz}$ is an experimental challenge. It is however a rich regime and is the situation one wants to reach in order to go towards quantum information processing with CNT's, or reveal spin-photon coupling. Coupling to inter-dot transitions can be treated using a cQED formalism [19], and a first approach of this is given below. We also give a quick overview of a possible circuit analysis for resonant dot-lead transitions, and an example of lead-coupling to inter-dot transitions.

4.2.5.1 Inter-dot transitions: charge qubit

Charge qubits in DQD devices are based on the dots' orbitals or their coherent superposition [48, 56, 119, 121], namely molecular bonding and anti-bonding states. We now consider a very closed system, so that the only contribution to the bare charge-photon coupling g_0 is geometric and can be expressed in terms of capacitance ratios, i.e. lever arms. Besides we decided to couple our devices with local gates, to ensure avoiding possible complex renormalisation effects or effective fields due to leads. We now assume a fully asymmetric coupling, to inter-dot transitions, and consider one orbital in each dot. The DQD therefore effectively behaves as a two level system (see figure 2.4) with a capacitive response only along the $\epsilon \sim 0$ line (analog to figure 4.5), in the gate region where the two dots' orbitals are close to degeneracy,

Because CPW resonators behave like Fabry-Perot resonators, the problem now reduces to the coupling of a harmonic oscillator to a qubit, with states $|B\rangle$ and $|AB\rangle$. The coupling constant g_0 is now defined within a Jaynes-Cummings hamiltonian [122]:

$$\mathcal{H} = \hbar\omega_c a^\dagger a + \hbar\frac{\Omega}{2}\sigma_z + \hbar g(\sigma_- a^\dagger + \sigma_+ a) \quad (4.17)$$

where $\hbar\Omega = \sqrt{(\epsilon)^2 + 4t^2}$ is the charge qubit Larmor frequency with ϵ the inter-dot energy detuning, $\sigma_z = |AB\rangle\langle AB| - |B\rangle\langle B|$, $\sigma_- = |B\rangle\langle AB| = \sigma_+^\dagger$, $a(a^\dagger)$ are the photonic annihilation(creation) operators, $\theta = \arctan \frac{2t}{\epsilon}$ and $g = g_0 \sin \theta$ is the dressed charge-photon coupling strength (see figure 2.4).

As in the previous sections, one wants to calculate the cavity frequency shift induced by the charge qubit. In order to do so, we can start with the standard unitary transformation [19]:

$$\tilde{\mathcal{H}} = \mathcal{U}\mathcal{H}\mathcal{U}^\dagger \text{ with } \mathcal{U} = e^{\frac{g}{\Delta}(\sigma_+a - \sigma_-a^\dagger)} \quad (4.18)$$

where $\Delta = \Omega - \omega_c$ is the cavity-qubit frequency detuning.

Using the Baker-Hausdorff identity⁵, one can obtain the standard dispersive effective Hamiltonian in the dispersive limit $g \ll \Delta$ (decoherence of the qubit is neglected for now):

$$\tilde{\mathcal{H}} = \hbar(\omega_c + \chi_{disp}\sigma_z)a^\dagger a + \hbar\left(\Omega + \frac{\chi_{disp}}{2}\right)\sigma_z \quad (4.19)$$

where $\chi_{disp} = \frac{g^2}{\Delta}$ is the dispersive charge susceptibility. It appears that the resonator frequency is now simply shifted by the “cavity pull”

$$\Delta f_c = \chi_{disp}\langle\sigma_z\rangle \quad (4.20)$$

which is to be compared for example to equation 4.10. Cavity frequency shift measurements now allow us to obtain both the charge susceptibility of the qubit and its σ_z , which relates to the populations of the charge states $|B\rangle$ and $|AB\rangle$ in the DQD. Section 4.3 further investigates the cavity response in a more general frame integrating the out of equilibrium charge dynamics. One can also notice the analogous of the cavity pull on the qubit frequency, given by $\chi_{disp}(n_{ph} + 1/2)/2$ (with n_{ph} the photon number), namely AC-Stark shift ([19, 96]).

Consistently, when the qubit is in its ground state ($\sigma_z = -1$), $\Delta f_c < 0$ when $\Omega > \omega_c$ and this recovers the sign of the low frequency limit (section 4.2.2 and 4.2.4), with now $\Delta f_c = -\frac{g^2}{\Delta}$.

⁵ $\tilde{\mathcal{H}} = \mathcal{U}\mathcal{H}\mathcal{U}^\dagger = H + [\chi, H] + \frac{1}{2}[\chi, [\chi, H]] + \dots$

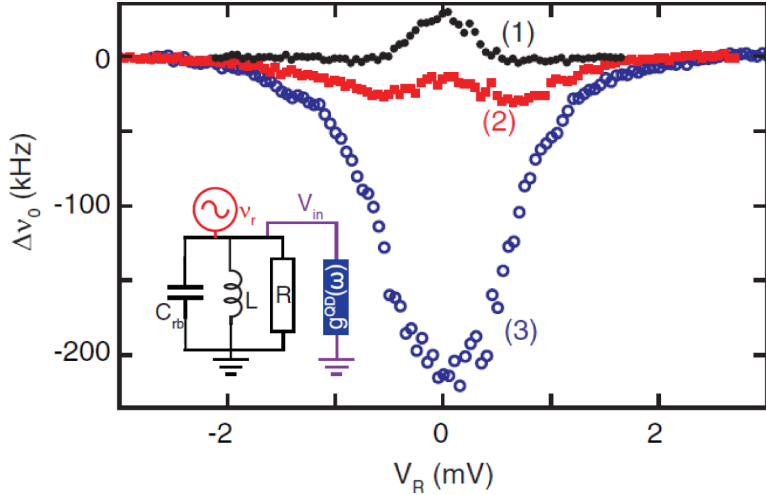


FIGURE 4.6: Resonator frequency shift (here referred to as $\Delta\nu_0$) as a function of the effective single dot gate voltage V_R , for three different coupling rates Γ_{lead} . Estimated Γ_{lead} 's are (1)20MHz, (2)58MHz and (3)125MHz. $f_c = 6.7GHz$. Inset: equivalent circuit with quantum dot admittance $g^{QD}(\omega)$ connected to the resonator lumped element circuit. Source: [120]

4.2.5.2 Dot-lead transitions: charge relaxation and quantum capacitance return

Leaving the quantum information goal aside for a while, one can look at what happens when dot-lead transitions take place with a coupling rate to the continua comparable with the resonator frequency or even smaller, $\Gamma_{lead} < f_c$. This has been studied by the Zurich's group in [120] with a GaAs 2DEG-based effective single dot - single lead device gate-coupled to a CPW cavity. As in the case of inter-dot transitions (sections 4.2.5.1 and 4.3), the sign of the cavity frequency shift can change with the characteristic dot frequency (here Γ_{lead}), see figure 4.6. In this experiment, data is interpreted in a non interacting formalism using scattering matrix theory [103], recalling the model of the quantum capacitance. As Γ_{lead} decreases, the contribution of the dot system to the resonator circuit is interpreted to be a crossover from capacitive to inductive. This kind of experiment could be used to perform high frequency resistance measurement in which universal charge relaxation can play a role [123].

4.2.5.3 Coupling to inter-dot transitions via lead coupling

It is possible to address inter-dot transitions using a lead coupling scheme [32]. Devices are usually very closed ($U, U_m \gg \Gamma_{lead,1(2)}$) and more exotic coupling mechanisms and screening effects such as mentioned in section 4.2.2 should be irrelevant. It allows a large and maximally asymmetric coupling between the dots of a DQD. This method is particularly adapted to quantum wires such as CNT's, or semiconducting nanowires

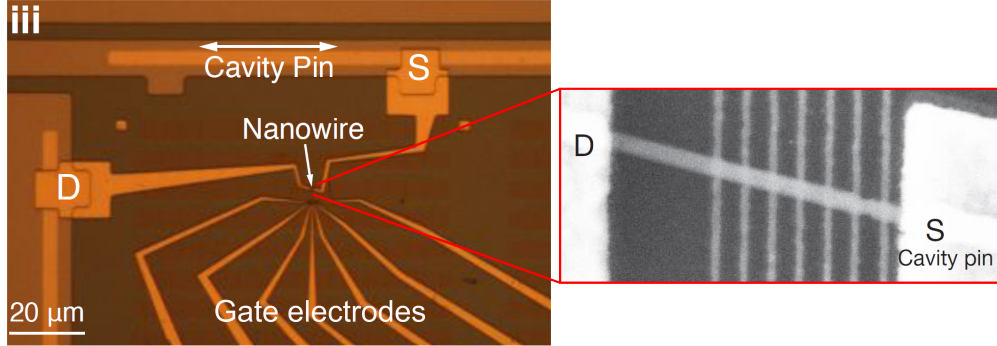


FIGURE 4.7: Lead coupling geometry for asymmetric coupling. The resonator transmission line is connected to the source electrode (S) of the DQD made out of an InAs nanowire. For DC measurement, DC current therefore flows through the cavity pin and and CPW ground plane. Source: [32]

as it is the case in [32] with InAs. It is however a priori limiting for scalability since different devices in such an architecture would be galvanically connected to each other via source and drain electrodes.

4.3 Equation of motion for a DQD charge qubit in a cavity

This section provides theoretical background and quantitative understanding relating to most experimental results presented in chapter 5. In contrast with section 4.2, we write here the equation of motion of the operators involved in the Hamiltonian to calculate the cavity frequency shift in both the dispersive and resonant regime. The DQD states form a charge qubit which can be readout using the cavity dispersive shift (sections 4.3.2 and 4.3.5), but also driven out of equilibrium by DC transport or cavity photons (sections 4.3.3 and 4.3.4 respectively). This treatment thus goes further than the theory developed for example in [124] and [31, 32] by integrating non-linear regime with $\sigma_z \neq -1$.

4.3.1 Master equation

Let us start with the Hamiltonian of the system, recalling 4.17 and adding crucial ingredients in order to conveniently describe electronic transport and out of equilibrium effects. The relevant states of the DQD are now: $\{|\emptyset\rangle, |B\rangle, |AB\rangle, |2\rangle\}$ where $|\emptyset\rangle$ and $|2\rangle$ are the empty and doubly occupied states respectively. In this situation, it is convenient to introduce the following operators : $\sigma_{AB} = |AB\rangle\langle AB|$, $\sigma_B = |B\rangle\langle B|$, $\sigma_\emptyset = |\emptyset\rangle\langle \emptyset|$ and $\sigma_2 = |2\rangle\langle 2|$. We also have $\sigma_- = |B\rangle\langle AB| = \sigma_+^\dagger$ and $\sigma_z = \sigma_{AB} - \sigma_B$. The Hamiltonian now writes:

$$\begin{aligned}\mathcal{H} = & \hbar\omega_c a^\dagger a + \hbar\frac{\Omega}{2}\sigma_z + E_0\sigma_0 + E_2\sigma_2 + \hbar g (\sigma_- a^\dagger + \sigma_+ a) \\ & + \hbar\epsilon_{in} (e^{-i\omega_d t} a^\dagger + e^{i\omega_d t} a) + \mathcal{H}_{Bath} + \mathcal{H}_{Bath}^{coupling}\end{aligned}\tag{4.21}$$

where ϵ_{in} is related to the microwave drive amplitude at the input of the cavity and ω_d its pulsation. The Hamiltonian \mathcal{H}_{Bath} describes environmental degrees of freedom like electronic leads ($\mathcal{H}_{lead} = \sum_{q,r} \hbar\omega_{q,r} b_{q,r}^\dagger b_{q,r}$ with $b_{q,r}$ the creation fermionic operator in the lead r) but also phonons, fluctuators, and the external photonic modes of the microwave cavity. It controls the decoherence processes of the DQD-cavity system. $\mathcal{H}_{Bath}^{coupling}$ couples the baths to the system.

One can write the coupled equations of motion (EOM)⁶ for the charge qubit-cavity system in a transport situation, i.e. when a finite bias is applied to the source-drain electrodes of the double quantum dot. In the following, we only consider the coupling to the electronic bath

$$\mathcal{H}_{Bath}^{coupling} = \sum_{q,r} \gamma_r (\sigma_+ b_{q,r} + \sigma_- b_{q,r}^\dagger)$$

and the dephasing term Γ_ϕ arising for example from low frequency charge noise acting on the detuning ϵ , yielding a $\langle\sigma_z\rangle$ term. In the rotating frame of the driving field which oscillates at ω_d , the system of equations to be solved within the rotating wave approximation is :

$$\frac{d}{dt} \langle a \rangle = -(\kappa/2 + i\Delta_{cd}) \langle a \rangle - i\epsilon_{in} - ig \langle \sigma_- \rangle \tag{4.22}$$

$$\frac{d}{dt} \langle \sigma_- \rangle = -(\gamma/2 + \Gamma_\phi + i\Delta) \langle \sigma_- \rangle + ig \langle a \langle (\sigma_{AB} - \sigma_B) \rangle \tag{4.23}$$

$$\frac{d}{dt} \langle \sigma_{AB} \rangle = -ig (\langle a \sigma_+ \rangle - \langle a^\dagger \sigma_- \rangle) + \sum_{i \neq AB} (\Gamma_{AB \leftarrow i} \langle \sigma_i \rangle - \Gamma_{i \leftarrow AB} \langle \sigma_{AB} \rangle) \tag{4.24}$$

$$\frac{d}{dt} \langle \sigma_B \rangle = ig (\langle a \sigma_+ \rangle - \langle a^\dagger \sigma_- \rangle) + \sum_{i \neq B} (\Gamma_{B \leftarrow i} \langle \sigma_i \rangle - \Gamma_{i \leftarrow B} \langle \sigma_B \rangle) \tag{4.25}$$

$$\frac{d}{dt} \langle \sigma_j \rangle = \sum_{i \neq j} (\Gamma_{j \leftarrow i} \langle \sigma_i \rangle - \Gamma_{i \leftarrow j} \langle \sigma_j \rangle) \tag{4.26}$$

where $\Delta = \Omega - \omega_d$ is now the qubit-drive detuning, $\Delta_{cd} = \omega_c - \omega_d$, κ is the total decay rate of the cavity. The coupling to the reservoir continuum $\Gamma_{\alpha \leftarrow \beta}$ is determined by a Fermi golden rule:

⁶For an operator A , $\frac{d}{dt} A = \frac{i}{\hbar} [\mathcal{H}, A]$

$$\begin{aligned}\Gamma_{\alpha \leftarrow \beta} &= \Gamma_{\alpha \leftarrow \beta}^L + \Gamma_{\alpha \leftarrow \beta}^R \\ \Gamma_{\alpha \leftarrow \beta}^{r=1(2)} &= \frac{2\pi}{\hbar} |\gamma_r|^2 \nu_r f_r (E_\alpha - E_\beta)\end{aligned}\tag{4.27}$$

where $\nu_{r=1(2)}$ is the density of state in reservoir 1(2) and $f_{r=1(2)}(E_\alpha - E_\beta)$ its Fermi function taken at energy difference between states $|\alpha\rangle$ and $|\beta\rangle$.

In order to obtain a closed system of equations, we make use of a semi-classical approximation for the cavity field which leads to: $\langle a(\sigma_{AB} - \sigma_B) \rangle \approx \langle a \rangle \times \langle (\sigma_{AB} - \sigma_B) \rangle$ and $\langle a\sigma_+ \rangle \approx \langle a \rangle \times \langle \sigma_+ \rangle$. This is justified in our case since we generally perform measurements with a number of photons in the cavity of the order of few 10 – 100. In the stationary regime, equations 4.23 and 4.22 yield:

$$\langle \sigma_- \rangle = \frac{\chi}{g} \langle a \rangle \langle \sigma_z \rangle \tag{4.28}$$

$$\langle a \rangle = \frac{-i\epsilon_{in}}{i\Delta_{cd} + \frac{\kappa}{2} + i\chi \langle \sigma_z \rangle} \tag{4.29}$$

where χ is the charge susceptibility of the system:

$$\chi = \frac{(g_0 \sin \theta)^2}{-i(\gamma/2 + \Gamma_\phi) + \Delta} = \frac{g^2}{-i\Gamma_2 + \Delta} \tag{4.30}$$

where $\Gamma_2 = \gamma/2 + \Gamma_\phi$ is the inverse of the T_2^* time of the charge qubit. Expression 4.29 yields a cavity shift of the form (see also section 4.4):

$$\Delta f_c = \Re[\chi] \langle \sigma_z \rangle \tag{4.31}$$

This expression of the cavity frequency shift is the same as in equation 4.20, but is now valid in an electronic transport situation. The expression of $\langle \sigma_z \rangle = \langle \sigma_{AB} - \sigma_B \rangle$ stems for the system of equation, arising from equations 4.24 to 4.26:

$$\begin{aligned}
-2g^2 \Im m[\chi] \langle \sigma_{AB} - \sigma_B \rangle |\langle a \rangle|^2 &= \sum_{i \neq AB} (\Gamma_{AB \leftarrow i} \langle \sigma_i \rangle - \Gamma_{i \leftarrow AB} \langle \sigma_{AB} \rangle) \\
2g^2 \Im m[\chi] \langle \sigma_{AB} - \sigma_B \rangle |\langle a \rangle|^2 &= \sum_{i \neq B} (\Gamma_{B \leftarrow i} \langle \sigma_i \rangle - \Gamma_{i \leftarrow B} \langle \sigma_B \rangle) \\
\langle \sigma_2 \rangle &= \frac{\Gamma_{2 \leftarrow AB} \langle \sigma_{AB} \rangle + \Gamma_{2 \leftarrow B} \langle \sigma_B \rangle}{\Gamma_{B \leftarrow 2} + \Gamma_{AB \leftarrow 2}} \\
\langle \sigma_\emptyset \rangle &= 1 - \langle \sigma_2 \rangle - \langle \sigma_B \rangle - \langle \sigma_{AB} \rangle
\end{aligned} \tag{4.32}$$

The overall set of equations thus accounts for the effects of electronic transport and microwave drive over the charge qubit populations and resulting frequency shift. It also captures in principle effects similar to stimulated emission, with the interplay between the photon number in the cavity $|\langle a \rangle|^2$ and the electronic drive of the populations by the Γ 's, which could be the emergence of effects such as lasing.

4.3.2 Linear regime

In the linear regime, the hierarchy of the energy scales $eV_{SD} < k_B T \ll \Omega$ and $\Im m[\chi] n_{ph} \ll \gamma$ ensure that the system is on average close to its ground state, $\sigma_z \approx -1$. We can then determine the microwave phase response of the DQD (i.e. cavity frequency shift measured at f_c) as a function of DC gate voltages:

$$\Delta f_c = -\Re e[\chi] = -g^2 \frac{\Delta}{\Gamma_2^2 + \Delta^2} \tag{4.33}$$

where ϵ is directly controlled by gate voltages, and it is recalled that $\Delta = \sqrt{(\epsilon)^2 + 4t^2} - f_c$. As shown in figure 4.8, if $2t$ is much larger than f_c , we recover a response qualitatively similar to the low frequency response of section 4.2.4. However, when the qubit frequency crosses the resonator frequency, then detuning Δ changes sign and so does Δf_c . The shape of the susceptibility χ then depends rather strongly on the decoherence of the qubit (see figure 4.8), and would blow up to its maximum value of g in the case of strong coupling (i.e. $g > \Gamma_2, \kappa$ with κ the cavity linewidth).

The behaviour of figure 4.8 is observed experimentally as reported in section 5.1.2. Fitting the data with this theory allows us to extract orders of magnitude for g_0 , Γ_2 and t .

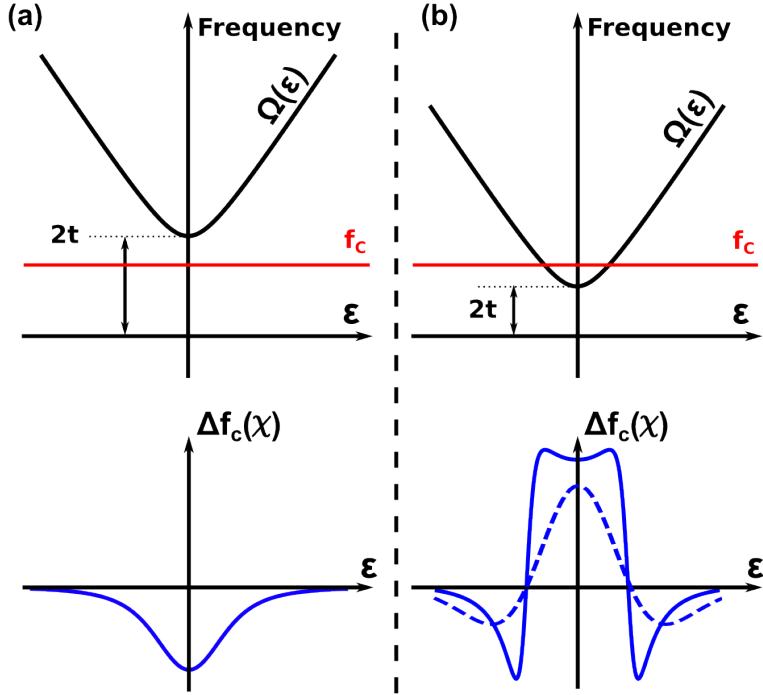


FIGURE 4.8: Dispersion relation $\Omega(\epsilon)$ and corresponding charge susceptibility χ of a DQD charge qubit, readout through a coupled cavity, in the linear regime. (a) Non resonant case where the qubit frequency is always detuned from the cavity frequency ($2t - \Gamma_2 > f_c$), i.e. always dispersive. (b) when $2t < f_c$, cavity and qubit spectral lines cross in the weak coupling regime ($g_0 < \Gamma_2$). The susceptibility changes sign with detuning Δ and qualitatively depends on whether decoherence is strong (dashed line) or weaker (full line).

4.3.3 Finite DC bias

When a finite bias is applied to the double quantum dot, electronic transport sets in and $\langle \sigma_\emptyset \rangle \neq 0$ and $\langle \sigma_2 \rangle \neq 0$ in general. In this situation, the full set of equation (4.32) has to be solved in order to find $\langle \sigma_z \rangle$. As depicted in figure 4.9, electrons can jump in and out the DQD from the fermi seas of the electrodes. Populations are thus driven out of equilibrium so that σ_z is determined by the different lead couplings $\Gamma_{B(AB)\leftrightarrows i}$'s.

Knowing the charge susceptibility χ from measurements in the linear regime, we now have a direct measurement of the qubit z projection $\langle \sigma_z \rangle$ when a finite electronic current is driven through the double dot. Using the low power limit ($\Im m[\chi]n_{ph} \ll \gamma$), this allows us to produce the theory plots of figure 5.9 right panel (chapter 5).

4.3.4 Large number of photons

The number of photons n_{ph} in the cavity being $|\langle a \rangle|^2$, we can compute the cavity read-out power dependence in the case of no transport $\langle \sigma_\emptyset \rangle = \langle \sigma_2 \rangle = 0$ (we neglect thermal

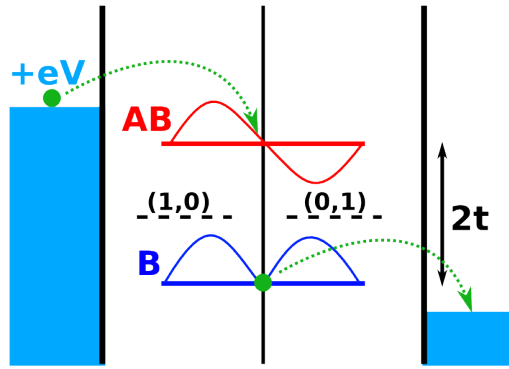


FIGURE 4.9: Schematic of the transport mechanism taking place in the DQD when a large bias $V_{SD} > 2t$ is applied. Anti-bonding and bonding states populations are driven out of equilibrium and depend on the coupling to the leads.

excitation of the AB state since $k_B T \ll \Omega$ and we neglect the self-consistency for determining the number of photons arising from the set (4.22, 4.24, 4.25, 4.26, 4.23) due to the weak coupling strength g_0):

$$\langle \sigma_z \rangle = \langle \sigma_{AB} - \sigma_B \rangle = \frac{-1}{1 + 4\Im m[\chi]n_{ph}/\gamma} \quad (4.34)$$

This formula yields the red solid line fitting the power dependence of $\langle \sigma_z \rangle$ in figure 5.10 (chapter 5). Again, we can use the measure of χ from the linear regime; the cavity input power dependence of $\langle \sigma_z \rangle$ then allows to calibrate directly n_{ph}/γ . The exact calibration of microwave wiring attenuation at low temperature is often a problem in cQED setups. AC-stark shift methods turn out not to be so easy to perform, and our method could thus be used to calibrate n_{ph} in the case of precise knowledge of the qubit relaxation γ through Rabi oscillation for example.

4.3.5 Microwave ("two-tone") spectroscopy

The microwave spectroscopy of a device can unveil features such as fine structure of a DQD excited states or the dispersion relation of a qubit or a multi-level system. This can be done in a cavity by reading the DQD response at resonant frequency f_c while applying a second microwave tone of which we sweep the frequency $f_{d2} = 2\pi\omega_{d2}$. For the sake of simplicity, we consider the case where no transport occurs. The Hamiltonian reduces to the basic Jaynes-Cummings Hamiltonian of equation 4.17 plus the two driving tones:

$$\mathcal{H} = \hbar\omega_c a^\dagger a + \hbar\frac{\Omega}{2}\sigma_z + \hbar g(\sigma_- a^\dagger + \sigma_+ a) + (\epsilon_{d1} e^{-i\omega_{d1}t} a^\dagger + \epsilon_{d2} e^{-i\omega_{d2}t} a^\dagger + h.c.) \quad (4.35)$$

Similarly to section 4.2.5.1 (equation 4.18), we perform the unitary dispersive transformation $\mathcal{U} = e^{\frac{g}{\Delta_{\Omega_c}}(\sigma_+ a - \sigma_- a^\dagger)}$ where $\Delta_{\Omega_c} = \Omega - \omega_c$ to obtain the dispersive Hamiltonian:

$$\begin{aligned} \tilde{\mathcal{H}} = & \hbar(\omega_c + \chi_d \sigma_z) a^\dagger a + \hbar\left(\Omega + \frac{\chi_d}{2}\right)\sigma_z + \frac{g}{\Delta_{\Omega_c}} \left((\epsilon_{d1} e^{-i\omega_{d1}t} + \epsilon_{d2} e^{-i\omega_{d2}t}) \sigma_+ \right. \\ & \left. + (\epsilon_{d1} e^{-i\omega_{d1}t} + \epsilon_{d2} e^{-i\omega_{d2}t}) a^\dagger + h.c. \right) \end{aligned} \quad (4.36)$$

where $\chi_d = \frac{g^2}{\Delta_{\Omega_c}}$. Going into the rotating by performing the time-dependent unitary transformation $\tilde{\mathcal{U}} = e^{ia^\dagger a \omega_{d1} t} e^{i\sigma_z \omega_{d2} t / 2}$, one obtains (supplementary information of [125]):

$$\tilde{\tilde{\mathcal{H}}} = \hbar(\Delta_{cd1} + \chi_d \sigma_z) a^\dagger a + \hbar\left(\Delta_{\Omega d2} + \frac{\chi_d}{2}\right)\sigma_z + \epsilon_{d1}(a + a^\dagger) + \epsilon_{d2} \frac{g}{\Delta_{\Omega_c}} (\sigma_- + \sigma_+) \quad (4.37)$$

where $\Delta_{cd1} = \omega_c - \omega_{d1}$ and $\Delta_{\Omega d2} = \Omega - \omega_{d2}$. It is assumed that tone 1 is almost resonant with the cavity and tone 2 is weakly detuned from the qubit, so that terms oscillating at high frequencies $\omega_{d1} - \omega_{d2}$ are neglected. We can now write the equation of motion for a , σ_- and σ_z :

$$\begin{aligned} \frac{d}{dt}\langle a \rangle &= -(\kappa/2 + i\Delta_{cd1})\langle a \rangle - i\epsilon_{d1} - i\chi_d \langle a \sigma_z \rangle \\ \frac{d}{dt}\langle \sigma_- \rangle &= -(\gamma/2 + \Gamma_\phi + i\Delta_{\Omega d2})\langle \sigma_- \rangle - i\frac{\chi_d}{2}\langle \sigma_- \rangle - i\chi_d \langle a^\dagger a \sigma_- \rangle + 2i\epsilon_{d2} \frac{g}{\Delta_{\Omega_c}} \langle \sigma_z \rangle \\ \frac{d}{dt}\langle \sigma_z \rangle &= -\gamma(\langle \sigma_z \rangle + 1) - 2i\epsilon_{d2} \frac{g}{\Delta_{\Omega_c}} (\langle \sigma_+ \rangle - \langle \sigma_- \rangle) \end{aligned} \quad (4.38)$$

In the stationary regime, with the semi-classical decoupling, the above system yields

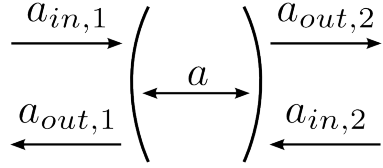


FIGURE 4.10: Schematic representation of the cavity field and the input/output fields. Physically, we use port 1 as an *input* port for the drive of the cavity, which is then readout through the *output* port 2.

$$\begin{aligned}\langle \sigma_z \rangle &= \frac{-1}{1 + \frac{4\Omega_R^2}{\gamma} \frac{\Gamma_2}{\Gamma_2^2 + \tilde{\Delta}_{\Omega d2}^2}} \\ \langle a \rangle &= \frac{-i\epsilon_{d1}}{\frac{\kappa}{2} + i(\Delta_{cd1} + \chi_d \langle \sigma_z \rangle)}\end{aligned}\tag{4.39}$$

where $\Omega_R = \epsilon_{d2} \frac{g}{\Delta_{\Omega c}}$ and $\tilde{\Delta}_{\Omega d2} = \Delta_{\Omega d2} + \chi_d \langle a^\dagger a \rangle + \frac{1}{2}$ is the detuning with the stark-shifted qubit frequency. We get a resonant frequency shift which consistently recalls previous equations 4.31 and 4.34:

$$\Delta f_c = \chi_d \langle \sigma_z \rangle = \frac{g^2}{\Delta_{\Omega c}} \frac{-1}{1 + \frac{4\alpha\Omega_R^2}{\gamma} \frac{\Gamma_2}{\Gamma_2^2 + \tilde{\Delta}_{\Omega d2}^2}}\tag{4.40}$$

The added parameter α is a coupling constant between the second tone drive amplitude ϵ_{d2} which depends on whether the second tone is applied through the input port of the cavity or on a side port directly to a gate on the double quantum dot.

4.4 Input-output theory for resonator transmission phase and amplitude measurements

In practice our microwave measurements give access to both phase and amplitude of the microwave field transmitted through the cavity. As discussed in section 3.2.3, amplitude variations are sometimes trickier to interpret, but could also carry rich information about the system. This section gives a quantitative way to obtain phase and amplitude from the susceptibility χ using an input-output theory [32, 126]. It is widely used in chapter 5 for fitting experimental data, and is useful to understand features such as in figure 5.7 for instance.

Let us consider the bath of bosonic modes coupled to the cavity through the ports 1 and 2 with coupling rates κ_1 and κ_2 . The total decay rate of the cavity is $\kappa = \kappa_{int} + \kappa_1 + \kappa_2$ with κ_{int} the internal loss rate. The equation of motion for the cavity mode a now writes:

$$\frac{d}{dt}a = (\kappa/2 + i\Delta_{cd})a + \sqrt{\kappa_1}a_{in,1} + \sqrt{\kappa_2}a_{in,2} - ig\sigma_- \quad (4.41)$$

where $a_{in,1(2)}$ represent the annihilation operators propagating towards the cavity from the physical transmission lines of the setup, see figure 4.10. $a_{in,2}$ is given by thermal or quantum noise that we neglect here because we consider large photon number and suppose a good experimental isolation and thermalisation on the output port 2 (see section 3.2). The input-output relation on port 2 writes:

$$a_{out,2} = \sqrt{\kappa_2}a - a_{in,2} \quad (4.42)$$

In the semi-classical limit of a large drive at the input of the cavity, we make the approximation $a_{in,1} \sim \alpha_{in}$. We can then define the complex transmission coefficient of the cavity from input port 1 with a probe tone α_{in} , to output port 2, $S_{21} = a_{out,2}/\alpha_{in}$. Using equation 4.23, one gets phase and amplitude variation in the stationary regime (neglecting self-consistency):

$$\begin{aligned} S_{21} &= \frac{\sqrt{\kappa_1\kappa_2}}{i\Delta_{cd} + \kappa/2 + i\chi\langle\sigma_z\rangle} \\ \Delta\varphi &= -\arg(S_{21}) \\ \frac{\Delta A}{A} &= \frac{|S_{21}|}{|S_{21}(g_0 = 0)|} - 1 \end{aligned} \quad (4.43)$$

where χ is the susceptibility defined in equation 4.30 ($\chi = \frac{g^2}{-i\Gamma_2 + \Delta}$). Such a definition of $\Delta\varphi$ (with a minus sign) comes from the actual behaviour of the resonator which experimentally shows $\varphi(\omega) = -\arctan(2\frac{\omega - \omega_c}{\kappa})$.

In the limit of small shifts, i.e. $\chi \ll \kappa$, phase and amplitude measurements are related to real and imaginary parts of the susceptibility (experimentally, $\chi \approx 10\text{kHz}$ and $\kappa \approx \text{MHz}$ in this thesis). Assuming that we indeed do the readout at resonance, $\omega_c = \omega_d$, to the first order in χ/κ :

$$\begin{aligned}\Delta\varphi &\approx \frac{2}{\kappa} \Re e[\chi] \langle \sigma_z \rangle \\ \frac{\Delta A}{A} &\approx \frac{2}{\kappa} \Im m[\chi] \langle \sigma_z \rangle\end{aligned}\tag{4.44}$$

With our writing convention for χ , $\Re e[\chi] \langle \sigma_z \rangle$ rather relates to a pure frequency shifts whereas $\Im m[\chi]$ degrades the cavity Q factor adding up to the total *bare* decay rate κ^7 , see section 5.1.2.3 for experimental discussion. Note that equations 4.44 account well for the sign of the phase shifts observed in chapter 5.

One can also compute the photon number $n_{ph} = \langle a^\dagger a \rangle$ in the cavity in a useful form:

$$n_{ph} = \frac{10^{\frac{P_{in}}{10}-3} \times 10^{s_{21}/20}}{\pi h f_c \Delta_{f,BW}}\tag{4.45}$$

where P_{in} is the power (in dBm) at the input (formally given by $P_{in} = 10 \times \log(\hbar\omega\alpha_{in}^2/1mW)$), s_{21} is the measured transmission of the cavity (in dB) and $\Delta_{f,BW}$ if the measured frequency bandwidth of the cavity ($\Delta_{f,BW} = \kappa/2\pi$).

4.5 Parasitic transmission, *Fano-shaped* resonances and quadrature offsets

This section discusses the influence of parasitic (*aerial*) transmission happening inside the sample holder (see figure 3.9). This can be due to the coupling of the input and output SMA ports of the sample holder⁸, via more or less discrete modes of the sample holder itself, in parallel with the transmission through the cavity. We assume that this parallel transmission channel can be characterised by a general scattering matrix:

$$S^{parasitic} = e^{i\zeta} \begin{pmatrix} \sqrt{1-T}e^{i\theta} & -i\sqrt{T} \\ -i\sqrt{T} & \sqrt{1-T}e^{-i\theta} \end{pmatrix}\tag{4.46}$$

where T is the transmission probability of the channel. In the limit of small transmission $T \ll 1$, we can sum the contribution of the channel ($(\begin{smallmatrix} a_{out,1} \\ a_{out,2} \end{smallmatrix}) = S^{parasitic} (\begin{smallmatrix} a_{in,1} \\ a_{in,2} \end{smallmatrix})$) with

⁷ $A \approx \frac{2\sqrt{\kappa_1\kappa_2}}{\kappa^2} (\kappa + 2\Im m[\chi] \langle \sigma_z \rangle)$

⁸ Micro-bondings could also play the role of antennas

that of the cavity (coupled temporal mode theory, [127]). The input-output relation 4.42 now writes:

$$a_{out,2} = -i\sqrt{T}e^{i\zeta}a_{in,1} + \sqrt{1-T}e^{i(\zeta-\theta)}a_{in,2} + \sqrt{\kappa_2}a - a_{in,2} \quad (4.47)$$

As in the previous section, we neglect $a_{in,2}$ and make the approximation $a_{in,1} \sim \alpha_{in}$. In the stationary regime, we now obtain:

$$S_{21} = -i\sqrt{T}e^{i\zeta} + \frac{\sqrt{\kappa_1\kappa_2}}{i\Delta_{cd} + \kappa/2 + i\chi\langle\sigma_z\rangle} \quad (4.48)$$

Figure 4.11 shows plots of equation 4.48 and of the associated theoretical $\Delta\varphi$ and $\Delta A/A$ with $f_c = 7GHz$, $\kappa = 2MHz$, $\sqrt{\kappa_1\kappa_2} = 200kHz$. The line-shape of the transmission (figure 4.11(a)) reproduces well the *Fano*-shaped experimental data, such as figure 3.13(b) with $T = 10^{-3}$ and $\zeta = \pi/10$. Figures 4.11(b and c) compare the phase and amplitude variations as a function of a given Δf_c (pure frequency shift) for the Fano resonance of 4.11a and for the corresponding Lorentzian transmission ($T = 0$ and $\zeta = 0$). The phase $\Delta\varphi$ is weakly affected for frequency shifts of the order of $10kHz$ (i.e. what we measure experimentally). However, the amplitude variation is qualitatively different and “*contaminated*” by the phase signal. Importantly, it can show a positive sign, that could be for example miss-interpreted as photon emission from the coupled DQD.

The strength of the effect depends on the ratio between $\frac{\sqrt{\kappa_1\kappa_2}}{\kappa}$ and the transmission T . This is directly observable in figure 3.13(a and b) where $\frac{\sqrt{\kappa_1\kappa_2}}{\kappa}$ is respectively ≈ 1 and $\approx 1/10$, with T probably essentially the same (same sample holder). Figures 4.11(d and e) show the phase and amplitude response as a function of the double quantum dot detuning ϵ with $g_0 = 10MHz$, $2t = 5GHz$ and $\Gamma_2 = 500MHz$. More particularly, figure 4.11(e) reproduces some of the discrepancy observed in figure 5.7 and is a possible explanation. Note however that it is not possible to follow a fully consistent fitting procedure. Specifically, phase and amplitude of the bare resonance cannot be fitted together. In addition, the T and ζ obtained by the best fit of the bare transmission are not compatible with a good fit of $\Delta A/A$ such as presented in figure 5.7 (green dashed line). This could arise for instance from the coupling to several modes in the sample holder and not only one. It should be avoided in any case by tuning $\frac{\sqrt{\kappa_1\kappa_2}}{\kappa} \approx 1$ (over-coupled cavity).

Equation 4.48 also points out that the addition of a constant offset to the transmission can produce distortions on the signal. Another cause for observing distorted (e.g. *Fano*-shaped) resonances can thus simply be offsets on the quadratures coming from the detection scheme. Although it is done at finite frequency, the homodyne detection mostly

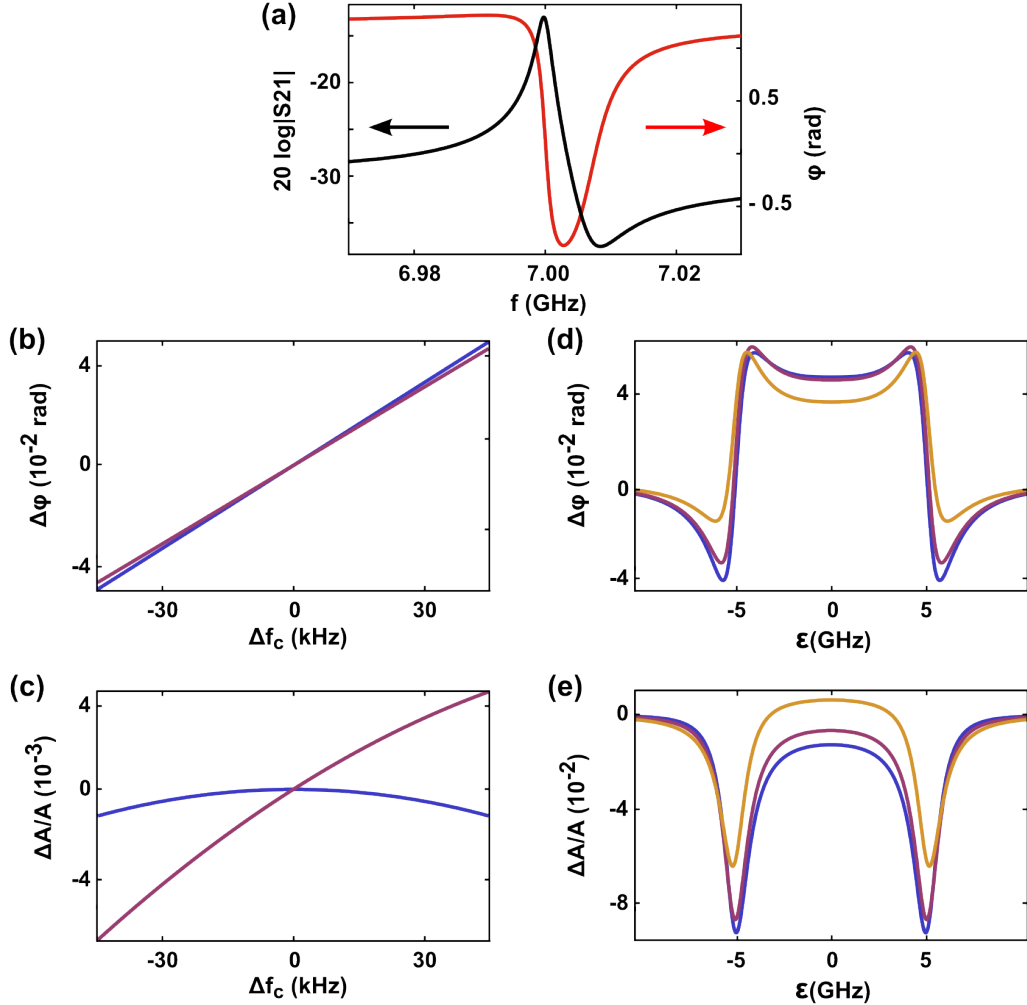


FIGURE 4.11: (a) Amplitude and phase of a transmission with a parasitic channel in parallel with the cavity, using equation 4.48. With the realistic parameters $f_c = 7\text{GHz}$, $\kappa = 2\text{MHz}$, $\sqrt{\kappa_1\kappa_2} = 200\text{kHz}$, $T = 10^{-3}$ and $\zeta = \pi/10$, we reproduce rather well the experimental data of figure 3.13(b). (b) and (c) Phase and amplitude variation as a function of Δf_c , for a purely Lorentzian transmission ($T = 0$ and $\zeta = 0$, blue) and for the Fano-shaped transmission of (a) (in purple). (d) and (e) Phase and amplitude variation as a function of DQD detuning ϵ , for a Lorentzian (blue), Fano as in (b and c) (purple), and stronger parasitic transmission ($T = 0.02$ and $\zeta = \pi/10$, orange) which shows $\Delta A/A > 0$ around zero detuning. Susceptibility was computed with $g_0 = 10\text{MHz}$, $2t = 5\text{GHz}$ and $\Gamma_2 = 500\text{MHz}$.

used for this thesis can suffer from such cross-talk offsets (see section 3.2.3). However this can be most of the time disentangled from the effect of parallel transmission in the sample holder. Indeed room temperature cross-talks can be calibrated and removed from the true signal⁹ whereas interferences phenomena happening in the sample holder cannot.

⁹It however becomes a bit tricky at very low power (see section 3.2.3).

Chapter 5

Charge qubit in a microwave cavity

5.1	Linear regime	78
5.1.1	Symmetric coupling	78
5.1.2	Asymmetric coupling	82
5.2	Out of equilibrium	87
5.2.1	Finite bias	88
5.2.2	Finite microwave power	88
5.3	Microwave spectroscopy	90
5.4	Decoherence and charge noise	92

The electron charge is naturally coupled to electric fields and this is the first physical effect that one can observe in these hybrid cavity-quantum dot architectures. This coupling is also at the foundation of most spin-photon coupling proposals ([14, 32, 106–109]) which convert an electric field into an effective magnetic field. It is therefore of fundamental interest to understand this coupling mechanism in order to go towards more complex hybrid systems. A discriminating way to characterise the charge coupling is to push the system out of equilibrium and look at its response by measuring both DC current and microwave signal. This chapter gives experimental results obtained on the charge degree of freedom of double quantum dots coupled to microwave cavities. The first two sections present results both at equilibrium (linear regime) and out of equilibrium. Section 5.3 is about the microwave spectroscopy of a charge qubit whereas the decoherence and charge noise properties of our devices are finally discussed in section 5.4.

5.1 Linear regime

As it is already discussed in chapter 4, the electric field of the cavity can be coupled to different dipoles in a double quantum dot. Depending on the dipole, the cavity response can be either sensitive to transitions between electronic states inside the DQD, namely inter-dot, or transitions involving states belonging to the continuum of the electrodes, namely dot-lead. One way to design which of these transitions will be coupled is to play with the symmetry of the coupling; experimental realisation of this task is given in the following two sections.

5.1.1 Symmetric coupling

As described in section 4.2.1, coupling between the cavity mode and the chemical potential of the DQD can be understood in terms of lever arms, and these lever arms are simply ratios of capacitances (see equation 4.2). From our experience, if one just places a DQD next to a CPW resonator, the most common is that coupling capacitances $C_{c,i}$ are different but in the same order of magnitude, so that the total coupling lever arm of the two dots $\alpha_{d1(2)} = \sum_i \alpha_{i/1(2)}$ are comparable. The resulting coupling is symmetric, $\alpha_{d1} \approx \alpha_{d2}$ and it is often experimentally easier to achieve than a strong asymmetric coupling $\alpha_{d1} \gg \alpha_{d2}$ (see section 4.2.4).

Figure 5.1 shows optical and SEM micrograph of a device fabricated in the vicinity of a resonator, with no particular engineering of the capacitance between the transmission line and the electrodes. The double quantum dot is visible in figure 5.1(c), with a central

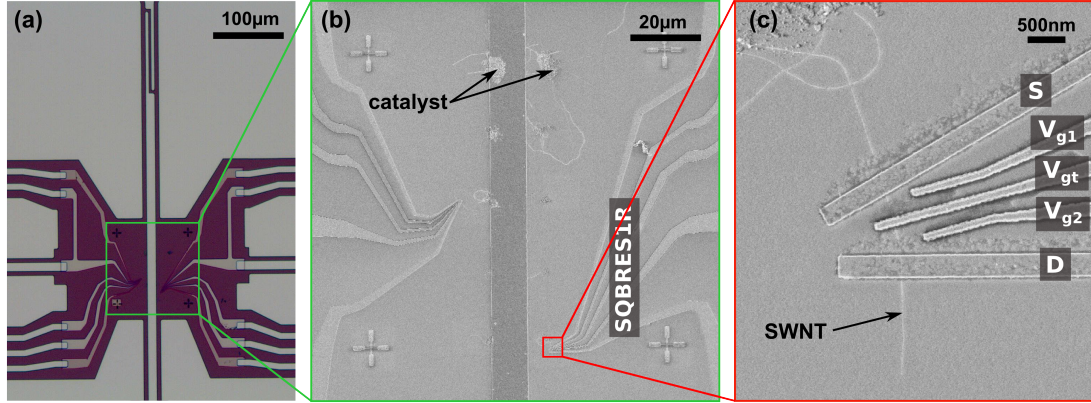


FIGURE 5.1: (a) Optical micrograph of the device *SQBRES1R*. (b) SEM picture of the device. At this stage two devices were embedded in each electric field anti-node of the cavity. The device shown here is sitting on the right. Catalyst particules can be seen around the devices. (c) SEM picture zoomed on the device. Source (S), Drain (D) and gate electrodes (V_g 's) are connected to the SWNT. V_{g1} and V_{g2} where then designed as side gates.

top gate and source and drain electrodes deposited over a carbon nanotube. The local gates controlling the dot's potential (V_{g1} and V_{g2}) are side gates in this device. The microwave resonator was here severely affected by CVD growth residues (c.f. chapter 3) and did not show a sharp resonance in the superconducting state. The microwave signal was here measured through another mode localised in the sample holder with quality factor $Q \approx 100$ at $f_c \approx 6.92\text{GHz}$.

A stability diagram measurement of the device is given in figure 5.2. The DC current measurement (figure 5.2(a)) shows the characteristic honey-comb pattern of double quantum dot devices. Using DC transport spectroscopy such as in figures 5.2(a) and 5.3a, we can extract orders of magnitudes for the tunnel rates of the barrier constituting the DQD (coulomb peak width for lead coupling and curvature at the triple points for the interdot coupling t , see chapter 2 for details). It turns out that all these rates are here much larger than the resonator frequency $f_c = 6.92\text{GHz}$: $\Gamma_{\text{lead},1} \sim 100\mu\text{eV}(25\text{GHz})$, $\Gamma_{\text{lead},2} \sim 200\mu\text{eV}(50\text{GHz})$ and $t \sim 60\mu\text{eV}(2t \sim 30\text{GHz})$. We are therefore rather in the *low frequency limit*, in which the quantum capacitance of the DQD can be calculated following section 4.2.4.

Figure 5.2(b and c) and 5.3(a and c) show positive phase shifts, therefore positive cavity frequency shift Δf_c . We interpret this positive sign as the consequence of indirect coupling through the leads (see section 4.2.3). From figure 5.1, we can already expect the five electrodes to be coupled to the electric field with a similar strength (possibly weaker coupling for V_{g1} and V_{g2} as they are slightly screened). Because the device is controlled with side gates, source and drain electrodes have dominating lever arms on the DQD states ($C_{Li} \gg C_{gi}$)

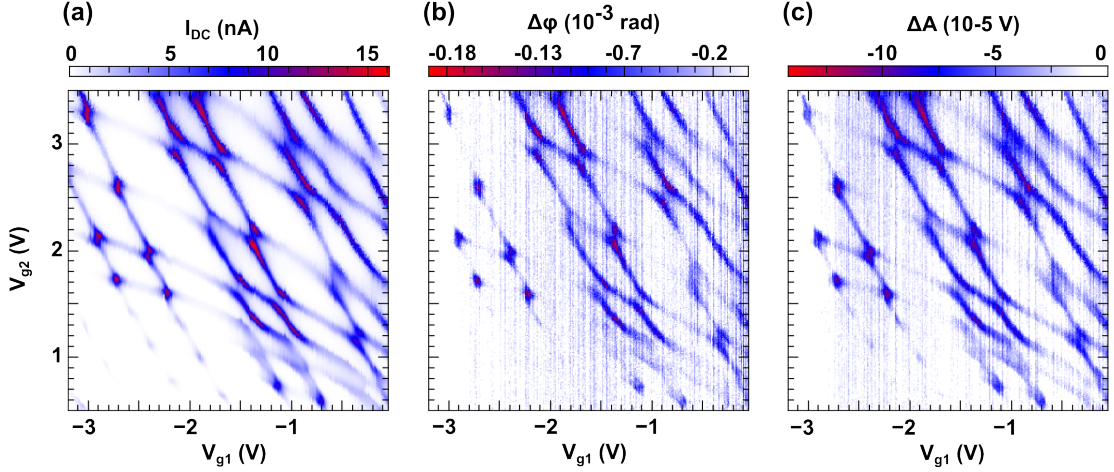


FIGURE 5.2: Stability diagram measurement of a symmetrically coupled DQD at finite bias $V_{SD} = 1mV$ (and $V_{gt} = -0.2V$). (a) DC current flowing through the DQD measured as a function of V_{g1} and V_{g2} . (b),(c) Phase and amplitude variation of the microwave signal, measured simultaneously with (a). *Sample:SQBRES1R*

The DC current measurement also indicates rather symmetric dot-lead couplings, $\Gamma_{lead,1} \approx \Gamma_{lead,2}$, and this points towards symmetric coupling of the dots to the electric field, $C_{L1} \approx C_{L2}$. The weight of the symmetric and asymmetric coupling constants α_{d1} and α_{d2} is directly observable in figure 5.3. Figure 5.3(c) shows two quantum capacitance phase peaks separated mainly by the mutual charging energy $U_m \approx 500\mu eV$. The height of these peaks is proportional to α_{d1}^2 and α_{d2}^2 and is about $2 \times 10^{-4} rad$. In figure 5.3(e) however, the phase signal is much smaller ($\Delta\varphi < 5 \times 10^{-5} rad$) indicating a very weak asymmetric response, proportional to $(\alpha_{d1} - \alpha_{d2})^2$. The comparison of the data in figure 5.3(c and e) thus reveals $(\alpha_{d1} - \alpha_{d2})^2 \ll \alpha_{d1}^2, \alpha_{d2}^2$, so the DQD is mainly symmetrically coupled to the resonator and $g_{inter-dot} \ll g_{dot-lead}$ (see section 4.2.4).

On the way towards coherent spin control and spin-photon coupling, proposals are generally based on hybridised charge states within the two dots of a DQD ([14, 32, 106–109]) and thus transitions involving inter-dot quantum states. Here, it is not possible to address these transitions because they are very weakly coupled to the electric field ($\alpha_{d1} \approx \alpha_{d2}$). Moreover the device presented here exhibits a large inter-dot tunnel coupling ($2t \sim 30GHz$), far detuned from resonant frequency ($6.9GHz$), settling us in the low frequency regime. We therefore have to access to the quantum capacitance of the double quantum dot, but it cannot be used as a qubit and no internal information such as the populations of the dots' states can be extracted from the cavity readout.

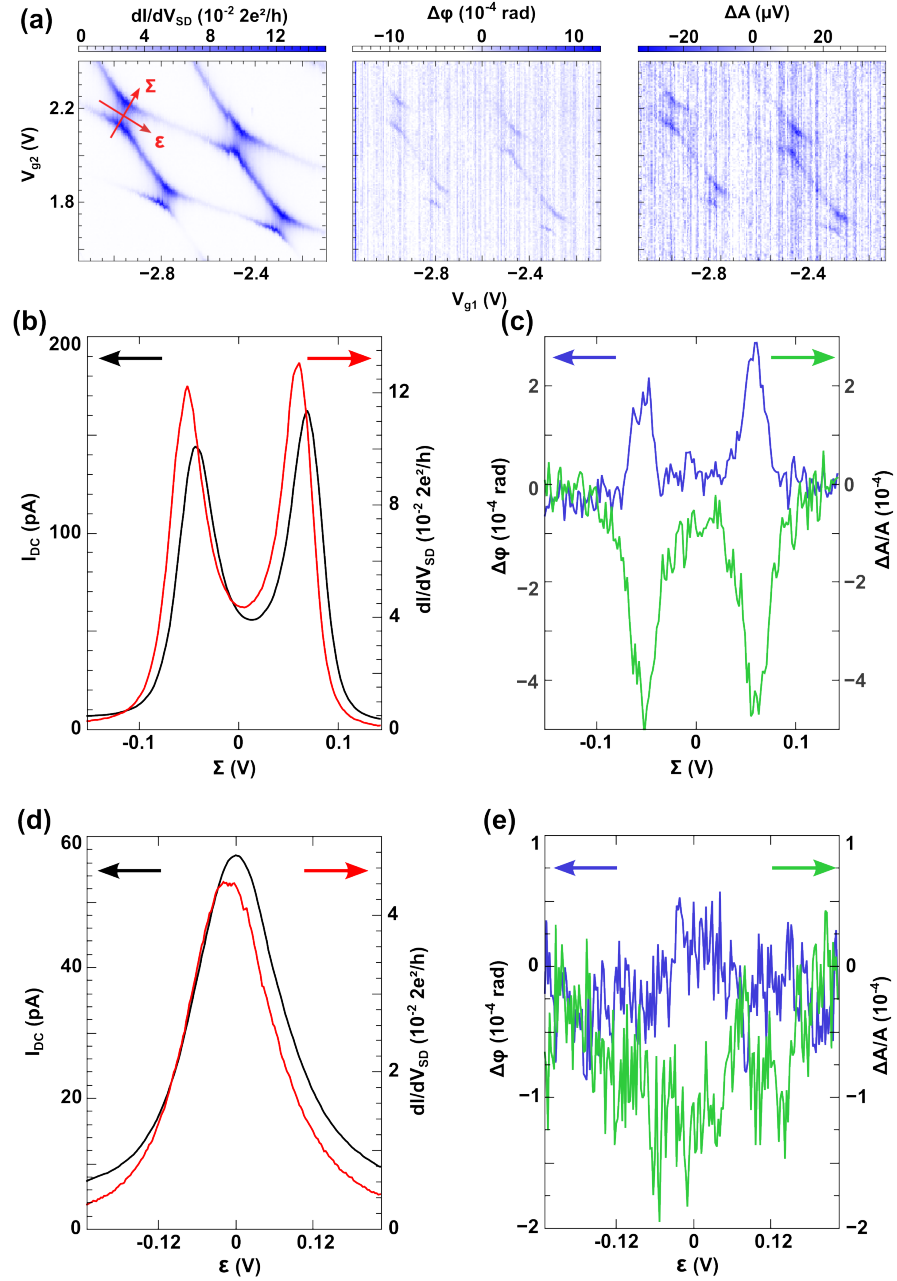


FIGURE 5.3: (a) Measurement of a smaller gate region of the stability diagram of the device at small bias $V_{sd} \approx 15\mu V$ (and $V_{gt} = -0.2V$). The three panels show greyscales of the low frequency differential conductance, microwave phase shift and microwave amplitude variation. (b) DC current and differential conductance traces along the Σ direction given in (a). (c) Simultaneously measured microwave response along the same gate direction Σ . (d) and (e) Simultaneous DC and microwave measurements taken along the ϵ gate direction. *Sample:SQBRES1R*

5.1.2 Asymmetric coupling

Addressing left-right transitions in a double quantum dot requires very asymmetric lever arms in order to couple to the inter-dot energy detuning ϵ . This is non trivial especially if one wants to keep a fully capacitive coupling (i.e. no galvanic coupling to the resonator in order to keep the possibility to embed more than one device in a CPW cavity), see chapter 4.

5.1.2.1 Device

The device (*SQBRES35R*) presented in the rest of this chapter is shown in figure 5.4 and all the data displayed comes from this sample unless specified. We used our stamping technique (section 3.1.4) to fabricate this sample and thus demonstrate the possibility to embed a high quality SWNT in a high finesse microwave cavity. The quality factor of the fundamental mode is here about 3500 (see figure 5.4e) corresponding to a linewidth $\kappa \approx 2MHz$.

The asymmetry of the coupling is engineered by connecting on the dots' top gates to a rather big superconducting pad having a large capacitance to the transmission line of the resonator (figure 5.4b and c).

5.1.2.2 Dispersive regime

One can start by looking at the stability diagram of the device in the linear regime¹ as in figure 5.5. DC current measurement shows features similar as in figure 5.2a but with some essential differences. First, the co-tunnelling lines of the honey-comb pattern are narrower as Γ_{lead}/U is smaller. Second, there is an important mutual charge energy $U_m \sim$ few $100\mu eV$ compared to the Γ_{lead} 's, yielding a well defined zero detuning $\epsilon = 0$ region, where we can use the device as a charge qubit². Note that current lines are less tilted than in figure 5.2a because we use top-gates instead of side-gates, yielding stronger gate lever-arms.

The phase response given in figure 5.5b is now very different from the DC current response. It exhibits *sticks* localised between the triple points of the honey-comb. This is a signature of asymmetric coupling, i.e. to the left-right transitions [118, 119]. By looking at the curvature of the current lines at the triple points, we can estimate that

¹being in the linear regime can only be ensured a posteriori, but generally corresponds to a small number of photons $n_{ph} \sim$ few $10 - 100$ (to satisfy $\Im m[\chi]n_{ph} \ll \gamma$) and $eV_{SD} < 2t$

²The qubit states could also be encoded by left and right states but the resonator is coupled to their hybridised version, namely bonding (B) and anti-bonding (AB) states.

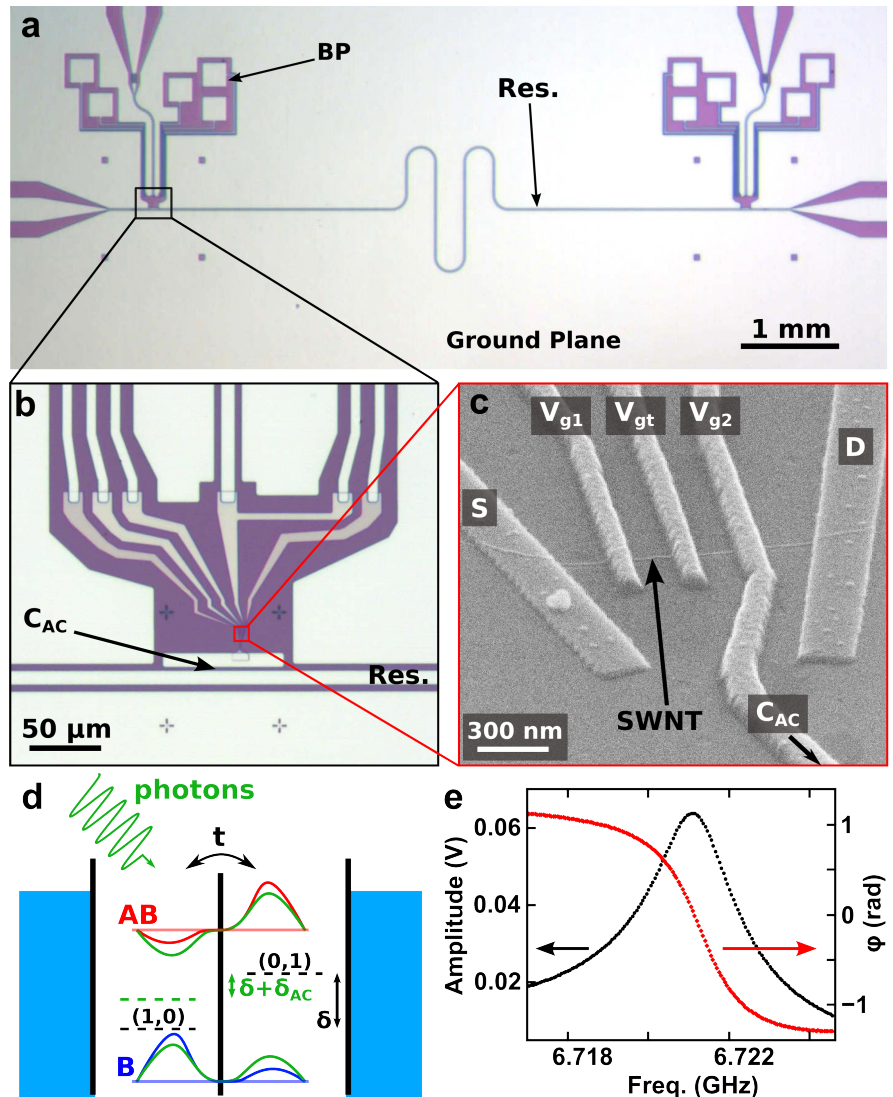


FIGURE 5.4: (a) Optical micrograph of the coplanar wave-guide microwave resonator (Res.). Bonding pads (BP) are isolated from the ground plane and carry DC voltage or current. (b) An extra superconducting pad is placed next to the resonator line, providing a large capacitance C_{AC} . (c) Scanning electron micrograph of the double quantum dot device. A single wall carbon nanotube (SWNT) is connected to source and drain electrodes (S and D), as well as three top gates V_{g1} , V_{g2} and V_{gt} . V_{g2} is directly connected to the capacitance C_{AC} . (d) Schematic of the coupling mechanism between the microwave photons and bonding (B) and anti-bonding (AB) states of the double quantum dot. (e) Amplitude and phase response of the microwave cavity in its fundamental mode measured in transmission. *Sample:SQBRES35R*

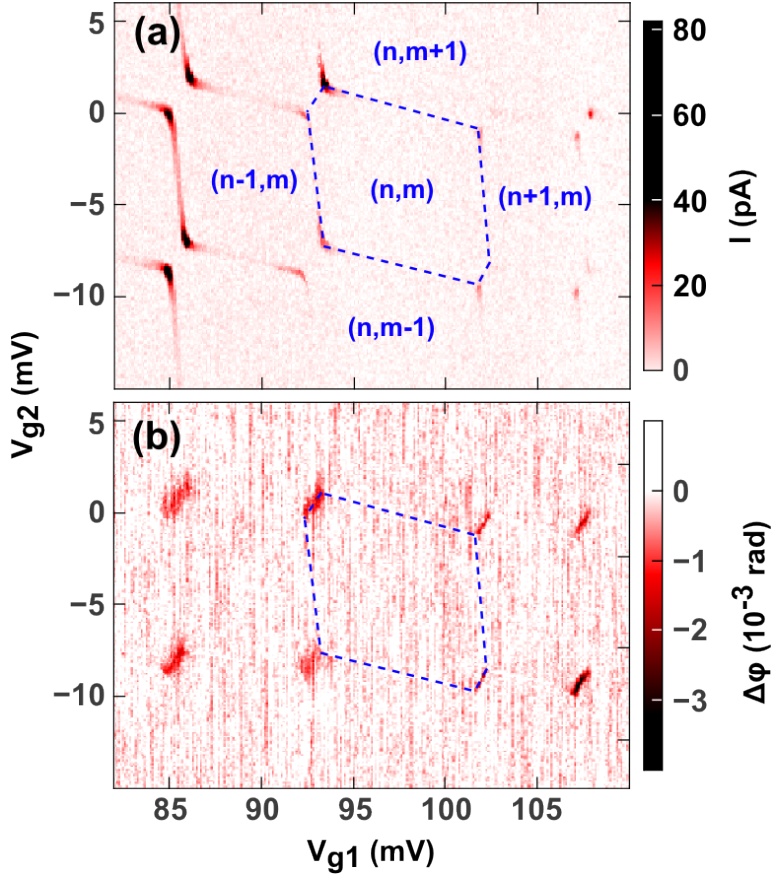


FIGURE 5.5: (a) Direct current flowing through the device as a function of V_{g1} and V_{g2} measured at $V_{sd} = 200\mu V$ ($V_{gt} = 0mV$). The dashed lines follow co-tunneling lines, outlining the stability diagram of charge states (n, m) in the DQD. (b) Phase variation of the transmitted microwave signal measured at cavity resonance ($\approx 6.72GHz$), simultaneously with the direct current of (a). The associated charge susceptibility is maximum at degeneracy between $(n + 1; m)$ and $(n; m + 1)$, demonstrating an asymmetric coupling between the cavity and the two dots.

inter-dot coupling is large, $2t \gtrsim 200\mu V$ (estimated for the lowest-right region of figure 5.5 where it is the smallest of the data displayed here). The phase response, revealing the charge susceptibility χ , confirms that we are here in the case where $2t > \omega_c + \Gamma_2$; the cavity and the charge qubit are never resonant in this region, see figure 5.8(a) for the profile of such *sticks*.

5.1.2.3 Resonant regime

Figure 5.6 shows a similar measurement as figure 5.5 but zoomed over a single left-right degeneracy line, with different gate settings. The direct current (figure 5.6a) resembles the bottom right region of figure 5.5(a), with two triple points separated by a mutual charging energy ($U_m \approx 100\mu eV$). Although it is still spanning along the zero detuning line, the phase $\Delta\varphi$ now looks different from figure 5.5(b). It is mainly positive and shows

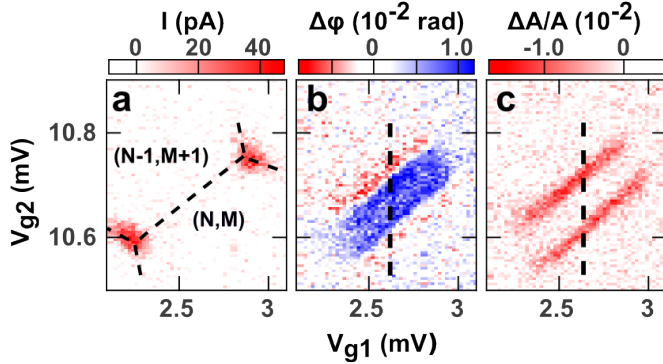


FIGURE 5.6: Double quantum dot response for $V_{gt} = -242\text{mV}$ and $V_{sd} \approx 20\mu\text{V}$. (a) Direct current measurement showing the triple points and the associated stability diagram with charge states (N, M) and $(N - 1, M + 1)$. (b) and (c) In this gate voltage region, the lower value $2t$ of the energy splitting between bonding and anti-bonding states becomes smaller than the cavity frequency. The microwave phase variation $\Delta\varphi$ changes sign and the microwave amplitude $\Delta A/A$ exhibits two parallel lines corresponding to the regions where the bonding/anti-bonding Larmor frequency equals the cavity frequency.

two satellite negative dips. Along the line where the phase changes sign, the microwave amplitude A reduces of about 1%, showing two lines parallel to the zero detuning line. This feature is similar to what is observed in [33], but we simply interpret this as a consequence of the fact that the dephasing Γ_2 is smaller than the spacing between the two lines defined by $\Omega(\epsilon) = \omega_c$ (see figure 4.8). Indeed $\Omega = \omega_c$ implies that the real part of the susceptibility³ changes sign due the sign change of the cavity-qubit detuning $\Delta = \Omega - \omega_c$, hence the sign change of $\Delta\varphi$, see equation 4.44. It also implies that $\Im m[\chi]$ is at its maximum of g^2/Γ_2 , therefore showing maximum amplitude response. Along these lines, the resonator and the qubit are more hybridised so that the resonator linewidth is more affected by the large spectral linewidth of the qubit, thus yielding more dissipation (i.e. lower effective Q factor).

The profiles of $\Delta\varphi$ and $\Delta A/A$ at $V_{g1} = 2.62\text{mV}$ (dashed line of figure 5.6b,c) are given in figure 5.8(c) and 5.7 respectively. We are in the regime where $2t < \omega_c + \Gamma_2$, with a tunnel coupling of about $2t \approx 5\text{GHz}$ or $t \approx 10\mu\text{eV}$. Remarkably, such an opaque tunnel barrier turns out to be non trivial to obtain with conventional CNT's [6]. The solid red line of figure 5.7 comes from equation 4.43 using parameters g_0 , Γ_2 and t extracted from the phase response (figure 5.8(c)). Even if one forgets the asymmetry between negative and positive detuning (ϵ or ΔV_{g2}), theory does not really agree with data. Releasing the fitting parameters from the previous phase fit does not allow better agreement to the data. It is particularly not possible to reproduce the behaviour close to zero detuning while keeping the dips width reasonable. This issue is very likely to come from experimental artefacts; it is possible to reproduce this feature by introducing a

³ $\Re e[\chi] = g^2 \frac{\Delta}{\Gamma_2^2 + \Delta^2}$; $\Im m[\chi] = g^2 \frac{\Gamma_2}{\Gamma_2^2 + \Delta^2}$

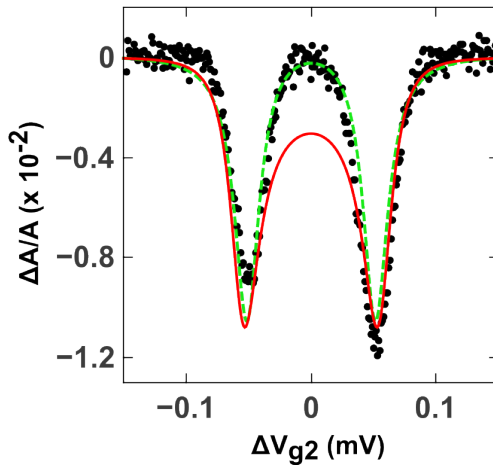


FIGURE 5.7: Microwave cavity amplitude variation as a function of DQD inter-dot gate detuning. Black dotted curve is the measured profile of the amplitude data presented in figure 5.6c. Red solid line is theory described in sections 4.3.2 and 4.4 with the same fitting parameters as in figure 5.8(c). Green dashed line is the same theory with the same parameters but accounting for a Fano shape of the transmission (see section 4.5, $T = 4 \times 10^{-3}$, $\zeta = 1.24$ which would fit well the bare transmission)

parallel transmission in the sample holder giving rise to interferences, see section 4.5 (and section 3.2.3, figure 3.13). However such a fitting procedure cannot be fully consistent with respect to phase variations. It could also come from some incompleteness of the theory; for instance we neglected the self consistency of the EOM for the determination of $\langle a \rangle$ (in equations 4.22 - 4.26), or from the contribution of other transitions, see section 6.1. Other groups have also reported issues fitting experimental amplitude variations with a similar EOM model, such as in [31].

Figure 5.8 compares three typical phase profiles corresponding to three different charge susceptibilities, as in figure 4.8. Figure 5.8(a) ressembles the low frequency response $\Delta C_{inter-dot}$ of equation 4.16 and figure 4.5 but with a quantitatively different contrast, now determined by g_0^2/Δ instead of g_0^2/t . Figure 5.8(b) and (c) are both in the case of $2t < \omega_c + \Gamma_2$ so that the phase contrast is now mainly determined by g_0^2/Γ_2 . The shape of the two curves is qualitatively different. In (c), decoherence becomes smaller than the spacing between the two lines where $\Omega(\epsilon(V_{g2})) = \omega_c$, i.e. $\Gamma_2 < 2\sqrt{4t^2 - \omega_c^2}$.

Fitting the data of figure 5.8 with the theory given in section 4.3.2 and 4.4, we can extract g_0 , Γ_2 and t using $\langle \sigma_z \rangle = -1$ and lever arms extracted from DC measurements to convert gate voltage into energy. Depending on the settings of the 3 gates, we get values for g_0 and $\gamma/2 + \Gamma_\phi$ ranging from $3MHz$ to $12MHz$ and from $450MHz$ to $3GHz$ respectively (with tunnel couplings $2t = 11.7GHz$, $5.3GHz$ and $5.5GHz$ in figure 5.8(a), (b) and (c) respectively). These figures are comparable to what is found in 2DEGs [31, 33], in InAs nanowires [32], and in graphene [34]. Note however that we cannot with this analysis

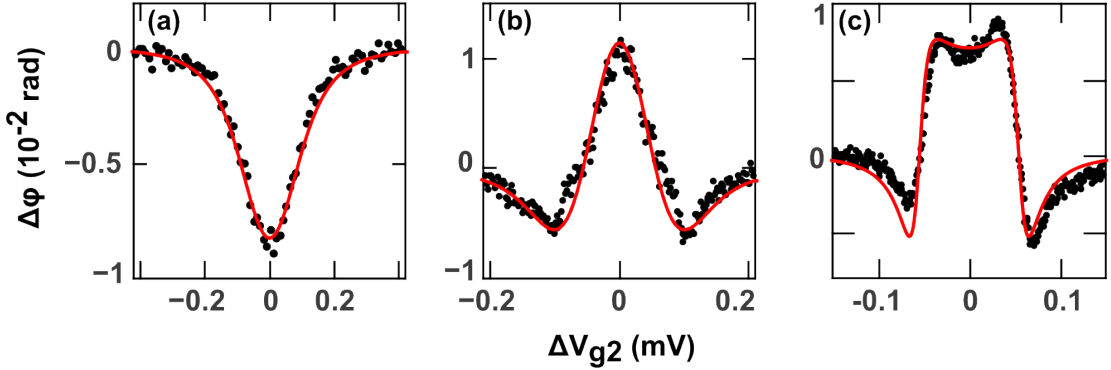


FIGURE 5.8: Microwave cavity phase response profiles as a function of DQD inter-dot gate detuning. Black dots are measurement data and solid red line fits come from the theory described in sections 4.3.2 and 4.4. (a) Phase profile in a non-resonant region ($2t \approx 11.7\text{GHz} > \omega_c + \gamma_2$) similar to figure 5.5. (b) Phase response in a region where $2t \approx 5.3\text{GHz} < \omega_c$ but with a *large* decoherence ($V_{gt} = 0$). (c) Phase response in the region showed in figure 5.6 (dashed line of (b)), where $2t \approx 5.5\text{GHz} < \omega_c$ and decoherence is smaller (Γ_2 compared to $\sqrt{4t^2 - \omega_c^2}$) yielding shoulders. The middle top gate is here $V_{gt} = -242\text{mV}$

determine separately charge relaxation γ and dephasing Γ_ϕ . In the next section, we use the cavity as a spectrum analyser to perform this task [126]. More generally, the non-linear photonic and/or electronic regimes allow us to get a deeper understanding of the double-dot/cavity hybrid system.

The charge coupling strength we extract is rather a bit smaller than what is reported in other systems [32–34] (from 15MHz up to 50MHz [31]). This is likely to arise from a lack of optimization in the geometry resulting in a reduced coupling strength $g_{\text{inter-dot}} = e |\alpha_{d1} - \alpha_{d2}| V_{RMS}$. The device probably suffers from cross talks between the gates (see section 4.2.4). It could also be an underestimation, due to the presence of spin susceptibilities (see section 6.1).

5.2 Out of equilibrium

In the linear regime, the qubit is in its ground state and $\langle \sigma_z \rangle = -1$. The response of the cavity in the presence of the double dot is fully controlled by the finite frequency charge susceptibility χ of the DQD [32, 119, 124]. In the non-linear regime, $\langle \sigma_z \rangle$ is not -1 and depends on the applied bias and on the number of photons in the cavity. A large number of photons provides a transverse torque to the qubit hosted by the double dot which modifies the projection of the Bloch vector on the z axis. A finite current also implies a change of the probabilities of both bonding and anti-bonding states. Using the EOM theory given in section 4.3, we can extract all the relevant parameters for the

hybrid device such as relaxation rate, dephasing rate and photon number via the out of equilibrium measurements presented in the next two sections.

5.2.1 Finite bias

The easiest way to drive the system out of equilibrium is to apply a large DC bias on the DQD (keeping a low microwave power). Figure 5.9 displays the DC current and the cavity response for $V_{SD} = -350\mu V$, $50\mu V$, and $250\mu V$. In this situation, as illustrated schematically in figure 4.9, the finite current changes the stationary populations of the bonding and anti-bonding states. This leads to characteristic transport triangles in the transport spectroscopy. These triangles indicate that the populations of the ground and first excited states are strongly out of equilibrium leading to $\langle \sigma_z \rangle \neq -1$ under the triangles. The cavity dispersive shift allows here to read-out directly $\langle \sigma_z \rangle$, which is not straightforward using only DC current in the general case.

For $V_{SD} = 50\mu V$, the phase contrast seems weakly affected despite non linear regime imposed by a bias larger than qubit splitting ($eV_{SD} \gtrsim 2t \approx 40\mu V$). This is only because bias triangles appear to be small compared to the total distance between the triple points, $U_m + 2t \approx U_m \approx 800\mu eV$, see section 2.1.2. At $V_{SD} = 250\mu V$, the degeneracy line shrinks with weak phase contrast under the top red triangle and a moderate contrast under the bottom red triangle. This means that $\langle \sigma_z \rangle$ is strongly reduced under the top triangle (equal population for the bonding and anti-bonding states) whereas it stays finite (negative) under the bottom triangle. This shows the interest of the microwave phase signal in this out of equilibrium situation. The top and bottom triangles are nearly identical and have similar current contrast, whereas the phase contrast is markedly different, because it directly reveals the value of $\langle \sigma_z \rangle$. For opposite bias ($V_{sd} = -350\mu V$), $\langle \sigma_z \rangle$ goes to zero under both triangles as illustrated in the top panel of figure 5.9. This signals symmetric (and stronger) coupling to the DQD leads. As shown in the rightmost panels of figure 5.9, we are able to reproduce the observed features with the theory which is developed in section 4.3.3. Reproducing these features strongly constraints the bare lead couplings to $\gamma_{1(2)} \approx 300(1600)MHz$ for $V_{SD} > 0$ and $\gamma_{1(2)} \approx 10(10)GHz$ for $V_{SD} < 0$. The latter large values probably signal that co-tunnelling contributes for this bias, although it is not visible in the current. Although it is not as restrictive as for the lead coupling, the internal relaxation rate is also constrained: $\gamma \approx 300MHz$.

5.2.2 Finite microwave power

The power dependence of the phase contrast at zero detuning allows one to determine the ratio between the relaxation rate and the cavity photon number at a given power. As

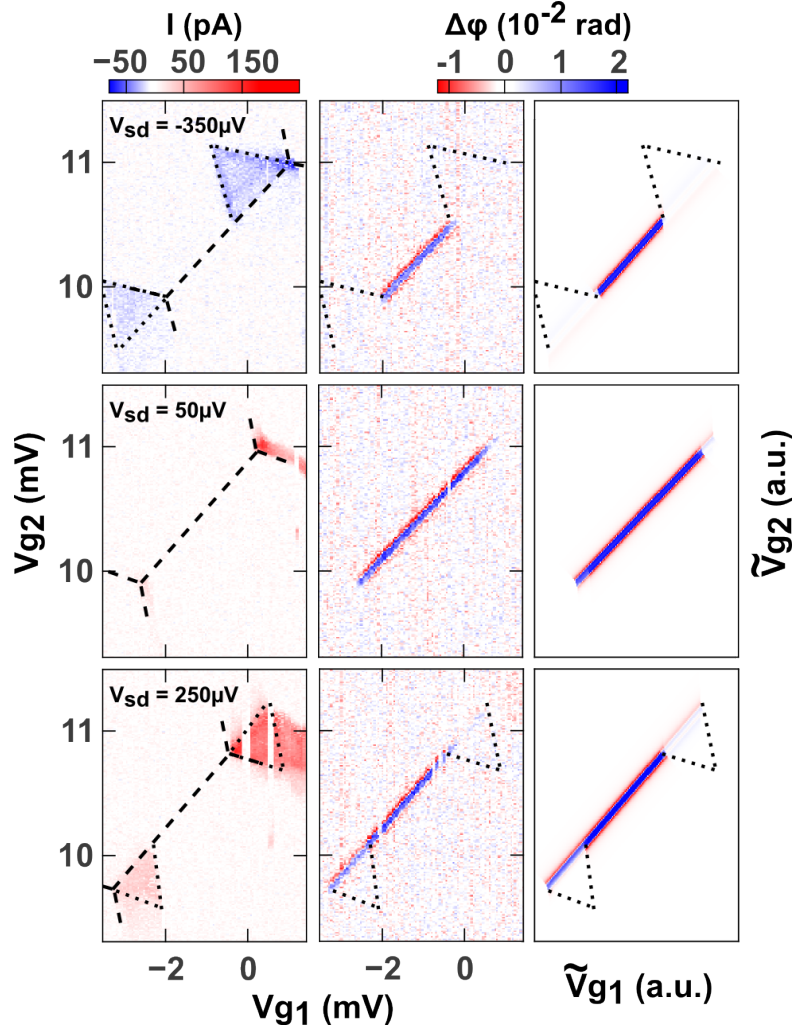


FIGURE 5.9: Measured direct current (first column), measured microwave phase (second column) and theory for microwave phase (third column) of the device at three different bias, as a function of gate voltages V_{g1} and V_{g2} ($V_{gt} = -242\text{mV}$). Big dashed lines outline the charge stability diagram of the double quantum dot. The direct current signal shows the characteristic bias triangles (marked with small dashed lines) developing next to the triple points. The phase signal is unchanged between the bias triangles, where the charge remains blockaded, whereas it is modified in the regions where transport is allowed.

depicted in the inset of figure 5.10, on average photons exert a transverse torque on the qubit state vector, towards the equatorial plane of the Bloch sphere, thereby reducing the value of $\langle \sigma_z \rangle$. Since the photons *drive* the effective spin, the efficiency of this process is directly related to the relaxation rate of the charge states. It is convenient to normalize the phase contrast by its value at very low power. This gives a direct measurement of the expectation value $\langle \sigma_z \rangle$, displayed in figure 5.10 at zero inter-dot detuning for a power ranging from -104dBm to -74dBm at the cavity input.

The average projection $\langle \sigma_z \rangle$ increases from its ground state value -1 up to ≈ -0.2 . Equation 4.34 implies $4\Im m[\chi]n_{ph}/\gamma = 1$ when $\langle \sigma_z \rangle = -0.5$ and we know $\Im m[\chi]$ from

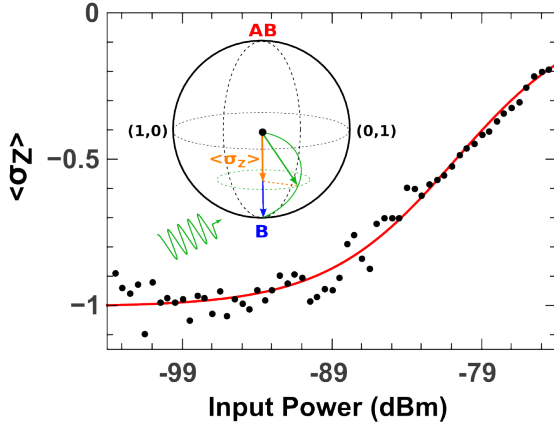


FIGURE 5.10: Measured $\langle \sigma_z \rangle$ value (black points) obtained from the phase variation as a function of the estimated microwave power at the input of the cavity. Red line is theory described in section 4.3.4. Inset : Bloch sphere of the charge qubit with bonding and anti-bonding states. A large number of readout photons weakly detuned from the qubit excites transitions on average, and imposes $\langle \sigma_z \rangle > -1$. At the inflection point, Equation 4.34 yields $\langle \sigma_z \rangle = -1/2$ when $4\Im m[\chi]n_{ph} = \gamma$.

low power study, similarly to that of figure 5.6 and 5.8. We can in principle determine directly γ provided n_{ph} is accurately known, but precise knowledge of attenuation on such setup is in general non trivial. One could actually think of the opposite and use a precise knowledge of the qubit relaxation (i.e. through Rabi manipulation) to determine n_{ph} . Here we can fit the power dependence of $\langle \sigma_z \rangle$ (see red line) using equation 4.34. This yield $\gamma/n_0 = 6.43MHz$ with $n_{ph} = n_0 \times 10^{(P+104)/10}$ (P in dBm), n_0 being the number of photons in the cavity for an input power of $-104dBm$. We can then compare this value with the relaxation rate estimated via DC bias study (previous section) and the measurement line attenuation measured at room temperature . Using $\gamma \approx 300MHz$ we find $n_0 \approx 45$. The value of n_0 is about $5dB$ smaller than the one expected from our microwave chain attenuation at room temperature. Attenuation along the microwave cables changes with temperature. Even more importantly, this value does not take into account the micro-bondings from the sample holder to the cavity input, which are different from sample to sample and can yield significant attenuation. In general, calibration of the measurement chain at low temperature is a problem, and the measurement of figure 5.10 is a way to address this problem.

5.3 Microwave spectroscopy

A microwave spectroscopy of the double dot can be performed by measuring $\langle \sigma_z \rangle$ through the phase at cavity frequency, while exciting the DQD with a second coherent tone of which we sweep frequency f_{d2} . This is conveniently done when the cavity and the DQD are not in resonance, i.e. in the dispersive regime [96] ($2t \gtrsim \omega_c + \Gamma_2$ as in figure

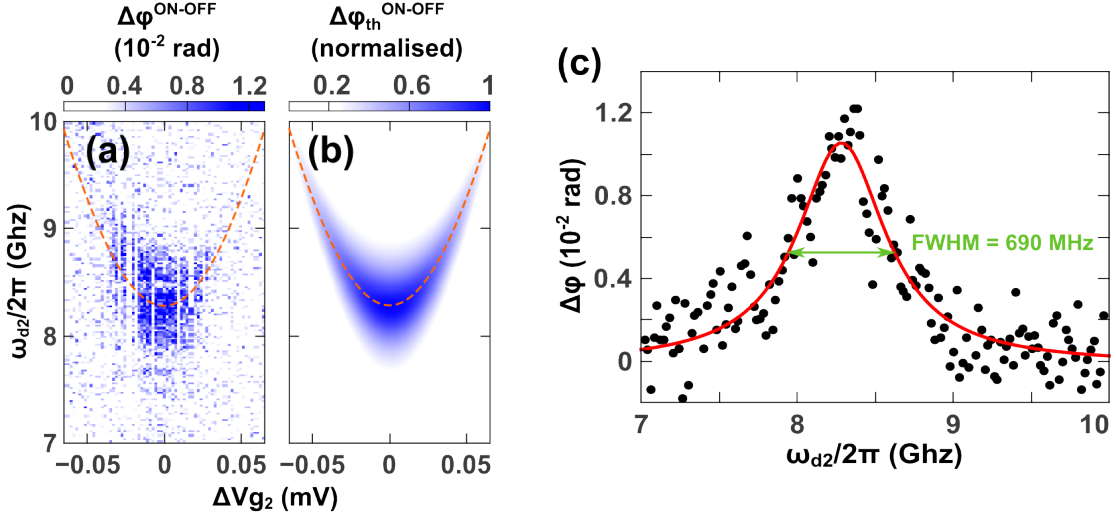


FIGURE 5.11: Two tone spectroscopy. (a) Cavity phase measurement as a function of the double dot detuning and the second tone frequency f_{d2} . Orange dashed line is the expected dispersion relation of the charge qubit. (b) Corresponding simulation using formula 4.40. The phase contrast has been normalized to the maximum. (c) Vertical profile of the two tone spectroscopy measurement at zero detuning (black circles). The lorentzian fit in red solid line gives a full width at half maximum (FWHM) of 690MHz which is a direct measurement of $\Gamma_2 = \gamma/2 + \Gamma_\phi \approx 345\text{MHz}$.

5.8(a)). One can bring f_{d2} in resonance with the bonding/antibonding doublet energy Ω . For every point of the measurement, we acquire the phase response $\Delta\varphi$ both with the second tone *ON* and *OFF* and then subtract the *OFF* part to obtain $\Delta\varphi^{\text{ON-OFF}}$. This operation has the advantage of removing the contribution from the ground state susceptibility and from some spurious qubit-independent signal. The resulting phase contrast is presented in figure 5.11(a). We observe a spot in the detuning-second tone frequency plane around 8GHz which is spreading around the zero detuning point. This spot follows roughly the dispersion of the charge qubit, as highlighted by the dashed lines corresponding to the expected doublet frequency $\Omega(\epsilon)$. Figure 5.11(b) displays the result of the simulation according to formula 4.40, in good agreement with the experimental map.

As one can see from formula 4.40, such a measurement allows us to directly access $\Gamma_2 = \gamma/2 + \Gamma_\phi$ (which appears naturally in $\Im m[\chi](\omega_d = \omega_{d2})$) when the drive amplitude is sufficiently low ($\Im m[\chi](\omega_d = \omega_{d2})n_{\text{drive}}/\gamma \ll 1$). We have checked that we were indeed in this regime for the measurements presented here. A trace of the measurement at zero detuning is presented in figure 5.11(c). We observe a resonance centred around $\approx 8\text{GHz}$ with an amplitude of about $1.2 \times 10^{-2}\text{rad}$, large compared to the total signal (about 60%). The surprisingly large amplitude could arise from the contribution of other transitions to the total susceptibility χ (see [128] and section 6.1). We can still fit the data with the Lorentzian line shape shown in red line. The full width at half maximum (FWHM) of about 690MHz allows us to get $\Gamma_2 \approx 345\text{MHz}$, which is a bit lower than

with the previous estimate of $450MHz$ extracted from 5.8(c) (same gate region). The latter fact is consistent with the $1/2t$ scaling law predicted by the simple dephasing model (see next section), since $2t = 8.28GHz$ is slightly higher here than in the previous sections ($2t = 5.5GHz$ in figure 5.8(c), slightly different gate set).

Eventually, such a microwave spectroscopy provides a direct and *absolute* measurement of the inter-dot tunnel coupling t : in contrast to the fits shown in figure 5.8 which resolutely rely on the gates lever arms, the present measurement scale is directly given by a commercially calibrated RF source. Indeed the lever arms necessary to convert gate voltage into energy are extracted from stability diagrams, obtained with DC current measurement at finite bias which are not always complete, or as regular as one could expect. The microwave spectroscopy also provides an independent measurement of the dephasing time of the charge qubit $\Gamma_2 = 1/T_2^*$, also more reliable than the susceptibility fits of figure 5.8.

5.4 Decoherence and charge noise

The amount of charge noise in a solid state environment is very important for future development of devices exploiting other degrees of freedom like spin or valley in carbon nanotubes. It is a priori the limiting factor for dephasing time of spin qubits in the absence of nuclear spins. The direct measurement of $\Gamma_2 = \gamma/2 + \Gamma_\phi$ in the previous section, as well as the estimates made for γ allow us to determine $\Gamma_\phi \approx 300MHz$ for the presented regions where $V_{gt} = -242mV$ (figures 5.6, 5.8(c), 5.9, 5.10 and 5.11)⁴. This value of dephasing rate Γ_ϕ is almost an order of magnitude lower than those reported in ref [31] and [32]. We now make the assumption that charge noise is the dominating mechanism for dephasing in order to give an upper bound of the typical charge noise in our device. Indeed, the magnitude of the dephasing rate Γ_ϕ is likely to be due to $1/f$ charge noise in the environment of the CNT. Using a simple semi-classical model for dephasing at second order in the charge fluctuation [129, 130], we can make a link between the extracted Γ_ϕ 's and the power spectral density of charge noise. At zero detuning, the system is insensitive to charge noise at first order; assuming that the power spectral density is of the form $\langle\sigma_\epsilon\rangle^2/f$:

$$\Gamma_\phi \approx \frac{d^2\Omega}{d\epsilon^2} \langle\sigma_\epsilon\rangle^2 \approx \frac{\langle\sigma_\epsilon\rangle^2}{2t} \quad (5.1)$$

Using $2t = 5.5GHz$ we get typically $\langle\sigma_\epsilon\rangle = 5\mu eV$ when $V_{gt} = -242mV$. With a typical charging energy of $10meV$ in the device, one can convert $\langle\sigma_\epsilon\rangle$ into a charge noise of

⁴ $\Gamma_\phi \longrightarrow 3GHz$ in other regions such as 5.8(b)

$5 \times 10^{-4} e/\sqrt{Hz}$ at 1Hz. Generally, this allows us to give an upper bound for the charge noise in our device of $5 - 15 \times 10^{-4} e/\sqrt{Hz}$ at 1Hz, depending on gate settings. This value compares favourably to other systems (record value^[56] reported in GaAs two dimensional electron gas: $2 \times 10^{-4} e/\sqrt{Hz}$) and is an important figure of merit for future carbon nanotube based quantum information devices [14, 75]. Our CNT device thus turns out to be a very quiet hybrid DQD-cavity system, an order of magnitude better than those reported in ref [31] and [32].

Chapter 6

Possible spin-photon coupling in a cQED architecture

6.1	Equation of motion for the Ferromagnetic spin qubit	95
6.1.1	Multilevel equation of motion	96
6.1.2	Experimentally possible regimes and associated cavity response	97
6.2	Ferromagnetic interfaces	100
6.2.1	Magnetic Force Microscope (MFM) characterisation	100
6.2.2	Double quantum spin valve	100
6.3	Superconducting resonator measurement with external magnetic field	103
6.4	Magnetic field dependence of the dispersive shift	103
6.5	Microwave spectroscopy	107
6.6	Discussion and perspectives	109

In a *solid-state* context, the electronic spin quantum degree of freedom is naturally much more isolated from its environment than the electronic charge, and is thus a good candidate for quantum information. The counter part of this weak coupling to the environment is the equivalently weak coupling of a single electronic spin to the electromagnetic field of a cavity, which is about 10Hz ¹ in the standard CPW geometries. This central point is what makes cQED experiments with spins much more challenging than with charges. To couple to a single spin, one must therefore find tricks to increase the effective spin-photon coupling by *converting* the charge-electric field coupling to an effective spin-electric field coupling, while keeping the quantum states protected. In a nuclear spin free host material, one can expect to reach spin dephasing times of the order of $1\mu\text{s}$ [14, 58]. Reaching the strong coupling regime would then require $g_{\text{spin}} > \text{MHz}$, more than five orders of magnitude larger than the natural spin-magnetic field coupling. Although very challenging, such an achievement would allow to use of the readily available cQED techniques for spin qubits (manipulation and QND readout [20, 131], amplification [21, 132], quantum feedback [22, 23], scalability [97], etc) and would allow to tackle fundamental problems such as distant spin coupling [106–109] or quantum simulation on spin chains.

To achieve a large coupling constant g_S , proposals rely on the naturally large charge-photon coupling and find a way couple to spin either with intrinsic properties such as Overhauser fields [107, 109]², spin-orbit [32, 106] or extrinsically engineered coupling such as spin-charge entanglement [108] or artificial spin-orbit [14]. This chapter presents preliminary results on the realisation of the later proposal (discussed in section 2.4) which exploits effective magnetic fields induced by interface exchange fields from ferromagnetic electrodes. The first section gives elements of the possible response of such a system in different regimes. Section 6.2 goes into MFM and magneto-resistance measurements demonstrating that we have active ferromagnetic interfaces. Sections 6.3 to 6.5 present measurements and potential signatures of spin-photon coupling in our system through microwave response, and the last section of this chapter discusses issues and perspectives.

6.1 Equation of motion for the Ferromagnetic spin qubit

Lifting the spin degeneracy of a DQD bonding and anti-bonding charge states yields four states that can be coupled to the cavity harmonic oscillator through six transitions

¹The natural coupling term is $g_S \sim g_{\text{Lande}}\mu_B B_{\text{res}}/2 \approx 10\text{GHz}/T$. B_{res} is the magnetic field associated to one photon trapped in the cavity, $B_{\text{res}} \sim \mu_0 I_{\text{RMS}}/(2\pi d)$ with μ_0 the permeability, $I_{\text{RMS}} = V_{\text{RMS}}/50\Omega$ the root mean square current and d the distance between the spin and the transmission line. With $d = 10\mu\text{m}$, $B_{\text{res}} \approx 10^{-8}\text{T}$ hence $g_{\text{spin}} \approx 10\text{Hz}$ which is roughly consistent with [44].

²Gradient of magnetic field due to nuclear spins

and their susceptibilities. In this section we investigate the cavity response of a coupled multilevel³ spectrum, followed the expected response of the ferromagnetic spin qubit in different regimes.

6.1.1 Multilevel equation of motion

We calculate here the dispersive shift of a cavity coupled to a generic multilevel system using the formalism of section 4.3 ([122]). The Hamiltonian of the coupled cavity-multilevel system writes:

$$\begin{aligned} \mathcal{H} = & \hbar\omega_c a^\dagger a + \sum_n E_n |n\rangle\langle n| + \hbar \sum_{\substack{n,m \\ n < m}} g_{nm} (\sigma_{nm}^- a^\dagger + \sigma_{nm}^+ a) \\ & + \hbar\epsilon_{in} (e^{-i\omega_d t} a^\dagger + e^{i\omega_d t} a) + \mathcal{H}_{Bath} + \mathcal{H}_{Bath}^{coupling} \end{aligned} \quad (6.1)$$

where $|n\rangle$ is the n^{th} state with energy E_n , $\sigma_{nm}^- = |n\rangle\langle m|$ and g_{nm} is the coupling constant between the photonic mode and the transition between states n and m . The bath only accounts here for decoherence effects (e.g. no transport). In the semi-classical photonic regime, with the same decoupling and rotating wave approximation as in section 4.3, the equations of motion of $\langle a \rangle$ and $\langle \sigma_{nm}^- \rangle$ yield [133]:

$$\begin{aligned} \frac{d}{dt} \langle a \rangle &= -(\kappa/2 + i\Delta_{cd}) \langle a \rangle - i\epsilon_{in} - i \sum_{\substack{n,m \\ n < m}} g_{nm} \langle \sigma_{nm}^- \rangle \\ \frac{d}{dt} \langle \sigma_{nm}^- \rangle &= -(\Gamma_{2,nm} + i(\Omega_{nm} - \omega_d)) \langle \sigma_{nm}^- \rangle \\ &\quad + i \underbrace{\sum_{\substack{p,k \\ p < k}} g_{pk} \left(\langle [\sigma_{pk}^-, \sigma_{nm}^-] a^\dagger \rangle + \langle [\sigma_{pk}^+, \sigma_{nm}^-] a \rangle \right)}_{\mathcal{A}} \end{aligned} \quad (6.2)$$

where $\hbar\Omega_{nm} = E_n - E_m$. There are both diagonal (populations) and non-diagonal (coherences) terms in \mathcal{A} :

³more than two energy levels

$$\mathcal{A} = ig_{nm}\langle(|m\rangle\langle m| - |n\rangle\langle n|)a\rangle + i \sum_{\substack{(p,k)\neq(n,m) \\ p < k; n < m}} g_{pk}\langle(\delta_{nk}|p\rangle\langle m| - \delta_{mp}|n\rangle\langle k|)a^\dagger + (\delta_{np}|k\rangle\langle m| - \delta_{mk}|n\rangle\langle p|)a\rangle$$

Where $\delta_{ij} = 1$ if $i = j$, 0 otherwise. One can compute the EOM of the diagonal terms $|n\rangle\langle n|$ in the stationary regime, which turn out to be of the order $1 - \chi/\gamma$ in the linear regime, similarly to section 4.3.4. We therefore neglect coherences which are only of the order χ/g (experimentally, $\chi \sim 10 - 100\text{kHz}$, $g \sim 10\text{MHz}$ and $\gamma \sim 100\text{MHz}$). This approximation is besides always valid in the dispersive regime. Finally, equations 6.2 yield (in the stationary regime):

$$\langle a \rangle = \frac{-i\epsilon_{in}}{\frac{\kappa}{2} + i\Delta_{cd} + i \sum_{n < m} \frac{g_{nm}^2}{-i\Gamma_{2,nm} + \Delta_{nm,d}} (\langle \sigma_m \rangle - \langle \sigma_n \rangle)} \quad (6.3)$$

where $\Delta_{nm,d} = \Omega_{nm} - \omega_d$ and $\langle \sigma_n \rangle = |n\rangle\langle n|$ is the population of the n^{th} state. The cavity frequency shift is therefore of the form:

$$\begin{aligned} \Delta f_c &= \sum_{\substack{n,m \\ n < m}} \Re e[\chi_{nm}] \langle \sigma_{nm}^z \rangle \\ &= \sum_{\substack{n,m \\ n < m}} g_{nm}^2 \frac{\Delta_{nm,d}}{\Gamma_{2,nm}^2 + \Delta_{nm,d}^2} (\langle \sigma_m \rangle - \langle \sigma_n \rangle) \end{aligned} \quad (6.4)$$

One can also compute the analogue of equation 4.40 in the multilevel case, solving the system of equations on the populations σ_{nm}^z .

6.1.2 Experimentally possible regimes and associated cavity response

We now give details about the expected frequency shift of a cavity coupled to the ferromagnetic spin qubit as proposed in [14] (section 2.4) and for other realistic sets of parameters. As in section 2.4, we assume only one charge orbital in each dot coupled through t , an equal effective Zeeman splitting δ in both the dots, with a quantization

axis in dot 2 tilted by θ compared to that of dot 1. The coupling strength of the cavity to the transitions between the four states are given by

$$g_{nm} = \mathcal{C}_{nm} g_{charge} \quad (6.5)$$

Where the coupling constants \mathcal{C}_{nm} are the matrix elements (equation 2.8) which depend on t, δ, θ and the inter-dot detuning ϵ .

If we were in the strong coupling limit, the response of the cavity would be rather simple; f_c would not only be shifted by Δf_c but would show an anti-crossing with the strongly coupled transitions, with a splitting g_{nm} and a phase shift of $\pi/2$. Note that in this case, our semi-classical treatment would not be correct any more⁴. If there was such a transition, with $g_{nm} > \kappa, \Gamma_{2,nm}$, this a priori would be a spin transition with a frequency mainly given by the Zeeman splitting 2δ . δ must be comparable to t in order to achieve a small hybridisation with the charge (necessary for a transverse coupling to the electric field), and it must be comparable to f_c in order to have a large susceptibility with the cavity. Because we did not have a sufficient control over this parameter so far, it was not possible to reach such a regime. We therefore have to consider the dispersive response given by equation 6.4. Figure 6.1 shows the spectrum and the transition frequencies of the four states in the limit of a small exchange field compared to t (a), large exchange field (b), and the ideal case where they are comparable.

In the absence of nuclear spins, we expect dephasing to be mainly due to charge noise for all transitions [14]⁵. If we assume that relaxation is negligible compared to dephasing, one can thus calculate the $\Gamma_{2,nm}$ using the semi-classical model of section 5.4 (adding first and second order contributions). From the estimates of charge noise spectral density $\langle \sigma_\epsilon \rangle = 5\mu eV$ and charge coupling strength g_{charge} obtained in chapter 5, one can therefore compute the frequency shift Δf_c for all parameters. Figure 6.2 shows the ground state susceptibilities of a singly occupied DQD calculated with a tunnel coupling $2t = 5.5GHz$ and a cavity mode at $6.7GHz$. Figure 6.2(a) and (b) give the response in the case of a small and large exchange field respectively. There is no qualitative difference between the two total susceptibilities as they correspond to transitions between charge doublets with almost independent spin populations⁶. Although there would be strong qualitative differences in the susceptibility if we could reach $2\delta \approx 2t \approx f_c$, it is still

⁴although it does reproduce an anti-crossing in the strong coupling limit, but in the classical regime for the cavity (large number of photons)

⁵This yields pure spin transitions to have unreasonably low dephasing rates, but these are then not coupled to the cavity and do not contribute to the total susceptibility

⁶though in the case of the right panel, it is a spin-orbit-like transition, but with a very small spin component when $\theta = \pi/6$. This would be a better spin-orbit qubit in some anti-parallel configuration, e.g. $\theta = \pi + \pi/6$

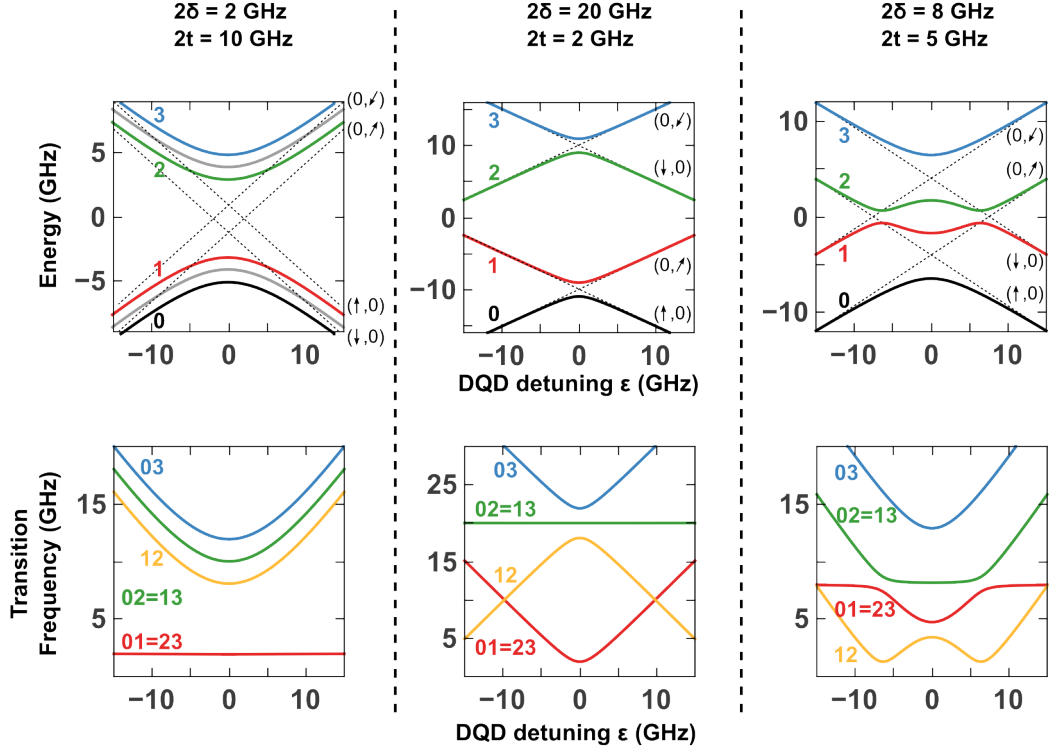


FIGURE 6.1: Spectrum and transition frequencies of a singly occupied double quantum dot with homogeneous exchange field δ with a tilt $\theta = \pi/6$ between the two dots. (a), (b) and (c) show three different limit for tunnel coupling t and exchange field δ . Spin-charge hybridisation, required for transverse spin-photon coupling, only appears when $t \sim \delta$ as in (c).

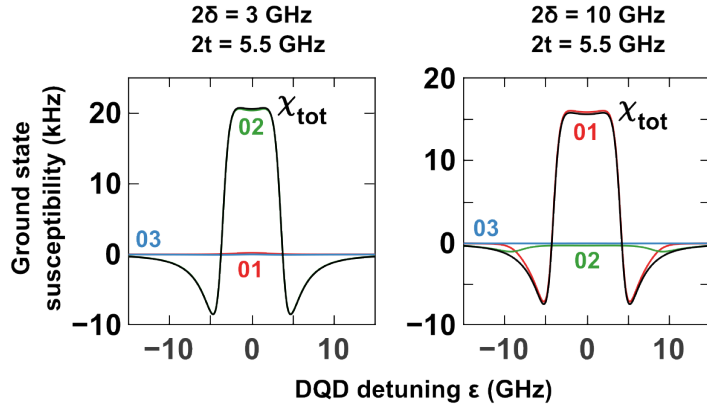


FIGURE 6.2: Computed susceptibilities of the ground state with $\theta = \pi/6$, a charge noise $\langle \sigma_\epsilon \rangle = 5\mu eV$, a coupling strength $g_{charge} = 5MHz$ and a cavity mode at $6.7GHz$.

impossible to discriminate between small and large exchange field here. In order to try to do so, we can apply an external magnetic field or perform the microwave spectroscopy of the device, as we discuss in sections 6.4 and 6.5.

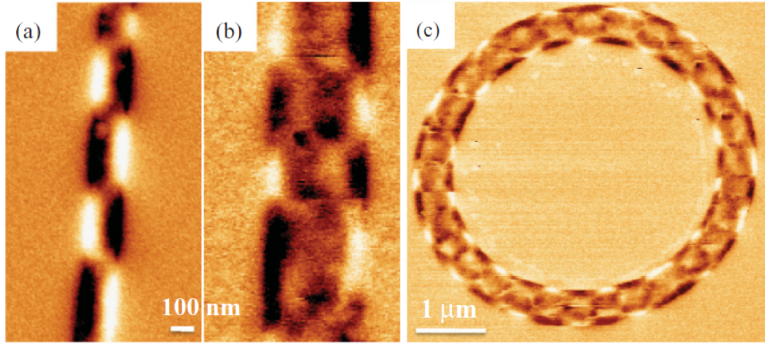


FIGURE 6.3: MFM images of several PdNi nanostructures with 30nm thickness. (a) 150nm -wide and (b) 450nm -wide nanostrip. (c) nanoring with 500nm width and $5\mu\text{m}$ diameter. Source: [134]

6.2 Ferromagnetic interfaces

6.2.1 Magnetic Force Microscope (MFM) characterisation

Our architecture requires non collinear ferromagnetic electrodes to obtain the effective magnetic fields necessary for coherent spin manipulation [57, 72]. The first step is therefore the systematic control over the orientation of a ferromagnet compatible with connection to carbon nanotubes. PdNi alloy can form good contacts with CNT's [13, 82] and thin films magnetization direction can be systematically controlled by the shape of the electrode [82]. Indeed Chauleau et al. ([134]) showed that for thin PdNi⁷ layer (30nm), electrodes narrower than 500nm systematically present a transverse magnetisation, see figure 6.3(b and c). The alternating dark and light regions of these MFM images show magnetic charges demonstrating a magnetisation perpendicular to the axis of the electrode. For 150nm wide electrodes (figure 6.3(a)), the strip presents clear magnetic domains with orientation orthogonal to the longitudinal direction that minimizes the magnetostatic energy. Taking advantage of this knowledge, we can therefore define the magnetization direction of our electrodes at the lithography fabrication step (chapter 3). Figure 6.4 shows a topography (AFM) and stray field map (MFM) of a CNT-based double quantum dot connected to non collinear PdNi, similarly to figure 5.4(c). In this case the ferromagnets were tilted with an angle $\theta = \pi/6$ with respect to each other.

6.2.2 Double quantum spin valve

The first thing one can do to characterise *in-situ* the magnetic interfaces of a device such as presented in figure 6.4 is a low temperature tunnelling magneto-resistance (TMR) measurement as a function of external magnetic field [135]. One can forget the double

⁷ $Pd_{1x}Ni_x$ with $x \approx 0.7$

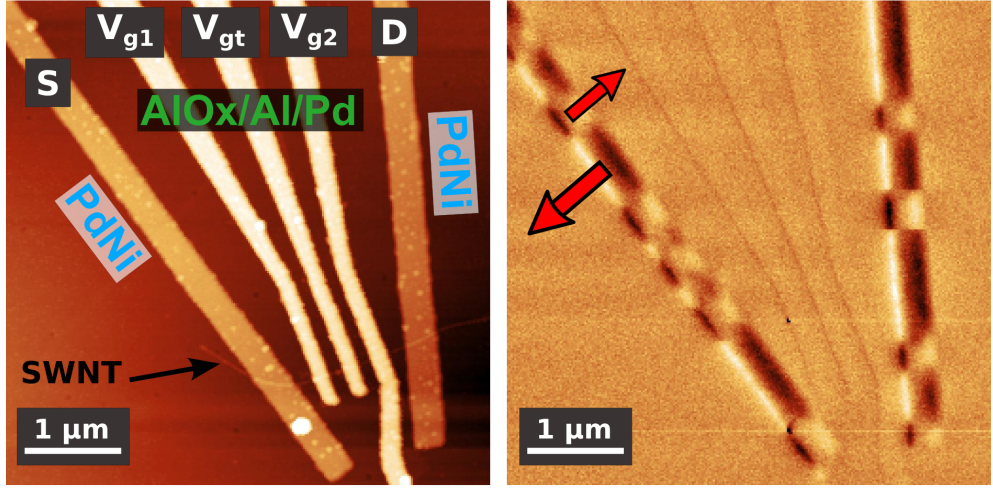


FIGURE 6.4: (a) AFM and (b) MFM image of a CNT-based double quantum dot device connected to three top gates(AlOx/Al/Pd) and two non collinear PdNi electrodes (30nm thick, 250nm wide, covered with 4nm of Pd). It is the same device as in figure 5.4.

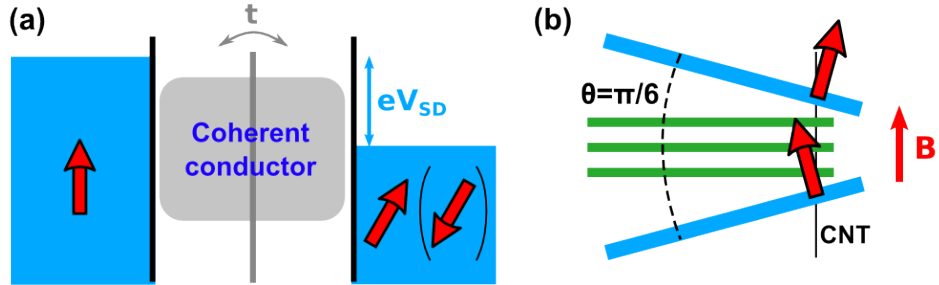


FIGURE 6.5: (a) Principle of the spin valve measurement. One can measure DC current flowing through the device at finite bias V_{SD} as a function of the external magnetic field B . When sweeping B past the coercive fields of the electrodes, their magnetization reverse causing a change in the conductance of the device. (b) Scheme of the experimental situation.

quantum dot picture for a moment and think of the device as a coherent conductor connected to two ferromagnets; it constitutes a molecular spin valve (figure 6.5(a)). Applying an external field B larger than the coercive fields of the electrodes, we can flip their magnetisations and thus investigate the transport dependence on the magnetisation direction. Carbon nanotube quantum dot spin valves have been already investigated experimentally with collinear magnetizations (e.g. [9, 10, 13, 82]). They show normal positive TMR as well as negative TMR, due to spin-dependent transport [13], spin-orbit interaction or quantum interferences [2]. The case of non-collinear ferromagnets has also been studied theoretically [83, 136], and recently experimentally [137].

Figure 6.6 shows measurements of the DC current I , at finite bias, as a function of the external magnetic field B . The magnetic field is applied approximately along the CNT axis, that is at the bisection between the two magnetizations (see figure 6.5(b)). We

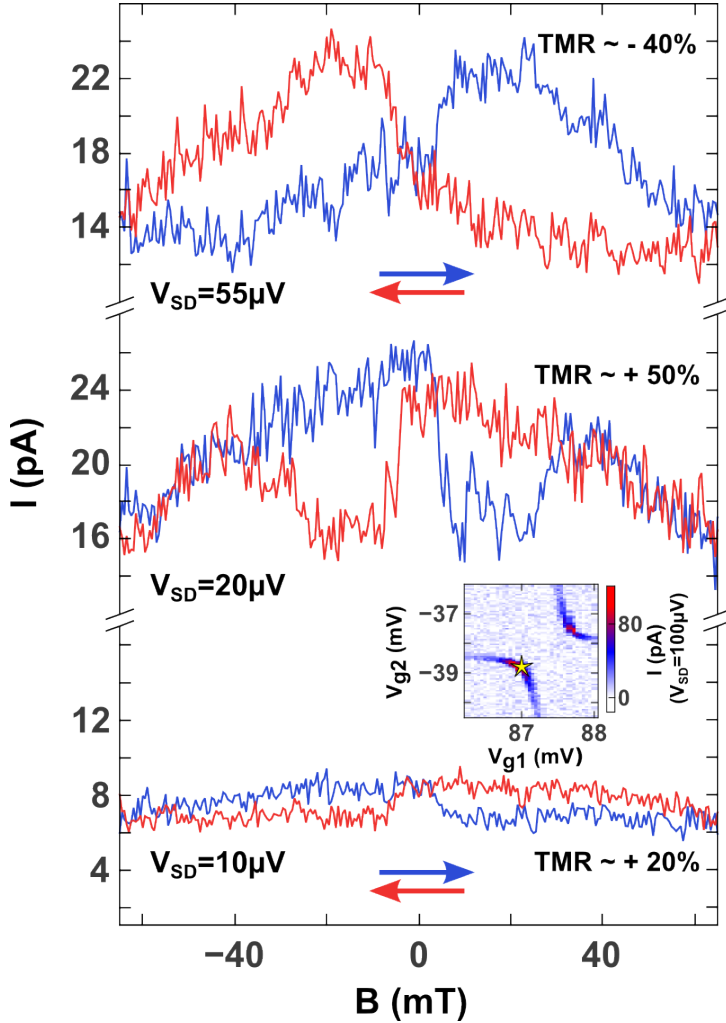


FIGURE 6.6: Current hysteresis and TMR as a function of bias V_{SD} . Inset: gate voltage map showing the point where data is taken. *Sample: SQBRES35R*

define the TMR as

$$TMR = \frac{R_{AP} - R_P}{R_P} = \frac{G_P - G_{AP}}{G_{AP}} \quad (6.6)$$

where $R_{P(AP)}$ and $G_{P(AP)}$ are the resistance and conductance of the device in the parallel (anti-parallel) configuration. Parallel and anti-parallel are defined as the configurations where the angle θ between the magnetizations is $\pm\pi/6$ and $\pi \pm \pi/6$ respectively⁸. Depending on bias voltage, we obtain a very different TMR, with both signs, and amplitude up to 50%. The TMR is also found to be very dependent on gate voltages. Local variations on $V_{g1(2)}$ (changes of left-right localisation), as well variations on the inter-dot tunnel coupling t (whole different gate set) show similar variations as those presented in figure 6.6.

⁸or for large fields, $\theta = 0$, parallel configuration

Although we did not perform a full systematic transport study of this behaviour, we suspect that these effects arise from strong interactions in the system. The double quantum dot nature of the device, or the non-collinear configuration of the magnetizations could also be partly responsible for such effects. Indeed, one can anticipate that as the inter-dot tunnel coupling t gets weaker, transport through the dots starts to involve tunnelling events which might depend on selection rules, similarly to Pauli spin blockade.

The essential point here is the manifestation of spin-dependent electronic DC transport. This is the signature of active ferromagnetic interfaces coupled to the orbitals of the DQD, which should thus yield interface exchange fields [9, 13].

6.3 Superconducting resonator measurement with external magnetic field

In order to correctly measure the cavity frequency shift Δf_c , we first have to account for the spurious dependence of our detector, that is a superconducting CPW resonator, on the external B field. Both the resonant frequency f_c and the quality factor are strongly dependent on B . In the measurements presented in this thesis, the cavity is made out of 150nm thick aluminium, and B is applied in plane (aligned with the CPW). In practice it becomes almost impossible to do measurements at fields larger than 20mT, as Q rapidly drops at higher fields, see figure 6.7. Probably because of the *Fano*-shaped transmission (see sections 4.5 and 3.2.3), the full width at half maximum of $|S_{21}|$ and the phase slope at resonance ($-\frac{d}{df} \arg(S_{21}(f))$) do not have the same dependence as a function of B , see figure 6.7. We therefore have to evaluate them separately in order to extract Δf_c or $\Delta A/A$ from phase and amplitude measurement. In practice, we proceed step by step. B is changed to a new value, f_c is determined by measuring $S_{21}(f)$, we acquire the data (e.g. phase shift) as a function of other parameters such as gate voltage, and we later on fit the cavity characteristics from the curve $S_{21}(f)$. We can then compute the correct Δf_c or $\Delta A/A$. Figure 6.7 displays the resonance frequency f_c , linewidth $\kappa/2\pi$, phase slope at resonance $\frac{d\varphi}{df}(f_c)$ and Q factor evaluated as ω_c/κ . All the cavity characteristics show a significant hysteresis, with non-monotonous behaviour, and different trends.

6.4 Magnetic field dependence of the dispersive shift

As DC transport is spin-dependent, one can also expect to see spin signal in the dispersive shift of the cavity. The first issue is that physical hysteretic signals have to

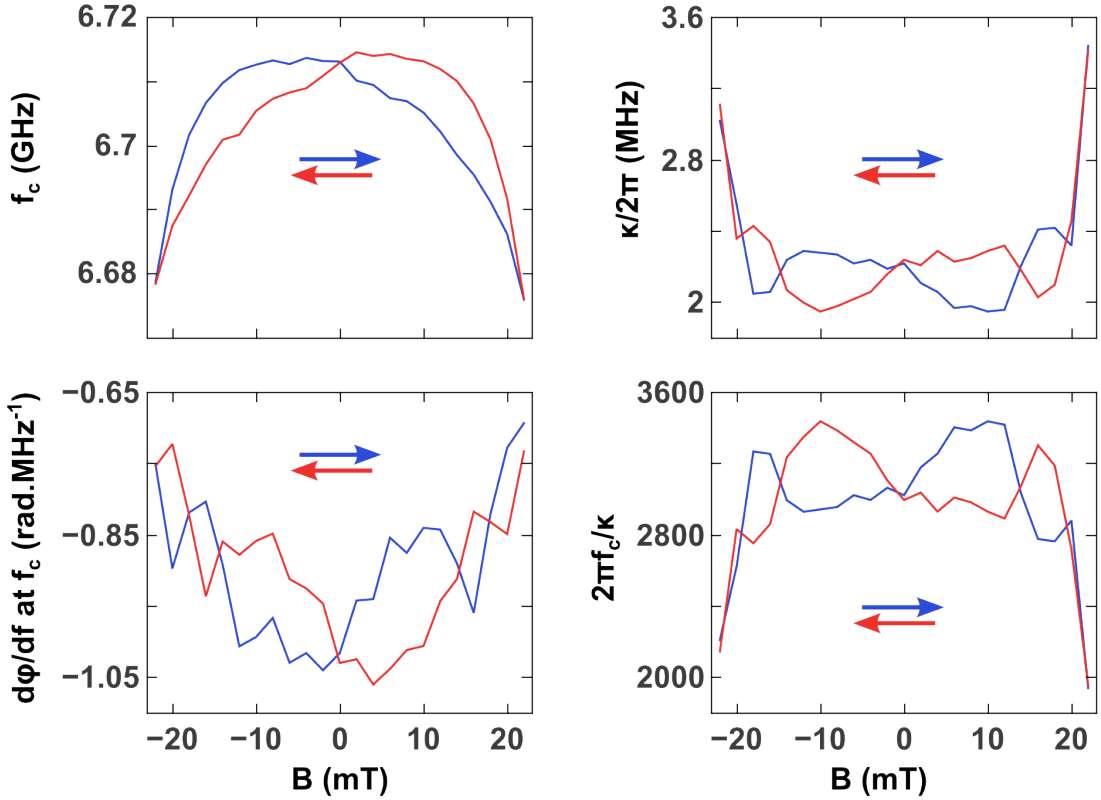


FIGURE 6.7: Superconducting aluminium CPW resonator behaviour as a function of external magnetic field B . Resonant frequency, phase and amplitude response all show different hysteretic variations.

be disentangled from the cavity spurious ones (figure 6.7). The second is that we are only able to measure a very limited range of magnetic field with our aluminium cavity. Figure 6.8 shows phase (inset) and corresponding frequency shift as a function of the external B field, at zero detuning of the double quantum dot ($\epsilon = 0$, away from the triple points). In this region $2t > f_c + \Gamma_2$, so $\Delta f_c < 0$. For each value of B , we extract the zero-detuning position by acquiring a full trace of $\Delta\varphi$ in gate voltage (V_{g2}). This ensures avoiding slow dispersion of the $\epsilon = 0$ point as a function of B .

We can expect Δf_c to vary for three interesting reasons. The first is that magnetizations can rotate with respect to each other, yielding a change in the spin coupling matrix element. Indeed, when this angle θ goes to zero, there cannot be a transverse coupling to the spin, g_{spin} is cancelled. The second reason is a change in a configuration of the magnetizations from parallel ($\theta = \pm\pi/6$) to anti-parallel ($\theta = \pi \pm \pi/6$). This effect can be included in the coupling matrix elements \mathcal{C}_{ij} , but it could also affect the populations of the DQD at finite detuning ϵ , and therefore change the charge quantum capacitance. This later effect is analogue to spin blockade⁹, which makes a spin to charge conversion. It was used in [32] to perform capacitive readout of spin states via spin-dependent charge

⁹although it is a different mechanism here, which only involves single occupation of the DQD.

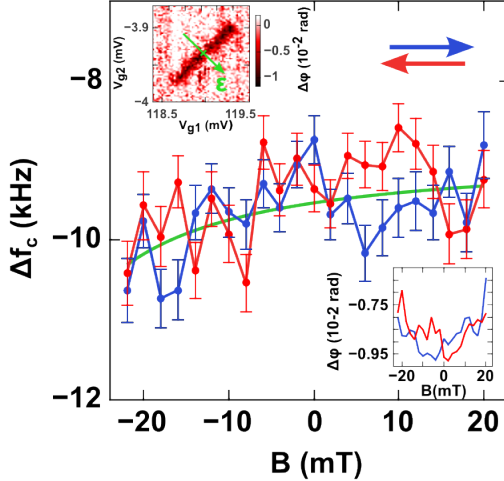


FIGURE 6.8: Measured frequency shift Δf_c at zero detuning ϵ as a function of external magnetic field and sweep direction. Solid green line: fit with theory and assumptions explained in the main text. Top-left inset: $V_{g1} - V_{g2}$ colour-scale map of the phase shift of the region, showing ϵ axis. Bottom-right inset: raw phase data as a function of external B -field.

transport due to conventional spin blockade. Last, the exchange Zeeman splitting in the dots has to be added to the contribution of the external B , yielding $\tilde{\delta} = \delta + g_{Lande}\mu_B B/2$. This causes a change in the spin susceptibility since it changes the frequency detuning between the cavity and a spin transition.

Although transitions potentially involve states that are spin and charge hybridised, and ϵ -dependant, we can conjecture the following *big picture*. A Zeeman splitting 2δ weakly detuned from f_c is likely to produce a strongly B -dependant Δf_c , as it would imply an (almost) resonant coupling to a transitions involving spin. 2δ is therefore probably much larger or much smaller than f_c in the present experiment, see figure 6.8. As soon as $\delta > k_B T$, we expect the capacitive response¹⁰ to be strongly dependent on the parallel/anti-parallel configuration of the electrodes. Figure 6.8 does not show any clear hysteresis and could be interpreted as arising from a very small exchange field δ . However, because of cavity re-scanning and long averaging, we are forced to measure very slowly (typically 10 minutes per B value), and it is likely that the electrodes relax within that time. We thus cannot ensure that we indeed measure in the anti-parallel configuration.

However there seems to be a small slope on the dependence of Δf_c for both increasing and decreasing magnetic field. This can arise from a change in the susceptibility due to the total Zeeman splitting $\tilde{\delta} = \delta + g_{Lande}\mu_B B/2$. In figure 6.9 we investigate further this dependence. Figure 6.9(a) shows again the measured frequency shift Δf_c , at zero detuning ϵ , but now in a region where $2t < f_c$. We again see a general slope with B ,

¹⁰susceptibility and/or populations

but with a different sign. The solid red line shows theory using equation 6.4 in the ground state ($\langle \sigma_0 \rangle = 1$) assuming that the angle between the electrode magnetizations is not affected by the external B field, $\theta = \pi/6$. Taking a g-factor $g_{Lande} = 3$ (see next section), g_{charge} and $2t$ extracted from the charge susceptibility measurement, and the charge noise measured in section 5.4, the only fitting parameter is the exchange field δ . As one can see in the inset of figure 6.9(a), there is a sharp peak the theoretical susceptibility around $40mT$. This corresponds to resonance between the cavity and a spin-orbit-like qubit in our model. More precisely, it is the transition between $|0\rangle$ and $|2\rangle$, involving fully hybridised charge states (bonding/anti-bonding, $\epsilon = 0$) and mixed spin states belonging to both the dots, with both $|\uparrow\rangle$ and $|\downarrow\rangle$ components ($|\nearrow\rangle$ and $|\swarrow\rangle$ in the right dot). Such a slope can be obtained on both sides of the resonance. Because we do not have the resolution to distinguish the curvature of the B -dependence, we can only fit the global slope and therefore only fit $f_c - 2\delta$. We estimate the Zeeman exchange field to be $2\delta \approx 9.7GHz/3.5GHz$ (i.e. $2\delta - f_c \approx +3GHz/-3.2GHz$) for the data given in figure 6.9. The sign of the slope indicates that the exchange field is in the opposite direction of the external magnetic field. We can get a similar estimate from the data presented in figure 6.8 (solid green line), which gives $2\delta \approx 10.5GHz/2.9GHz$ ($2\delta - f_c \approx \pm 3.8GHz$), now in the same direction as the magnetic field direction. These two regions correspond to two significantly different gate sets (in particular, $V_{gt} = 0$ in figure 6.8 and $V_{gt} = -242mV$ in figure 6.9). Note that a relative error on the determination of g_{Lande} yields the same relative error on our estimate of $f_c - 2\delta$. Figure 6.9(b) shows the full detuning map of the cavity frequency shift as a function of the magnetic field. There no qualitative change in this range of magnetic field, and the frequency shift only shows a measurable variation close to zero detuning ϵ . Using the estimate of $2\delta \approx 9.7GHz$, we can plot the theoretical frequency shift at all detuning on a larger range of magnetic field, see figure 6.9(c). This confirms no sensitive change of Δf_c away from zero detuning in our accessible range of B , and again shows the spin-orbit-like resonance at $B \approx 40mT$. The other possible value of $2\delta \approx 3.5GHz$ changes the position of the resonance to $\approx -40mT$ with essentially the same behaviour. We thus would have needed a cavity with a *critical field* at least twice as high as we have here in order to tune the spin-orbit (or spin) Larmor frequency $2\tilde{\delta} = 2\delta + g_{Lande}\mu_B B$ with our cavity at $6.7GHz$.

6.5 Microwave spectroscopy

A powerful way to investigate the fine level structure of the double quantum dot is to do its microwave spectroscopy, as shown already in section 5.3. Figure 6.10 shows such a measurement. As in figure 5.11, we present the phase shift of the cavity as a function

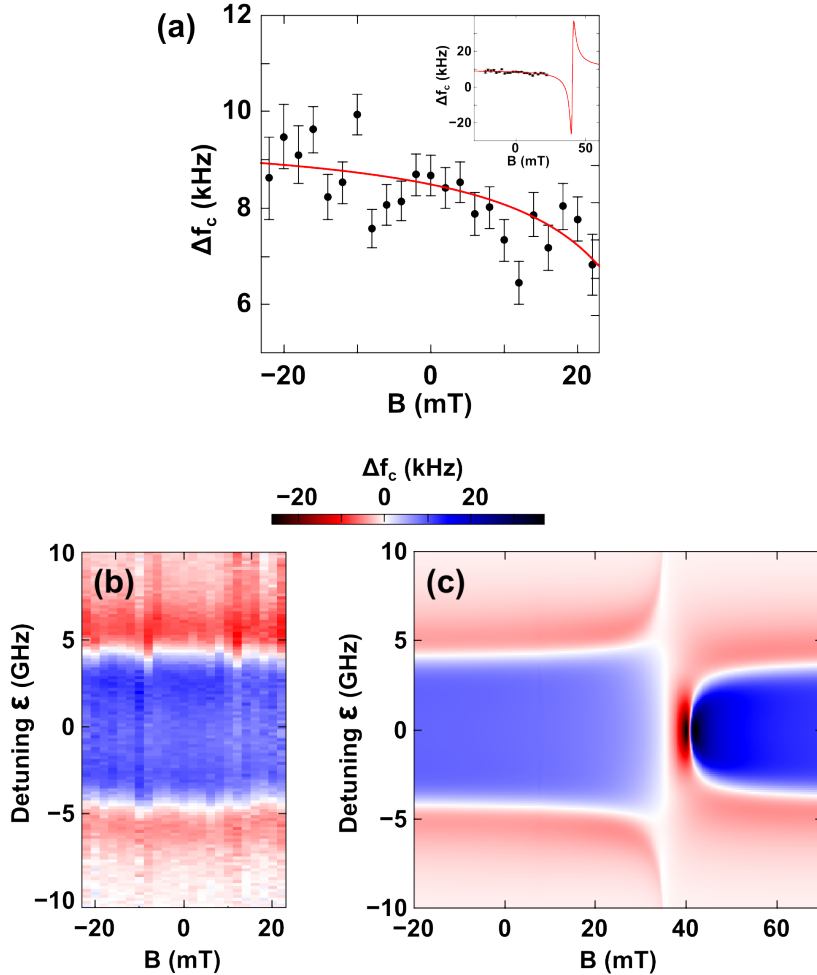


FIGURE 6.9: (a) Frequency shift Δf_c at $\epsilon = 0$ as a function of external magnetic field. Black dots is the measured data and solid red line is theory using an exchange field $2\delta = 9.7\text{GHz}$. Inset: Same data and theory displayed over a large range of magnetic field, showing a spin-orbit resonance around 40mT . (b) Full colour-scale map of the measured Δf_c as function of magnetic field B and detuning ϵ . (c) Theory plotted over a larger range of magnetic field, again showing the spin-orbit resonance around 40mT .

of second tone frequency and inter-dot gate detuning. Again, we measure both with the second tone *ON* and *OFF* and then subtract the *OFF* part in order to remove the contribution from the ground state susceptibility. We perform this measurement at zero external magnetic field, in a non-resonant region, where $2t > f_c$ in order to be mainly dispersive for all the gate range. The positive (blue) phase shift around 7GHz corresponds to the charge qubit expected from the susceptibility measurement in this region, and strongly recalls the measurement showed in figure 5.11. It shows a clear dispersion as a function of ΔV_{g2} , roughly with a hyperbola shape.

As shown in figure 6.10(b) the remarkable difference with the charge qubit spectroscopy of figure 5.11 is the appearance of other peaks, including peaks with a negative sign.

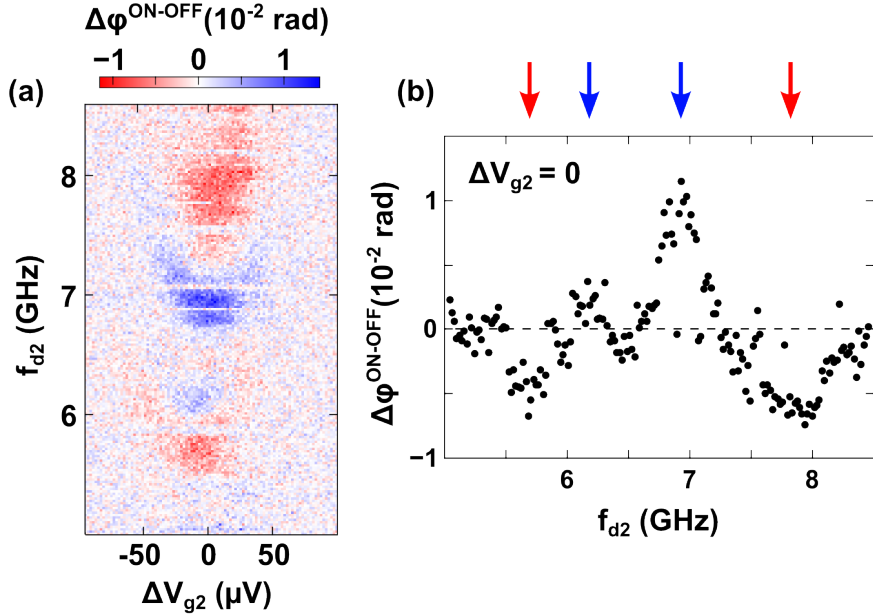


FIGURE 6.10: Zero magnetic field microwave (two tone) spectroscopy. (a) Colour-scale map of the cavity phase measurement as a function of the double dot detuning and the second tone frequency f_{d2} . (b) Vertical profile of the two tone spectroscopy measurement at zero detuning, showing both positive and negative phase shift

These peaks do not appear neither at lower frequencies nor at higher frequencies (measured up to 16GHz). Moreover the negative signal around 5.7GHz for $\Delta V_{g2} = 0$ does exhibit a dispersion as a function of detuning (lower red spot in figure 6.10(a)) and therefore must be related to a physical signal from the DQD spectrum. Here, a negative sign means that the phase shift measured with the spectroscopic tone *ON* is larger (more negative in this case) than the shift measured at thermal equilibrium. This cannot be explained with a two level formula such as in equation 4.40 ($-1 < \langle \sigma_z \rangle < 1 \Rightarrow -\Re[\chi] < \Delta f_c < \Re[\chi]$) and is the signature of a coupling to other transitions with other susceptibilities (see equation 6.4). There can be pumping effects, so that excited levels (e.g. $|1\rangle$) get populated and *turn on* other susceptibilities (e.g. χ_{12} and χ_{13}) which did not contribute without driving ($\langle \sigma_0 \rangle \approx 1 \Rightarrow \Delta f_c \approx -\Re[\chi_{01} + \chi_{02} + \chi_{03}]$). In this case the negative phase shift $\Delta\varphi^{\text{ON-OFF}}$ that we observe can be due to a larger excited state susceptibility $\sum_j \chi_{1j}$ than the ground state one. However frequency detuning between the transitions and the cavity can play a role, and simple addition of negative and positive susceptibilities can lead to a sign change as soon as some excited states get populated.

The fine level structure of a CNT-based double quantum dot can arise from the coupling of many degrees of freedom. Although these appear usually at higher energy scales, we should still consider states coming from valley and intrinsic spin-orbit coupling in the dots [6, 54, 75, 138] or coupling to phonons [61, 139]. One way to probe the nature of the states involved in the susceptibilities probed in figure 6.10 is to look at their

variation with the external magnetic field as in figure 6.11. Figure 6.11(a) and (b) show measurements of the gate dispersion at two different external B field. There is a qualitative difference between the spectroscopy at $-16mT$ and $+16mT$. The positive peak around $7GHz$ is almost unchanged, but other positive and negative peaks appear at $+16mT$ in figure 6.11(b). We can follow these changing peaks on the traces given in figure 6.11(c), which are taken at zero inter-dot detuning. We mainly identify two dispersing peaks which seem to follow a linear B dependence with an opposite slope of $\approx \pm 43GHz/T$ in this range of field. This corresponds to a Lande g-factor of about 3. These states could for example be Kramers doublets¹¹, and are not necessarily spin states caused by the exchange fields of the ferromagnetic electrodes. However we demonstrate here that exist some transitions between states of the double quantum dot, that are dependant on the external B field, and coupled to the cavity.

6.6 Discussion and perspectives

We can compare the estimate of our exchange field to what has already been measured in other experiments where CNT's were connected to ferromagnetic contacts. Reference [13] reports an estimated exchange field of $2.2T$ (i.e. $30GHz$ with $g_{Lande} = 2$) and reference [9] reports $0.6 - 1.1T$ (i.e. $8 - 15GHz$ with $g_{Lande} = 2$). These values are larger than our estimate (either $\delta \approx 1.5GHz$ or $\delta \approx 5GHz$) but come from experiments with much larger coupling to the leads. We can assume two contributions to the interface exchange field. The first effect can arise, at finite coupling to the lead Γ_{lead} , from the hybridisation of the electronic wavefunction in the dot with the first atomic layers of the contact. This effect will strongly depend on Γ_{lead} and since internal fields of ferromagnets can be large, we can expect very large fields for very transparent contacts, see figure 6.12(a). The second effect can simply arise from a spin-dependent confinement. One can imagine a very opaque tunnel barrier, with a reflection coefficient close to 1, but with a spin dependent phase, $r \sim e^{i\Delta\varphi_\sigma}$. This naturally yields a spin polarized spectrum in the dot and can survive even in the limit $\Gamma \rightarrow 0$, see figure 6.12(b). In the experiments reported in [13] and [9], coupling to the lead Γ_{lead} are much larger ($\sim 1meV$) than in our experiment ($\sim 1 - 10\mu eV$, see section 5.2.1), and this can explain the different exchange field values we obtain.

We can estimate the coupling strength we would obtain to the spin-orbit qubit appearing in the theoretical simulation of figure 6.9. Using the charge coupling strength in this region and the coupling matrix element $C_{02} \approx 0.5$ for the actual parameters, we obtain $g_{spin-orbit} \approx 1.7MHz$, for a dephasing rate estimated about $50MHz$. This is still far

¹¹Valley states coupled via spin-orbit interaction

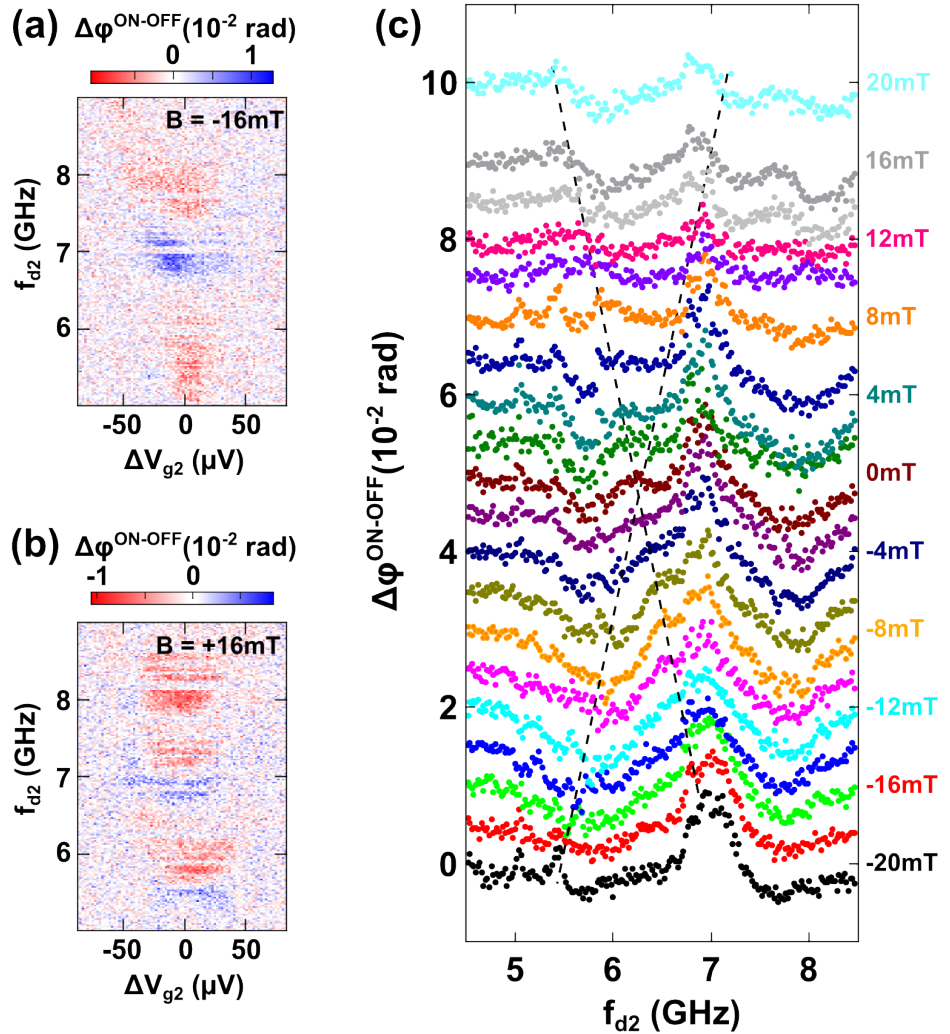


FIGURE 6.11: (a) and (b) Microwave spectroscopy as a function of inter-dot gate detuning at $B = -16\text{mT}$ and $+16\text{mT}$ respectively. (c) Microwave spectroscopy taken at $\epsilon = 0$ as a function of the external magnetic field B . Curves are shifted (by 0.5×10^{-2}) for clarity.

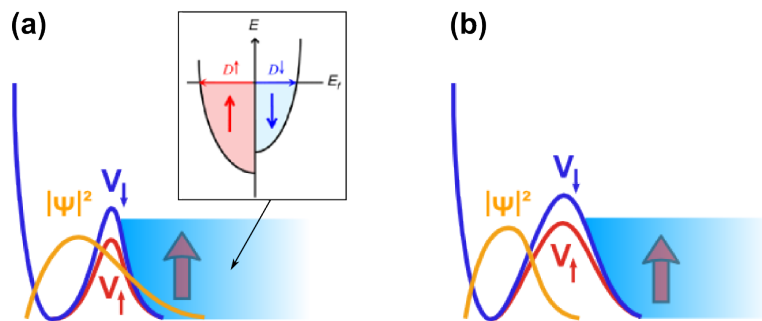


FIGURE 6.12: (a) Principle of the exchange field arising from the hybridisation of a quantum dot orbital with a ferromagnet that has a spin polarised density of state (inset). (b) Principle of the exchange field arising from a spin-dependent barrier at the interface between a quantum dot and a ferromagnet. Even at zero dot-lead coupling, there can be a finite exchange field in the quantum dot.

from the best parameter set theoretically found in [14] for a strong spin-photon coupling. In such set of parameter, we expect the coupling to the spin to be about 1/10 of the bare charge coupling strength. Although pure spin dephasing time in CNT's is unknown, we can expect it to be of the order of what has been measured in other solid-states spin-qubit hosted in nuclear spin free materials such as SiGe [58], that is about $0.1 - 1\mu s$. Assuming we can tune the device at will, we then need a bare charge coupling strength $g_{charge} > 10MHz$ and a quality factor $Q > 10^4$ to reach the strong coupling regime.

We believe we can significantly increase the coupling strength and cavity Q factor and improve the tunability of the system while keeping the same fabrication technique in a first step¹²:

- we developed a new coupling geometry in order to achieve a stronger asymmetric coupling (more selective, better shielded).
- our new geometry diminishes microwave leakage in the DC lines of the device as well as dissipation in the non superconducting parts of the device. This should enable us to work with Q factors in the range of 10^4 ($\kappa/2\pi < MHz$ meaning cavity decay time in the range of $1 - 10\mu s$).
- we are now working on reliable fabrication techniques for Nb-based cavities, which will allow us to apply larger magnetic fields while preserving the cavity resonance. We rely on the external magnetic field for a fine tuning of the exchange field δ in order to bring it into resonance with the cavity.
- we now fabricate devices with narrower PdNi electrodes in order to increase coercive fields. Together with a stronger angle θ between the electrodes, this should allow us to go to higher external magnetic fields while keeping the effective θ non zero.

¹²without using suspended ultra clean CNT's (see section 3.1.5), which would supposedly strongly increase the device tunability

Chapter 7

Conclusion and perspectives

Summary and conclusion

The present manuscript addressed the problem of coupling a single electron spin to single photons trapped in a cavity, in a solid state context. Carbon nanotubes are promising as a host material for confining electron spins as they are potentially nuclear spin free. They should therefore be able to carry long lived spin states, which is a requirement if one wants to reach a strong spin-photon coupling. We have developed new fabrication methods in order to combine high quality CVD-grown carbon nanotubes, with high finesse superconducting cavities. Our spin coupling scheme relies on a hybridisation of spin with charge, making the charge coupling mechanism at the heart of the problem. We have characterised this mechanism by looking at the charge dynamics in a double quantum dot coupled to a superconducting cavity. We have shown a resonant coupling in a rather isolated double quantum dot, which is non-trivial for carbon nanotube devices. We have determined the relevant parameters of this device by driving it out of equilibrium in a transport situation, or performing its microwave spectroscopy. We thereby demonstrate the feasibility of a CNT-based circuit QED architecture for future experiments exploiting the spin degree of freedom. To do so, our strategy is based on the use of ferromagnetic contacts to implement an artificial spin orbit for a local spin control. We demonstrate our ability to implement non-collinear ferromagnets systematically, and show via TMR measurements that these contacts form active interfaces with our CNT devices. Preliminary results seem to indicate exchange fields, or effective magnetic fields, in the microwave range, which should be tuned up in future experiments by means of an external magnetic field.

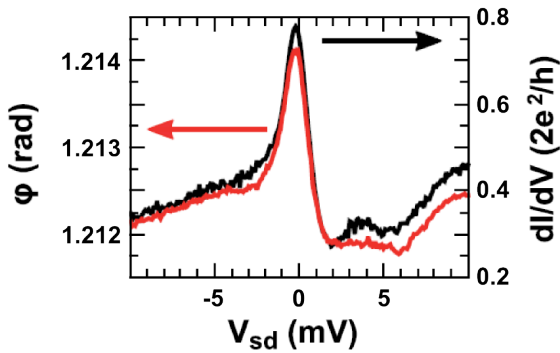


FIGURE 7.1: Measurement of the differential conductance (black) and microwave phase shift (red) as a function of quantum dot's bias V_{sd} , over a Kondo ridge in between two Coulomb peaks.

Perspectives

Further investigation of spin-photon coupling is a direct continuation of this thesis. We are currently working on technical improvements that should allow us to give a first estimation of a spin-photon coupling strength in our architecture. Further technical developments such as the implementation of ultra-clean suspended nanotubes would significantly improve the tunability of our devices, presumably as far as in other host materials such as InAs nanowires. Such a tunability would solve many issues in terms of confinement and exchange field control.

Besides, the architecture we have developed is compatible with many other hybrid experiments. Previous experiments [29] measured a finite frequency shift on a Kondo correlated quantum dot, see figure 7.1. Whether or not the charge susceptibility is zero in a Kondo dot is an open fundamental question. The answer could be related to the coupling mechanism via fermionic leads, or to the Kondo screening mechanism itself. Overall, the better control and understanding we acquired for this thesis should allow us to elucidate the problem at least partially in forthcoming experiments.

Because our setup is compatible with the connection to superconducting electrodes, it can be employed for a cooper pair beam splitter device [90]. Coupling such a device to a cavity is a way to probe the coherence of the split cooper pairs in the nanotube, by looking at the photon emission in the cavity and possibly lasing [140]. A microwave (two-tone) spectroscopy such as the one performed in this thesis could also be used to demonstrate the entanglements of the emitted pairs [141].

Finally, our setup could be used to probe exotic electronic systems. The possible existence of non-local, topologically protected Majorana fermions in nanowires has recently

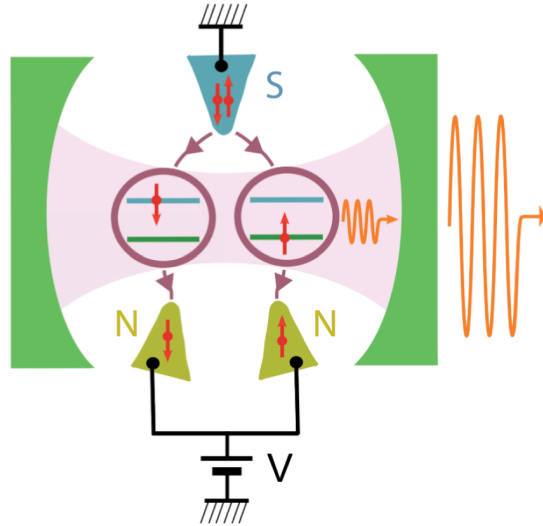


FIGURE 7.2: Scheme of a cooper pair beam splitter embedded in a microwave cavity. It is made out of a double-quantum dot coupled to a central superconducting contact (S) and two outer normal metal contacts (N) biased with a voltage V . The low energy level structure of the system allows photon emission which can be amplified through a lasing effect.

created a wide activity in mesoscopic physics [142, 143]. So far conductance measurements were performed and showed possible signatures of such zero-energy states [144, 145]. However such a probe is local and invasive. A susceptibility measurement could provide further insights on such a system, and Majorana bound states should yield resonator non-linearities that we would be able to measure with the setup developed during this thesis [146, 147]. Furthermore, by measuring charge susceptibility, we should be able to probe the exponential non-locality of the Majorana wave functions, see figure 7.3.

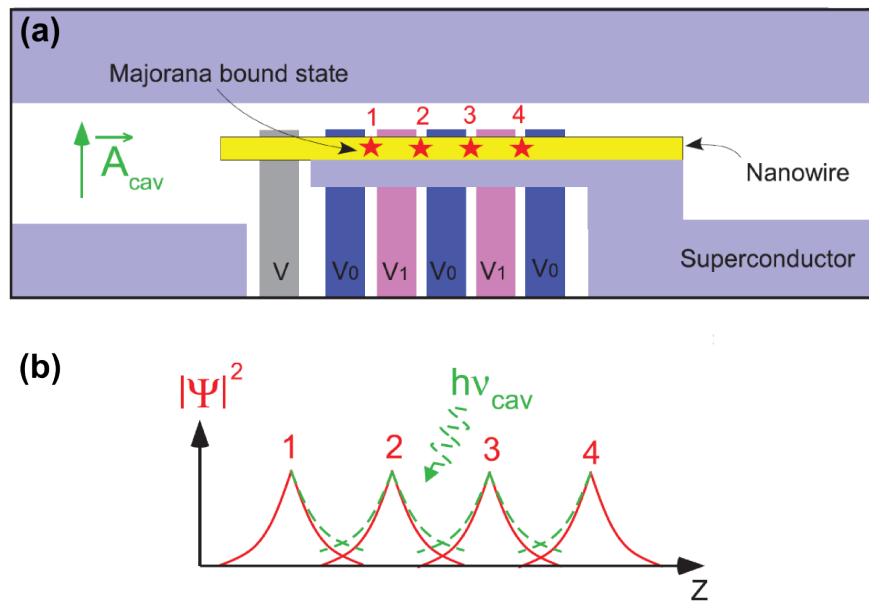


FIGURE 7.3: **(a)** Scheme of a setup with a microwave cavity (purple) coupled to a nanowire (yellow) placed between the center and ground conductors. It is tunnel contacted to a grounded superconducting contact (purple) and capacitively contacted to three gate electrodes. **(b)** In the right regime of parameters for electrochemical potentials and magnetic field, Majorana bound states can appear at the interface between topological and non-topological regions of the wire. In such a situation, capacitive coupling to a cavity can induce modulation of the overlap between the majorana wavefunctions thus changing their coupling with each other and their coupling to the cavity.

Appendix A

Nanofabrication processes

This Appendix gives details about some of the processes developed and used to fabricate our devices as explained in chapter 3. Not everything is reported but the main processes are here and can be recombined for a different goal. Some parameters are machine-dependent and should be adapted for a different tool. In the following, a is the aperture of the SEM beam; EHT is the acceleration voltage of the SEM; WF is the SEM write-field; U and V are coordinates on the SEM; US stands for ultrasonics. One layer of PMMA is baked for 15min at 165C.

Alignment mark on device (SiO_2/Si) chip

SEM lithography on single layer 550nm PMMA:

- $EHT = 20kV$, $a = 10\mu m$
- set focus, aperture alignment, etc
- Set origin and x-axis on sample's side.
- Set manually WF (1000 \times , 100 μm) on contamination dots, with a zoom at 0.96
- Save WF and column parameters
- Re-do at $a = 120\mu m$ and save parameters again
- Do litho with fine alignment mark (those within the device's 100 μm field) at $a = 10\mu m$ and the rest at $a = 120\mu m$.

Do development 2min MIBK. Do for instance 50nm gold evaporation. Do lift off.

Stamp quartz chip preparation

SEM lithograph on double layer $2 \times 550\text{nm}$ PMMA + 15nm Al:

- $EHT = 20\text{kV}$, $a = 10\mu\text{m}$
- set focus, aperture alignment, astigmatism etc
- Set origin and x-axis on sample's side.
- Set manually WF ($1000\times, 100\mu\text{m}$) on contamination dots, with a zoom at 0.96
- Do litho

Do KOH to remove covering Al layer. Do development 2min MIBK. Do (at least) 550nm Al evaporation. Do careful lift off as remaining parts of aluminium will play the role of a mask and create spurious stamps that can be an issue.

Possible cleaning step: optical lithography for protection on one layer AZ5214:

- bake $1\text{min}45\text{s}$ at 120C (solvents)
- Align and Expose : 30s exposure
- $2\text{min}30$ development

Cleaning step:

- $74\text{mL } H_3PO_4 + 2.5\text{mL } HNO_3 + 23.5\text{mL } H_2O$ (DI) at $45 - 50\text{C}$ for 10min .
- Rinse in water (DI)

Lift resist

Do RIE etching: $3 \times 20\text{min}$ with 100sccm of CHF_3 and 6sccm of O_2 at 50mTorr and 160W ($1\mu\text{m}$ quartz and 140nm Al etched per 20min). Do KOH to remove the remaining Al mask. Do catalyst deposition (after 1h US and 45min sedimentation). Do CNT growth.

Stamping and localisation

Stick stamp chips with PMMA on a glass mask. Align over the device chip (currently with UV masker). Bring to contact gently.

Localise CNT's on device's chip using SEM:

- $EHT = 2kV$, $a = 10\mu m$
- carefully set focus, aperture alignment, astigmatism, etc
- Set origin and x-axis on sample's side and do a 3-points alignment
- WF ($1000\times$, $100\mu m$) alignment on fine alignment marks (do slow scans for a precision below $50nm$)
- Take a global image of the $100\mu m$ field and zoomed images of desired CNT's

Gate electrodes and PdNi contacts

Gate SEM lithography on single layer $230nm$ PMMA:

- $EHT = 20kV$, $a = 10\mu m$
- Set focus, aperture alignment, astigmatism, etc
- Set origin and x-axis on sample's side and do a 3-points alignment
- WF ($1000\times$, $100\mu m$) alignment on fine alignment marks (do slow scans for a precision below $50nm$)
- Do litho

Do development $1min30s$ MIBK. Do evaporation:

- $2nm$ Al, leave $10min$ with $1mbar O_2$
- Repeat three times
- $50nm$ Al
- $20nm$ Pd (to avoid oxidation)

Do lift off.

PdNi contact, SEM lithography on single layer $230nm$ PMMA: same recipe. Evaporation: $30nm$ PdNi and $5nm$ Pd (to avoid oxidation). Do lift off.

Al resonator

Negative UV lithography on single layer AZ5214 ($1.4\mu m$):

- bake $1min30s$ at $120C$ (solvents).
- Align and Expose : $3s$ exposure
- Re-bake $1min45s$ at $125C$.
- Flood exposure $25s$
- Development $35s$ (control on sight).

Do $200nm$ Al evaporation. Do lift off.

Stamping CNT's one by one

The process is similar to what is given above, except lithographies of gate electrodes and contacts should be of course done before the stamping step. Once this is done, and before stamping, do holes in the device's chip at positions matching the position of the quartz pillars. In order to do so, do SEM lithography on a double layer $2 \times 550nm$ PMMA:

- $EHT = 20kV$, $a = 10\mu m$
- Set focus, aperture alignment, astigmatism, etc
- Set origin and x-axis on sample's side and do a 3-points alignment
- WF ($1000\times$, $100\mu m$) alignment on fine alignment marks (do slow scans for a precision below $50nm$)
- Do litho

Develop for $1min45s$. Do RIE etching:

- Etch SiO_2 , $\approx 15min$ with $100scm$ of CHF_3 at $50mTorr$ and $110W$ (untill saturation). Rates are $38nm/min$ for SiO_2 and $21nm/min$ for PMMA.
- Etch Si , $2min$ with $25scm$ of SF_6 at $30mTorr$ and $20W$. Rates are $200 - 250nm/min$ for Si and $45 - 50nm/min$ for PMMA.
- Remove the rest of the resist

- Do stripping O_2 for about 1min.

Total etching depth is about 1 *mum*, and can be easily more by making the second step longer since it is sufficiently selective. Can also do for instance 20s of SF_6 (30mTorr, 10W) right before stamping.

Appendix B

Dilution fridge wiring, RF setup and DC current amplification

This appendix gives estimations and explains choices we made for wiring up the dilution fridge. The last section gives an overview of the DC amplifier realised with the electronics staff.

B.1 Heat current - DC wires

The Wiedemann-Franz law states that the ratio of the electronic contribution to the thermal conductivity κ and the electrical conductivity σ of a metal is proportional to the temperature T :

$$\frac{\kappa}{\sigma} = LT, \text{ where } L \text{ is the Lorentz number, } L = \frac{\pi^2}{3} \left(\frac{k_B}{e} \right)^2 \quad (\text{B.1})$$

and the heat current flowing through a wire of section A is given by :

$$\frac{\dot{Q}}{A} = -\kappa \frac{\partial T}{\partial x} \quad (\text{B.2})$$

So that

$$\frac{d}{dt} Q = \frac{\pi^2}{3} \left(\frac{k_B}{e} \right)^2 \sigma A T \frac{\partial T}{\partial x}$$

$$\Rightarrow \frac{d}{dt}Q = \frac{\pi^2}{3} \left(\frac{k_B}{e} \right)^2 \frac{1}{R_{lin}[\text{in } \Omega/m]} \frac{\nabla(T^2)}{2} \simeq \frac{25}{R_{tot}[\text{in } \Omega]} \frac{T_{hot}^2 - T_{cold}^2}{2} [\text{in } nW]$$

The wires chosen for going from 300K to the mixing chamber are Lakeshore SS. These are supple coaxial cables and are characterised by $R_{lin}^{conductor} = 23.6 \Omega/m$ and $R_{lin}^{shield} = 3.6 \Omega/m$. The DC wires are thermalised at the 1K pot stage and the mixing chamber stage, and we assume that they are perfectly thermally anchored at these two points. Then, considering a length of 1 m until the 1K pot, and 0.5 m from 1K pot to Mix. Chamber, the heat current is:

$$\begin{aligned} \frac{d}{dt}Q_{1Kpot} &= 150 \text{ nW per wire} \Rightarrow \dot{Q}_{1Kpot}^{tot} = 1.8 \mu\text{W for 12 wires} \\ \frac{d}{dt}Q_{Mix.Ch.} &= 2.1 \text{ nW per wire} \Rightarrow \dot{Q}_{Mix.Ch.}^{tot} = 25.2 \text{ nW for 12 wires} \end{aligned}$$

B.2 Heat current - Microwave coaxial cables

B.2.1 General idea

One can integrate equation B.2 over a length l :

$$\frac{l}{A} \dot{Q} = - \int_0^l dx \kappa(x) \frac{\partial T}{\partial x} = - \int_{T1}^{T2} dT \kappa(T)$$

$\kappa(T)$ is then defined by segments between temperatures where it is known (i.e. tabulated data, see figure B.2):

$$\kappa(T) = \frac{\kappa_2 - \kappa_1}{T_2 - T_1} (T - T_1) + \kappa_1$$

$$\Rightarrow \frac{l}{A} \dot{Q} = - \frac{1}{2} (\kappa_1 + \kappa_2) (T_2 - T_1)$$

Therefore, knowing several points with different temperatures:

$$\frac{d}{dt}Q = \frac{A}{2l} \sum_i \frac{1}{2} (\kappa_i + \kappa_{i+1}) (T_i - T_{i+1}) \quad (\text{B.3})$$

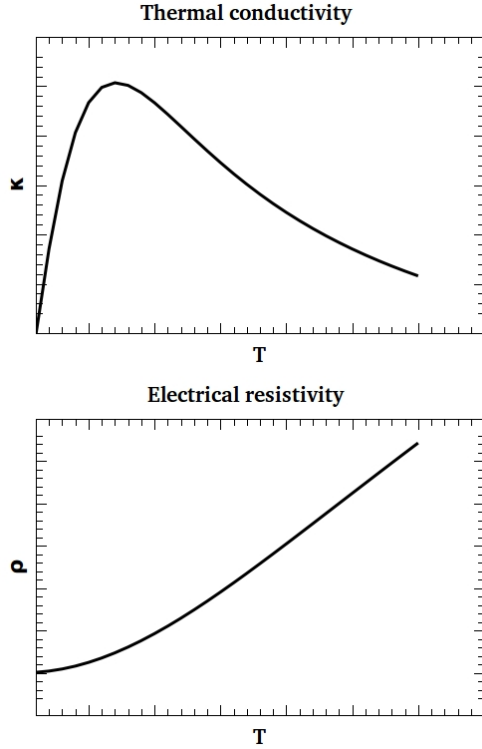


FIGURE B.1: Global form of the electrical resistivity ρ and the thermal conductivity κ in a normal metal as a function of temperature.

T (°K)	0,4	1	4	10	20	40	80	150	300
κ Cu RRR 100			630	1540	2430	1470	544	418	397
κ CuNi	0,2	0,8	1,5	3		14	20	25	30
κ SS 304	0,03	0,08	0,3	0,7		5	8	11	15
ρ Mang	0,02	0,06	0,5	2		7	13	16	22
ρ BeCu			1,9	5	11	21	36	41	9,7

FIGURE B.2: Thermal conductivity in $W.K^{-1}.m^{-1}$ of few materials for different temperatures

Note about $\kappa(T)$:

The electrical resistivity in a metal has the form $\rho_0 + \alpha T^2$ at low T and is then proportionnal to T , see figure B.1, with ρ_0 the resistance arising from impurities. Because of the Wiedemann-Franz law (B.1), the thermal conductivity shows a non monotonous behaviour (see figure B.1) with a maximum appearing at a temperature proportionnal to $\sqrt{\rho_0}$. Since we often don't know the exact value of ρ_0 we'll sometimes have to maximise the estimation of κ and assume it to be constant at low T in order to estimate the heat power going down the fridge.

B.2.2 Estimation of the heat power going down the fridge through the microwave wires

Using the data of figure B.2 and the quotation given by the manufacturer of our cables, *Coax Co.*, we can calculate the heat power dissipated at each stage of the dilution fridge. The results for different materials are gathered in the tables shown in figure B.3.

The other important property of a microwave cable is of course the linear attenuation undergone by the signal propagating through it, and also how this attenuation evolves with frequency. Indeed we want the frequency response of the circuit to be as flat as possible. Figure B.4 displays the attenuation of the previous materials for different frequencies (data: *Coax Co.*).

It turns out that BeCu wires exhibit an attenuation close to the one of stainless steel, while their thermal conductivity is close to the one of Cu. We thus decide to wire up the excitations lines with BeCu all the way down to the mixing chamber. The measurement line is terminated with NbTi from the 1K pot to the mixing chamber so that there is no attenuation on this line and no heat transfer either.

Assuming that cables are perfectly thermally anchored at each stage, the heat dissipated for each BeCu line is estimated to be:

$$P_{4K} = 2.5 \text{ mW} \quad (\text{B.4})$$

$$P_{1Kpot} \leq 10 \mu\text{W}$$

$$P_{100mKplate} \leq 3 \mu\text{W}$$

$$P_{Mix.Chamber} \leq 0.5 \mu\text{W}$$

At delivery, our dilution fridge had the following characteristics,

$$P_{Mix.Ch.}^{cold} = 250 \text{ mW} @ 100mK \quad (\text{B.5})$$

$$T_{Mix.Ch} = 7mK @ P_{Mix.Ch.} = 0$$

Cu/Cu		Inner	total (mW)
Param	Outer		
d ext(mm)	2,2	0,538037375	
d in (mm)	1,8	0	
L 300-77 (cm)	50	50	
L 77-4 (cm)	50	50	
L 4-1 (cm)	10	10	
L 1-0.02 (cm)	50	50	
300->77K	23,812504	4,30834004	28,120844
77K->4K	26,536768	3,022359962	29,559128
4K->1K	0,474768	0,085898652	0,56066665
1K->100mK	0,1424304	0,025769595	0,1682
100mK->10mK	0,01424304	0,00257696	0,01682

CuNi/CuNi (with CuNi 60/40 data whereas cable is 70/30)			
Param	Outer	Inner	Total (mW)
d ext(mm)	2,2	0,538037375	
d in (mm)	1,8	0	
L300-77 (cm)	50	50	
L77-4 (cm)	50	50	
L4-1 (cm)	10	10	
L1-0.02 (cm)	50	50	
300->77K	1,43184	0,259059425	1,69089943
77K->4K	0,2382632	0,043108397	0,2813716
4K->1K	0,0043332	0,000783996	0,0051172
1K->400mK	8,5408E-05	1,54527E-05	0,00010086

Coax SS/SS 2.2 (Stainless Steel)			
Param	Outer	Inner	Total (mW)
d ext(mm)	2,2	0,538037375	
d in (mm)	1,8	0	
L 300-77 (cm)	50	50	
L 77-4 (cm)	50	50	
L 4-1 (cm)	10	10	
L 1-0.02 (cm)	50	50	
300->77K	0,656888	0,118849193	0,77573719
77K->4K	0,0875432	0,015838984	0,10338218
4K->1K	0,00071592	0,00012953	0,00084545
1K->400mK	9,7968E-06	1,77251E-06	1,1569E-05

Coax BeCu/BeCu			
Param	Outer	Inner	Total (mW)
d ext(mm)	2,2	0,538037375	
d in (mm)	1,8	0	
L 300-77 (cm)	50	50	
L 77-4 (cm)	50	50	
L 4-1 (cm)	10	10	
L 1-0.02 (cm)	50	50	
300->77K	1,632172	0,29530502	1,92747702
77K->4K	0,39204784	0,070932289	0,46298013
4K->1K	0,0071592	0,001295297	0,0084545
1K->100mK	0,00214776	0,000388589	0,00253635
100->10mK	0,00021478	3,88589E-05	0,00025363

FIGURE B.3: Heat power transmitted by microwave coaxial wires in different materials.

Freq. (GHz)	Cu	CuNi	SS	BeCu
1	0.64	3.4	4.2	1.3
5	1.51	7.6	9.5	3
10	2.21	10.8	13.4	4.4
20	3.29	15.5	19.2	6.3

FIGURE B.4: Linear attenuation of microwave coaxial wires in different materials.

B.3 Radiation power on the microwave wires

The thermal noise spectral density in a coaxial cable, radiated at the output of an attenuator, at thermal equilibrium with temperature T is given by:

$$\frac{dP}{d\nu} = h\nu f_B(\nu, T) = \frac{h\nu}{e^{h\nu/k_B T} - 1}$$

This rewrites $k_B T$ at low frequency, and is cut off at frequencies of the order of $k_B T/h$. As detailed in *J. Gabelli, PhD Thesis, 2006*, one can write the power left after an attenuator of n dB at temperature T :

$$\frac{dP_{out}}{d\nu} = D^2 \frac{dP_{in}}{d\nu} + (1 - D^2) h\nu f_B(\nu, T) \quad (\text{B.6})$$

where D is the transmission, $D = 10^{-n/20}$.

Equation B.6 can be iterated for all the attenuators from the 1K pot to the mixing chamber. It turns out that a strong attenuation at the lowest temperature (i.e. mixing chamber) is best for having the lowest noise power, or the coldest photons. However, a strong attenuation is necessary on the 1K pot, where there is a rather strong cooling power, in order to relieve the stages beneath. The final wiring scheme is given in figure B.5. With such a scheme, including the directional coupler, and assuming a bandwidth of 40GHz, the integrated power down on the mixing chamber is of the order of: 260fW (or $3.6\mu VRMS$) on the excitation line and 3.3fW (or $0.4\mu VRMS$) on each fast gate

lines. If we set a $20dB$ attenuator on the mixing chamber instead of the directionnal coupler, the integrated power would only be of the order of $0.5fW$ (or $0.15\mu VRMS$) on the excitation line. Note that attenuators are also very important to ancor thermally the inner conductor of the coaxial cables at a given stage.

B.4 Thermalisation and filtering of the DC lines

B.4.1 Methods

There are many different possible options for setting up the DC wires, and many less available commercial parts than for RF compoments. We chose supple coaxial cables *Lakeshore SS* from the 300K panel, down to the mixing chamber. A first thermal ancor is set on the 1K pot stage, with $\simeq 3cm$ of copper thin films ($\simeq 50\mu m$ thick) on a kapton ($\simeq 200\mu m$ thick) sheet glued on the frame of the fridge. Each of the 12 inner conductors is soldered on a different copper thin film. The outer conductors are connected to ground plane (the fridge frame itself) by mechanic contact at the input and output of the thermal ancor. Another ancor is set on the mixing chamber stage, with the same principle but on $\simeq 5cm$ long.

After the second kapton based thermal ancor, we use normal copper wires, and then *Lakeshore* manganin wires down the sample holder. We embed these wires into a first box filled with *Eccosorb CRS 117*, and then in copper cylinders, also filled with the same material. This ensure a proper filtering of all the microwaves coming from the environment.

B.4.2 Thermalisation length

In order to have an idea on the length necessary to thermally anchor the cables on the kapton thin films, one can use the following simple model, directly following the idea given in *J. Gabelli, PhD Thesis, 2006*. Let's consider the situation described in figure B.5, with e and δ the thickness of the kapton and copper films respectively, κ_m and κ_i their thermal conductivity and T_0 the temperature of the fridge frame.

In a stationnary regime, the heat flux conservation in copper part between x and $x + dx$ writes:

$$\phi_m(x) = \phi_m(x + dx) + \phi_i(x)$$

Taking W as the width over which we consider the films, one can rewrite in terms of heat current J :

$$W\delta J_m(x) = W\delta J_m(x + dx) + WdxJ_i(x)$$

The Fourier's law then gives a relation between this heat current and the temperature gradient:

$$\begin{aligned} J_m(x) &= -\kappa_m \frac{dT}{dx} \\ J_i(x) &= -\kappa_i \frac{dT}{dy} \simeq -\kappa_i \frac{T(0) - T(x)}{e} \end{aligned}$$

Therefore

$$e\delta \frac{\kappa_m}{\kappa_i} \frac{d^2T}{dx^2} - T(x) = -T_0$$

Which finds a solution

$$T(x) = T_0 + cste^{-x/\lambda_{th}} \left(+cst'e^{x/\lambda_{th}} \right)$$

The characteristic length for a wire to be thermally well anchored on the kapton tracks is thus given by

$$\lambda_{th} = \sqrt{e\delta \frac{\kappa_m}{\kappa_i}}$$

Assuming $e = 200\mu m$, $\delta = 50\mu m$, $\kappa_{Kapton} = 2.5 \times T^2 \text{ mW.K}^{-1}.m^{-1}$, and $\kappa_{Cu} = 100 \times T \text{ W.K}^{-1}.m^{-1}$ (very uncertain at $20mK$):

$$L(1.5K) \simeq 1.6 \text{ cm}$$

$$L(20mK) \simeq 14 \text{ cm}$$

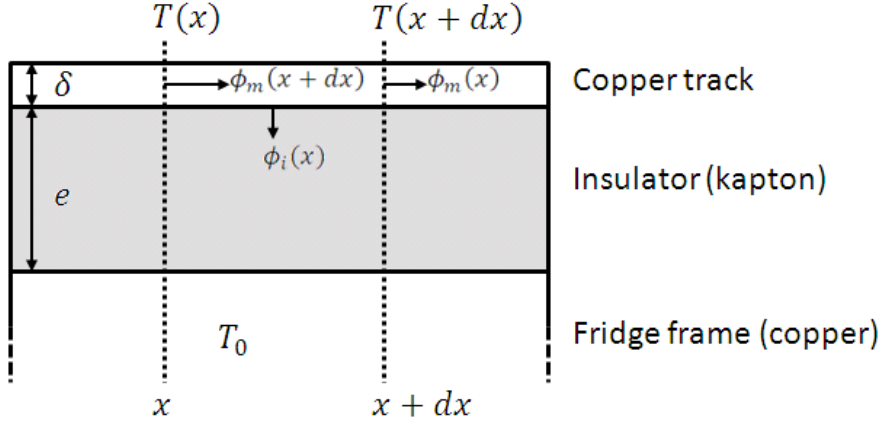


FIGURE B.5: Scheme of the model used to evaluate the thermalisation length of our DC lines on a kapton sheet..

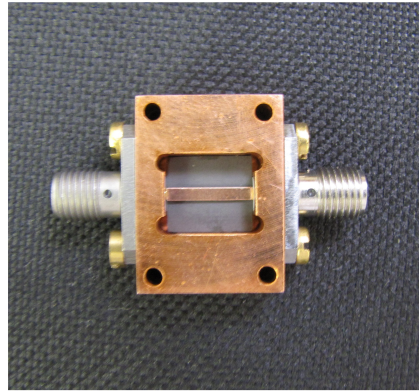
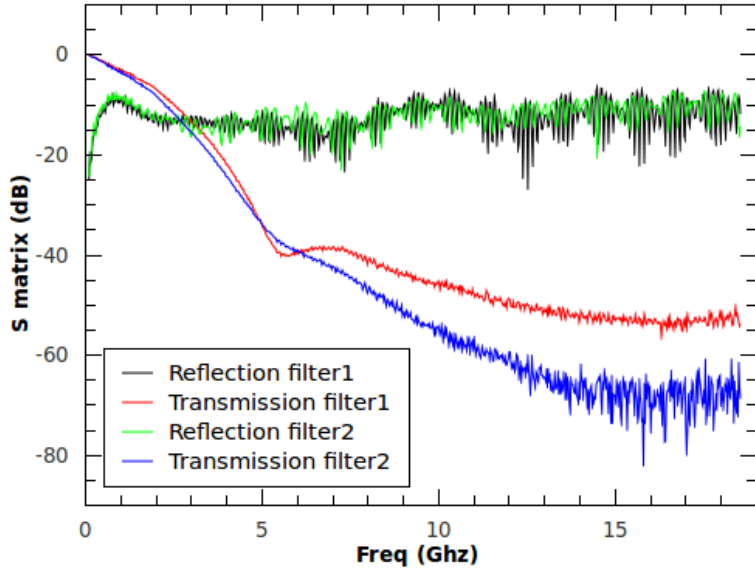


FIGURE B.6: 50Ω adapted filters

B.5 Attenuation, filtering and thermalisation of the microwave lines

If one wants to be able to change the operating point of the system quickly, for manipulation and readout, it can be necessary to apply fast voltage steps on " V_{gL} " and " V_{gR} ", with a risetime of 1GHz . If we assume our effective Zeeman splitting δ to be of the order of $10\mu\text{eV}$, then we need steps much larger than that, \simeq few $100\mu\text{eV}$. With the capacitance to the CNT, signal must be of the order of 1mV or -47dBm . Since the *AWG* can deliver $\simeq 1\text{V}$, we set 46 dB of attenuation along both " V_{gL} " and " V_{gR} " fast gate lines. On the top of these attenuators, we add home made 50Ω adapted filters with a -3dB bandwidth at 1GHz , so that higher frequencies are strongly attenuated, see figure B.7. The absorbant we use is *Eccosorb MF 117*, the design of these filters comes from *I. Siddiqi, arXiv:0903.1895v1*.

FIGURE B.7: Frequency response of two different 50Ω adapted filters.

B.6 Home made DC current analog amplifier

The low frequency DC current amplifier which has been developed along with the electronic staff of the lab is schematically represented in figure B.8. The upper part of the circuit corresponds to the power supply of the amplifier. This stage allows a robust and stable supply, and does not rely on the use of a battery, it can be directly connected to a commercial standard DC source. The lower part of the circuit is the amplifier itself. The first stage (*AD795JR*), which determines the added noise of the amplifier, is set to have a gain of 10^7 and a bandwidth of few $100Hz$. Two further stages are used to possibly increase the output voltage for very small current, and to ensure a strong attenuation from noise at the output port of the amplifier. As shown in figure B.9, the amplifier circuit board is embedded in a RF-tight thick aluminium box, which ensures electromagnetic shielding. It is still small enough to be placed next to the output port of the cryostat, avoiding long cables.

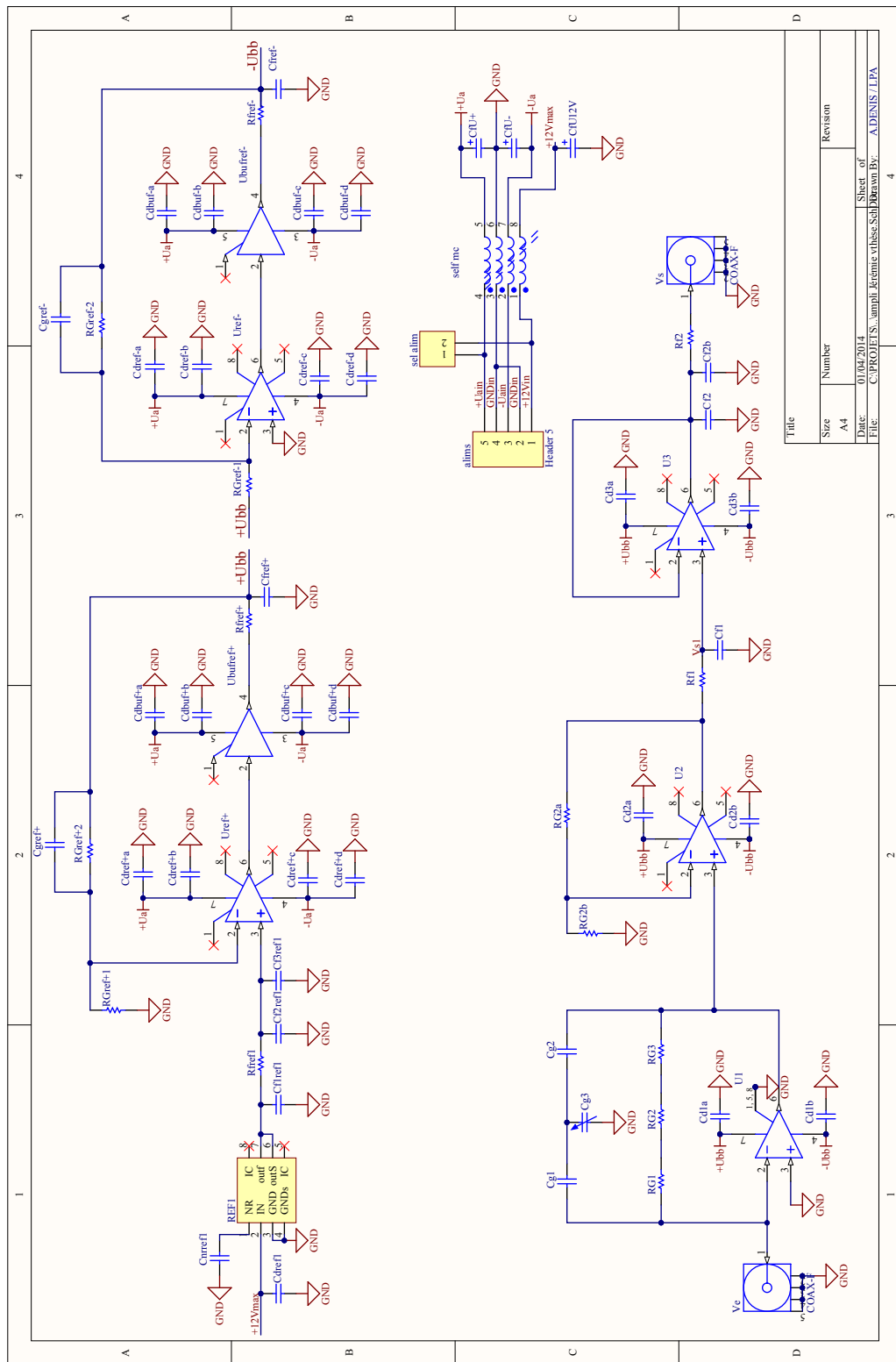


FIGURE B.8: Electrical schematic of our low frequency current amplifier. Source: *Anne Denis, LPA*.

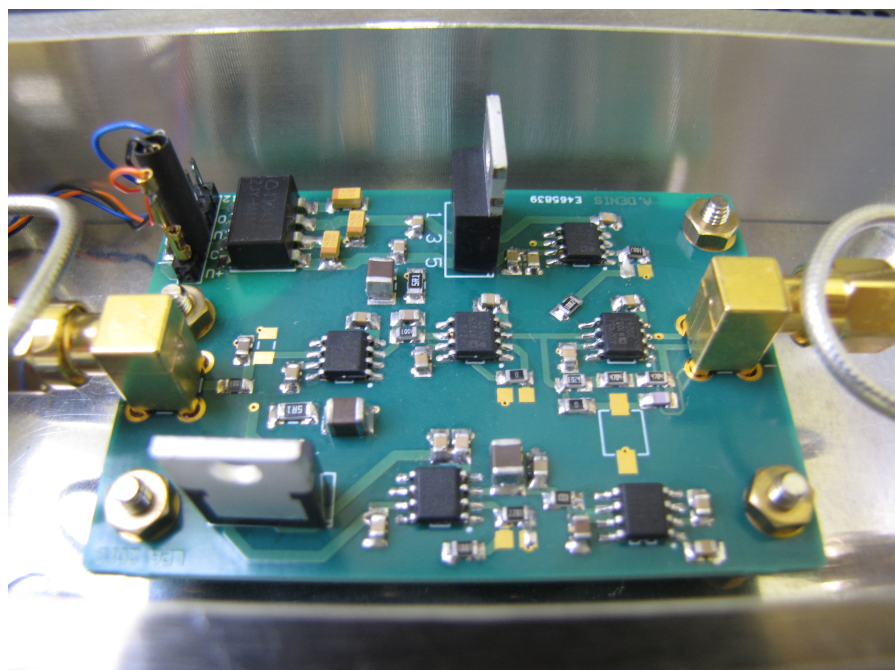


FIGURE B.9: Photograph of our low frequency current amplifier.

Appendix C

Supplementary DC current experiment

This appendix shows the experimental measurement of a double quantum dot connected to ferromagnetic contacts in a regime different from that of the main text. We compare this results with a scattering matrix theory approach.

C.1 Observation of multiple orbital anti-crossings

The first experiments we performed were not done in a resonator geometry. The idea was to readout the spin states in the device using DC current measurements. Figure C.1 shows a sample similar to the one that produced the following data. The devices we managed to obtain at that time could not be tuned into closed quantum dots with large charging energies (which is needed for a well defined two- or multi-level system). However we observed interesting features in some samples that could have been related to the effect of large exchange fields induced from the connection to ferromagnets. Although we did not perform a full transport study of these devices, it is interesting to notice the similarities with a non-interacting theory taking non collinear ferromagnets into account.

Figure C.2 shows a stability diagram measurement of the device. This measurement shows that the device is not a very hard coulomb blockade, with Γ_{lead} and inter-dot tunnel coupling t almost of the order of the on-site charging energy in some regions. The mutual charging energy is small, of the order of Γ_{lead} or smaller. Overall, interactions are much smaller than in the measurements of figure 5.5 for example. Interestingly, wide coulomb peaks on the dot controlled by V_{g2} (tilted horizontal lines) are coming with two thinner satellites. In some regions, we can observe avoided crossings of these levels with

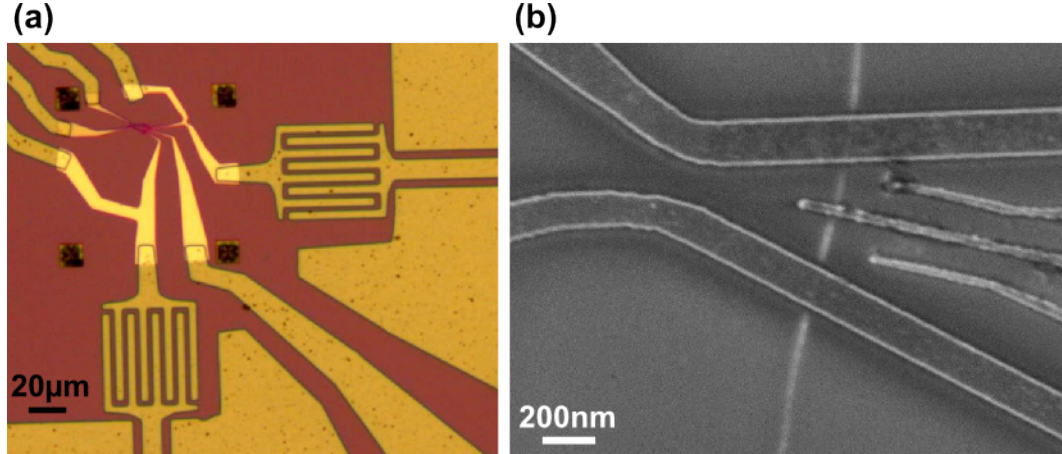


FIGURE C.1: (a) Optical micrograph of the device. Five DC lines allow to define source and drain contacts and three electrostatic gate voltages. Two CPW lines can possibly carry RF signals to the device, connected with a bias tee to the DC gate electrodes. (b) SEM image of the device, showing the nanotube connected to two PdNi ferromagnetic contacts, as well as a central top gate and two side gates.

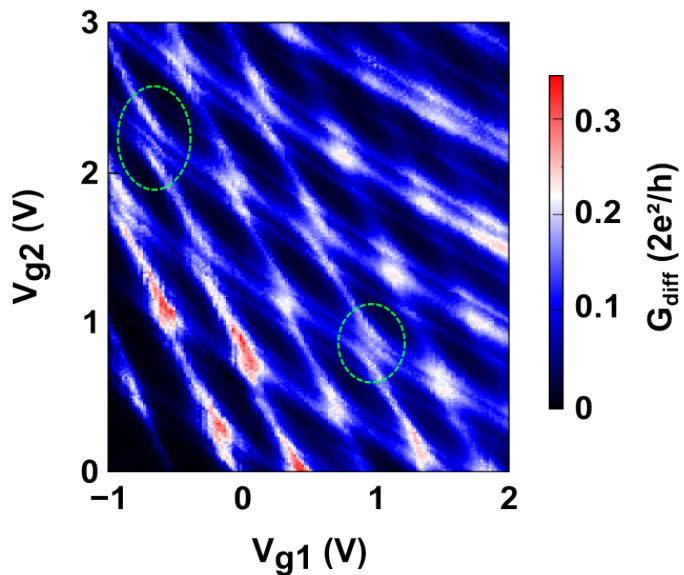


FIGURE C.2: Differential conductance of the device measured at $V_{SD} \approx 0$ as a function of the two side gate voltages. In some regions (e.g. dashed green circles), conductance peaks show unusual anti-crossing patterns involving three lines.

the orbitals of dot 1, see green dashed circled regions for instance. The characterisation of these states would have required further investigation, applying for example an external magnetic field to see if they are spin-dependent. But both technical problems and our will to obtain closed quantum dots took us somewhere else. Nonetheless, we can quickly compare this with a simple non-interacting theory and notice very similar features, see below.

C.2 Scattering matrix theory

A simple way to calculate the conductance of a coherent conductor with tunnel barriers and propagating portions is to use a scattering matrix formalism. A double dot is characterized by three tunnel junctions and two coherent conductors in between. In order to account for the spin dependence of the device, each scattering coefficient is composed by a 2×2 unitary matrix, in the spin Hilbert space $\{\uparrow, \downarrow\}$ [83], and satisfying the usual matrix product. We use the follow parametrisation for the ferromagnetic contacts:

$$S_n = \begin{pmatrix} \hat{r}_n & \hat{t}'_n \\ \hat{t}_n & \hat{r}'_n \end{pmatrix} \quad (\text{C.1})$$

with

$$\hat{r}_n = R_n + r_n \sigma_z \text{ where } \begin{cases} R_n = \frac{1}{2}(\sqrt{1 - T_n}) (e^{i\phi_n^\uparrow} + e^{i\phi_n^\downarrow}) \\ r_n = \frac{1}{2}(\sqrt{1 - T_n}) (e^{i\phi_n^\uparrow} - e^{i\phi_n^\downarrow}) \end{cases} \quad (\text{C.2})$$

$$\hat{t}_n = -i\sqrt{T_n}$$

For the central tunnel junction, there is no spin dependence as it is only an electrostatic stricture, and its blocks become

$$\hat{r}_K = \sqrt{1 - T_K} \text{ and } \hat{t}_K = -i\sqrt{T_K} \quad (\text{C.3})$$

The whole system is represented by five matrices for tunnel barrier $S_{L(R)}$ to the left (right) lead, inter-dot tunnel coupling S_K and two propagating parts. One can compute the transmission coefficient of the total scattering matrix composed with $S_L \circ S_1 \circ S_K \circ S_2 \circ S_R$:

$$\hat{t}_{tot} = -i\sqrt{T_K} \hat{t}_R D^{-1} \hat{t}_L e^{i(\delta_1 + \delta_2)} \quad (\text{C.4})$$

where

$$\begin{aligned} D &= \hat{\alpha} - \sqrt{1 - T_K} \hat{r}_R \hat{\alpha} e^{2i\delta_2} + T_K \hat{\alpha}^{-1} \hat{r}'_L \hat{r}'_R \hat{\alpha} e^{2i(\delta_1 + \delta_2)} \\ \hat{\alpha} &= -\sqrt{1 - T_K} \hat{r}'_L e^{2i\delta_1} \end{aligned} \quad (\text{C.5})$$

and $\delta_{1(2)}$ is the electronic path in dot 1(2) (i.e. the propagating parts), which is experimentally controlled by local gate voltages. \hat{t}_{tot} is diagonal if $\hat{r}_{L(R)}$ and $\hat{t}_{L(R)}$ are diagonal. However, the rotation of the magnetization of the ferromagnetic contacts is equivalent to a rotation in the spin Hilbert space. This rotation can be done for instance on the S_R blocks using a rotation matrix so that S_R takes the form

$$\left\{ \begin{array}{l} \hat{r}_R = R_R + r_R \cos(\theta) \sigma_z + r_R \sin(\theta) \sigma_x \\ \hat{t}_R = T_R + t_R \cos(\theta) \sigma_z + t_R \sin(\theta) \sigma_x \end{array} \right. \quad (\text{C.6})$$

This couples spin populations. Using equation C.4, one can compute the conductance $G = \frac{e^2}{h} \text{Tr} \left(\hat{t}_{tot} \hat{t}_{tot}^\dagger \right)$ as a function of δ_1 and δ_2 (or equivalently gate voltages). Figure C.3 shows such a conductance plot for a set of parameters that reproduces some of the features of figure C.2. The behaviour of this conductance strongly depends on the parameters of the scattering matrices, and in particular, on the phase difference between up and down spins reflection coefficients at the interface with the ferromagnets. It is still interesting to notice how such a simplistic model can yield similar features to those we observed, which thus might arise from a strong exchange field in one of the dot.

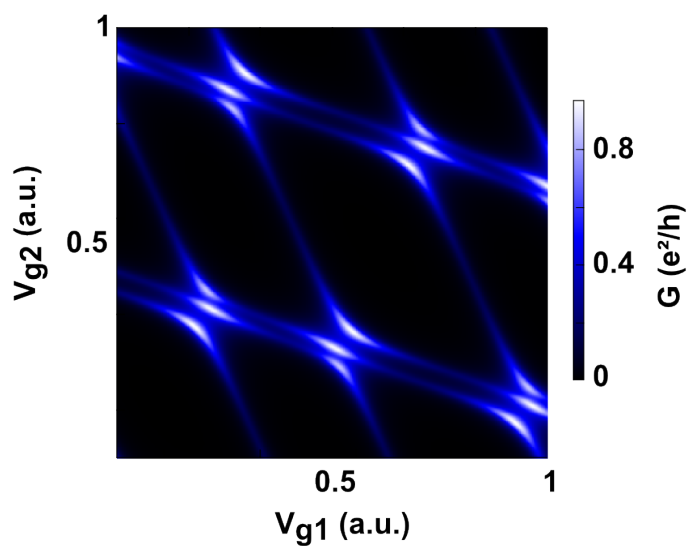


FIGURE C.3: Simulated conductance of a double quantum dot device connected to two non-collinear ferromagnetic electrodes, using a scattering matrix approach.

Bibliography

- [1] J. Raimond, M. Brune, and Serge Haroche. Manipulating quantum entanglement with atoms and photons in a cavity. *Reviews of Modern Physics*, 73(3):565–582, August 2001. ISSN 0034-6861. doi: 10.1103/RevModPhys.73.565. URL <http://link.aps.org/doi/10.1103/RevModPhys.73.565>.
- [2] Igor Žutić and S. Das Sarma. Spintronics: Fundamentals and applications. *Reviews of Modern Physics*, 76(2):323–410, April 2004. ISSN 0034-6861. doi: 10.1103/RevModPhys.76.323. URL <http://link.aps.org/doi/10.1103/RevModPhys.76.323>.
- [3] B. van Wees, H. van Houten, C. Beenakker, J. Williamson, L. Kouwenhoven, D. van der Marel, and C. Foxon. Quantized conductance of point contacts in a two-dimensional electron gas. *Physical Review Letters*, 60(9):848–850, February 1988. ISSN 0031-9007. doi: 10.1103/PhysRevLett.60.848. URL <http://link.aps.org/doi/10.1103/PhysRevLett.60.848>.
- [4] W. van der Wiel, Silvano De Franceschi, Jeroen M Elzerman, T. Fujisawa, Seigo Tarucha, and Leo. P. Kouwenhoven. Electron transport through double quantum dots. *Reviews of Modern Physics*, 75(1):1–22, December 2002. ISSN 0034-6861. doi: 10.1103/RevModPhys.75.1. URL http://rmp.aps.org/abstract/RMP/v75/i1/p1_1.
- [5] SJ Tans, M. H. Devoret, Hongjie Dai, and A Thess. Individual single-wall carbon nanotubes as quantum wires. *Nature*, 1997. URL http://ceesdekkerlab.tudelft.nl/wp-content/uploads/1997_Tans-3.pdf.
- [6] Fei Pei, E.A. Laird, Gary A. Steele, and Leo. P. Kouwenhoven. Valleyspin blockade and spin resonance in carbon nanotubes. *Nature Nanotechnology*, advance on, September 2012. ISSN 1748-3387. doi: 10.1038/nnano.2012.160. URL <http://dx.doi.org/10.1038/nnano.2012.160>.

- [7] J Waissman, M Honig, S Pecker, A Benyamini, A Hamo, and S. Ilani. Realization of pristine and locally tunable one-dimensional electron systems in carbon nanotubes. *Nature nanotechnology*, 8(8):569–74, August 2013. ISSN 1748-3395. doi: 10.1038/nnano.2013.143. URL <http://dx.doi.org/10.1038/nnano.2013.143>.
- [8] J-D. Pillet, C. H. L. Quay, P. Morfin, C. Bena, A. Levy Yeyati, and P. Joyez. Andreev bound states in supercurrent-carrying carbon nanotubes revealed. *Nature Physics*, 6(12):965–969, November 2010. ISSN 1745-2473. doi: 10.1038/nphys1811. URL <http://dx.doi.org/10.1038/nphys1811>.
- [9] J. R. Hauptmann, J. Paaske, and P. E. Lindelof. Electric-field-controlled spin reversal in a quantum dot with ferromagnetic contacts. *Nature Physics*, 4(5):373–376, March 2008. ISSN 1745-2473. doi: 10.1038/nphys931. URL <http://dx.doi.org/10.1038/nphys931>.
- [10] M Urdampilleta, S Klyatskaya, J-P Cleuziou, M Ruben, and W. Wernsdorfer. Supramolecular spin valves. *Nature materials*, 10(7):502–6, July 2011. ISSN 1476-1122. doi: 10.1038/nmat3050. URL <http://dx.doi.org/10.1038/nmat3050>.
- [11] J-P Cleuziou, W. Wernsdorfer, Vincent Bouchiat, T Ondarçuhu, and M Monthioux. Carbon nanotube superconducting quantum interference device. *Nature nanotechnology*, 1(1):53–9, October 2006. ISSN 1748-3395. doi: 10.1038/nnano.2006.54. URL <http://dx.doi.org/10.1038/nnano.2006.54>.
- [12] J Chaste, A Eichler, J Moser, G Ceballos, R Rurali, and A. Bachtold. A nanomechanical mass sensor with yoctogram resolution. *Nature nanotechnology*, 7(5):301–4, May 2012. ISSN 1748-3395. doi: 10.1038/nnano.2012.42. URL <http://dx.doi.org/10.1038/nnano.2012.42>.
- [13] Sangeeta Sahoo, Takis Kontos, Jürg Furer, Christian Hoffmann, Matthias Gräber, Audrey Cottet, and Christian Schönenberger. Electric field control of spin transport. *Nature Physics*, 1(2):99–102, October 2005. ISSN 1476-0000. doi: 10.1038/nphys149. URL <http://dx.doi.org/10.1038/nphys149>.
- [14] Audrey Cottet and Takis Kontos. Spin Quantum Bit with Ferromagnetic Contacts for Circuit QED. *Physical Review Letters*, 105(16), October 2010. ISSN 0031-9007. doi: 10.1103/PhysRevLett.105.160502. URL <http://prl.aps.org/abstract/PRL/v105/i16/e160502>.
- [15] Daniel Loss and David P. DiVincenzo. Quantum computation with quantum dots. *Physical Review A*, 57(1):120–126, January 1998. ISSN 1050-2947. doi: 10.1103/PhysRevA.57.120. URL <http://link.aps.org/doi/10.1103/PhysRevA.57.120>.

- [16] J. R. Petta, a C Johnson, J M Taylor, E.A. Laird, Amir Yacoby, Mikhail D. Lukin, C. M. Marcus, M P Hanson, and a C Gossard. Coherent manipulation of coupled electron spins in semiconductor quantum dots. *Science (New York, N.Y.)*, 309(5744):2180–4, September 2005. ISSN 1095-9203. doi: 10.1126/science.1116955. URL <http://www.ncbi.nlm.nih.gov/pubmed/16141370>.
- [17] Clément Sayrin, Igor Dotsenko, Xingxing Zhou, Bruno Peaudecerf, Théo Rybarczyk, Sébastien Gleyzes, Pierre Rouchon, Mazyar Mirrahimi, Hadis Amini, Michel Brune, Jean-Michel Raimond, and Serge Haroche. Real-time quantum feedback prepares and stabilizes photon number states. *Nature*, 477(7362):73–77, August 2011. ISSN 0028-0836. doi: 10.1038/nature10376. URL <http://dx.doi.org/10.1038/nature10376>.
- [18] D. Vion, A. Aassime, Audrey Cottet, P Joyez, H Pothier, C Urbina, D Esteve, and M. H. Devoret. Manipulating the quantum state of an electrical circuit. *Science (New York, N.Y.)*, 296(5569):886–9, May 2002. ISSN 1095-9203. doi: 10.1126/science.1069372. URL <http://www.sciencemag.org/content/296/5569/886.abstract>.
- [19] Alexandre Blais, Ren-Shou Huang, A. Wallraff, S. M. Girvin, and R. J. Schoelkopf. Cavity quantum electrodynamics for superconducting electrical circuits: An architecture for quantum computation. *Physical Review A*, 69(6), June 2004. ISSN 1050-2947. doi: 10.1103/PhysRevA.69.062320. URL <http://pra.aps.org/abstract/PRA/v69/i6/e062320>.
- [20] A. Wallraff, D. Schuster, Alexandre Blais, L. Frunzio, Ren-Shou Huang, J. Majer, S Kumar, S. M. Girvin, and R. J. Schoelkopf. Strong coupling of a single photon to a superconducting qubit using circuit quantum electrodynamics. *Nature*, 431(7005):162–7, September 2004. ISSN 1476-4687. doi: 10.1038/nature02851. URL <http://dx.doi.org/10.1038/nature02851>.
- [21] N. Bergeal, F. Schackert, M. Metcalfe, R. Vijay, V. E. Manucharyan, L. Frunzio, D. E. Prober, R. J. Schoelkopf, S. M. Girvin, and M. H. Devoret. Phase-preserving amplification near the quantum limit with a Josephson ring modulator. *Nature*, 465(7294):64–68, May 2010. ISSN 0028-0836. doi: 10.1038/nature09035. URL <http://dx.doi.org/10.1038/nature09035>.
- [22] R. Vijay, C. Macklin, D. H. Slichter, S. J. Weber, K. W. Murch, R. Naik, A. N. Korotkov, and I. Siddiqi. Stabilizing Rabi oscillations in a superconducting qubit using quantum feedback. *Nature*, 490(7418):77–80, October 2012. ISSN 0028-0836. doi: 10.1038/nature11505. URL http://www.nature.com/nature/journal/v490/n7418/full/nature11505.html?WT.ec_id=NATURE-20121004.

- [23] D. Ristè, M. Dukalski, C. A. Watson, G. de Lange, M. J. Tiggelman, Ya. M. Blanter, K. W. Lehnert, R. N. Schouten, and L. DiCarlo. Deterministic entanglement of superconducting qubits by parity measurement and feedback. *Nature*, 502(7471):350–354, October 2013. ISSN 0028-0836. doi: 10.1038/nature12513. URL <http://dx.doi.org/10.1038/nature12513>.
- [24] R. Barends, J. Kelly, A. Megrant, D. Sank, E. Jeffrey, Y. Chen, Y. Yin, B. Chiaro, J. Mutus, C. Neill, P. O’Malley, P. Roushan, J. Wenner, T. C. White, Andrew N. Cleland, and John M. Martinis. Coherent Josephson Qubit Suitable for Scalable Quantum Integrated Circuits. *Physical Review Letters*, 111(8):080502, August 2013. ISSN 0031-9007. doi: 10.1103/PhysRevLett.111.080502. URL <http://link.aps.org/doi/10.1103/PhysRevLett.111.080502>.
- [25] Brian Vlastakis, Gerhard Kirchmair, Zaki Leghtas, Simon E Nigg, Luigi Frunzio, S M Girvin, Mazyar Mirrahimi, M H Devoret, and R J Schoelkopf. Deterministically encoding quantum information using 100-photon Schrödinger cat states. *Science (New York, N.Y.)*, 342(6158):607–10, November 2013. ISSN 1095-9203. doi: 10.1126/science.1243289. URL <http://www.sciencemag.org/content/342/6158/607.short>.
- [26] J D Teufel, T Donner, Dale Li, J W Harlow, M S Allman, K Cicak, A J Sirois, J D Whittaker, K. W. Lehnert, and R W Simmonds. Sideband cooling of micromechanical motion to the quantum ground state. *Nature*, 475(7356):359–63, July 2011. ISSN 1476-4687. doi: 10.1038/nature10261. URL <http://dx.doi.org/10.1038/nature10261>.
- [27] V. Singh, S. J. Bosman, B. H. Schneider, Y. M. Blanter, A. Castellanos-Gomez, and Gary A. Steele. Optomechanical coupling between a graphene mechanical resonator and a superconducting microwave cavity. March 2014. URL <http://arxiv.org/abs/1403.5165>.
- [28] Bertrand Reulet, Michel Ramin, Hélène Bouchiat, and Dominique Mailly. Dynamic Response of Isolated Aharonov-Bohm Rings Coupled to an Electromagnetic Resonator. *Physical Review Letters*, 75(1):124–127, July 1995. ISSN 0031-9007. doi: 10.1103/PhysRevLett.75.124. URL <http://link.aps.org/doi/10.1103/PhysRevLett.75.124>.
- [29] M.R. Delbecq, V. Schmitt, F. Parmentier, Nicolas Roch, J. J. Viennot, G. Fève, B. Huard, C. Mora, Audrey Cottet, and Takis Kontos. Coupling a Quantum Dot, Fermionic Leads, and a Microwave Cavity on a Chip. *Physical Review Letters*, 107(25), December 2011. ISSN 0031-9007. doi: 10.1103/PhysRevLett.107.256804. URL <http://prl.aps.org/abstract/PRL/v107/i25/e256804>.

- [30] M.R. Delbecq, L. E. Bruhat, J. J. Viennot, S Datta, Audrey Cottet, and T Kontos. Photon-mediated interaction between distant quantum dot circuits. *Nature communications*, 4:1400, January 2013. ISSN 2041-1723. doi: 10.1038/ncomms2407. URL <http://dx.doi.org/10.1038/ncomms2407>.
- [31] T. Frey, P. J. Leek, M. Beck, Alexandre Blais, T. Ihn, Klaus Ensslin, and A. Wallraff. Dipole coupling of a double quantum dot to a microwave resonator. *Physical Review Letters*, 108(4):046807, August 2011. doi: 10.1103/PhysRevLett.108.046807. URL <http://link.aps.org/doi/10.1103/PhysRevLett.108.046807>.
- [32] K. D. Petersson, L. W. McFaul, M. D. Schroer, M. Jung, J. M. Taylor, A. A. Houck, and J. R. Petta. Circuit quantum electrodynamics with a spin qubit. *Nature*, 490(7420):380–383, October 2012. ISSN 0028-0836. doi: 10.1038/nature11559. URL http://www.nature.com/nature/journal/v490/n7420/full/nature11559.html?WT.ec_id=NATURE-20121018.
- [33] H. Toida, T. Nakajima, and S. Komiyama. Vacuum Rabi Splitting in a Semiconductor Circuit QED System. *Physical Review Letters*, 110(6):066802, February 2013. ISSN 0031-9007. doi: 10.1103/PhysRevLett.110.066802. URL <http://link.aps.org/doi/10.1103/PhysRevLett.110.066802>.
- [34] Shanhui Fan, Da Wei, J. R. Johansson, Miao-Lei Zhang, Shu-Xiao Li, Hai-Ou Li, Gang Cao, Ming Xiao, Tao Tu, Guang-Can Guo, Hong-Wen Jiang, Franco Nori, and Guo-Ping Guo. Circuit QED with a graphene double quantum dot and a reflection-line resonator. October 2013. URL <http://arxiv.org/abs/1310.6118>.
- [35] Y. Y. Liu, K. D. Petersson, J. Stehlik, J. M. Taylor, and J. R. Petta. Photon Emission from a Cavity-Coupled Double Quantum Dot. January 2014. URL <http://arxiv.org/abs/1401.7730>.
- [36] J. J. Viennot, J. Palomo, and T. Kontos. Stamping single wall nanotubes for circuit quantum electrodynamics. *Applied Physics Letters*, 104(11):113108, March 2014. ISSN 1077-3118. doi: 10.1063/1.4868868. URL <http://scitation.aip.org/content/aip/journal/apl/104/11/10.1063/1.4868868>.
- [37] J. J. Viennot, M.R. Delbecq, M. C. Dartailh, A. Cottet, and T. Kontos. Out-of-equilibrium charge dynamics in a hybrid circuit quantum electrodynamics architecture. *Physical Review B*, 89(16):165404, April 2014. ISSN 1098-0121. doi: 10.1103/PhysRevB.89.165404. URL <http://link.aps.org/doi/10.1103/PhysRevB.89.165404>.
- [38] Neill Lambert, Christian Flindt, and Franco Nori. Photon-mediated electron transport in hybrid circuit-QED. *EPL (Europhysics Letters)*, 103(1):17005, July 2013.

- ISSN 0295-5075. doi: 10.1209/0295-5075/103/17005. URL <http://dx.doi.org/10.1209/0295-5075/103/17005>.
- [39] L D Contreras-Pulido, C Emery, T Brandes, and Ramón Aguado. Non-equilibrium correlations and entanglement in a semiconductor hybrid circuit-QED system. *New Journal of Physics*, 15(9):095008, September 2013. ISSN 1367-2630. doi: 10.1088/1367-2630/15/9/095008. URL <http://iopscience.iop.org/1367-2630/15/9/095008/article/>.
- [40] C. Bergenfeldt and P. Samuelsson. Nonlocal transport properties of nanoscale conductor-microwave cavity systems. *Physical Review B*, 87(19):195427, May 2013. ISSN 1098-0121. doi: 10.1103/PhysRevB.87.195427. URL <http://link.aps.org/doi/10.1103/PhysRevB.87.195427>.
- [41] Christian Bergenfeldt, Peter Samuelsson, Björn Sothmann, Christian Flindt, and Markus Büttiker. Hybrid Microwave-Cavity Heat Engine. *Physical Review Letters*, 112(7):076803, February 2014. ISSN 0031-9007. doi: 10.1103/PhysRevLett.112.076803. URL <http://link.aps.org/doi/10.1103/PhysRevLett.112.076803>.
- [42] Pei-Qing Jin, Michael Marthaler, Jared H. Cole, Alexander Shnirman, and Gerd Schön. Lasing and transport in a quantum-dot resonator circuit. *Physical Review B*, 84(3):035322, July 2011. ISSN 1098-0121. doi: 10.1103/PhysRevB.84.035322. URL <http://link.aps.org/doi/10.1103/PhysRevB.84.035322>.
- [43] T. L. van den Berg, C. Bergenfeldt, and P. Samuelsson. Pump-probe scheme for electron-photon dynamics in hybrid conductor-cavity systems. page 5, February 2014. URL <http://arxiv.org/abs/1402.1351>.
- [44] Y. Kubo, F. Ong, P. Bertet, D. Vion, V. Jacques, D. Zheng, A. Dréau, J.-F. Roch, A. Auffeves, F. Jelezko, J. Wrachtrup, M. Barthe, P. Bergonzo, and D. Esteve. Strong Coupling of a Spin Ensemble to a Superconducting Resonator. *Physical Review Letters*, 105(14), September 2010. ISSN 0031-9007. URL <http://prl.aps.org/abstract/PRL/v105/i14/e140502>.
- [45] D. Schuster, A. Sears, E. Ginossar, L. DiCarlo, L. Frunzio, J. Morton, H. Wu, G. Briggs, B. Buckley, D. Awschalom, and R. J. Schoelkopf. High-Cooperativity Coupling of Electron-Spin Ensembles to Superconducting Cavities. *Physical Review Letters*, 105(14), September 2010. ISSN 0031-9007. doi: 10.1103/PhysRevLett.105.140501. URL <http://prl.aps.org/abstract/PRL/v105/i14/e140501>.
- [46] Y. Kubo, C. Grezes, A. Dewes, T. Umeda, J. Isoya, H. Sumiya, N. Morishita, H. Abe, S. Onoda, T. Ohshima, V. Jacques, A. Dréau, J.-F. Roch, I. Diniz,

- A. Auffeves, D. Vion, D. Esteve, and P. Bertet. Hybrid Quantum Circuit with a Superconducting Qubit Coupled to a Spin Ensemble. *Physical Review Letters*, 107(22), November 2011. ISSN 0031-9007. URL <http://prl.aps.org/abstract/PRL/v107/i22/e220501>.
- [47] Hans Huebl, Christoph W. Zollitsch, Johannes Lotze, Fredrik Hocke, Moritz Greifenstein, Achim Marx, Rudolf Gross, and Sebastian T. B. Goennenwein. High Cooperativity in Coupled Microwave Resonator Ferrimagnetic Insulator Hybrids. *Physical Review Letters*, 111(12):127003, September 2013. ISSN 0031-9007. doi: 10.1103/PhysRevLett.111.127003. URL <http://link.aps.org/doi/10.1103/PhysRevLett.111.127003>.
- [48] T. Hayashi, T. Fujisawa, H. Cheong, Y. Jeong, and Y. Hirayama. Coherent Manipulation of Electronic States in a Double Quantum Dot. *Physical Review Letters*, 91(22), November 2003. ISSN 0031-9007. doi: 10.1103/PhysRevLett.91.226804. URL <http://prl.aps.org/abstract/PRL/v91/i22/e226804>.
- [49] Leo. P. Kouwenhoven, S. Jauhar, J. Orenstein, Paul L. McEuen, Y. Naga-mune, J. Motohisa, and H. Sakaki. Observation of Photon-Assisted Tunneling through a Quantum Dot. *Physical Review Letters*, 73(25):3443–3446, December 1994. ISSN 0031-9007. doi: 10.1103/PhysRevLett.73.3443. URL http://prl.aps.org/abstract/PRL/v73/i25/p3443_1.
- [50] T. Oosterkamp, Leo. P. Kouwenhoven, A. Koolen, N. van der Vaart, and C. Harmans. Photon Sidebands of the Ground State and First Excited State of a Quantum Dot. *Physical Review Letters*, 78(8):1536–1539, February 1997. ISSN 0031-9007. doi: 10.1103/PhysRevLett.78.1536. URL http://prl.aps.org/abstract/PRL/v78/i8/p1536_1.
- [51] S. De Franceschi, J. A. van Dam, E. P. A. M. Bakkers, L. F. Feiner, L. Gurevich, and L. P. Kouwenhoven. Single-electron tunneling in InP nanowires. *Applied Physics Letters*, 83(2):344, July 2003. ISSN 00036951. doi: 10.1063/1.1590426. URL <http://scitation.aip.org/content/aip/journal/apl/83/2/10.1063/1.1590426>.
- [52] C. Fasth, a. Fuhrer, L. Samuelson, Vitaly N. Golovach, and Daniel Loss. Direct Measurement of the Spin-Orbit Interaction in a Two-Electron InAs Nanowire Quantum Dot. *Physical Review Letters*, 98(26):266801, June 2007. ISSN 0031-9007. doi: 10.1103/PhysRevLett.98.266801. URL <http://link.aps.org/doi/10.1103/PhysRevLett.98.266801>.
- [53] N Mason, M J Biercuk, and C. M. Marcus. Local gate control of a carbon nanotube double quantum dot. *Science (New York, N.Y.)*, 303(5658):655–8, January 2004.

- ISSN 1095-9203. doi: 10.1126/science.1093605. URL <http://www.sciencemag.org/content/303/5658/655.abstract>.
- [54] F. Kuemmeth, S. Ilani, D C Ralph, and Paul L. McEuen. Coupling of spin and orbital motion of electrons in carbon nanotubes. *Nature*, 452(7186):448–52, March 2008. ISSN 1476-4687. doi: 10.1038/nature06822. URL <http://dx.doi.org/10.1038/nature06822>.
- [55] S. J. Chorley, M. Galpin, F. Jayatilaka, C. Smith, D. Logan, and M. R. Buitelaar. Tunable Kondo Physics in a Carbon Nanotube Double Quantum Dot. *Physical Review Letters*, 109(15), October 2012. ISSN 0031-9007. doi: 10.1103/PhysRevLett.109.156804. URL <http://prl.aps.org/abstract/PRL/v109/i15/e156804>.
- [56] K. D. Petersson, J. R. Petta, H. Lu, and A. C. Gossard. Quantum Coherence in a One-Electron Semiconductor Charge Qubit. *Physical Review Letters*, 105(24): 246804, December 2010. ISSN 0031-9007. doi: 10.1103/PhysRevLett.105.246804. URL <http://link.aps.org/doi/10.1103/PhysRevLett.105.246804>.
- [57] K. C. Nowack, F H L Koppens, Yu. V. Nazarov, and L. M. K. Vandersypen. Coherent control of a single electron spin with electric fields. *Science*, 1430(2007): 24, July 2007. doi: 10.1126/science.1148092. URL <http://arxiv.org/abs/0707.3080>.
- [58] B M Maune, M G Borselli, B Huang, T D Ladd, P. W. Deelman, K S Holabird, A A Kiselev, I Alvarado-Rodriguez, R S Ross, A E Schmitz, M Sokolich, C A Watson, M F Gyure, and A T Hunter. Coherent singlet-triplet oscillations in a silicon-based double quantum dot. *Nature*, 481(7381):344–7, January 2012. ISSN 1476-4687. doi: 10.1038/nature10707. URL <http://dx.doi.org/10.1038/nature10707>.
- [59] K. Blum. *Density Matrix Theory and Applications*. 1996.
- [60] F H L Koppens, J A Folk, Jeroen M Elzerman, R. Hanson, L H Willems van Beveren, I T Vink, H P Tranitz, W Wegscheider, Leo. P. Kouwenhoven, and L. M. K. Vandersypen. Control and detection of singlet-triplet mixing in a random nuclear field. *Science (New York, N.Y.)*, 309(5739):1346–50, August 2005. ISSN 1095-9203. doi: 10.1126/science.1113719. URL <http://www.sciencemag.org/content/309/5739/1346.abstract>.
- [61] Sami Sapmaz, Carola Meyer, Piotr Beliczyński, Pablo Jarillo-Herrero, and Leo. P. Kouwenhoven. Excited state spectroscopy in carbon nanotube double quantum dots. *Nano letters*, 6(7):1350–5, July 2006. ISSN 1530-6984. doi: 10.1021/nl052498e. URL <http://dx.doi.org/10.1021/nl052498e>.

- [62] R. Hanson, J. R. Petta, Seigo Tarucha, and L. M. K. Vandersypen. Spins in few-electron quantum dots. *Reviews of Modern Physics*, 79(4):1217–1265, October 2007. ISSN 0034-6861. doi: 10.1103/RevModPhys.79.1217. URL http://rmp.aps.org/abstract/RMP/v79/i4/p1217_1.
- [63] H. O. H. Churchill, LHW Van Beveren, J. W. Harlow, F. Kuemmeth, D. Marcos, C. H. Stwertka, S. K. Watson, and C. M. Marcus. Electronnuclear interaction in ¹³C nanotube double quantum dots. *Nature Physics*, 5(5):321–326, April 2009. ISSN 1745-2473. doi: 10.1038/nphys1247. URL <http://dx.doi.org/10.1038/nphys1247>.
- [64] F. Molitor, H. Knowles, S. Dröscher, U. Gasser, T. Choi, P. Roulleau, J. Güttinger, A. Jacobsen, C. Stampfer, K. Ensslin, and T. Ihn. Observation of excited states in a graphene double quantum dot. *EPL (Europhysics Letters)*, 89(6):67005, March 2010. ISSN 0295-5075. doi: 10.1209/0295-5075/89/67005. URL <http://iopscience.iop.org/0295-5075/89/6/67005/fulltext/>.
- [65] S. J. Chorley, G. Giavaras, J. Wabnig, G. a. C. Jones, C. G. Smith, G. a. D. Briggs, and M. R. Buitelaar. Transport Spectroscopy of an Impurity Spin in a Carbon Nanotube Double Quantum Dot. *Physical Review Letters*, 106(20):206801, May 2011. ISSN 0031-9007. doi: 10.1103/PhysRevLett.106.206801. URL <http://link.aps.org/doi/10.1103/PhysRevLett.106.206801>.
- [66] J. Stehlik, Y. Dovzhenko, J. R. Petta, J. R. Johansson, F. Nori, H. Lu, and a. C. Gossard. Landau-Zener-Stückelberg interferometry of a single electron charge qubit. *Physical Review B*, 86(12):121303, September 2012. ISSN 1098-0121. doi: 10.1103/PhysRevB.86.121303. URL <http://link.aps.org/doi/10.1103/PhysRevB.86.121303>.
- [67] E. Dupont-Ferrier, B. Roche, B. Voisin, X. Jehl, R. Wacquez, M. Vinet, M. Sanquer, and Silvano De Franceschi. Coherent Coupling of Two Dopants in a Silicon Nanowire Probed by Landau-Zener-Stückelberg Interferometry. *Physical Review Letters*, 110(13):136802, March 2013. ISSN 0031-9007. doi: 10.1103/PhysRevLett.110.136802. URL <http://link.aps.org/doi/10.1103/PhysRevLett.110.136802>.
- [68] Jeroen M Elzerman, R. Hanson, and LHW Van Beveren. Single-shot read-out of an individual electron spin in a quantum dot. *Nature*, 430(July):431–435, 2004. doi: 10.1038/nature02747.1. URL <http://www.nature.com/nature/journal/vaop/ncurrent/abs/nature02693.html>.
- [69] K Ono, D G Austing, Y Tokura, and Seigo Tarucha. Current rectification by Pauli exclusion in a weakly coupled double quantum dot system. *Science (New York,*

- N.Y.), 297(5585):1313–7, August 2002. ISSN 1095-9203. doi: 10.1126/science.1070958. URL <http://www.sciencemag.org/content/297/5585/1313.short>.
- [70] J. R. Petta, H Lu, and A C Gossard. A coherent beam splitter for electronic spin states. *Science (New York, N.Y.)*, 327(5966):669–72, February 2010. ISSN 1095-9203. doi: 10.1126/science.1183628. URL <http://www.sciencemag.org/content/327/5966/669.abstract>.
- [71] K. C. Nowack, M Shafiei, M Laforest, G E D K Prawiroatmodjo, L R Schreiber, C Reichl, W Wegscheider, and L. M. K. Vandersypen. Single-shot correlations and two-qubit gate of solid-state spins. *Science (New York, N.Y.)*, 333(6047):1269–72, September 2011. ISSN 1095-9203. doi: 10.1126/science.1209524. URL <http://www.sciencemag.org/content/333/6047/1269.abstract>.
- [72] F H L Koppens, C Buizert, K J Tielrooij, I T Vink, K. C. Nowack, Tristan Meunier, Leo. P. Kouwenhoven, and L. M. K. Vandersypen. Driven coherent oscillations of a single electron spin in a quantum dot. *Nature*, 442(7104):766–71, August 2006. ISSN 1476-4687. doi: 10.1038/nature05065. URL <http://dx.doi.org/10.1038/nature05065>.
- [73] S. Nadj-Perge, S. M. Frolov, E. P. A. M. Bakkers, and Leo. P. Kouwenhoven. Spin-orbit qubit in a semiconductor nanowire. *Nature*, 468(7327):1084–7, December 2010. ISSN 1476-4687. doi: 10.1038/nature09682. URL <http://dx.doi.org/10.1038/nature09682>.
- [74] S. Nadj-Perge, V. S. Pribiag, J. W. G. van den Berg, K. Zuo, S. R. Plissard, E. P. A. M. Bakkers, S. M. Frolov, and Leo. P. Kouwenhoven. Spectroscopy of Spin-Orbit Quantum Bits in Indium Antimonide Nanowires. *Physical Review Letters*, 108(16):166801, April 2012. ISSN 0031-9007. doi: 10.1103/PhysRevLett.108.166801. URL <http://link.aps.org/doi/10.1103/PhysRevLett.108.166801>.
- [75] E.A. Laird, F Pei, and Leo. P. Kouwenhoven. A valley-spin qubit in a carbon nanotube. *Nature nanotechnology*, 8(8):565–8, August 2013. ISSN 1748-3395. doi: 10.1038/nnano.2013.140. URL <http://dx.doi.org/10.1038/nnano.2013.140>.
- [76] J Medford, J Beil, J M Taylor, S D Bartlett, A C Doherty, E I Rashba, D P DiVincenzo, H Lu, A C Gossard, and C M Marcus. Self-consistent measurement and state tomography of an exchange-only spin qubit. *Nature nanotechnology*, 8 (9):654–9, September 2013. ISSN 1748-3395. doi: 10.1038/nnano.2013.168. URL <http://dx.doi.org/10.1038/nnano.2013.168>.
- [77] Yun-Sok Shin, Toshiaki Obata, Yasuhiro Tokura, Michel Pioro-Ladrière, Roland Brunner, Toshihiro Kubo, Katsuharu Yoshida, and Seigo Tarucha. Single-Spin

- Readout in a Double Quantum Dot Including a Micromagnet. *Physical Review Letters*, 104(4), January 2010. ISSN 0031-9007. doi: 10.1103/PhysRevLett.104.046802. URL <http://prl.aps.org/abstract/PRL/v104/i4/e046802>.
- [78] M. Pioro-Ladrière, T. Obata, Y. Tokura, Y.-S. Shin, Toshihiro Kubo, K. Yoshida, T. Taniyama, and Seigo Tarucha. Electrically driven single-electron spin resonance in a slanting Zeeman field. *Nature Physics*, 4(10):776–779, August 2008. ISSN 1745-2473. doi: 10.1038/nphys1053. URL <http://arxiv.org/abs/0805.1083>.
- [79] H. O. H. Churchill, F. Kuemmeth, J. W. Harlow, LHW Van Beveren, E. Rashba, K. Flensberg, C. Stwertka, T. Taychatanapat, S. K. Watson, and C. M. Marcus. Relaxation and Dephasing in a Two-Electron C13 Nanotube Double Quantum Dot. *Physical Review Letters*, 102(16):2–5, April 2009. ISSN 0031-9007. doi: 10.1103/PhysRevLett.102.166802. URL <http://link.aps.org/doi/10.1103/PhysRevLett.102.166802>.
- [80] Hendrik Bluhm, Sandra Foletti, Izhar Neder, Mark Rudner, Diana Mahalu, Vladimir Umansky, and Amir Yacoby. Dephasing time of GaAs electron-spin qubits coupled to a nuclear bath exceeding $200\mu s$. *Nature Physics*, 7(2):109–113, December 2010. ISSN 1745-2473. doi: 10.1038/nphys1856. URL <http://www.nature.com/doifinder/10.1038/nphys1856>.
- [81] Alexei M Tyryshkin, Shinichi Tojo, John J L Morton, Helge Riemann, Nikolai V Abrosimov, Peter Becker, Hans-Joachim Pohl, Thomas Schenkel, Michael L W Thewalt, Kohei M Itoh, and S A Lyon. Electron spin coherence exceeding seconds in high-purity silicon. *Nature materials*, 11(2):143–7, February 2012. ISSN 1476-1122. doi: 10.1038/nmat3182. URL <http://dx.doi.org/10.1038/nmat3182>.
- [82] C. Feuillet-Palma, T. Delattre, Pascal Morfin, J.-M. Berroir, G. Fève, D. C. Glattli, B. Plaçais, Audrey Cottet, and T. Kontos. Conserved spin and orbital phase along carbon nanotubes connected with multiple ferromagnetic contacts. *Physical Review B*, 81(11):115414, March 2010. ISSN 1098-0121. doi: 10.1103/PhysRevB.81.115414. URL <http://link.aps.org/doi/10.1103/PhysRevB.81.115414>.
- [83] Audrey Cottet, Takis Kontos, W Belzig, Christian Schönenberger, and Christoph Bruder. Controlling spin in an electronic interferometer with spin-active interfaces. *Europhysics Letters (EPL)*, 74(2):320–326, April 2006. ISSN 0295-5075. doi: 10.1209/epl/i2006-10006-0. URL <http://stacks.iop.org/0295-5075/74/i=2/a=320>.
- [84] Matthew Neeley, Radoslaw C Bialczak, M Lenander, E Lucero, Matteo Mariantoni, A D O’Connell, D Sank, H Wang, M Weides, J Wenner, Y Yin,

- T Yamamoto, A N Cleland, and John M Martinis. Generation of three-qubit entangled states using superconducting phase qubits. *Nature*, 467(7315):570–3, September 2010. ISSN 1476-4687. doi: 10.1038/nature09418. URL <http://dx.doi.org/10.1038/nature09418>.
- [85] Jien Cao, Qian Wang, and Hongjie Dai. Electron transport in very clean, as-grown suspended carbon nanotubes. *Nature materials*, 4(10):745–9, October 2005. ISSN 1476-1122. doi: 10.1038/nmat1478. URL <http://dx.doi.org/10.1038/nmat1478>.
- [86] Matthew S Marcus, Jason M Simmons, Sarah E Baker, Robert J Hamers, and Mark a Eriksson. Predicting the results of chemical vapor deposition growth of suspended carbon nanotubes. *Nano letters*, 9(5):1806–11, May 2009. ISSN 1530-6992. doi: 10.1021/nl803726b. URL <http://www.ncbi.nlm.nih.gov/pubmed/19338285>.
- [87] Chung Chiang Wu, Chang Hua Liu, and Zhaohui Zhong. One-step direct transfer of pristine single-walled carbon nanotubes for functional nanoelectronics. *Nano letters*, 10(3):1032–6, March 2010. ISSN 1530-6992. doi: 10.1021/nl904260k. URL <http://dx.doi.org/10.1021/nl904260k>.
- [88] J Chaste, L Lechner, Pascal Morfin, G Fèvre, T Kontos, J-M Berroir, D. C. Glattli, H Happy, P Hakonen, and B Plaçais. Single carbon nanotube transistor at GHz frequency. *Nano letters*, 8(2):525–8, February 2008. ISSN 1530-6984. doi: 10.1021/nl0727361. URL <http://dx.doi.org/10.1021/nl0727361>.
- [89] J. Basset, A. Yu. Kasumov, C. P. Moca, G. Zaránd, P. Simon, Hélène Bouchiat, and R. Deblock. Measurement of Quantum Noise in a Carbon Nanotube Quantum Dot in the Kondo Regime. *Physical Review Letters*, 108(4):046802, January 2012. ISSN 0031-9007. doi: 10.1103/PhysRevLett.108.046802. URL <http://link.aps.org/doi/10.1103/PhysRevLett.108.046802>.
- [90] L. G. Herrmann, F Portier, P Roche, A. Levy Yeyati, Takis Kontos, and C Strunk. Carbon nanotubes as cooper-pair beam splitters. *Physical review letters*, 104(2): 026801, January 2010. ISSN 1079-7114. URL <http://www.ncbi.nlm.nih.gov/pubmed/20366615>.
- [91] J. Schindele, A. Baumgartner, and C. Schönenberger. Near-Unity Cooper Pair Splitting Efficiency. *Physical Review Letters*, 109(15):157002, October 2012. ISSN 0031-9007. doi: 10.1103/PhysRevLett.109.157002. URL <http://link.aps.org/doi/10.1103/PhysRevLett.109.157002>.

- [92] H. O. H. Churchill. *Quantum Dots in Gated Nanowires and Nanotubes*. PhD thesis, 2012.
- [93] B. Gao, Y. Chen, M. Fuhrer, D. Glattli, and A. Bachtold. Four-Point Resistance of Individual Single-Wall Carbon Nanotubes. *Physical Review Letters*, 95(19):196802, October 2005. ISSN 0031-9007. doi: 10.1103/PhysRevLett.95.196802. URL <http://link.aps.org/doi/10.1103/PhysRevLett.95.196802>.
- [94] J. P. Cleuziou, N. G. NGuyen, S. Florens, and W. Wernsdorfer. Interplay of the Kondo Effect and Strong Spin-Orbit Coupling in Multihole Ultraclean Carbon Nanotubes. *Physical Review Letters*, 111(13):136803, September 2013. ISSN 0031-9007. doi: 10.1103/PhysRevLett.111.136803. URL <http://link.aps.org/doi/10.1103/PhysRevLett.111.136803>.
- [95] V. K. Sangwan, V. W. Ballarotto, M. S. Fuhrer, and E. D. Williams. Facile fabrication of suspended as-grown carbon nanotube devices. *Applied Physics Letters*, 93(11):113112, September 2008. ISSN 00036951. doi: 10.1063/1.2987457. URL <http://link.aip.org/link/?APPLAB/93/113112/1>.
- [96] D. Schuster, A. Wallraff, Alexandre Blais, L. Frunzio, R.-S. Huang, J. Majer, S. M. Girvin, and R. Schoelkopf. ac Stark Shift and Dephasing of a Superconducting Qubit Strongly Coupled to a Cavity Field. *Physical Review Letters*, 94(12):123602, March 2005. ISSN 0031-9007. doi: 10.1103/PhysRevLett.94.123602. URL <http://link.aps.org/doi/10.1103/PhysRevLett.94.123602>.
- [97] J. Majer, J M Chow, J M Gambetta, Jens Koch, B R Johnson, J A Schreier, L. Frunzio, D. Schuster, A A Houck, A. Wallraff, Alexandre Blais, M. H. Devoret, S. M. Girvin, and R. J. Schoelkopf. Coupling superconducting qubits via a cavity bus. *Nature*, 449(7161):443–7, September 2007. ISSN 1476-4687. doi: 10.1038/nature06184. URL <http://dx.doi.org/10.1038/nature06184>.
- [98] J. M. Fink, M. Göppl, M Baur, R. Bianchetti, P. J. Leek, Alexandre Blais, and A. Wallraff. Climbing the Jaynes-Cummings ladder and observing its nonlinearity in a cavity QED system. *Nature*, 454(7202):315–8, July 2008. ISSN 1476-4687. doi: 10.1038/nature07112. URL <http://dx.doi.org/10.1038/nature07112>.
- [99] Max Hofheinz, H. Wang, M. Ansmann, Radoslaw C. Bialczak, Erik Lucero, Matthew Neeley, A D O’Connell, D. Sank, J. Wenner, John M. Martinis, and Andrew N. Cleland. Synthesizing arbitrary quantum states in a superconducting resonator. *Nature*, 459(7246):546–9, May 2009. ISSN 1476-4687. doi: 10.1038/nature08005. URL <http://dx.doi.org/10.1038/nature08005>.

- [100] Gerhard Kirchmair, Brian Vlastakis, Zaki Leghtas, Simon E Nigg, Hanhee Paik, Eran Ginossar, Mazyar Mirrahimi, Luigi Frunzio, S. M. Girvin, and R J Schoelkopf. Observation of quantum state collapse and revival due to the single-photon Kerr effect. *Nature*, 495(7440):205–9, March 2013. ISSN 1476-4687. doi: 10.1038/nature11902. URL <http://dx.doi.org/10.1038/nature11902>.
- [101] G. Binnig and C. F. Quate. Atomic Force Microscope. *Physical Review Letters*, 56(9):930–933, March 1986. ISSN 0031-9007. doi: 10.1103/PhysRevLett.56.930. URL <http://link.aps.org/doi/10.1103/PhysRevLett.56.930>.
- [102] R. J. Abraham, J. Fisher, and P. Loftus. *Introduction to NMR Spectroscopy*. 1992.
- [103] A. Prêtre, H. Thomas, and M. Büttiker. Dynamic admittance of mesoscopic conductors: Discrete-potential model. *Physical Review B*, 54(11):8130–8143, September 1996. ISSN 0163-1829. doi: 10.1103/PhysRevB.54.8130. URL <http://link.aps.org/doi/10.1103/PhysRevB.54.8130>.
- [104] S. J. Chorley, J. Wabnig, Z. V. Penfold-Fitch, K. D. Petersson, Nathan R. Franklin, C. G. Smith, and M. R. Buitelaar. Measuring the complex admittance of a carbon nanotube double quantum dot. page 4, September 2011. URL <http://arxiv.org/abs/1109.1827>.
- [105] Erik Lucero, R. Barends, Yu Chen, J. Kelly, M. Mariantoni, A. Megrant, P. O’Malley, D. Sank, A. Vainsencher, J. Wenner, T. White, Y. Yin, Andrew N. Cleland, and John M. Martinis. Computing prime factors with a Josephson phase qubit quantum processor. *Nature Physics*, advance on, August 2012. ISSN 1745-2473. doi: 10.1038/nphys2385. URL <http://dx.doi.org/10.1038/nphys2385>.
- [106] Mircea Trif, Vitaly N. Golovach, and Daniel Loss. Spin dynamics in InAs nanowire quantum dots coupled to a transmission line. *Physical Review B*, 77(4), January 2008. ISSN 1098-0121. doi: 10.1103/PhysRevB.77.045434. URL <http://prb.aps.org/abstract/PRB/v77/i4/e045434>.
- [107] Pei-Qing Jin, Michael Marthaler, Alexander Shnirman, and Gerd Schön. Strong Coupling of Spin Qubits to a Transmission Line Resonator. *Physical Review Letters*, 108(19):5, May 2012. ISSN 0031-9007. doi: 10.1103/PhysRevLett.108.190506. URL <http://link.aps.org/doi/10.1103/PhysRevLett.108.190506>.
- [108] L. Childress, A. Sørensen, and M. Lukin. Mesoscopic cavity quantum electrodynamics with quantum dots. *Physical Review A*, 69(4):042302, April 2004. ISSN 1050-2947. doi: 10.1103/PhysRevA.69.042302. URL <http://link.aps.org/doi/10.1103/PhysRevA.69.042302>.

- [109] Guido Burkard and Atac Imamoglu. Ultra-long-distance interaction between spin qubits. *Physical Review B*, 74(4):041307, July 2006. ISSN 1098-0121. doi: 10.1103/PhysRevB.74.041307. URL <http://link.aps.org/doi/10.1103/PhysRevB.74.041307>.
- [110] Sylvain Hermelin, Shintaro Takada, Michihisa Yamamoto, Seigo Tarucha, Andreas D Wieck, Laurent Saminadayar, Christopher Bäuerle, and Tristan Meunier. Electrons surfing on a sound wave as a platform for quantum optics with flying electrons. *Nature*, 477(7365):435–8, September 2011. ISSN 1476-4687. doi: 10.1038/nature10416. URL <http://dx.doi.org/10.1038/nature10416>.
- [111] Michihisa Yamamoto, Shintaro Takada, Christopher Bäuerle, Kenta Watanabe, Andreas D Wieck, and Seigo Tarucha. Electrical control of a solid-state flying qubit. *Nature nanotechnology*, 7(4):247–251, March 2012. ISSN 1748-3395. doi: 10.1038/nnano.2012.28. URL <http://dx.doi.org/10.1038/nnano.2012.28>.
- [112] Luka Trifunovic, Oliver Dial, Mircea Trif, James R. Wootton, Rediet Abebe, Amir Yacoby, and Daniel Loss. Long-Distance Spin-Spin Coupling via Floating Gates. *Physical Review X*, 2(1):011006, January 2012. ISSN 2160-3308. doi: 10.1103/PhysRevX.2.011006. URL <http://link.aps.org/doi/10.1103/PhysRevX.2.011006>.
- [113] P. Goy, J. Raimond, M. Gross, and S. Haroche. Observation of Cavity-Enhanced Single-Atom Spontaneous Emission. *Physical Review Letters*, 50(24):1903–1906, June 1983. ISSN 0031-9007. doi: 10.1103/PhysRevLett.50.1903. URL <http://link.aps.org/doi/10.1103/PhysRevLett.50.1903>.
- [114] A D O’Connell, Max Hofheinz, M. Ansmann, Radoslaw C. Bialczak, M. Lenander, Erik Lucero, Matthew Neeley, D. Sank, H. Wang, M. Weides, J. Wenner, John M. Martinis, and Andrew N. Cleland. Quantum ground state and single-phonon control of a mechanical resonator. *Nature*, 464(7289):697–703, April 2010. ISSN 1476-4687. doi: 10.1038/nature08967. URL <http://dx.doi.org/10.1038/nature08967>.
- [115] Joerg Bochmann, Amit Vainsencher, D. Awschalom, and Andrew N. Cleland. Nanomechanical coupling between microwave and optical photons. *Nature Physics*, September 2013. ISSN 1745-2473. doi: 10.1038/nphys2748. URL <http://www.nature.com/nphys/journal/vaop/ncurrent/pdf/nphys2748.pdf>.
- [116] M. Goppl, A Fragner, M Baur, R. Bianchetti, S Filipp, J. M. Fink, P. J. Leek, G Puebla, L Steffen, and A. Wallraff. Coplanar waveguide resonators for circuit quantum electrodynamics. *Journal of Applied Physics*, 104(11):113904, 2009. ISSN

- 0021-8979. URL http://ieeexplore.ieee.org/xpls/abs_all.jsp?arnumber=4919088.
- [117] M.R. Delbecq. *Coupling quantum dots to microwave cavities*. PhD thesis, 2013.
- [118] Audrey Cottet, Christophe Mora, and Takis Kontos. Mesoscopic admittance of a double quantum dot. *Physical Review B*, 83(12):1–4, March 2011. ISSN 1098-0121. doi: 10.1103/PhysRevB.83.121311. URL <http://link.aps.org/doi/10.1103/PhysRevB.83.121311>.
- [119] K. D. Petersson, C G Smith, D Anderson, P Atkinson, G A C Jones, and D A Ritchie. Charge and spin state readout of a double quantum dot coupled to a resonator. *Nano letters*, 10(8):2789–93, August 2010. ISSN 1530-6992. doi: 10.1021/nl100663w. URL <http://dx.doi.org/10.1021/nl100663w>.
- [120] T. Frey, P. J. Leek, M. Beck, J. Faist, A. Wallraff, K. Ensslin, T. Ihn, and M. Büttiker. Quantum dot admittance probed at microwave frequencies with an on-chip resonator. *Physical Review B*, 86(11):115303, September 2012. ISSN 1098-0121. doi: 10.1103/PhysRevB.86.115303. URL <http://link.aps.org/doi/10.1103/PhysRevB.86.115303>.
- [121] K. Wang, C. Payette, Y. Dovzhenko, P. W. Deelman, and J. R. Petta. Charge Relaxation in a Single-Electron Si/SiGe Double Quantum Dot. *Physical Review Letters*, 111(4):046801, July 2013. ISSN 0031-9007. doi: 10.1103/PhysRevLett.111.046801. URL <http://link.aps.org/doi/10.1103/PhysRevLett.111.046801>.
- [122] D. Walls and G. Milburn. *Quantum Optics*. 1994.
- [123] L. E. Bruhat, J. J. Viennot, M.R. Delbecq, R. Lopez, D. Sanchez, Audrey Cottet, and T. Kontos. Charge relaxation in an interacting quantum RC circuit. *In preparation*.
- [124] M. D. Schroer, M. Jung, K. D. Petersson, and J. R. Petta. Radio Frequency Charge Parity Meter. *Physical Review Letters*, 109(16), October 2012. ISSN 0031-9007. doi: 10.1103/PhysRevLett.109.166804. URL <http://link.aps.org/doi/10.1103/PhysRevLett.109.166804>.
- [125] K. W. Murch, U. Vool, D. Zhou, S. J. Weber, S. M. Girvin, and I. Siddiqi. Cavity-Assisted Quantum Bath Engineering. *Physical Review Letters*, 109(18):183602, October 2012. ISSN 0031-9007. doi: 10.1103/PhysRevLett.109.183602. URL <http://link.aps.org/doi/10.1103/PhysRevLett.109.183602>.
- [126] A. A. Clerk, S. M. Girvin, Florian Marquardt, and R. J. Schoelkopf. Introduction to quantum noise, measurement, and amplification. *Reviews of Modern Physics*,

- 82(2):1155–1208, April 2010. URL http://rmp.aps.org/abstract/RMP/v82/i2/p1155_1.
- [127] Shanhui Fan, Wonjoo Suh, and J. D. Joannopoulos. Temporal coupled-mode theory for the Fano resonance in optical resonators. *Journal of the Optical Society of America A*, 20(3):569, 2003. ISSN 1084-7529. doi: 10.1364/JOSAA.20.000569. URL <http://josaa.osa.org/abstract.cfm?URI=josaa-20-3-569>.
- [128] Vladimir E. Manucharyan, Nicholas A. Masluk, Archana Kamal, Jens Koch, Leonid I. Glazman, and Michel H. Devoret. Evidence for coherent quantum phase slips across a Josephson junction array. *Physical Review B*, 85(2):024521, January 2012. ISSN 1098-0121. doi: 10.1103/PhysRevB.85.024521. URL <http://link.aps.org/doi/10.1103/PhysRevB.85.024521>.
- [129] Audrey Cottet. *Implementation of a quantum bit in a superconducting circuit*. PhD thesis, 2002.
- [130] G. Ithier, E. Collin, P. Joyez, P. Meeson, D. Vion, D. Esteve, F. Chiarello, A. Shnirman, Y. Makhlin, J. Schrieffl, and G. Schön. Decoherence in a superconducting quantum bit circuit. *Physical Review B*, 72(13):134519, October 2005. ISSN 1098-0121. doi: 10.1103/PhysRevB.72.134519. URL <http://link.aps.org/doi/10.1103/PhysRevB.72.134519>.
- [131] François Mallet, Florian R. Ong, Agustin Palacios-Laloy, François Nguyen, Patrice Bertet, Denis Vion, and Daniel Esteve. Single-shot qubit readout in circuit quantum electrodynamics. *Nature Physics*, 5(11):791–795, September 2009. ISSN 1745-2473. doi: 10.1038/nphys1400. URL <http://dx.doi.org/10.1038/nphys1400>.
- [132] R. Vijay, DH Slichter, and I. Siddiqi. Observation of Quantum Jumps in a Superconducting Artificial Atom. *Physical Review Letters*, 106(11), March 2011. ISSN 0031-9007. doi: 10.1103/PhysRevLett.106.110502. URL <http://prl.aps.org/abstract/PRL/v106/i11/e110502>.
- [133] Claude Cohen-Tannoudji, Jacques Dupont-Roc, and Grynberg Gilbert. *Photons and Atoms: Introduction to Quantum Electrodynamics*. 1997.
- [134] J.-Y. Chauleau, B. J. McMorran, R. Belkhou, N. Bergeard, T. O. Mente, M.Á. Niño, A. Locatelli, J. Unguris, S. Rohart, J. Miltat, and A. Thiaville. Magnetization textures in NiPd nanostructures. *Physical Review B*, 84(9):094416, September 2011. ISSN 1098-0121. doi: 10.1103/PhysRevB.84.094416. URL <http://link.aps.org/doi/10.1103/PhysRevB.84.094416>.

- [135] M. Julliere. Tunneling between ferromagnetic films. *Physics Letters A*, 54(3):225–226, September 1975. ISSN 03759601. doi: 10.1016/0375-9601(75)90174-7. URL <http://www.sciencedirect.com/science/article/pii/0375960175901747>.
- [136] Matthias Braun, Jürgen König, and Jan Martinek. Theory of transport through quantum-dot spin valves in the weak-coupling regime. *Physical Review B*, 70(19):195345, November 2004. ISSN 1098-0121. doi: 10.1103/PhysRevB.70.195345. URL <http://link.aps.org/doi/10.1103/PhysRevB.70.195345>.
- [137] A.D. Crisan, S. Datta, J. J. Viennot, M.R. Delbecq, Audrey Cottet, and T. Kontos. Current induced magnetoresistance reversal in a quantum dot. *In preparation*, 2014.
- [138] T. S. Jespersen, K. Grove-Rasmussen, J. Paaske, K. Muraki, T. Fujisawa, J. Nygård, and K. Flensberg. Gate-dependent spinorbit coupling in multielectron carbon nanotubes. *Nature Physics*, 7(4):348–353, January 2011. ISSN 1745-2473. doi: 10.1038/nphys1880. URL <http://dx.doi.org/10.1038/nphys1880>.
- [139] R. Leturcq, Christoph Stampfer, Kevin Inderbitzin, Lukas Durrer, Christofer Hierold, Eros Mariani, Maximilian G. Schultz, Felix von Oppen, and Klaus Ensslin. FranckCondon blockade in suspended carbon nanotube quantum dots. *Nature Physics*, 5(5):327–331, April 2009. ISSN 1745-2473. doi: 10.1038/nphys1234. URL <http://dx.doi.org/10.1038/nphys1234>.
- [140] Audrey Cottet, Takis Kontos, and Alfredo Yeyati. Subradiant Split Cooper Pairs. *Physical Review Letters*, 108(16), April 2012. ISSN 0031-9007. doi: 10.1103/PhysRevLett.108.166803. URL <http://prl.aps.org/abstract/PRL/v108/i16/e166803>.
- [141] Audrey Cottet. Microwave spectroscopy of a Cooper pair beam splitter. *Physical Review B*, 86(7):075107, August 2012. ISSN 1098-0121. doi: 10.1103/PhysRevB.86.075107. URL <http://link.aps.org/doi/10.1103/PhysRevB.86.075107>.
- [142] A Yu Kitaev. Unpaired Majorana fermions in quantum wires. *Physics-Uspekhi*, 44(10S):131–136, October 2001. ISSN 1468-4780. doi: 10.1070/1063-7869/44/10S/S29. URL <http://stacks.iop.org/1063-7869/44/i=10S/a=S29>.
- [143] Yuval Oreg, Gil Refael, and Felix von Oppen. Helical Liquids and Majorana Bound States in Quantum Wires. *Physical Review Letters*, 105(17):177002–, October 2010. ISSN 0031-9007. doi: 10.1103/PhysRevLett.105.177002. URL <http://link.aps.org/doi/10.1103/PhysRevLett.105.177002>.

- [144] V Mourik, K Zuo, S M Frolov, S R Plissard, E. P. A. M. Bakkers, and Leo. P. Kouwenhoven. Signatures of Majorana fermions in hybrid superconductor-semiconductor nanowire devices. *Science (New York, N.Y.)*, 336(6084):1003–7, May 2012. ISSN 1095-9203. doi: 10.1126/science.1222360. URL <http://www.sciencemag.org/content/336/6084/1003.abstract>.
- [145] Anindya Das, Yuval Ronen, Yonatan Most, Yuval Oreg, Moty Heiblum, and Hadas Shtrikman. Zero-bias peaks and splitting in an AlInAs nanowire topological superconductor as a signature of Majorana fermions. *Nature Physics*, 8(12):887–895, November 2012. ISSN 1745-2473. doi: 10.1038/nphys2479. URL <http://dx.doi.org/10.1038/nphys2479>.
- [146] Mircea Trif and Yaroslav Tserkovnyak. Resonantly Tunable Majorana Polariton in a Microwave Cavity. *Physical Review Letters*, 109(25):257002, December 2012. ISSN 0031-9007. doi: 10.1103/PhysRevLett.109.257002. URL <http://link.aps.org/doi/10.1103/PhysRevLett.109.257002>.
- [147] Audrey Cottet, Takis Kontos, and Benoit Douçot. Squeezing light with Majorana fermions. *Physical Review B*, 88(19):195415, November 2013. ISSN 1098-0121. doi: 10.1103/PhysRevB.88.195415. URL <http://link.aps.org/doi/10.1103/PhysRevB.88.195415>.